UNIVERSITÀ DEL SALENTO

DIPARTIMENTO DI FISICA

Dottorato di ricerca in FISICA

TESI DI DOTTORATO

AEROSOL CHARACTERIZATION BY GROUND- AND SATELLITE- BASED REMOTE SENSING TECHNIQUES

Tutore:

Ch.ma Prof.ssa Maria Rita Perrone

Co-Tutore:

Dott. Ferdinando De Tomasi

DOTTORANDA:

Monica Santese

XX CICLO

CONTENTS

INTRODUCTION

During the last years, several studies have demonstrated that climate changes are the results of both feedback processes inside the climate System and natural and anthropogenic factors that have important effects on the Earth's energy balance called 'radiative forcing'. Natural and anthropogenic aerosols represent one of the main atmospheric components responsible of the Earth-Atmospheric System climate changes. Aerosols influence the climate via two ways: the direct effect by scattering and absorbing incoming solar radiation, and the indirect effect which modify the microphysical and hence the radiative properties, amount and lifetime of clouds (Schwartz, 1996). As a consequence of the aerosols short lifetime (figure i.1) and of their high spatial and temporal variability, the uncertainty of estimating human-induced aerosol forcing in climate is very high.

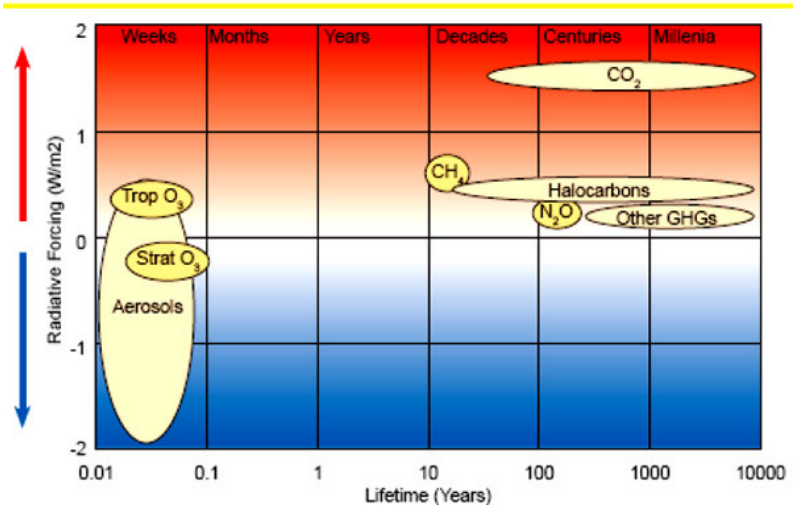

Figure i.1. Radiative forcings and lifetimes of the principal atmospheric components

In accordance with the Working Group I of the *Intergovernmental Panel of Climate Change* (IPCC-WKG1) Fourth Assessment Report (IPCC, 2007) anthropogenic contributions to aerosols produce a cooling effect with a total direct radiative forcing of -0.5 W/m². The

scientific understanding of the direct and indirect effects of aerosols obtained in the year 2007 is better than that reported in the year 2005 (figure i.2). However, the need to obtain a global characterization of the aerosol distribution represents one of the major challenges today (Kaufman et al., 2002).

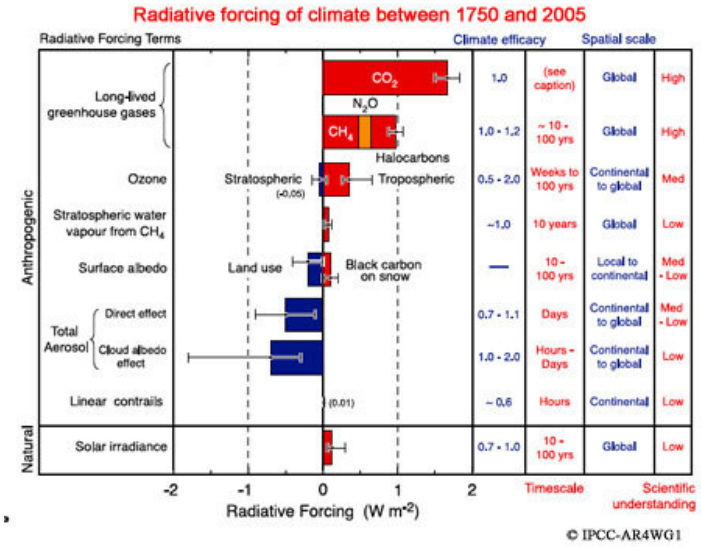

Figure i.2. Global mean radiative forcings of climate from year 1750 to 2005.

The approaches seek to combine satellite and surface-based observations to provide near-global retrievals of aerosol properties.

Renewed interest and greater understanding of aerosol processes have necessitated an emphasis in monitoring by ground remote sensing approaches. For instance, the Aerosol Robotic Network (AERONET), a federate network of more than 400 automatic sun/sky radiometers worldwide (Holben et al., 1998), is the most globally distributed ground based system resulting in a database of widely variable atmospheric conditions.

In contrast to ground-based instruments that acquire continuous measurements at fixed locations, polar-orbiting sun-synchronous satellite sensors provide a global coverage at nearly constant local solar times, once or twice a day in tropics to mid latitude and multiple

overpasses in polar regions (Chu et al., 2003). Therefore, operational remote sensing of aerosols from long term satellites provides a means to achieve a global and seasonal characterization of aerosols. Satellite sensors view the entire earth and produce global images thus resolving the spatial patterns resulting from the spatial inhomogeneities of aerosol sources. In particular, the Moderate Resolution Imaging Spectroradiometer (MODIS) onboard NASA's Earth Observing System has a sufficient spectral diversity and the ability to separate aerosols by size that can be used as a proxy for separating human-generated aerosol from natural sources, which aids substantially in estimating global human-induced aerosol forcing (Kaufman et al., 2002).

Moreover, to estimate the effects of the aerosols on climate, regional and global scale chemical transport models have been developed based on several processes including emission, transport, conversion and removal. The development of modelling tools capable to assessing the impacts of human activities on the regional/global climate and air quality, represents a major scientific challenge to the community of atmospheric scientists, as well as an important need for policymakers in order to design strategies for mitigating adverse environmental impacts.

The main goal of this PhD thesis is to contribute to the characterization of the main optical and microphysical properties of the aerosols of different types over the Mediterranean basin. To this aim, data from passive and active remote sensing measurements performed at the University of Salento of Lecce , on south-east Italy, (40.33ºN, 18.10ºE) and simulations made with a regional climate model (RegCM) have been used. Lecce offers a good opportunity to study aerosols from different sources, being away from large cities and industrial areas, ~ 20 km away from the Adriatic and Ionian Seas and ~ 800 km away from the African coast.

The Mediterranean basin had a particular relevance in this research activity as this area is particularly affected by air pollution. In addition to sea-spray aerosols and mineral dust

particles from North Africa, long-range transported urban/industrial and biomass burning aerosols from Northern and Eastern Europe regions converge in the Mediterranean. As a consequence, several studies indicate that the aerosol radiative forcing is among the highest in the world over the Mediterranean summer (e.g. Haywood and Boucher, 2000; Lelieveld et al., 2002; Andreae et al., 2002). A Regional Climate Change Index (RCCI) has been defined by Giorgi (2006) to identify the most responsive regions to climate changes, or Hot-Spot. According to Giorgi (2006), the two most prominent Hot-Spots emerging from the RCCI analysis are the Mediterranean and North Eastern Europe regions.

In the research activities of the PhD course retrievals from the AERONET sunphotometer have been analyzed to retrieve both optical (e.g. aerosol optical depth) and microphysical (columnar volume size distribution, refractive indices,..) aerosol properties. Moreover, satellite retrievals (aerosol optical depth, fine fraction parameter, volume size distribution..) are correlated with corresponding aerosol retrievals to contribute to the validation of MODIS aerosol products and to understand to what extent the Lecce's AERONET site can be considered representative of a larger area. Finally, a regional climate model (RegCM) has been used to perform a simulation of a dust event and to compare modelled and experimental data.

In Chapter 1 of this thesis the AERONET sun/sky radiometer operating at Lecce will be described and an example of AERONET aerosol parameters for two days characterized by different advection patterns will be provided.

In Chapter 2 some results on the temporal evolution of the main AERONET aerosol parameters retrieved for the year 2006 will be presented.

Chapter 3 will be devoted to provide results on the aerosol characterization over the Mediterranean analyzing one year of AERONET measurements performed from March 2003 to March 2004.

In Chapter 4 aerosol measurements from the AERONET station in Lecce combined with five-day backtrajectories will be analyzed to study the mixing of different aerosol types over the Mediterranean.

Chapter 5 will be report a description of the MODIS Sensor Instrument design onboard the EOS Terra and Aqua satellites and the MODIS retrieval algorithms.

Chapter 6 will be devoted to comparison between AERONET sunphotometer measurements performed at Lecce with similar MODIS data retrieved at different spatial resolutions (50x50, 100x100 and 300x300 km²) around the AERONET monitoring site. The aim of this chapter will be to contribute to the validation of satellite's data and to understand to what extent locally-derived aerosol parameters can be of use in General Circulation and Chemical Transport Models (Kinne et al., 2003, Guibert et al., 2005).

The latter two chapters of this thesis, chapters 7 and 8, will be devoted to the characterization of aerosol properties during some Sahara dust events occurred in the Mediterranean.

In Chapter 7 MODIS aerosol products and corresponding AERONET data retrieved during Sahara dust outbreaks over four sites of the Mediterranean basin will be correlated.

In the last period of my PhD course the research activity has been devoted to the study and the implementation of a regional climate model (RegCM) with the aim to test the model performance in the Mediterranean area.

Chapter 8 will report the results obtained by the comparison between two model simulations made during a dust event over the Mediterranean and experimental data. The main objective of this chapter will be to test the RegCM model in order to contribute to the establishment of models more dependent on measurements.

Finally, concluding remarks will be given.

CHAPTER 1

THE AERONET SUNPHOTOMETER

Several studies have demonstrated in the past that the understanding of aerosols effects on climate is particularly difficult because aerosols are of quite different type and shape, ranging from desert dust to urban pollution, and because aerosol concentrations vary strongly over time and space. Aerosol parameters can be measured in situ or by remote sensing from ground, aircraft, or satellite. All these methods are important and complementary. The application of automatic, ground-based remote sensing techniques to investigate aerosol effects on climate has advanced significantly in the last years.

In particular, remotely measured atmospheric aerosol optical parameters are important for various applications including the validation of satellite remote sensing retrievals.

The Aerosol Robotic Network (AERONET) program, which is an international network founded in 1993 and coordinated by NASA Goddard Space Flight Center (http://aeronet.gsfc.nasa.gov/) and LOA-PHOTONS (http://www-loa.univ-lille1.fr/photons/) that maintains more than 400 automatic sun/sky radiometers worldwide (figure 1.1), represents two of the scientific community efforts to reduce existing uncertainties in aerosol forcing estimates (Holben et al., 1998).

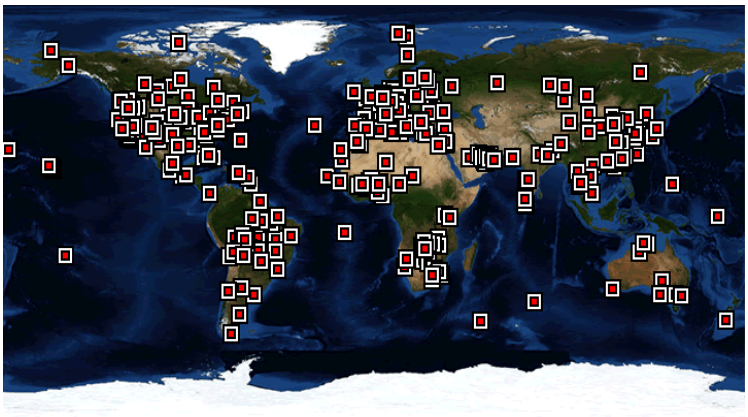

Figure 1.1. World-wide sun photometers of the AERONET Network.

The goal of AERONET is to assess aerosol optical properties and provide much of the ground-based validation data required for future remote sensing programs and may provide

basic information necessary for improved assessment of aerosols impact on climate forcing (Holben et a;l.,1998). To this end, the network imposes standardization of instruments, calibration, and processing. The AERONET program provides a long-term, continuous and readily accessible public domain database of aerosol optical, microphysical and radiative properties for aerosol research and characterization, validation of satellite retrievals, and synergism with other databases.

The AERONET sun/sky radiometer used in this work is located on the roof of the Physics Department of Salento's University, on a flat, sub-urban area of south-east of Italy, which is approximately 20 km away from both the Adriatic and the Ionic Seas and approximately 800 km from the North African coastas.

The CIMEL AERONET collaboration provides globally distributed observations of spectral aerosol optical depths (AOD), inversion products, and the precipitable water in diverse aerosol regimes. Aerosol optical depth data are computed for three data quality levels: Level 1.0 (unscreened), Level 1.5 (**cloud-screened**), and Level 2.0 (cloud-screened and **quality-assured**). In this study, cloud screened (level 1.5) and quality assured (level 2.0) retrievals from sun/sky radiometer measurements are used (Smirnov et al., 2000). Two different versions of a flexible inversion algorithm, Version1 (V1) and Version2 (V2), have been developed in the papers of Dubovik and King (2000a) and Dubovik at al., 2006, respectively. The processing algorithms have evolved from Version 1 to Version 2.0 (fully released in July 2006) and now are available from the AERONET and PHOTONS web sites. In particular, the V2 level 2 inversion products are released and available trough the AERONET web site since November 2006, while the V2 level 1.5 was being reprocessed later and was available since few weeks after November 2006. Inversion algorithms allow retrieving the columnar volume size distributions, refractive indices (n and k), and single scattering albedos SSAs from direct-sun and diffuse-sky radiance measurements. A brief discussion on the accuracy retrievals from V1 is reported in Dubovik et al, (2000b, 2002a),

Dubovik et al., 2004. In contrast, the accuracy criteria for V2 are not still available (http://aeronet.gsfc.nasa.gov/new_web/optical_properties.html).

In this chapter a brief description of the AERONET Cimel 318A sun/sky photometer used in this work is at first given. Then, V2 AERONET aerosol parameters obtained for two days characterized by different advection patterns are analyzed.

1.1. The Cimel 318A sun/sky photometer

The CIMEL Electronique 318A spectral radiometer manufactured in France is a solar-powered weather hardy robotically pointed sun and sky spectral radiometer. A sensor head fitted with 25 cm collimators is attached to a 40 cm robot base which systematically points the sensor head at the sun in accordance with a preprogrammed routine. The Cimel controller, batteries, and Vitel satellite transmission equipment are usually deployed in a weatherproof plastic case of 30 cm x 62 cm x 46 cm dimensions. The total weight of the Cimel sun photometer itself is approximately 15 kg, with an additional 22 kg contributed by the control box, battery, transmitter, the weatherproof case, and other materials.

The instrument has approximately a 1.2º full angle field of view and two detectors for measurements of direct sun, aureole, and sky radiance. The sun/aureole collimator is protected by a quartz window allowing observations with a UV enhanced silicon detector for spectral observations between 300 nm and 1020 nm.

Figure 1.2. Picture of the sun photometer located on the roof of the Physics Department of Salento's University.

The sky collimator has the same field of view, but an order of magnitude larger aperture-lens system allows better dynamic range for the sky radiances (Holben et al., 1998).

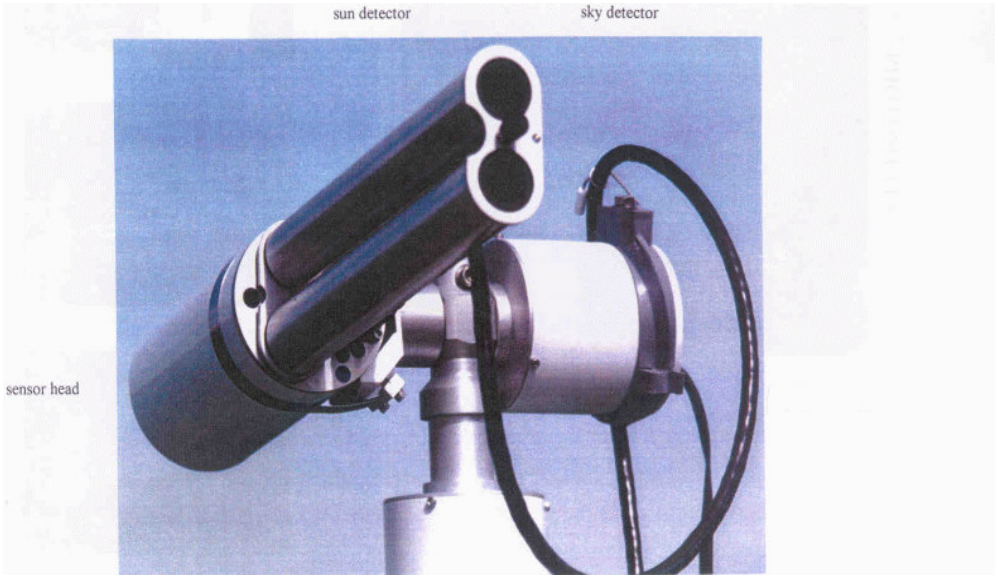

Figure 1.3. Main components of the Cimel 318A sun photometer.

The component of the sensor head (figure1.3) are sealed from moisture and desiccated to prevent damage to the electrical components and interference filters. The sensor head is pointed by stepping azimuth and zenith motors with a precision of 0.05º. A microprocessor

computes the position of the Sun based on time, latitude and longitude. After the routine measurement is completed, the instrument returns in the "park" position awaiting the next measurement sequence (figure 1.4).

The direct Sun measurements are made in eight spectral bands (between 340 and 1020 nm; 340, 380, 440, 500, 670, 870, 940, 1020 nm) and are used to calculate the aerosol optical depth AOD, the precipitable water, *PW*, and the Angstrom coefficient Å.

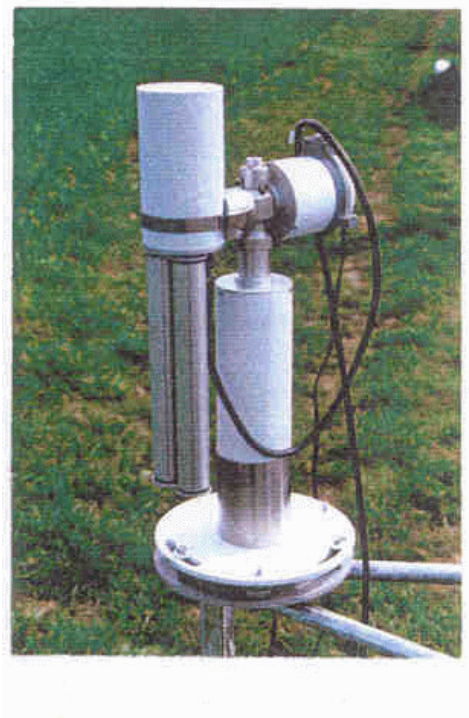

Figure 1.4. Park position of the sun photometer.

Sky measurements are performed at 440 nm, 670 nm, 870 nm, and 1020 nm and two basic sky observation sequences are made, the "almucantar" and the "principal plane". Both "almucantar" and "principal plane" measurements are nowadays inverted by inversion algorithm to retrieve aerosol size distributions (*dV/dlnr*), the real and imaginary refractive indices (*n* and *k*), the phase function (P(θ)), the aerosol optical depth (AOD) and the Angstrom coefficient (Å). The V2 version output provides new calculated aerosol parameters such as the spectral and broad-band fluxes and the radiative forcing.

A more detailed description on the sun photometer measurements concept and on the data transmission is reported in the paper of Holben et al., 1998.

1.1.1. Measurements Concepts

The radiometer makes only two basic measurements, either direct Sun or sky, both within several programmed sequences (Table 1.1). The direct Sun measurements are made in eight spectral bands (between 340 and 1020 nm; 340, 380, 440, 500, 670, 870, 940, 1020 nm) requiring approximately 10 s and the eight deposition interference filters are located in a filter wheel which is rotated by a direct drive stepping motor. A sequence of three such measurements are taken 30s apart, creating a triplet observation per wavelength that is used to calculate the aerosol optical depth AOD, the precipitable water, *PW*, and the Angstrom coefficient Å and for the cloud screening. The time variation of clouds are typically greater than that of aerosols, causing an observable variation in the triplets that can be used to screen clouds in many cases. Triplet standard observations are made during morning and afternoon at standard 15–min intervals in between and for an air mass between m =2 a.m. and m = 2 p.m., where the air mass is defined as m= sec Z, with Z representing the solar zenith angle (figure1.5).

The final sequence of direct sun measurements are called “Langley” and they allow the instrument calibration. During the large air mass periods (5<m<7) direct sun measurements are made at 0.5 mass intervals, while at smaller air masses (2<m<5) are made at 0.25 mass intervals.

Sky measurements are performed at 440 nm, 670 nm, 870 nm, and 1020 nm. A single spectral measurements sequence (Langly sky) is made immediately after the Langley airmass direct Sun measurements, 20 ° from the Sun.

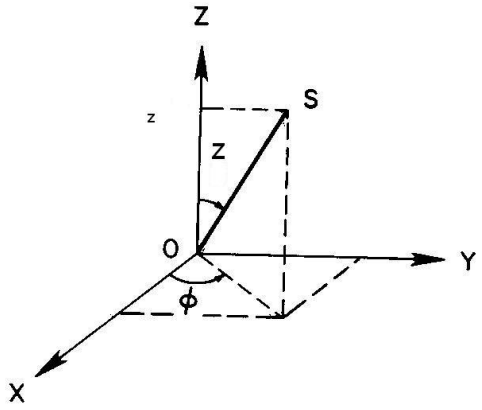

Figure 1.5. Spherical coordinates

This is used to assess the stability of the Langley plot analysis in accordance with O'Neill and Miller (1984). Two basic sky observation sequences are made, the "almucantar" and the "principal plane". The philosophy is to acquire aureole and sky radiances observations through a large range of scattering angles from the Sun and to retrieve the size distributions, the phase functions, and the aerosol optical thickness assuming a constant aerosol profile. An "almucantar" is a series of measurements taken at the elevation angle of the Sun for specified azimuth angles relative to the position of the Sun (figure 1.5). The range of scattering angles decrease as the solar zenith angle decreases.

During an "almucatar" measurement, observations from a single channel are made in a sweep at a constant elevation angle (Z) across the solar disk and continues trough 360º of the azimuth (φ) in about 40 s. This is repeated for each channel. 72 measurements are made daily during the "almucantar" sequences at an optical air masse of 4, 3, 2 and 1.7 both morning and afternoon and, an almucatar is made hourly between 9 a.m. and 3 p.m. local solar time.

The standard "principal plane" sequences measures in much the same manner as the "almucantar" but in the principal plane of the Sun at a constant azimuth angle φ, with varied scattering angles. This measurements sequences begins with a sun observation, moves 6º

below the solar disk, and then sweeps trough the sun taking about 30 s for each of the four spectral bands (Table 1.2). "Principal plane" observations are made hourly when the optical air mass is less than 2 to minimize the variations in radiance due to the change in optical air mass.

Data are trasmitted from the memory of the sun photometer via the Data Collection system (DCS) to the geostationary satellites GOES-E, GOES-W, or METEOSAT and then retransmitted to the appropriate ground receiving station. The data can be retrieved for processing either by modem or Internet linkage, resulting in near real-time acquisition from almost any site on the globe excluding poleward of 80º latitude. The DCS is a governmental system operated for the purpose of transmitting low volume environmental data from remote sites for various institutions and government agencies. Typically the data are maintained in the receiving station computers for 3-5 days before they are overwritten. The data are retrieved daily from the central receiving station which we term near real-time.

Table 1.1. Measurements sequences of the Cimel sun/sky scanning spectral radiometer

	Spectral range (nm)	Target	N.Observ.	Observ Interval	Application
Direct Sun					
Triplet observ	340/1020	Sun	3	3 at 30s apart	AOD,*PW*,Å,
Standard sequence	340/1020	Sun	variable:depend on the day length	ea.15 min, m=2a.m. to m=2 p.m.	AOD,*PW*,Å, Cloud screening
Langley	340/1020	Sun	18 ,between m=2 and m=7	m=7-5,incr.of 0.5 , m = 5-2,incr. of 0.25	Cal, AOD,*PW*,Å
Basic sky					
Langly sky of	440/1020	Sky	16 between m=7 and m=2	m=7-5, incr. of 0.5m M =5-2, incr.of 0.25m	stability Langley plot
Almucantar	440/1020	Sky	72	>8/day:m = 4,3,2,1.7 Hourly 9a.m. to 3 p.m.	*dV/dlnr, P(θ),*AOD*,* Å
Principal plane	440/1020	Sky	42	Hourly;9 a.m. to 3 p.m	*dV/dlnr, P(θ),*AOD*,* Å

Table 1.2. "Almucantar" and "Principal plane"sequences

	Sun	Sky
ALMUCANTAR azimuth angle relative to sun	0˚	6.0, 5.0, 4.5, 4.0, 3.5, 3.0, 2.5, 2.0, -2.0, -2.5, -3.0, -3.5, -4.0, -4.5, -5.0, -6.0, -8.0,-10.0, -12.0, -14.0, -16.0, -18.0, -20.0, -25.0, -30.0, -35.0, -40.0, -45.0, -50.0, -60.0, -70.0, -80.0, -90.0, -100.0, -110.0, -120.0, -130.0, -140.0, -160.0,-180.0
PRINCIPAL PLANE Scattering angle from sun	0˚	-6.0,-5.0,-4.5,-4.0,-3.5, -3.0,-2.5,- 2.0, 2.0 ,2.5,3.0, 3.5, 4.0, 4.5, 5.0, 6.0,8.0, 10.0, 12,0, 14.0, 16.0, 18.0, 20.0, 25.0, 30.0, 35.0, 40.0, 45.0, 50.0, 60.0, 70.0, 80.0, 90.0, 100.0, 110.0, 120.0, 130.0, 140.0

1.2. Examples of Sun photometer V2 retrievals

In this section sun photometer V2 aerosol parameters for two days (30 June and 27 July) of the 2006 year characterized by different advection patterns, are analyzed to show the sensitivity of sun photometer retrievals on aerosol properties and hence, on particles of different origin.

1.2.1 Satellite Images and analytical back-trajectories of 30 June 2006 and 27 July 2006

In order to highlight the sensitivity of the AERONET aerosol parameters on aerosol types, Aeronet retrievals of two days (30 June and 27 July) of the year 2006 characterized by aerosol masses of different origin and of about the same aerosol load are studied. The 7-day analytical back-trajectories relative to 30 June and 27 July, 2006 at 1200 UTC are reported in figure 1.6a and figure1.6b, respectively. The pressure level change as a function of time for each back trajectory is also shown in Figure 1.6.

The back trajectories are provided by NASA GSFC (http://www.aeronet.gsfc.nasa.gov/) for two arrival times (00:00 UTC and 12:00 UTC) and for six distinct arrival height levels (950, 850, 700, 500 hPa, 300 hPa and 200 hPa). In particular, in figure 1.5 only the back trajectories at four arrival height levels (950, 850, 700, and 500 hPa) are reported since lidar measurements at Lecce revealed that the aerosol load extends up to ~ 5 km from ground (De Tomasi et al., 2006).

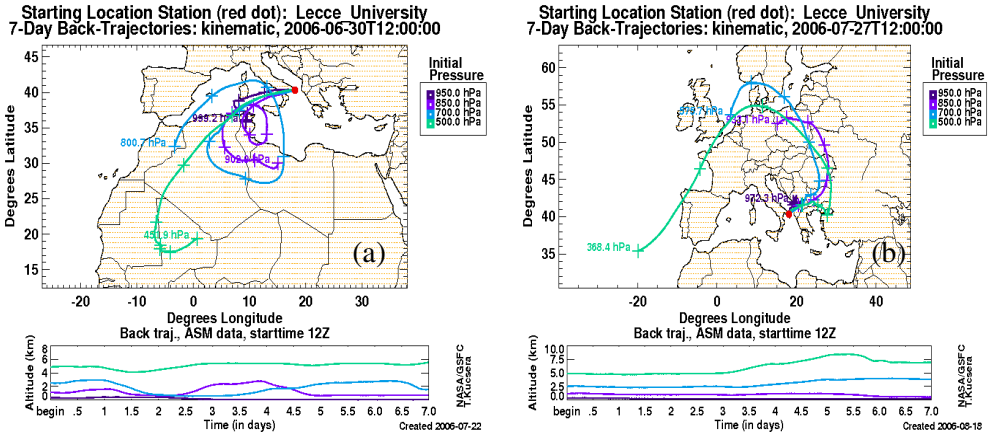

Figure 1.6. 5 –day analytical back trajectories at 950, 850, 700 and 500 hPa of (a) 30 June 2006 and (b) 27 July 2006 at 1200 UTC arrival time. Altitude change as a function of time of each back trajectory is also reported.

Figure1.6 clearly shows that the two investigated days are characterized by air masses with completely different origins: in particular, figure 1.6a shows that on 30 June 2006 the air

masses from North Africa are advected over Lecce. In contrast, figure 1.6b shows that the 27 July 2006 was characterized by air masses coming from North, North-West Europe. Then, the back trajectories reported in figure 1.6a allow inferring that the 30 June 2006 was characterized by the advection of Sahara dust particles. The last hypothesis is supported by figures 1.7a and 1.7b that show the true colour images provided by the MODIS Sensor (http://modis-atmos.gsfc.nasa.gov./) on board the Terra satellite at 10:10 UTC (figure 1.7a) and the sensor on board the Aqua satellite at 11:45 UTC (figure 1.7b). Figures 1.7a and 1.7b show that the dust plume from North-west Africa was over Lecce during satellite overpasses. Figure 1.7c shows the MODIS Sensor image at 11:30 UTC by the Aqua satellite for the 27 July 2006. Figure 1.7c clearly shows the 27 July 2006 as a dust-free day.

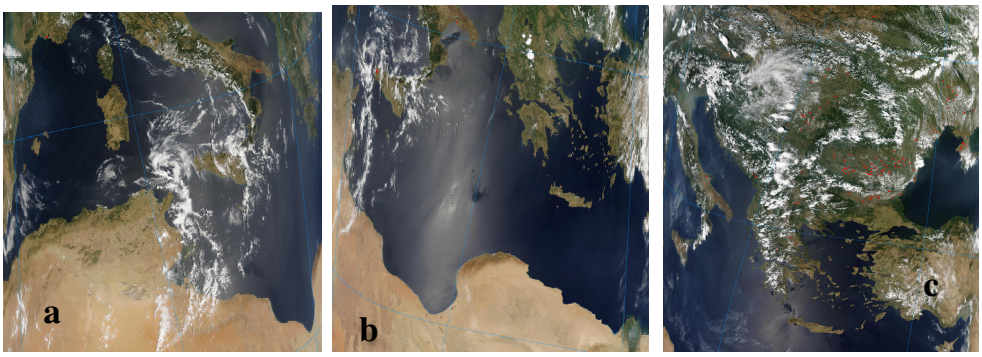

Figure 1.7. True color images provided by the Moderate Resolution Imaging Spectroradiometer (MODIS) sensor on board the NASA EOS (a) Terra Spacecraft at 1010 UTC on 30 June 2006 , (b) Aqua Spacecraft at 1145 UTC on 30 June 2006, (c) Aqua Spacecraft at 1130 UTC on 27 July 2006.

1.2.2 AERONET aerosol retrievals analysis on 30 June and 27 July 2006

In this paragraph, the evolutions of the V2 AERONET retrievals for the 30 June and the 27 July 2006 are considered to provide preliminary results from the V2 inversion algorithm. In particular, results are presented in terms of the temporal evolution of the aerosol optical

depth (AOD), the Angstrom exponent (Å), the fine fraction parameter (η), the real (*n*) and imaginary (*k*) refractive index, the single scattering albedo (SSA), the radiative forcing at the top of the atmosphere (TOA) and at the surface (BOA), and the radiative forcing efficiency (TOA and BOA). Seasonal volume size distributions are also reported.

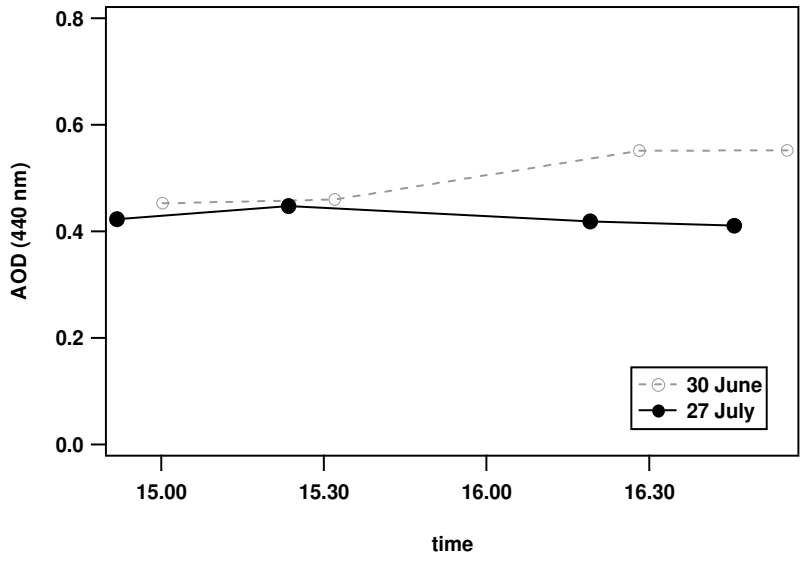

Figure 1.8. Aerosol optical depth AOD as function of the time for 30 June 2006 (dashed grey line) and 27 July 2006 (black solid line).

Figure 1.8 shows the AERONET aerosol optical depth AOD at 440 nm retrieved on 30 June 2006 (dashed grey line) and on 27 July 2006 (solid black line). The aerosol optical depth AOD is a parameter related to the aerosol load in atmosphere and it is calculated by sun photometer measurements using the following equation according to Beer-Bouger law (Liou, 1980):

$$I_{d\lambda} = I_{0\lambda} \exp(-m * AOD) \qquad (1.1)$$

Where $I_{d\lambda}$ is the direct spectral irradiance measured by the sun photometer, I_0 is the atmospheric spectral irradiance and *m* is the air mass (equal to secZ, with Z solar zenith angle).

We can note from figure 1.8 that on 27 July AODs vary in the range 0.41-0.45, while during the 30 June assume higher values between 0.46 and 0.55.

Figure 1.9 shows the fine fraction parameter (η) at 440 nm for different hours of the day retrieved on 30 June 2006 (dashed grey line) and on 27 July 2006 (solid black line) by the Lecce AERONET sun photometer measurements.

The AERONET V2 inversion algorithm allows retrieving aerosol volume distributions in the range sizes 0.05μm ≤ r ≤ 15 μm and the inversion code finds the minimum within the size interval from 0.194 μm to 0.576 μm. This minimum is used as a separation point between fine and coarse mode particles. η is the ratio between fine mode and total optical depth at 440 nm retrieved from AERONET measurements.

The fine fraction contribution to the total optical thickness is an important parameter to assess the climate impact of anthropogenic aerosols (Kaufmann et al., 2002): it helps us to discriminate natural aerosols (largely, mechanically-generated dust and sea salt particles) from anthropogenic ones (largely, combustion-generated sulfates, organics, and black carbon particles).

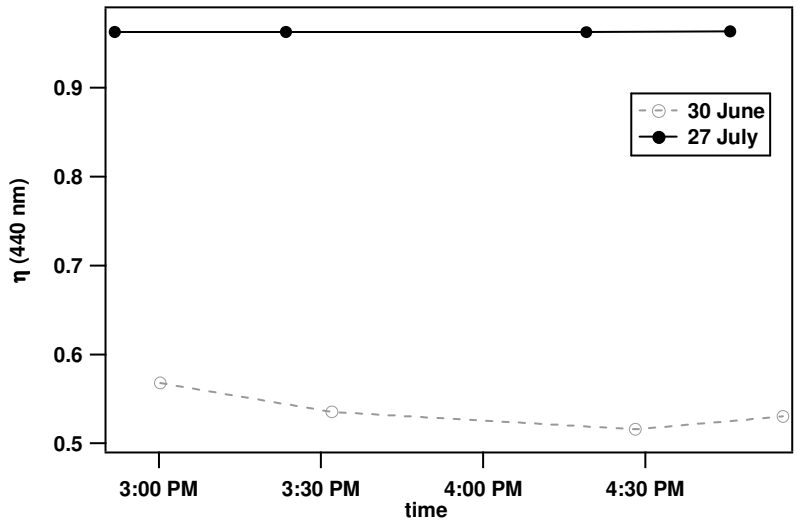

Figure 1.9. Fine fraction parameter η as function of the time for 30 June 2006 (dashed grey line) and 27 July 2006 (black solid line).

From figure 1.9 one can observe that η is characterized by quite different values during the two studied days. Infact η span the range 0.51 – 0.57 on 30 June 2006 and are ~ 0.96 on 27 July 2006. Hence, the latter results allow to suppose that, in accordance with the back trajectories of figure 1.6, fine-mode particles dominate during the day 27 July 2006, while the 30 June 2006 was characterized by a larger contribution of coarse-mode particles. Moreover, the values assumed by η on 27 July 2006 and 30 June 2006 (figure 1.9) are in good accordance with the values provided in literature for aerosol of continental and desert origin, respectively. The volume size distributions retrieved by AERONET measurements during the two investigated days are reported in figure 1.10a (30 June 2006) and 1.10b (27 July 2006) to further support the data of figure 1.9.

The volume particle size distribution $dV/dlnr$ ($\mu m^3 / \mu m^2$) is retrieved by the data V2 AERONET inversion algorithm in 22 logaritmically equidistant bins in the range sizes $0.005\mu m \leq r \leq 15\mu m$ and is defined as a bimodal lognormal function of the type:

$$\frac{dV(r)}{d\ln r} = \sum_{i=1}^{2} \frac{C_{v,i}}{\sqrt{2\pi}\sigma_i} \exp\left[-\frac{\left(\ln r - \ln r_{v,i}\right)}{2\sigma_i^{\,2}}\right] \qquad (1.2)$$

where $C_{v,i}$ denotes the particle volume concentration, $r_{v,i}$ is the median radius and σ_i is the standard deviation (Dubovik and King 2000a, Dubovik et al., 2000b).

Curves of different colors in figure 1.10 refer to different day hours. Figure 1.10 shows that the size distribution profiles retrieved for the two days differ significantly. On 30 June 2006 the contribution of coarse-mode particles is predominant and increases from the 15:00UTC up to the 16:55 UTC in the afternoon. In contrast, the contribution of coarse-mode particles is negligible on July 27. It worth noting that the peaks at 2.24 µm (figure 1.10a) and 0.19 µm (figure 1.10b) are typical of dust and continental aerosol, respectively (Santese et al., 2007, D'Almeida, 1991).

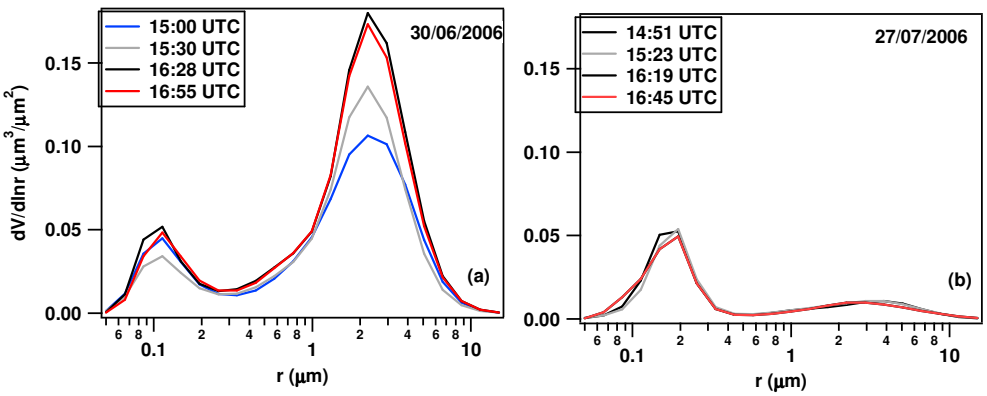

Figure 1.10. Volume size distribution profiles retrieved at (a) 30 June 2006 and (b) 27 July 2006. Curves of different colours correspond to different hours in the day.

The real *n* and imaginary *k* refractive index for the two investigated days are represented in figure 1.11. Larger *n* values lead to larger scattering coefficients, whereas larger *k* values lead to larger absorption coefficients.

One can observe from figure 1.11 that 30 June 2006 is characterized by *n* and *k* values in the range 1.43 – 1.53 and 0.005 – 0.01 respectively with a daily average of 1.47 ± 0.03 and 0.008 ± 0.002, respectively. On the contrast, on 27 July 2006 *n* varies between 1.46 – 1.51 and *k* between 0.009 – 0.016, with a daily average of 1.48 ± 0.01 and 0.013 ± 0.002, respectively.

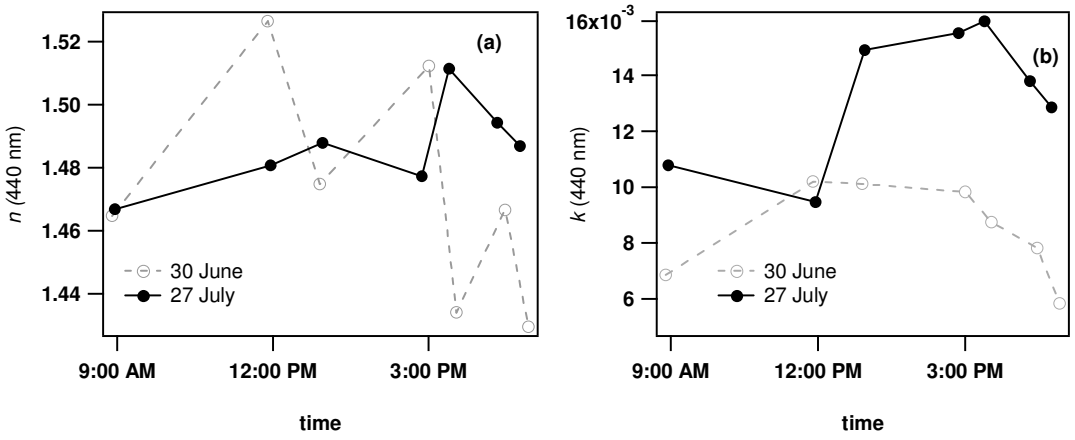

Figure 1.11. (a) Real part and (b) imaginary part of the refractive index as function of the time for 30 June 2006 (dashed grey line) and 27 July 2006 (black solid line).

Several models suggest that the real part of the refractive index of dust is 1.53 for the visible spectral region (Shettle and Fenn 1979, Koepke et al., 1997). However, the in situ measured values reported in the literature may deviate from 1.53 (due to the differences in the dust composition and probably also due to differences in the measurements techniques) with a range of about ± 0.05 or more (Patterson et al.,1997, Sokolik and Toon, 1999). Thus, the retrieved values on 30 June 2006 also agree in general with available dust measurements. Moreover, the results reported in this work for *k* on 30 June 2006 are in accordance with the 0.008 value given for the visible spectrum by several models (Shettle and Fenn 1979). The results shown in figure 1.11 for the 27 July 2006 agree with the results provided by independent studies for continental-type particles. Namely, the data estimated by Dubovik et al., 2002a for the 8 years-averaged values of *k* obtained worldwide are 0.003 ± 0.003 for GSFC Greenbelt, 0.009 ± 0.004 for Crete-Paris, 0.014 ± 0.006 for Mexico City and 0.011 ± 0.007 for Maldives: the three sites are all affected by industrial, urban aerosols.

The single scattering albedo depends on the chemical aerosol composition and, hence, it is linked to the real and imaginary refractive indices of aerosol particles.

The single scattering albedo is a parameter that depends on scattering and absorption properties of atmospheric particles and it is 0 and 1 for absorbent and non-absorbent aerosol, respectively. It is defined as:

$$\omega = \frac{C_{scat}}{C_{ext}} \tag{1.3}$$

where C_{scat}, in units of m^2, is the single-particle scattering cross section and $C_{ext} = C_{abs} + C_{scat}$ is the extinction cross section and is due to the combined effect of scattering and absorption.

The single scattering albedo (SSA) values at 440 nm as function of the time during the day are reported in figure 1.12 for 30 June 2006 (dashed grey line) and 27 July 2006 (solid black line). It worth mentioning, that the data reported in figure 1.12 are level 1.5 data (cloud screened) since level 2 SSA values are not available.

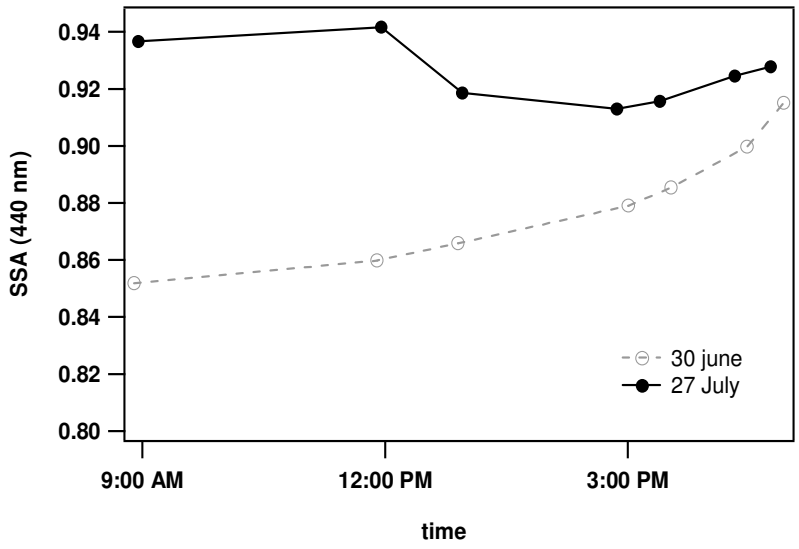

Figure1.12. Single scattering albedo SSA at 440 nm as function of the time for 30 June 2006 (dashed grey line) and 27 July 2006 (black solid line).

Figure 1.12 shows that the 30 June 2006 is characterized by SSA values that vary between 0.85 – 0.91, while on 27 July 2006 SSA assume higher values in the range 0.91 – 0.93. The results of figure 1.12 are in good accordance with the ones that will be reported in chapter 4 which are based on 2003 – 2004 Aeronet retrievals. Infact, it will be shown, in the chapter 4, that "continental average aerosols" are characterized by SSA values between 0.8 and 1, while aerosol coming from Sahara desert assume SSA values between 0.89 and 0.99.

Figure 1.13a shows the daily average phase function P(θ) (the amount of light for unit incident irradiance scattered into a unit solid angle about a given direction (Bohren and Huffman, 1998)) at 440 nm vs the scattering (θ) angles for the 30 June (red curve) and 27 July (black curve) 2006. Another significant parameter that is calculated from the phase function P(θ) is the asymmetry factor *g*. The asymmetry factor *g* is related to the re-distribution of radiation after a scattering event and it assume the value $g = +1$ for aerosols that scatter forward and $g = 0$ for aerosols that scatter symmetrically. Since forward scattering strength is correlated with particles size, the value of g is also a good indicator for size.

Figure 1.13b shows the asymmetry factor as function of the time during the two studied days.

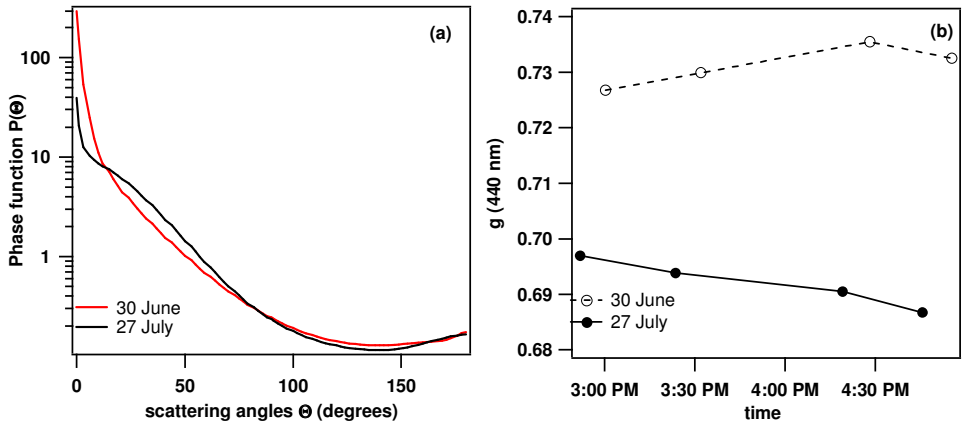

Figure 1.13. (a) Phase function versus scattering angles at 30 June 2006 (red line) and 27 July 2006 (black line); (b) Asymmetry factor *g* at 440 nm as function of the time for 30 June 2006 (dashed grey line) and 27 July 2006 (black solid line).

One observes form figure 1.13b that the asymmetry factor varies between 0.72 – 0.73, and 0.68 – 0.69 on 30 June and 27 July 2006, respectively. The higher *g* values assumed on 30 June 2006 are probably due to the larger size of dust particles. According to d'Almeida et al., 1991 and Dubovik et al., 2002a, figure1.13b indicates that the dashed grey and solid black lines can be considered representative of continental and dust aerosols, respectively. It is interesting to compare figure 1.13a with figure 1.14 that represents the phase functions at 870 nm for particles of different size with radii of r = 0.05 μm and r = 0.5 μm. One can see from figure 1.14 that particles of large size (r = 0.5 μm) are characterized by P(θ) that assume higher values for smaller scattering angles (θ) and tends to 0 faster than that associated to particles of smaller size (r = 0.05 μm).

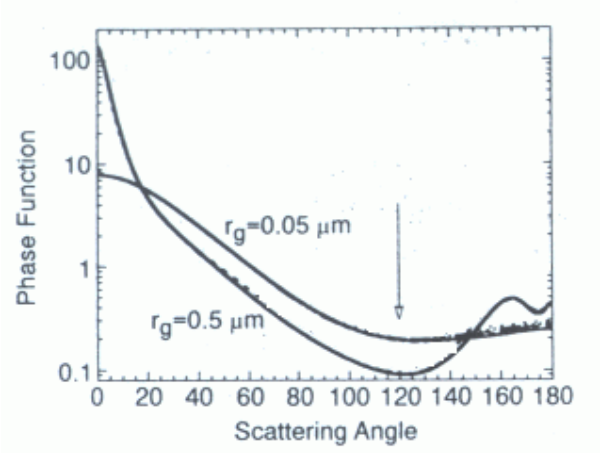

Figure 1.14. Phase functions versus scattering angles at 870 nm for particles of different sizes.

One can observe in figure 1.13a that the red curve, relative to 30 June 2006, assumes higher values for smaller scattering angles (θ ≤ 20μm) like in figure1.14. In addition to columnar optical and microphysical properties the V2 algorithm includes a new set of data

that are important for the comprehensive interpretation of the aerosol effects on climate, such as the broad-band and the spectral fluxes, the radiative forcing and the radiative forcing efficiency.

A common way to quantify impacts of aerosol changes to the Earth- Atmosphere-System is the determination of the associated change to the radiative energy balance. The so-called direct radiative effects (DRE) at the top of the atmosphere (TOA) (at an altitude of ~ 120 km) ΔF_{TOA} and at the bottom of the atmosphere (BOA) (at an altitude of ~ 300m) ΔF_{BOA} are defined as:

$$\Delta F_{TOA} = F^{\uparrow}_{TOA} - F^{\uparrow 0}_{TOA} \qquad (1.4)$$

$$\Delta F_{BOA} = F^{\downarrow}_{BOA} - F^{\downarrow 0}_{BOA} \qquad (1.5)$$

where $F^{\uparrow}_{TOA}$ and $F^{\uparrow 0}_{TOA}$ are the TOA up ward fluxes calculated with and without aerosols, respectively, while $F^{\downarrow}_{BOA}$ and $F^{\downarrow 0}_{BOA}$ are the BOA down ward fluxes calculated with and without aerosol, respectively. In particular, ΔF_{TOA} summarizes the impact to the entire Earth-Atmosphere-system, while ΔF_{BOA} captures the impact of exchange processes between the atmosphere and the Earth's surface.

Figure 1.15 represents the solar (0.2 – 4 µm) radiative effect (W/m^2) calculated at the TOA (figure1.15a) and at the BOA (figure 1.15b) as function of the day time.

Figure 1.15a shows that ΔF_{TOA} assumes negative values and this demonstrates a cooling of the Earth-Atmosphere-system by aerosols, since mainly extra solar radiation is reflected back to space. Figure 1.15a reveals that on 30 June and 27 July ΔF_{TOA} assume values ranging between -19 W/m² to 26 W/m², and -14 W/m² to -17 W/m², respectively.

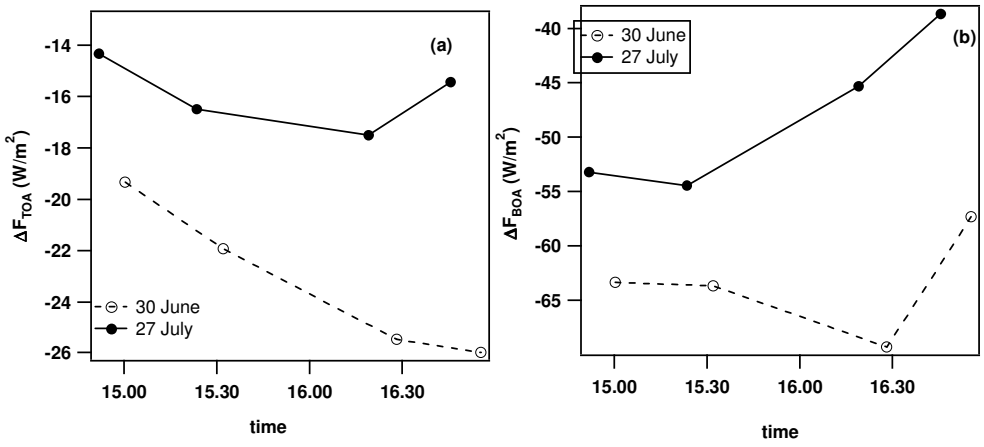

Figure 1.15. Aerosol Direct radiative effect at the (a) top of atmosphere and (b) bottom of the atmosphere on 30 June 2006 (grey dashed line) and 27 July 2006 (black solid line).

In addition, figure 1.15b shows that the radiative forcing at the bottom of the atmosphere ΔF_{BOA} assume values between -57 W/m² and -60 W/m² on 30 June and between -38 W/m² and -54 W/m² on 27 July. These results are in accordance with the time evolution of the AOD (figure 1.8). The plot shows that the aerosol load is larger on 30 June.

Aerosol associated reductions of the downward solar radiation at the Earth's surface are larger, since aerosols not only scatter but also absorb solar radiation: larger aerosol solar absorptions determine larger differences between TOA and surface aerosol DREs. Figures 1.15a and 1.15b show that ΔF_{TOA} is larger than ΔF_{BOA} during both the days.

The DRE efficiency (W/m^2), defined as the DRE per unit of aerosol optical depth AOD at 550 nm, at the top $\Delta F^{eff}{}_{TOA}$ and at the bottom $\Delta F^{eff}{}_{BOA}$ of atmosphere as function of the time is reported in figure 1.16a and 1.16b, respectively. If only data on aerosol optical depth are available, such as from satellite retrievals, then it is often desirable to know the local aerosol DRE efficiency to translate AOD values into associated aerosol ΔFs: aerosol forcing efficiencies are mainly dependent on aerosol type.

In figure 1.16a one can observe that $\Delta F^{eff}{}_{TOA}$ assume values between -50 W/m^2 and -55 W/m^2 on 30 June and between -50 W/m^2 and -61 W/m^2 on 27 July.

In particular, from figure 1.16a we observe that between 15:00 UTC and 15:30 UTC the percentage differences between $\Delta F^{eff}{}_{TOA}$ retrieved on 30 June and 27 July are of about 2%, while around 16:30 UTC the difference increases up to 13%.

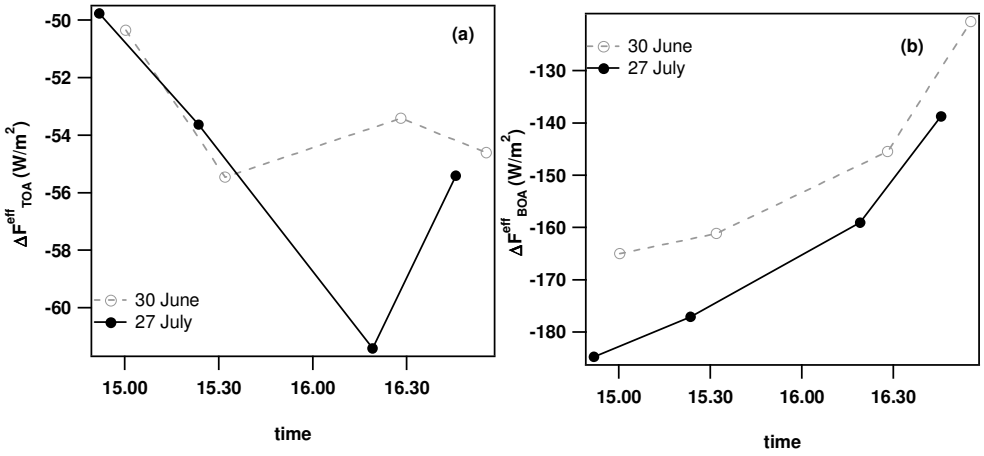

Figure 1.16. DRE efficiency at the (a) top of atmosphere TOA and (b) bottom BOA of the atmosphere at 30 June 2006 (grey dashed line) and 27 July 2006 (black solid line).

This latter result may suggest that, between 15:00 UTC and 15:30 UTC, the two investigated days are characterized by particles of rather similar optical properties, while aerosol properties differ significantly in the afternoon. Figure 1.16b shows that $\Delta F^{eff}{}_{BOA}$ vary in the range ~ -120 W/m^2 - -165 W/m^2 on 30 June and ~ -138 W/m^2 - -174 W/m^2 on 27 July. The higher values assumed by $\Delta F^{eff}{}_{BOA}$ during the 30 June may be related to the result of figure 1.13b. In fact, the higher contribution of particles that forward scatter the radiation on 30 June may be responsible of the higher BOA downward flux calculated with aerosol and then, to the less negative values assumed by $\Delta F^{eff}{}_{BOA}$.

1.3 Conclusions

In this chapter daily temporal evolutions of retrievals from the AERONET sun photometer measurements performed at Lecce during two days during the year 2006 are used to get preliminary results from the new version of the AERONET inversion algorithm (V2). The main investigated parameters were: the fine fraction parameter, the volume size distributions, the real and imaginary refractive index, the single scattering albedo, the asymmetry factor and the direct radiative forcing.

In particular, two days (30 June and 27 July 2006) with different advection patterns have been studied to infer how aerosol optical properties depend on particle type. It is demonstrated that, on 30 June 2006, when all the air masses are coming from the Sahara desert, there is a predominance of larger size (with a volume median radius of r_v = 2.24 μm and an asymmetry factor of 0.72≤ g ≤0.73) and more absorbent (0.85≤ SSA ≤0.91) particles. On the contrary, the 27 July 2006 is characterized by small (with r_v = 0.19 μm and asymmetry factor of 0.68≤ g ≤0.69) and poor absorbing (0.91≤ SSA ≤0.93) particles. Back trajectories come over Lecce from the North, North-West Europe, on this last day.

The aerosol DRE temporal plot has also demonstrated that on 30 June and 27 July ΔF_{TOA} assume values ranging between -19 W/m² to 26 W/m², and -14 W/m² to -17 W/m², respectively, while ΔF_{BOA} assumes values between -57 W/m² and -60 W/m² on 30 June and between -38 W/m² and -54 W/m² on 27 July. These results are in accordance with the time evolution of the AOD and the SSA of figures 1.8 and 1.12 that show an higher aerosol load and a contribution of more absorbing aerosol on 30 June.

Finally, time evolutions of the aerosol DRE efficiency (W/m^2) have shown that ΔF^{eff}_{TOA} assume values between -50 W/m^2 and -55 W/m^2 on 30 June and between -50 W/m^2 and -61

W/m^2 on 27 July, while $\Delta F^{eff}{}_{BOA}$ vary in the range ~ -120 W/m^2 - -165 W/m^2 on 30 June and ~ -138 W/m^2 - -174 W/m^2 on 27 July.

Since aerosol forcing efficiencies are dependent on the aerosol type, these last results further more show the dependence of aerosol DREs on particle typ

CHAPTER 2

2006 AERONET PRODUCTS

As discussed in Chapter 1, a sun/sky radiometer operating within AERONET at the Physics Department of Salento University is used to characterize aerosol properties by columnar values of the aerosol optical depth, the fine fraction parameter, the volume size distribution, the real and imaginary refractive index, the single scattering albedo and the direct radiative forcing.

The main objective of this chapter is to provide some results on the temporal evolution of the main aerosol parameters retrieved from the V2 inversion algorithm level 2 for the year 2006.

2.1 Seasonal variability of AERONET retrievals for the year 2006

Figure 2.1a shows the V2 AOD values at 440 nm for all the year 2006. Red full dots shows all available measurements while full black dots represent monthly averaged values and error bars represent ±1 standard deviation.

The larger AOD values observed in spring - summer may be due to a larger columnar content of aerosol particles and/or to a larger content of aerosol particles characterized by higher scattering and/or absorption coefficients. In fact, AODs depend on the aerosol extinction coefficient that is made of two parts: the scattering and the absorption component. In addition, we mention that Lidar measurements performed at Lecce within the EARLINET Project (Matthias et al., 2004) revealed that aerosol load and height reduce from summer to winter (e.g. De Tomasi and Perrone, 2003): aerosol up to 7 and 3 km have been detected by the lidar in summer and winter, respectively.

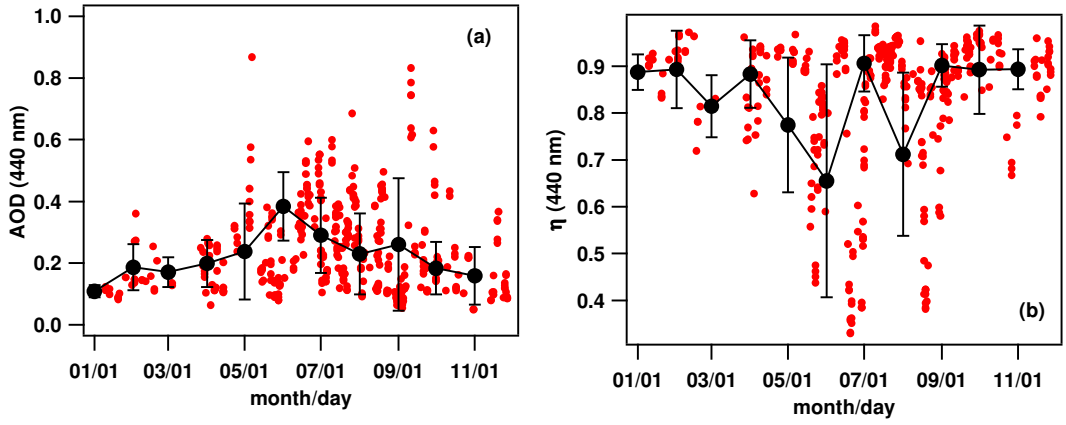

Figure 2.1. Temporal evolution at 440 nm of (a) AOD values and (b) fine fraction values. Full black dots represent monthly averaged values and vertical bars are the ±1 standard deviations;

We believe that the AOD seasonal variability revealed by figure 2.1a is partially determined by the seasonal dependence of aerosol removal processes. The weather stability typical of summer regimes favours the accumulation of atmospheric particles all over Europe and over the Atlantic, that besides North Africa, represent the main source regions of aerosols advected to Lecce. As a consequence, the contribution of long-range transported particles is expected to be larger in summer over south-east Italy. Moreover, the aerosol wet removal is practically absent over the south east Mediterranean basin in summer and the larger amount of solar radiation reaching the earth's surface may favour photochemical reactions that affect optical and microphysical properties of the accumulated atmospheric particles.

The temporal evolution of the fine fraction parameter η at 440 nm, reported in figure 2.1b, also reveals a seasonal variability. In particular, one can observe that monthly averaged η values assume lower values in spring – summer except for the month of July.

The higher η values assumed on July 2006 is probably due to the high concentration of forest fires occurred during July 2006, as it is demonstrated by the fire map retrieved by MODIS satellite images

(http://maps.geog.umd.edu/firms/maps.asp) during all the month of July 2006 (figure 2.2).

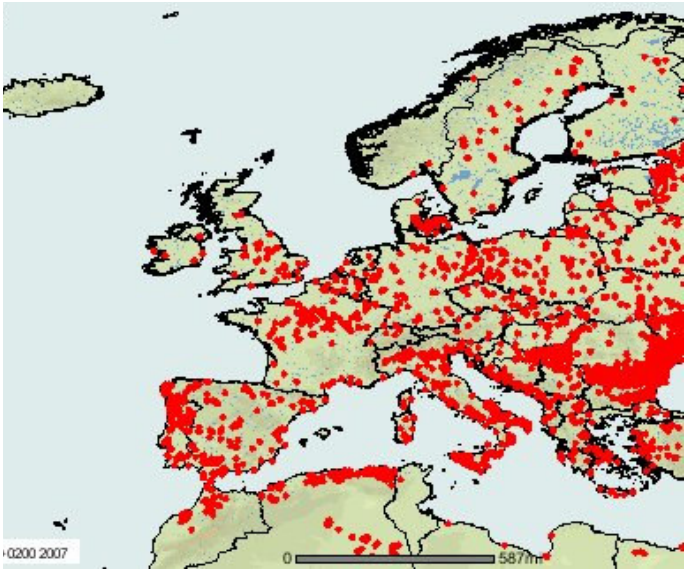

Figure 2.2. Fire map retrieved by MODIS satellite images on July 2006.

To this end, it worth mentioning that the back trajectory analysis for the month of July 2006 has revealed that most of the air masses reaching Lecce come from the North, North-West of Europe and then they cross the areas affected by the fires. Studies by Dubovik et al., 2002a revealed that aerosol affected by biomass burning particles are usually characterized by larger AOD and η values, according to the results obtained on July 2006 and reportedin figure 2.1a and 2.1b.

The smaller η values of June and August 2006 (figure 2.1b) let us to suppose that there is a predominant contribution of coarse-mode particles in those months. In fact, the back trajectory analysis has demonstrated that rather frequent dust events occurred during the months of June and August 2006.

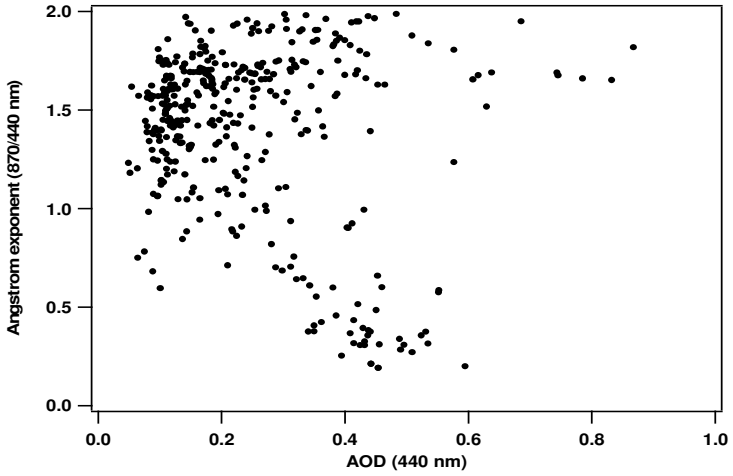

Figure 2.3. Scatter plot of the Angstrom exponent Å calculated from AOD at 870 and 440 nm and the AOD at 440 nm retrieved from AERONET measurements during all the year 2006.

Figure 2.3 shows the scatter plot of the Angstrom exponent Å (calculated from AOD at 870 and 440 nm) versus the aerosol optical depth AOD (440 m) for all the year 2006. The Angstrom exponent describes the dependence of the aerosol optical depth on wavelength and it is calculated by:

$$AOD_{\lambda} = AOD_{\lambda 0}\left(\frac{\lambda}{\lambda_0}\right)^{-\mathring{A}} \qquad (2.1)$$

where AOD_{λ} is the optical depth at wavelength λ and $AOD_{\lambda 0}$ is the optical depth at the reference wavelength λ_0. It can be shown that Å is inversely related to the average size of the aerosol particles: the smaller the particles, the larger the exponent. For example, values of Å greater than 2.0 indicate the presence of fine mode particles (e.g. smoke particles and sulfates), while values of Å near to zero indicate the presence of coarse mode particles such as desert dust (Eck et al., 1999).

Then, since AOD is related to the amount of particles and Å to the size, the plot in figure 2.3 can help us to individuate aerosols with different properties and, then, of different type.

Figure 2.3 shows that Å and AOD values vary within the 0.2 – 2 and 0 – 0.6 range, respectively. Three main groups of particles can be identified in figure 2.3: the first one include data with large values of AOD ($0.3 \leq AOD \leq 0.6$) and low values of Å ($Å \leq 0.6$); the second one contains points with low values of ($0 \leq AOD \leq 0.2$) and large values of Å ($1 \leq Å \leq 2$) and the third group is made of $0.2 \leq AOD \leq 0.9$ and $1.5 \leq Å \leq 2$. According to Pace et al., 2006, the first group of data points may be ascribed to the Sahara dust aerosol. We observe from figure 2.3 that the group of data points due to the Sahara dust particles belong to the months of June and August 2006. Hence, the second group of data points is representative of marine aerosols. Pace et al., (2006) also demonstrate that aerosols of maritime origin are characterized by AOD values ranging between 0.11 and 0.19 and Å values that vary in the range 0.5-1.2. Finally the third group is typical of urban-industrial and biomass burning aerosols.

One can observe from figure 2.3 that particles corresponding to aerosols of urban-industrial origin are predominant during the year 2006.

The above reported discussion is confirmed by figure 2.4 showing the averaged volume size distributions, obtained by averaging all the profiles relative to the four seasons: Winter (December, January and February, DJF) (figure 2.4a), Spring (March, April, May, MAM) (figure 2.4b), Summer (June, July, August, JJA) (figure 2.4c) and Autumn (September, October and November, SON) (figure 2.4d). Vertical error bars represent ±1 standard deviation from the seasonal average value and represent the size distribution variability. In particular, one can see from figure 2.4 that aerosols with a predominant contribution of small particles are advected over

Lecce on Winter, Spring and Autumn (figure 2.4a, 2.4b and 2.4d), while Summer (figure 2.4c) is characterized by a larger contribution of coarse particles.

In fact, the profile of figure 2.4c shows a coarse-mode peaked at 2.24 µm that assume *dV/dlnr* values larger than those assumed by the second peak in figure 2.4a, 2.4b and 2.4d. Finally, figure 2.4 reveals a predominant contribution of fine-mode particles in Winter, Spring and Autumn. The fine-mode particle volume is peaked at $r_{vf} \sim 0.148\mu m$.

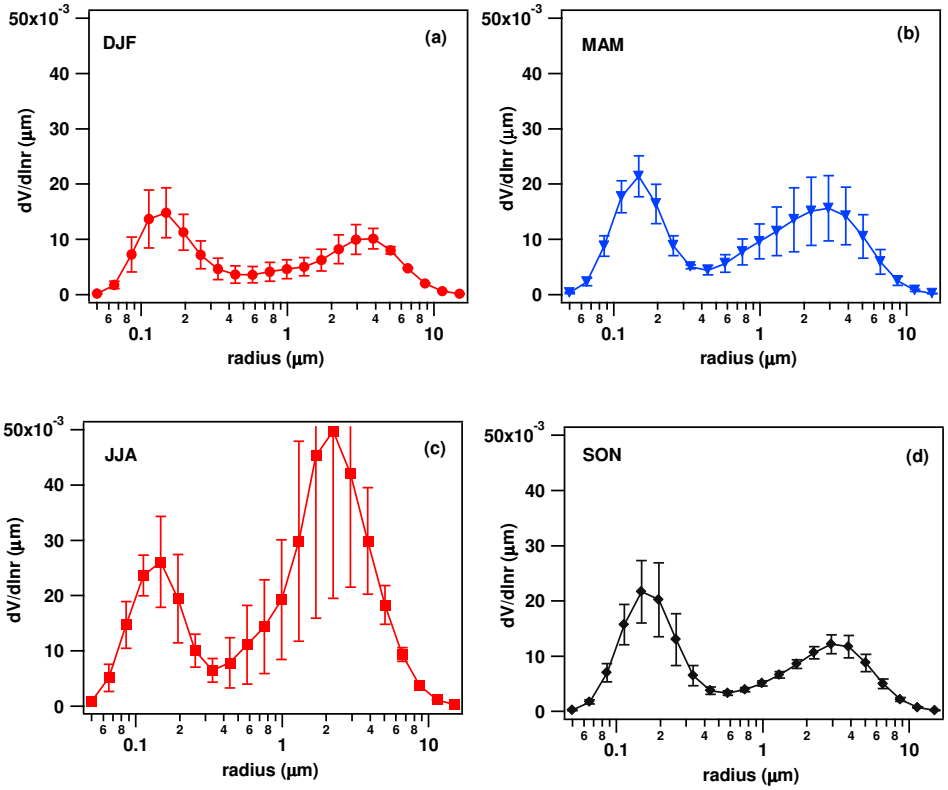

Figure 2.4. Volume size distribution profiles retrieved on (a) Winter (December-January-February), (b) spring (March-April-May), (c) summer (June-July-August), and (d) autumn (September-October-December) during all the 2006 year.

Comparing the particle size distribution of urban-industrial aerosols reported in previous studies, with the results reported in figure 2.4a, 2.4b and 2.4d, one can note that our size distribution retrievals agree well with those reported by authors.

The urban-industrial aerosol particle size distributions retrieved by Hignett et al (1999) from an airborne optical particle counter and by Russell et al. (1999) with a nephelometer measurements, show a domination of fine mode-particles with a radius for the fine-mode at r_{vf} ~ 0.1- 0.2μm. Moreover, the volume particle size distributions for urban-industrial aerosols found by Dubovik et al. (2002a) for the Mexico City site and by Baumgardener et al. (2000) show a maximum at r_{vf} ~ 0.14 μm and r_{vf} ~ 0.15μm, respectively, which are in good agreement with the results of this chapter.

The yearly evolution of the real and imaginary part of the refractive index is represented in figure 2.5. One observes from figure 2.5 that monthly averaged *n* and *k* values are not significantly dependent on seasons and they assume values between 1.46 and 1.51 and 0.014 – 0.037, respectively during all the year. It worth noting that the AERONET sunphotometry inversion algorithm (Dubovik and King, 2000a) assumes $1.33 \leq n \leq 1.6$.

According to Dubovik et al., 2002a that have analyzed 8- year worldwide distributed AERONET data, the *n* and *k* values retrieved at Lecce on year 2006, are typical of urban-industrial aerosols. In fact, Dubovik et al. 2002a found that urban-industrial aerosols are characterized by low values of the real part of the refractive index (1.39 for GSFC, 1.40 for Creteil, 1.47 for Mexico City, and 1.44 for Maldives) and high *k* values varying between 0.003 and 0.014.

Moreover, Koepke et al. 1994 and Shettle and Fenn, 1979, found that water-soluble particles, that include particles of sulfates, nitrates and other soluble substances, the main component of urban-industrial aerosols (Ackermann, 1998), are characterized in dry state by *n* and *k* values of 1.53 and 0.005 at 450 nm.

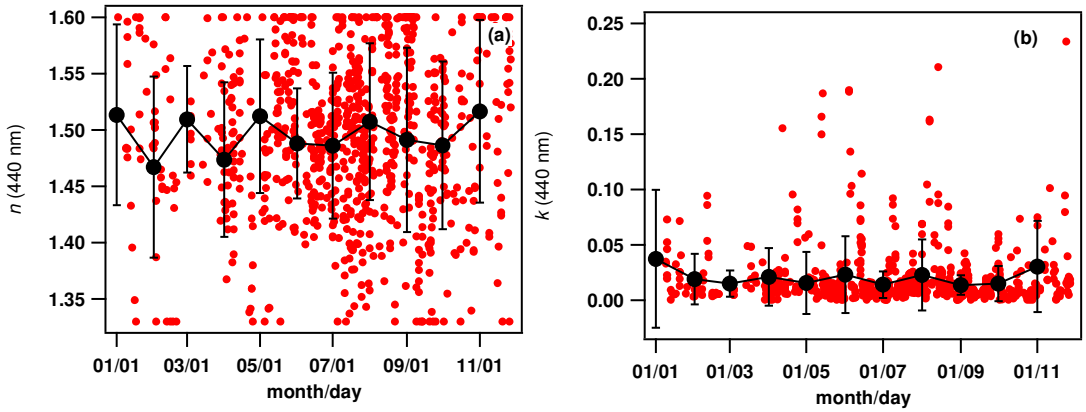

Figure 2.5. Temporal evolution at 440 nm of the (a) real part and (b) imaginary part of the refractive indix. Full black dots represent monthly averaged values and vertical bars are the ±1 standard deviations;

The results on *n* and *k* values are supported by the temporal evolution of the AERONET single scattering albedo SSA at 440 nm that is reported in figure 2.6.

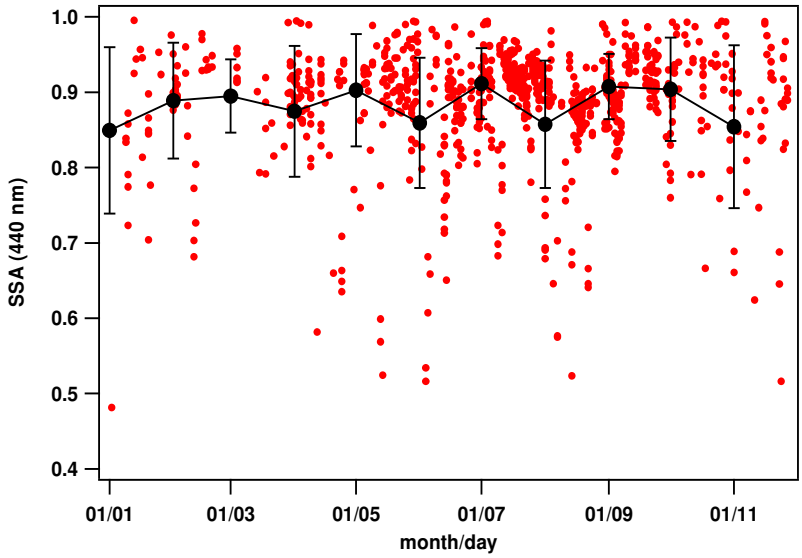

Figure 2.6. Temporal evolution at 440 nm of SSA. Full black dots represent monthly averaged values and vertical bars are the ±1 standard deviations.

It is worth noting that SSA values are level 1.5 V2 AERONET data since, as was mentioned, SSA level 2 data are not available. Figure 2.6 reveals that monthly averaged SSA values span the range 0.85 – 0.9 during all the year, without a marked seasonal variability. In accordance with literature data (D'Almeida et al., 1991,

Dubovik et al., 2002a), this result may led assuming that moderately-absorbing aerosol, probably of urban origin, dominate all year long. However, one can observe from figure 2.5 that from May to September some days are characterized by rather low SSAs value (red full dots) reaching 0.5. Even if these data points are rather few and don't significantly affect the monthly averaged SSA values, they allow assuming that the contribution of more absorbent aerosols is larger on spring-summer.

In conclusion, figures 2.4-2.6 suggest that the dominant aerosol type at Lecce during the year 2006 are of urban-industrial origin. According to SSA temporal evolution of figure 2.6, it is worth noting from figure 2.5b that on spring-summer *k* values (red full dots) reach higher values up to 0.2 and this result can be ascribed to the large presence of more absorbent particles in that period.

The broad-band direct radiative forcing data relative to the spectral range 0.2 - 0.4 µm are shown in figure 2.7. In particular, ΔF_{TOA} (figure 2.7a) and ΔF_{BOA} (figure 2.7b) represent the direct radiative forcing at the top (TOA) and the bottom (BOA) of atmosphere. Black full dots represent monthly averaged values, while vertical bars are the ±1 standard deviations.

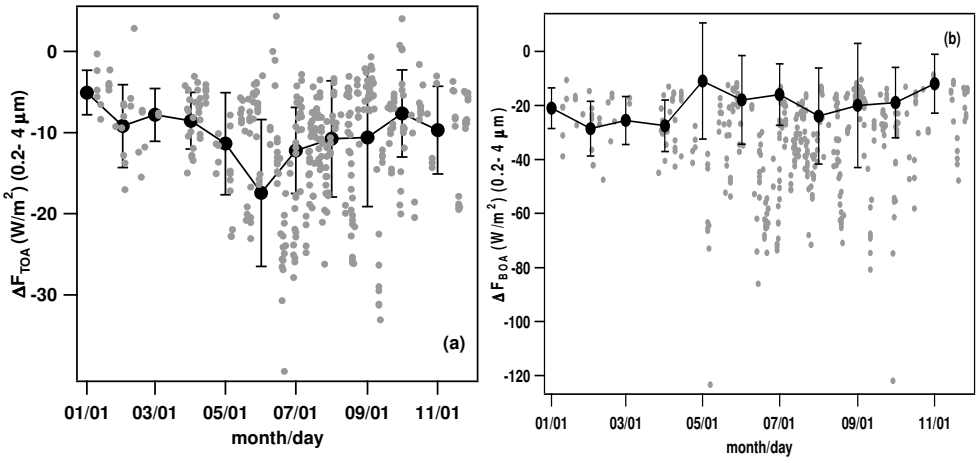

Figure 2.7. Temporal evolution of the broad-band (0.2- 0.4 µm) radiative forcing at the (a) top TOA and (b) bottom BOA of atmosphere. Full black dots and red bars represent monthly averaged values and vertical bars are the ±1 standard deviations.

Figure 2.7a reveals a marked seasonal evolution of the aerosol DRE (Direct Radiative Effect) at the top of atmosphere during the year 2006. Figure 2.7a also shows that the monthly averaged values of ΔF_{TOA} ranges from ~ -5W/m^2 in January to ~ -17.45W/m^2 in August. The seasonal changes of the aerosol properties are a contributing factor and are mainly responsible for the asymmetric trend of the aerosol ΔF_{TOA} variability. Figures 2.1a and 2.1b have revealed that the aerosol loads and the contribution of small particles are maxima in summer and minima in winter. Figures 2.6 and 2.5b have also demonstrated the presence of a large contribution of absorbent particles during spring-summer. As it has been told, the summer time over the Mediterranean is characterized by strong sunlight causing photochemical smog (Smolik et al., 2003) and by stable atmospheric conditions, which favour the accumulation of aerosol particles. Forest fires, which occur during the summer months in the Mediterranean region and North Africa, also contribute to increase black carbon and fine particle emission during summer months (Pace et al., 2006). Hence, the more negative values assumed by ΔF_{TOA} in summer are probably due to large aerosol load that contribute to the absorption of the solar radiation, decreasing the solar flux reaching the top of the atmosphere. Moreover, the presence of aerosols above clouds, which can decrease cloud brightness to space, may be an additional reason for a less negative ΔF_{TOA} during the winter months. Aerosol radiative forcing calculations over the Mediterranean by Lelieveld et al., 2002 provide a DRE of more than -11W/m^2 on summer, as consequence of the solar radiation by aerosol absorption by black carbon, and possibly by dust, fly ash or organic carbon, much of which is in the lower 4 km. According to Lelieveld et al., 2002, the large reduction in surface solar radiation by aerosol, occurring on summer over the Mediterranean, is

similar to that observed over the northern Indian Ocean in Asian pollution outflow (Ramanathan et al., 2001)

Figure 2.8 shows the temporal evolution of DRE efficiency at the top (figure 2.8a) and at the bottom (figure 2.8b) of atmosphere. $\Delta F^{eff}{}_{TOA}$ in figure 2.8a are almost constant during the entire year at a value of about ~ -60 – -65 W/m^2 except on November.

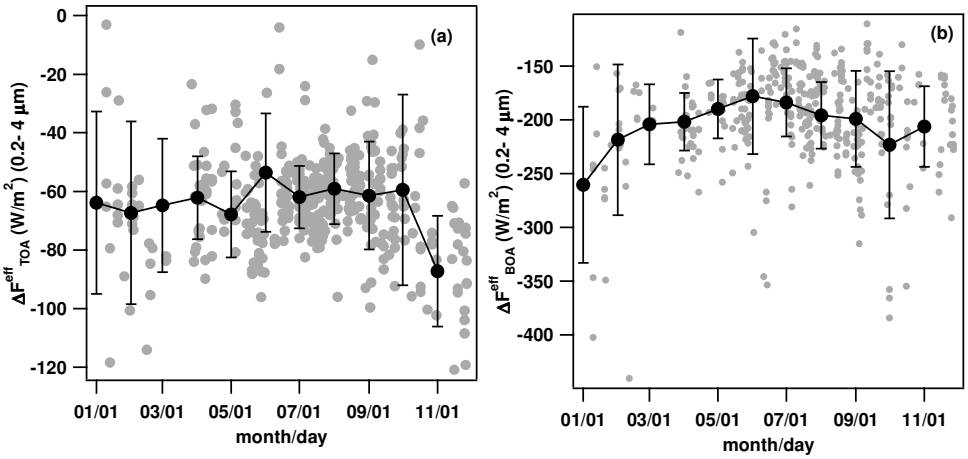

Figure 2.8. Temporal evolution of the broad-band (0.2- 0.4 μm) DRE efficiency at the (a) top TOA and (b) bottom BOA of atmosphere. Full black dots and red bars represent monthly averaged values and vertical bars are the ±1 standard deviations.

This is the result of competing effects by SSA and AOD, as both influence the aerosol radiative forcing at the TOA (Satheesh, 2002, Meloni et al., 2005). The ΔF_{TOA} increases with larger SSA and larger AOD values and figures 2.1a and 2.6 show that on spring-summer AODs and SSA take higher and smaller values, respectively. Hence the larger absorption combines with the larger scattering due to smaller size particles to produce a balance effect.

2.2. Conclusions

In this chapter temporal evolutions of aerosol products from the AERONET sun photometer measurements performed at Lecce during the year 2006 are used to get preliminary results from the new version of the AERONET inversion algorithm (V2).

The temporal evolutions of the main aerosol parameters retrieved over Lecce during all the year 2006 have demonstrated a significant seasonal variability. In particular, the aerosol optical depths AODs monthly averaged assume values ~ 0.1 – 0.2 in autumn-winter and ~ 0.2 – 0.4 in spring-summer, the fine fraction parameter vary in the range ~ 0.7- 1 in autumn-winter and between 0.6 – 0.9 in spring – summer. In addition, temporal plots of the monthly averaged values of the single scattering albedo SSA and the imaginary and real part of the refractive index k and n appear to not have a marked seasonal variability. However, one can observe that in spring-summer SSA and n and k assume lower and higher values, respectively, than in autumn – winter. Then, the latter results let to assume that small, absorbing urban-industrial aerosols dominate in spring-summer at Lecce.

Finally, the temporal evolution of the DRE at the TOA have shown a seasonal variability with absolute values in spring-summer and this result can be ascribed to the increase of the aerosol load that tends to absorb the solar radiation, decreasing the solar flux reaching the top of the atmosphere, as well as to larger solar flux reaching the Earth surface on spring-summer over the Mediterranean basin.

CHAPTER 3

AEROSOL LOAD CHARACTERIZATION OVER SOUTH-EAST ITALY BY AERONET SUNPHOTOMETER MEASUREMENTS

As it has been shown in previous chapters, passive remote sensing devices such as sun photometers are peculiar tools to follow the spatial and temporal evolution of aerosol loads and get data to properly characterize aerosol optical and microphysical properties. In particular, it has been shown the CIMEL sun/sky radiometer is used at the Physics Department of the University of Salento to assess aerosol properties by columnar values of the aerosol optical depth, the single scattering albedo, the particle size distribution, the Angstrom exponent and the real and imaginary refractive index.

The main goal of this chapter is to contribute to the aerosol characterization over the Mediterranean basin providing results on the aerosol characterization over south-east Italy. Sun/sky radiometer measurements performed from March 18, 2003 to March 27, 2004 are used in this study to get preliminary results characterizing aerosol properties and corresponding seasonal evolutions, by daily-averaged values of aerosol optical depths (AOD), single scattering albedos (SSA), Angstrom coefficients, size distributions, real (n) and imaginary (k) refractive indices. These parameters are needed to incorporate aerosol particles into global climate models and evaluate climate forcing effects produced by aerosols of different origin and composition. Temporal evolutions and basic statistical properties of the investigated aerosol parameters together with frequency of occurrence plots are presented and discussed in this chapter. Links between aerosol properties and air mass history are investigated on high optical thickness days. Particular attention is devoted to the aerosol advected from the North Africa desert, since desert aerosols can be monitored at Lecce early in their life time.

3.1 Seasonal variability and frequency distributions of aerosol parameters

Daily averaged values of cloud screened retrievals (level 1.5) from Version1 (V1) inversion algorithm (Dubovik and King, 2000a) are analyzed in this section. A

brief discussion on the accuracy of individual retrievals is reported in Dubovik et al., (2002a).

Figures 3.1a-3.5a (open dots) show daily-averaged-value time-evolutions of AOD, SSA, *n,* and *k* at 441 nm, and of the Angstrom coefficient calculated from AOD values at 441 and 873 nm. The parameters retrieved on dust event days are marked by ticker black open dots. To this end, it is worth mentioning that *n* values along dust events (Fig. 3.3a, ticker black open dots) are obtained from the non-spherical aerosol retrieval method (Dubovik et al., 2002b). True colour images provided by the Sea-viewing Wide Field-of-view Sensor (SeaWiFS) (http://seawifs.gsfc.nasa.gov) and by MODIS (http://modis-atmos.gsfc.nasa.gov), and 4-day analytical back-trajectories are used to characterize Sahara dust outbreaks over Lecce, which is generally affected by Sahara dust events occurring over the central and east Mediterranean basin. Back-trajectories used in this chapter are provided by the German Weather Service (*Kottmeier and Fay,* 1998) for six distinct arrival height pressure levels (975, 850, 700, 500, 300, and 200 hPa) and for two arrival times (13:00 UTC and 19:00 UTC) on a day–by-day basis.

Full red dots in Figs.3.1a-3.5a represent fifteen-day averaged values and errors bars represent ±1 standard deviation. Figures 3.1a-3.5a show that AOD, Å and *k* generally take larger fifteen-day averaged values in spring and summer. On the contrary, Figs. 3.2a and 3.3a show that SSA and *n* take larger fifteen-day averaged values in autumn-winter. These results reveal that concentrations, size distributions and chemical compositions of aerosol particles depend on seasons and lead at first to assume that higher aerosol loads with a predominant contribution of smaller, absorbing particles dominate over south-east Italy in spring-summer. Frequency distributions of daily averaged aerosol parameters are investigated to infer aerosol properties and aerosol types with larger frequency of occurrence. Figs. 3.1c, 3.2b,

3.3b, 3.4b and 3.5b (full dots) show the frequency distribution of AOD , SSA, *n, k,* and Å, respectively. Error bars represent $\pm\sqrt{N_i}$, where N_i is the number of point data in each bin. Frequency distribution reveal the presence of individual modes relative to the seasonal dependence of the aerosol properties and/or to the presence of aerosols from different sources and hence of different types. Frequency of occurrence data are fitted by multimodal lognormal distributions (O'Neill et al., 2000), to infer mode parameters. Solid lines represent in each graph of Figs. 3.1c, 3.2b, 3.3b, 3.4b and 3.5b best fitting curved and dashed and dotted lines represent individual modes. F_i and x_i represent mode amplitude and peak value, respectively whereas σ_i represents mode width. A more detailed analysis of all investigated parameters is reported below to better infer main aerosol properties, dominating aerosol types and seasonal changes:

3.1.1. *Aerosol optical depth analysis*

The AOD seasonal variability is clearly revealed by Fig. 3.1a showing that AODs at 441 nm take fifteen-day averaged values larger than 0.2 from April to October, 2003 and lower than 0.2 from October, 2003 to March, 2004.

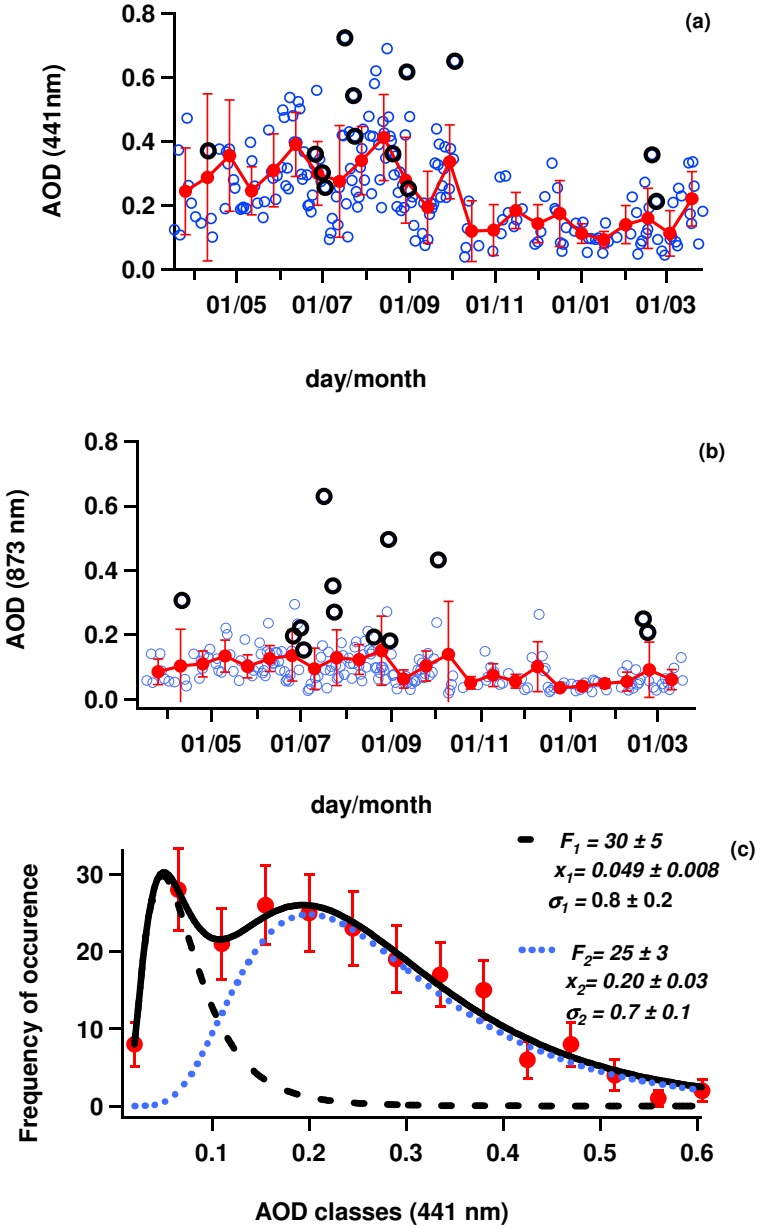

Figure 3.1 :Temporal plots of AOD values (a) at 441 nm and (b) at 873 nm. (c) Frequency of occurrence plot of AOD values at 441 nm (full dots).

The larger AOD values observed in spring-summer may be due to a larger concentration of aerosol particles and/or to a larger concentration of aerosol particles characterized by higher scattering and/or absorption coefficients.

In fact, according to the results obtained for the AOD temporal plot during the year 2006 reported in chapter 2 (paragraph 2.3.2.), we believe that the weather stability typical of summer is the main responsible of the accumulation of particles

and, hence, of the higher AOD values during the summer months. In addition, it worth mentioning that it is currently thought that aerosols often exist initially as external mixtures near aerosol sources and that the aerosols gradually tend toward an internal mixture as they age (*Levoni et al.,* 1997). To this end, it is worth mentioning that the back trajectory analysis for the studied period has not revealed significant changes of the advection patterns to Lecce as result of the transition between summer and autumn regimes. Moreover, the more abundant solar flux in summer is likely to enhance the occurrence of photochemical effects and them the production of secondary aerosols (Seinfeld and Pandis, 1998).

Moreover, fig. 3.1b shows that AOD fifteen-day averaged values vary from 0.05 to 0.15 at 873 nm and the comparison of Fig. 3.1a and Fig. 3.1b reveals that AODs generally reduce more than 50% as the monitoring wavelength increases from 441 nm to 873 nm. Then, the aerosol screening effects on the incoming solar radiation are quite large in the UV spectral region and reduce significantly in the infrared spectral region.

Figure 3.1c (full dots) shows that the 441 nm-AOD frequency distribution allows the fitting by a bimodal lognormal distribution with the largest amplitude mode (F_1=30±5) peaked at x_1 = 0.049±0.008 and the lower amplitude mode (F_2=25±3) peaked at x_2 = 0.20±0.03: the latter mode is mainly representative of AODs > 0.15, while the mode peaked at x_1 = 0.049±0.008 mainly represents AODs < 0.15. The comparison of Fig. 3.1c to Fig. 3.1a allows recognizing that the AOD bimodal distribution is mainly determined by its seasonal evolution: the mode at x_1 = 0.049 and at x_2 = 0.2 allows characterizing the AOD distribution in autumn-winter and spring-summer, respectively. AERONET sunphotometer measurements performed from June to September along several years (1993-2000) at GSFC, USA

and along the 1999 year at Creteil-Paris, France to characterize urban-industrial aerosols, reveal that AODs at 440 nm span the range 0.1-1.0 at GSFC and the range 0.1-0.9 at Creteil-Paris and are characterized by an average value of 0.24 and of 0.26 at GSFC and Creteil-Paris, respectively (Dubovik et al., (2002a). The latter results are in good accordance with variability range and mean value of the mode peaked at $x_2 = 0.2$ that characterizes Lecce's spring-summer AODs. To this end, it is worth mentioning that the contribution of anthropogenic-polluted air masses of local origin or long-range transported from Central and Eastern Europe and from the Atlantic Ocean is expected to be larger in spring-summer at Lecce, as it is demonstrated by the back trajectories analysis and as a consequence of the weather stability.

3.1.2. *Single scattering albedo analysis*

The temporal plot of SSA values at 441 nm are reported in figure 3.2a. Open and full dots represent daily and 15-day averaged values, respectively. Black open dots represent values retrieved along dust events. Frequency of occurrence plot (full dots) of SSA are shown in fig. 3.2b. Error bars are $\pm\sqrt{N_i}$, where N_i is the number of data point in each bin. The solid line represents the bimodal lognormal fitting curve, dotted and dashed lines represent individual modes.

Fig. 3.2a shows that SSAs mainly vary in the 0.90-0.99 range at 441 nm. Quite few days as June 27th are characterized by 0.85<SSA<0.90.

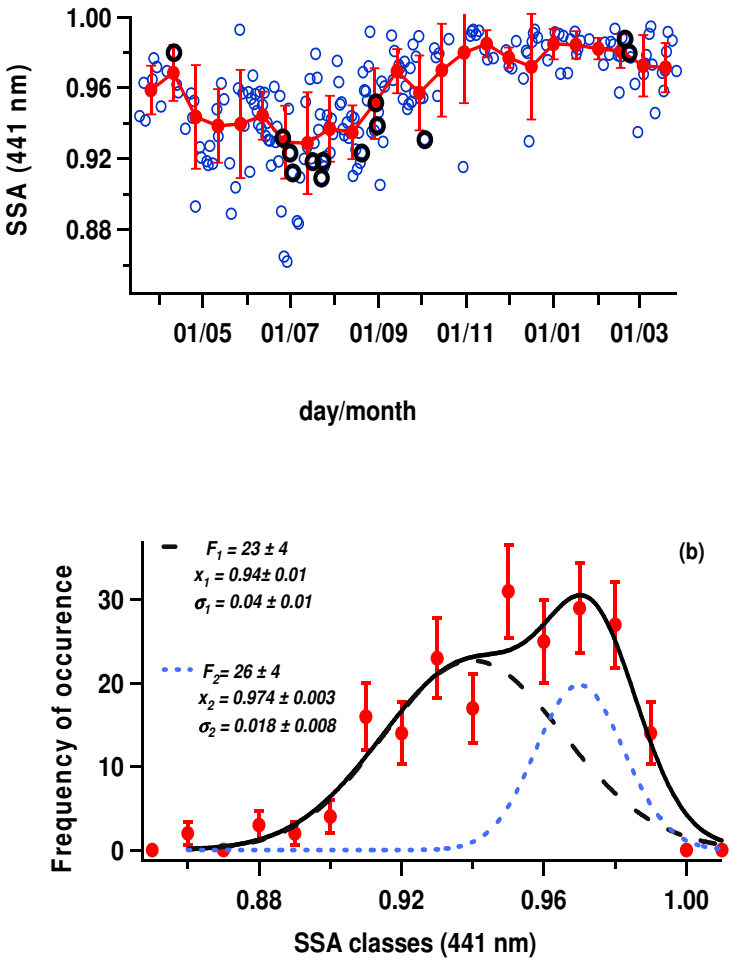

Figure 3.2.: (a) Temporal plots of SSA values at 441 nm. (b) Frequency of occurrence plot (full dots).

A rather marked SSA seasonal variability is revealed by Fig.3.2a: fifteen day averaged-values vary from 0.93 to 0.95 from May till September, 2003 and take values close to 0.98 from November, 2003 to February, 2004. SSAs of urban and maritime-polluted aerosols span the 0.942-0.984 and the 0.957-0.993 range, respectively as relative humidity vary in the 0-99% range (d'Almeida et al., 1991). Lecce is expected to be rather affected by maritime aerosols along all year as a consequence of its geographical location (De Tomasi and Perrone, 2003).

But, the contribution of long-range transported polluted air masses is expected to be more significant in summer for the weather stability and the larger growth of the

PBL in summer regimes. Then, the SSA temporal plot (Fig. 3.2a) may lead to assume that moderately absorbing urban-industrial aerosols dominate in spring-summer, while maritime-polluted aerosols dominate in autumn–winter, in accordance to literature data (e.g. d'Almeida et al., 1991; Levoni et al., 1997; Dubovik et al., 2002b). The last comment is supported by the SSA frequency distribution that is given in Fig. 3.2b and allows the fitting by a bimodal lognormal distribution with the larger amplitude mode peaked at 0.974±0.003 and the lower amplitude mode peaked at 0.94±0.01 that is characterized by a larger width (σ_2 = 0.04±0.01). The comparison of Figs. 3.2a and 3.2b leads to assume that the mode peaked at 0.94±0.01 that spans the 0.86-0.99 range, is mainly representative of spring-summer SSAs. As mentioned before, urban-aerosols are characterized at 450 nm by SSAs spanning the 0.942-0.984 range (d'Almeida et al., 1991), and in particular, the SSA that is 0.94 for dry externally mixed urban aerosols reduces to 0.91 for dry internally mixed urban aerosols (Levoni et al., 1997). Hence, urban–industrial aerosols dominate in spring-summer at Lecce. The SSA values retrieved at GSFC and Creteil-Paris (Dubovik et al., 2002a) further more support this conclusion.

The comparison of Figs. 3.2a and 3.2b reveals that the mode peaked at 0.974±0.03 is mainly representative of autumn-winter SSAs. The latter mode is representative of high SSA particles such us sea-salt particles. SSAs of the maritime-polluted aerosol model span the 0.96-0.99 range at 450 nm as relative humidity is varied from 0% to 99%, accordingly to d'Almeida (1991). Then, the latter observation may lead to assume that maritime-polluted aerosols dominate in autumn-winter a Lecce. The last conclusion is also supported by the low AOD values observed in autumn-winter and mainly represented by the mode peaked at x_1 = 0.049±0.008 of Fig. 3.1c (Smirnov et al., 2003).

3.1.3. *Real and imaginary refractive index analysis*

The temporal evolution of real and imaginary refractive index *n* and *k* values at 441 nm are reported in figure 3.3a and 3.4a, respectively. Figures 3.3a and 3.4a show that *n* and *k* take smaller 15-day averaged values in spring–summer and autumn–winter, respectively. Therefore, aerosol particles leading on average to smaller scattering and larger absorption coefficients predominate over south–east Italy in spring–summer. Figures 3.3a and 3.4a show that 15-day averaged *n*- and *k*-values span the range 1.47–1.40 and 0.007–0.003, respectively from April to September and may lead to the assumption that water soluble particles dominate in summer. In fact, water soluble particles are characterized at 450 nm by *n* and *k* values spanning the 1.53–1.35 and 0.005–0.0003 range as the relative humidity varies from 0% to 95%.

Besides hydrophilic organics (d'Almeida et al., 1991), sulphates and nitrates are the main constituents of water soluble particles (Ackermann, 1998) and the level of sulphates of local origin or long-range transport are elevated during summer in the eastern Mediterranean according to Formenti et al. (2001b). The weather stability and the absence of wet removal may favour in summer the persistence of smaller radius particles such as sulphates. In addition the solar intensity favors photochemical reactions in summer.

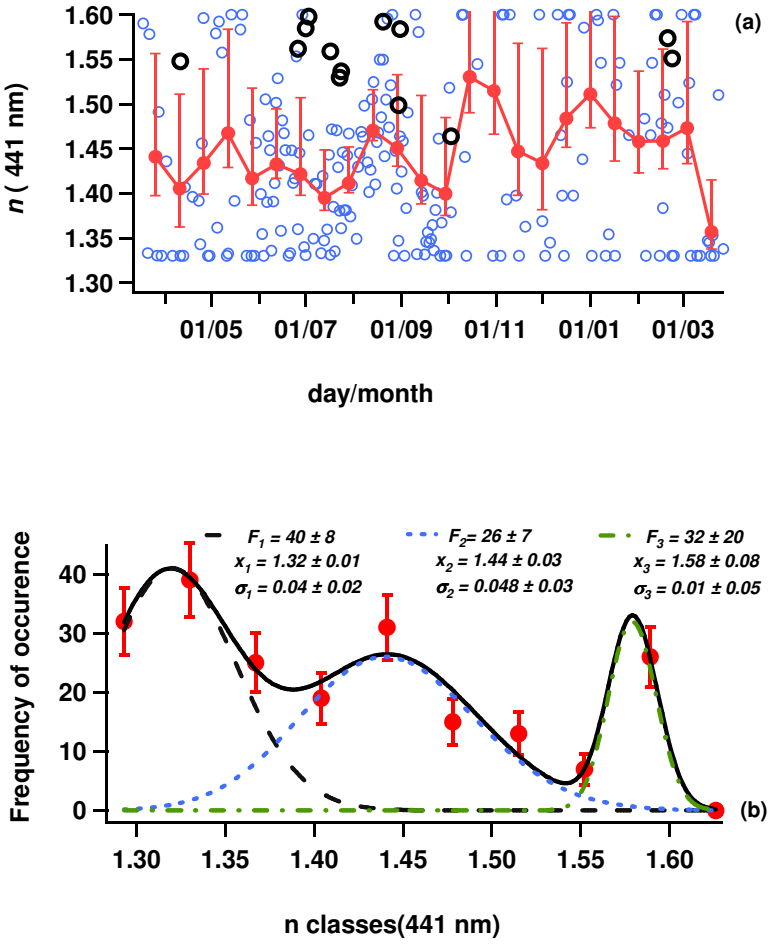

Figure 3.3. (a) Temporal plots of *n* values at 441 nm. (b) Frequency of occurrence plot (full dots).

The *n* and *k* frequency of occurrence plots are shown in Figures 3.3b and 3.4b, respectively, and both permit fitting by a trimodal lognormal distribution which allows recognition of three main aerosol constituents.

In particular, we believe that the *n* mode peaked at 1.32±0.01 is mainly representative of water-soluble and sea-salt particles quite affected by water uptake (d'Almeida et al., 1991): water is characterized at 450 nm by a real refractive 1.34. The mode peaked at 1.58±0.08 (figure. 3.3b) can mainly be representative of aerosol constituents characterized by a real refractive index that spans the range 1.54–1.6 such as minerals and soot (Ackermann, 1998).

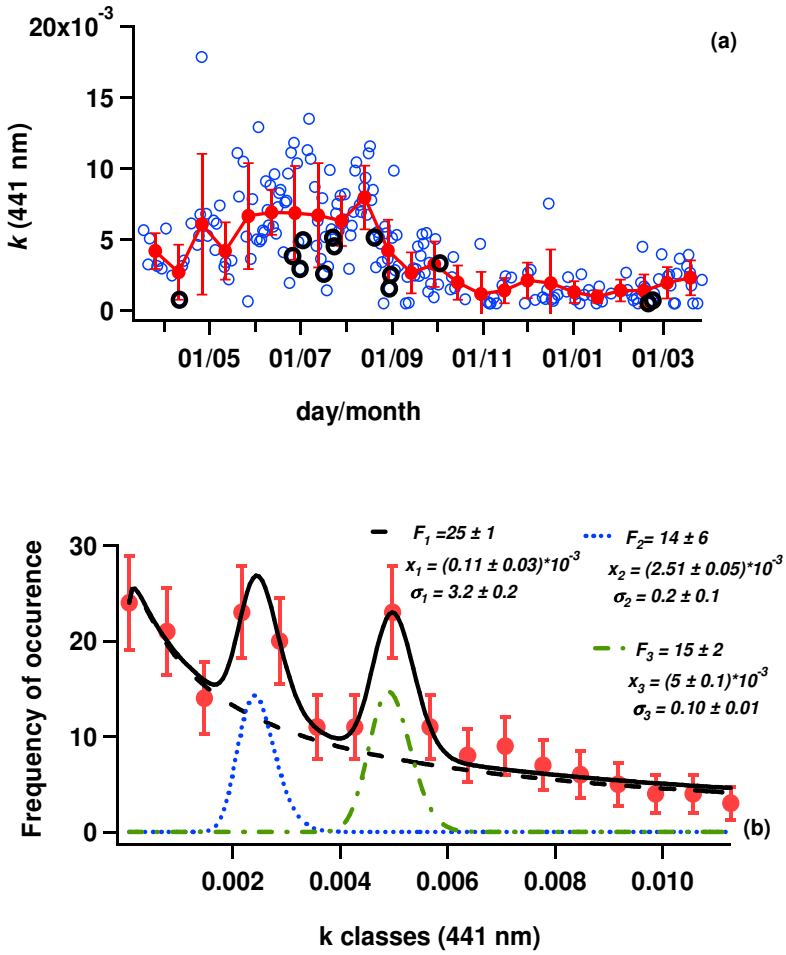

Figure 3.4. (a) Temporal plots of *k* values at 441 nm. (b) Frequency of occurrence plot (full dots).

All carbonaceous substances, hydrophobic organics, and fly ash are termed "soot" (d'Almeida et al., 1991). Finally, the mode peaked at 1.44±0.03 can mainly be considered representative of water soluble particles (Ackermann, 1998; d'Almeida et al., 1991).

The *k* frequency of occurrence plot of figure 4.4b clearly shows that aerosols with rather low imaginary refractive index dominate over south–east Italy: 70% of *k* daily averaged-values span the range $0.0005<k<0.005$. Then, the *k* frequency distribution is mainly represented by largest-amplitude mode peaked at $(0.11\pm0.03)\times10^{-3}$ that leads to assume that moderately absorbing particles dominate

at Lecce. Two lower amplitude modes peaked at $(2.50\pm0.05)\times10^{-3}$ and $(5\pm1)\times10^{-3}$, respectively, are also revealed by figure 3.4b. We believe that these last two modes can be representative of the wet and dry water soluble aerosol component. The dry imaginary refractive index of water soluble particles that is equal to 0.005 at 450 nm (d'Almeida et al., 1991), reduces of about 50% when relative humidity is 50%. Water soluble particles represent one of the main components of maritime and urban–industrial aerosols: the dominant aerosol types at Lecce in autumn–winter and spring–summer, respectively.

3.1.4. *Angstrom coefficient analysis*

The predominant contribution of smaller radius particles in summer is also clearly revealed by the seasonal evolution of the Angstrom coefficient (figure 3.5a) and of the ratio between fine and coarse number of particles per cross section of the atmospheric column, N_f (cm^{-2}) and N_c (cm^{-2}), respectively (figure 3.6).

Figure 3.5a reveals that 70% of the Å values span the 1.5–2 range and 14% span the 0–1 range mainly for the presence of dust outbreaks occuring from June to September. Then, the Angstrom coefficient seasonal (figure 3.5a) that shows a pattern similar to the AOD pattern (figure 3.1a), may indicate that the large spring–summer AOD values can be ascribed to a larger formation of submicron aerosols in the accumulation mode, such as the ammonium salts of sulphate and nitrate (Robles Gonzalez et al., 2003). The 1.5–2 Å range observed at Lecce from June to September is larger than the typical values of 1.13–1.4 indicated by Hess et al. (1998) for continental polluted air masses containing insoluble particles, water-soluble particles such as sulphate and nitrate aerosols, and soot. However, Angstrom coefficients spanning the 1.2–2.5 and 1.2–2.3 range have been retrieved at GSFC, USA and

Creteil-Paris, France, respectively from AERONET sunphotometer measurements performed from June to September to characterize urban–industrial aerosols (Dubovik et al., 2002a). It is also worth observing from figure 3.5a that 15-day averaged Å-values span the range 1.0–1.5 from October 2003 to March 2004.

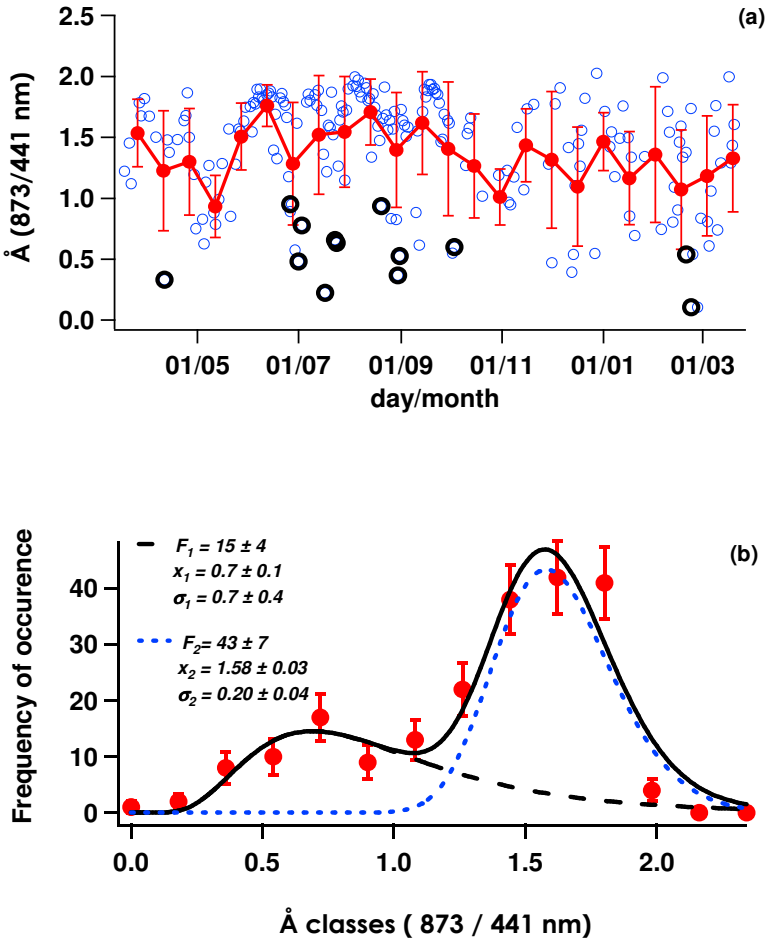

Figure 3.5. (a) Temporal plots of Angstrom coefficients (873nm/ 441 nm (b) Frequency of occurrence plot (full dots).

The contribution of large size aerosols such as dust and coarse mode sea-salt particles leading to Angstrom coefficients smaller than 1, is expected to be significant during all the year at Lecce, being ~20 km away from both the Adriatic and Ionic Sea, respectively, and about 800 km away from the African coast (De

Tomasi and Perrone, 2003). In fact, figure 3.5a shows that Å daily averaged-values ranging from 0.2 to 1 are observed throughout the year. However, the contribution of large size aerosols can be larger in autumn–winter as a consequence of the lower AODs mainly due to the reduced contribution of long-range transported fine particles and to the local reduced weather stability that does not favour the accumulation of fine particles. Angstrom coefficients in the 0.35–0.41 range are indicated by Hess et al. (1998) for polluted maritime air masses and between 0.08 and 0.12 for clean maritime air masses.

The Angstrom coefficient frequency distribution shown on figure 3.5b allows the fitting by a bimodal lognormal distribution with the larger amplitude mode peaked at 1.58±0.03 and the lower amplitude mode peaked at 0.7±0.1. The bimodal structure of the Angstrom coefficient frequency distribution also supports the assumption that two main aerosol types dominate at Lecce: urban–industrial in spring–summer and maritime-polluted in autumn–winter. The variability range of the mode peaked at 0.7±0.1 spans the 0–2 range, but most data points are within the 0–1 range. This mode is representative of large size particles such as mineral aerosols and large size sea-salt particles.

AERONET data from three island locations in the Atlantic (Bermuda), Pacific (Lanai, Hawaii), and Indian (Kaashidhoo, Maldives) Ocean, respectively, have been used by Smirnov et al. (2003) to characterize maritime aerosols and it is worth observing that

the Angstrom coefficient frequency of occurrence plots of the three sites are rather similar to the frequency distribution plot of mode 1 (dashed line) of figure 3.5b. In particular, it has been found that the 2 parameter frequency distribution has a maximum at 1.3 for Kaashidhoo, peaks at 0.9 for Bermuda, and is skewed towards smaller 2~0.7 for Lanai. To this end, it is worth observing that the Lanai frequency

distribution of daily averaged AODs (500 nm) shows that most of the optical depths are less than 0.1 and that the peak value is situated at about 0.06, as it is revealed by the higher amplitude mode of figure 3.1c (dashed line) of this paper that mainly represents autumn–winter AODs.

The larger Å-amplitude mode of figure 3.5b (dotted line) that spans the 1–2 range and is peaked at 1.58±0.03, can be considered representative of small radius particles such as those transported by anthropogenic polluted air masses of local origin or long-range transported from the Atlantic, Central and Eastern Europe. The industrial–urban aerosols over GSFC, USA and Creteil-Paris, France were also characterized by Angstrom coefficients spanning the 1.2–2.5 range.

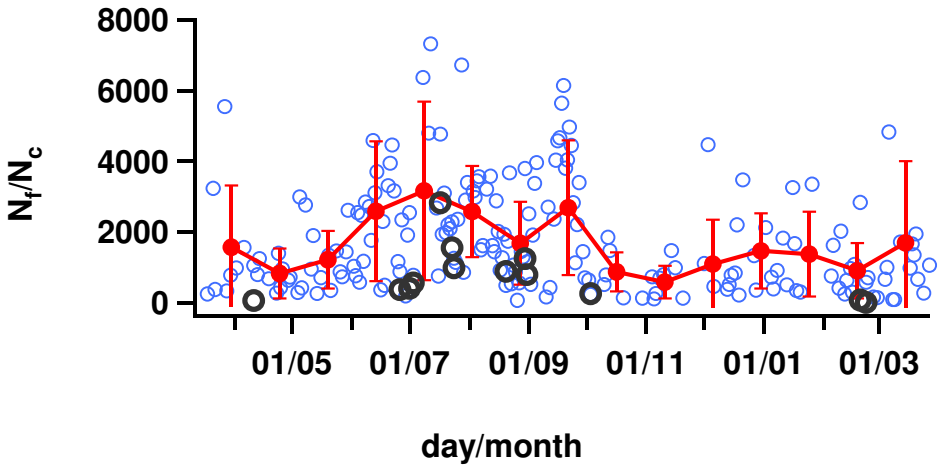

Figure 3.6. Temporal plot of the ratios of fine and coarse number of particles per cross section of the atmospheric column (cm^{-2}).

3.2. High-aerosol-load days analysis

It is worth observing from figure 3.1a that 6 days (crossed symbols), 3 of which are Sahara dust days, are characterized by AODs larger than 0.6. These high-aerosol-load days are considered in this study to obtain a first insight between aerosol

properties and air mass backtrajectories. Daily averaged values of AOD, SSA, Å, *n*, and *k* of the six high AOD days are given in Table 1. Errors associated with daily averaged parameters are estimated according to the procedure described in Dubovik et al. (2000b), or represent ±1 standard deviation from daily averaged values. The accuracy of the Angstrom coefficient is estimated by considering the uncertainties of the AOD values used to retrieve Å values.

Table 1 Daily-averaged aerosol parameters at 441 nm of six selected high-AOD days of the year 2003

month/day	AOD	SSA	n	k	Å
06/09	0.82±0.01	0.94±0.03	1.34±0.04	0.007±0.003	1.82±0.06
07/17	0.72±0.01	0.92±0.03	1.33±0.04	0.003±0.001	0.22±0.04
08/08	0.6±0.1	0.93±0.03	1.50±0.07	0.010±0.004	1.83±0.01
08/16	0.7±0.2	0.92±0.03	1.46±0.09	0.011±0.004	1.75±0.07
08/30	0.6±0.2	0.95±0.03	1.35±0.04	0.0015±0.0006	0.37±0.07
10/03	0.65±0.01	0.93±0.03	1.38±0.04	0.003±0.001	0.60±0.04

Daily-averaged volume size distributions of the 6-high-AOD days are plotted in figure 3.7a-b.

Four-day analytical back trajectories of June 9, July 17, August 8, and August 16 are shown in figures 3.8a–c and 3.9a. The advection pattern of August 30 and October 3rd is similar to that of July 17 and they are not given. Figures 3.7a and 3.8a–c, and Table 1 show that aerosols with a predominant contribution of small (Å=1.82±0.06), moderately absorbing (*k*=0.007±0.003; SSA=0.94±0.03) particles are advected to Lecce from east-Europe on June 9.

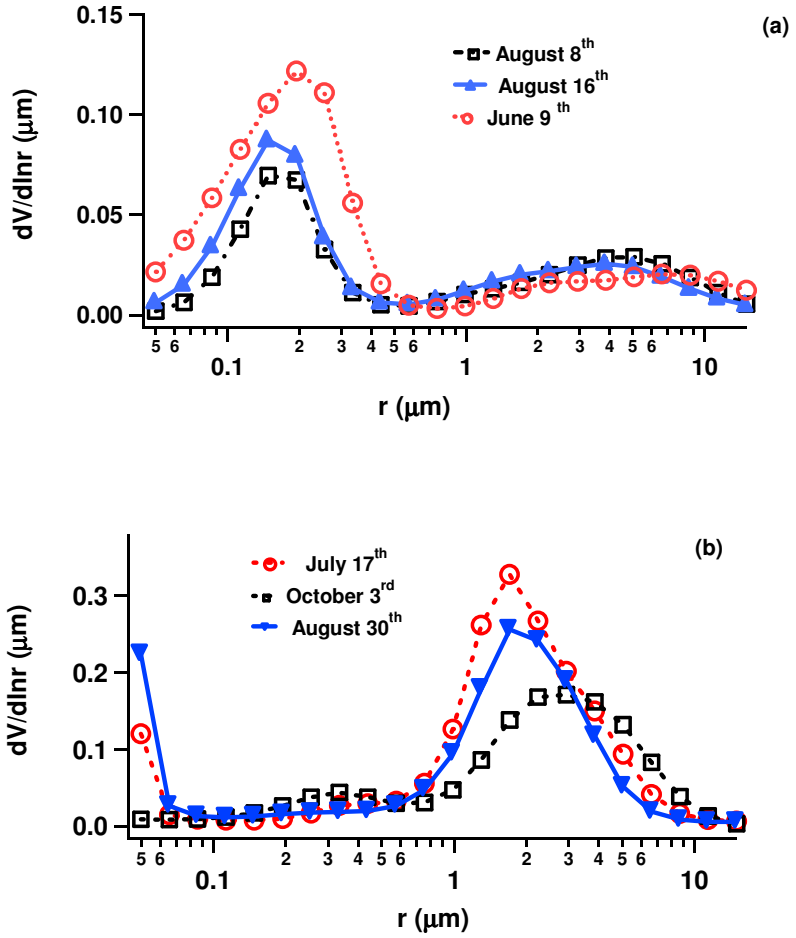

Figure 3.7. Daily averaged volume size distributions obtained from the non-spherical aerosol retrieval method, for high aerosol optical depth days of the 2003 year: (a) June 9th (AOD (441nm)=0.82); August 8th (AOD (441nm)=0.62); August 16th (AOD (441nm)=0.69); (b) July 17th, (AOD (441nm)=0.72); August 30th (AOD (441nm)=0.62); October 3rd (AOD (441nm)=0.65).

Aerosols with a predominant contribution of small, absorbing particles are also advected on August 8 and 16 from north (figure 3.8b) and west-Europe (figure 3.8c), respectively. Air masses coming from eastern, northern, and western Europe have the common property to travel across several large cities and industrialized European areas before reaching Lecce (figures 3.8a–c) and as a consequence these air masses can all be quite affected by urban–industrial aerosols (e.g. De Tomasi and Perrone, 2003), as well as by seasonal biomass burning (e.g. Balis et al., 2003). To this end, it is worth mentioning that SSAs of urban aerosols span the 0.942–0.984 range at 450

nm as relative humidity is varied from 0% to 99%, according to d'Almeida et al. (1991). Moreover, Levoni et al. (1997) have shown that the 450 nm-SSA that is 0.94 for dry externally mixed urban aerosols reduces to 0.91 for dry internally mixed urban aerosols.

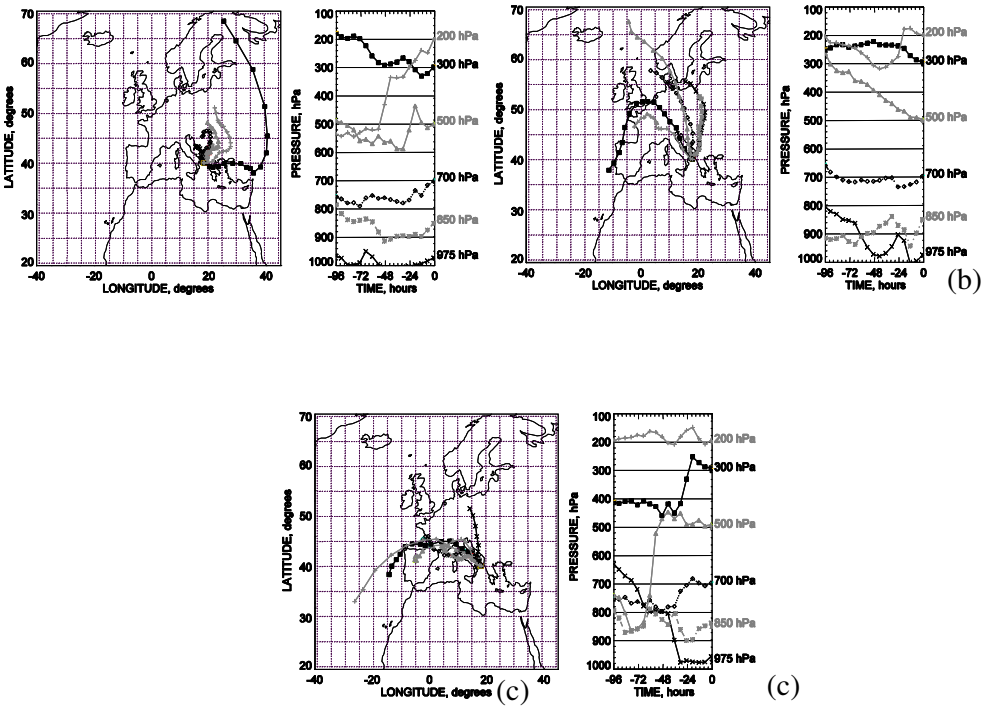

Figure 3.8. Four-day analytical backtrajectories at 13 UTC of high AOD days: (a) June 9th (AOD=0.82); (b) August 8th (AOD=0.62); (c) August 16th (AOD=0.69).

Table 1 shows that the SSA takes averaged values 0.94±0.03, 0.93±0.03, and 0.92±0.03 on June 9, August 8, and August 16, respectively, and the comparison of the aerosol volume size distributions of figure 3.7a and those reported by Dubovik et al. (2002a) for urban/industrial aerosols, reveals that they are rather similar to the ones observed at GSFC (USA) and Creteil-Paris (France): the total volume of fine-mode particles is clearly larger than the total volume of coarse mode particles and

both increase with AODs. SSA values in Creteil-Paris also are rather similar to those retrieved (Table 1) on the days of figure 3.7a.

The back trajectories of figure 3.9a show that Sahara dust particles are advected on July 17.

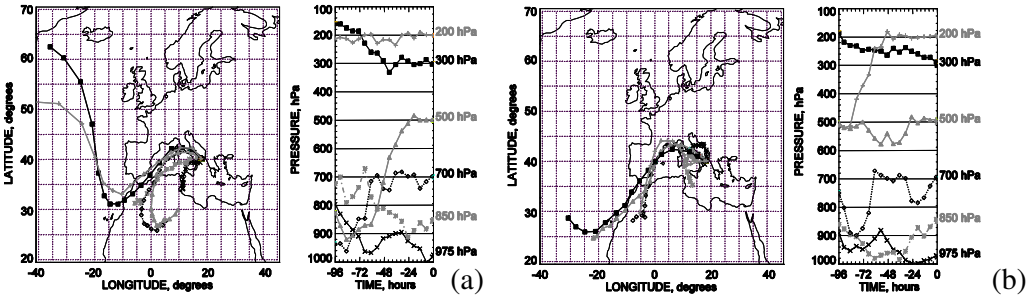

Figure 3.9. Four-day analytical back trajectories at 13 UTC of high AOD days: (a) July 17th, (AOD=0.72); (b) June 27th, (AOD=0.56)

North–west Africa also is the source region of the back trajectories of August 30 and October 3. The daily-averaged volume size distributions of the three dust days obtained from the non-spherical aerosol retrieval method (Dubovik et al., 2002b) are plotted on figure 3.7b and reveal that the coarse mode volume distribution is predominant and as a consequence Angstrom coefficients take averaged values lower than 0.6 on these dust days, in accordance with typical desert aerosol properties (e.g. Dubovik et al., 2002a).

Hence, aerosols of different origin and type can be advected at Lecce. However, depending on travel distance and residence time over source regions and monitoring site, the particle number concentrations, the physical and chemical state, and thus the optical properties of aerosols change.

In particular, the comparison between figure 3.1a and b indicates that the optical and chemical properties of Sahara dust particles are quite less dependent on wavelength.

Indeed, comparison of figures 3.1a and b may lead to the assumption that the lower AOD dependence on wavelength can be used as marker for the dominant contribution of desert type particles. AODs reduce by 13%, 19%, and 33% on July 17, August 30, and October 3, respectively, as the wavelength is varied from 441 to 873 nm. As a consequence, the Angstrom coefficient takes values ranging from 0.1 to 1 along dust events (figure 3.5a). The AOD wavelength dependence is determined by size distribution, shape and chemical composition (real and imaginary refractive indices) of aerosol particles and desert aerosols mainly consist of the water soluble component and the nuclei, accumulation, and coarse mode of mineral particles (Ackermann, 1998; d'Almeida et al., 1991). Extinction coefficients of the water soluble component decrease with k and can mostly be approximated by $k^{-1.4}$ to $k^{-1.6}$ in the 400–900 nm range, according to Volger et al. (1996). Therefore, the AOD wavelength dependence revealed by figures 3.1a and b for desert aerosols is mainly determined by the mineral component.

Recent characterizations of water-insoluble components of Sahara dust samples from rainfall residues collected at Lecce have shown that dust particles with a high content of illite are mainly advected over the Mediterranean basin during dust storms (Blanco et al., 2003). These results are also in satisfactory accordance with those obtained by Avila et al. (1997) by analyzing 11-year records of Africa dust rain in the Montseny mountain (north eastern Spain). They have observed that illite was the most abundant mineral identified in all dust samples by X-ray diffraction and that the illite concentration was 41% when the source region was western Sahara, and 34.5% for the air masses coming from central Algeria. They have also shown that the differences in mineralogy between source regions were significant for the lower content minerals, smectite, kaolinite, quartz and dolomite.

Results on the wavelength dependence of illite, kaolinite, and quartz extinction coefficients are reported by Sokolik and Toon (1999) and it is shown that extinction coefficients increase with wavelength and in the 400–900 nm range can fitted by $\lambda^{0.1}$ and $\lambda^{1.6}$ for lognormal size distributions with the median radius of 0.5 and 0.7 μm, respectively. It is also reported that SSAs of illite and kaolinite calculated at 440 nm for lognormal size distributions with median radius of 0.25, 0.5, and 0.7 μm vary from about 0.93–0.99 and that the illite real and imaginary refractive indices take the value of 1.4 and 0.001 at 440 nm, respectively (Sokolik and Toon, 1999). SSAs varying from 0.92 to 0.98 (figure 3.2a), real and imaginary refractive indices in the range 1.46–1.60 (figure 3.3) and 0.005–0.05 (figure 3.4a), respectively have been retrieved at 441 nm by sunphotometer measurements along dust events. Therefore, according to the data of Sokolik and Toon (1999) and by taking into account the accuracy of sunphotometry retrievals (Dubovik et al., 2000b), we believe that the AERONET aerosol parameters retrieved during dust events support experimental findings (e.g. Avila et al., 1997; Blanco et al., 2003) indicating that dust particles with a high content of illite are mainly advected over the Mediterranean basin during Sahara dust storms in our study. Finally, it is worth mentioning that *k* values ranging from 0.002 to 0.0175 in the UV (360 nm) have recently been obtained from satellite observations in north–west Africa (Colarco et al., 2002), in agreement with sunphotometer retrievals reported in this chapter.

3.3. Basic statistical analysis

Average (±1 standard deviation), maximum, and minimum values of all investigated parameters in paragraph 3.1 are given in Table 2 at different

wavelengths to summarize aerosol properties and facilitate comparison with literature data. Table 2 reveals that only AOD values are quite dependent on wavelength. The mean AOD value that is 0.25±0.15 at 441 nm, takes the value 0.10±0.08 at 873 nm the value 0.10±0.08 at 873 nm. Average, maximum, and minimum AOD values of Table 2 are in good accordance with those recently reported by Gerasopoulos et al. (2003) for Mount Athos Observatory (MAO), 40º 23'N, 23º 57' E, a rural area in the Chalkidi peninsula of Greece that is situated along the expected pathway through which pollution from central and eastern Europe influences aerosol loading over the Eastern Mediterranean. On the contrary, a mean value of 1.6±0.3 has been calculated at Thessaloniki that is 100 km away from MAO (Gerasopoulos et al., 2003). The larger Å mean value of Thessaloniki can be due to a larger contribution of fine urban/industrial particles such as carbonaceous particles, and anthropogenic or biogenic sulphates (d'Almeida et al., 1991). Å mean values (670 nm/443 nm) of 1.6 and 1.5 for the year 1996 and for the first 6 months of the year 1997, respectively have also been retrieved at Thessaloniki by Balis et al. (2000) from CIMEL sunphotometer measurements. In particular, larger Å values (>1.6) have been detected in September–October 1996 and in March–April 1997, the months corresponding to periods with usual urban activities in the area. A significant seasonal variability of the AOD at 532 nm with maximum monthly values of 0.35

Table 2: Basic statistical parameters at different wavelengths calculated from daily-averaged values of aerosol optical depths (AOD), single scattering albedos (SSA), real (*n*) and imaginary (*k*) refractive indices, and Angstrom exponents (Å). Average values are provided with ±1 standard deviation.

AOD				
	441 nm	**673 nm**	**873 nm**	**1022nm**
Average	0.26 ± 0.15	0.14 ± 0.08	0.10 ± 0.08	0.09 ± 0.08
Maximum	0.82	0.66	0.63	0.61
Minimum	0.04	0.02	0.02	0.02
SSA				
	441 nm	**673 nm**	**873 nm**	**1022 nm**
Average	0.95 ± 0.03	0.95 ± 0.03	0.94 ± 0.04	0.94 ± 0.04
Maximum	0.99	0.99	0.99	0.99
Minimum	0.86	0.84	0.80	0.79
n				
	441 nm	**673 nm**	**873 nm**	**1022 nm**
Average	1.43 ± 0.09	1.45 ± 0.08	1.46 ± 0.07	1.49 ± 0.07
Maximum	1.6	1.60	1.6	1.60
Minimum	1.33	1.34	1.35	1.36
k				
	441 nm	**673 nm**	**873 nm**	**1022 nm**
Average	0.004 ± 0.003	0.004 ± 0.003	0.004 ± 0.003	0.004 ± 0.003
Maximum	0.018	0.022	0.025	0.024
Minimum	0.0005	0.0005	0.0005	0.0005
Å				
	870/440 nm		**340/440 nm**	
Average	1.4 ± 0.45		1.4 ± 0.4	
Maximum	2.0		2.6	
Minimum	0.1		0.1	

during spring for clear sky conditions, and minimum values of 0.15 during late autumn and winter, has also been detected at Thessaloniki by Balis et al. (2000), in accord with the plot of figure 3.1a.

3.4 Conclusions

Temporal plots and frequency of occurrence distributions of daily-averaged retrievals of AERONET sun photometer measurements performed at Lecce from March 18, 2003 to March 27, 2004 are used to get results on the characterization of aerosol load and dominant aerosol types over south–east Italy. 4-day-analytical back trajectories are used to show the impact of continental pollution from Central and Eastern Europe, of maritime and long-range transported polluted air masses from the Atlantic Ocean, of mineral dust from North Africa, and of sea spray from the Mediterranean Sea itself.

Temporal plots of the main aerosol parameters at 441 nm reveal a significant seasonal variability of aerosol load, particle size distribution and chemical composition. It is shown that AODs and SSAs take 15-day-averaged values spanning the 0.2–0.4 and 0.93–0.95 range in spring–summer, respectively. AOD and SSA 15-day-averaged values vary in the 0.1–0.2 and 0.97–0.98 range respectively in autumn–winter. As a consequence, the AOD frequency distribution shows two dominant modes peaked at 0.049±0.008 and 0.20±0.03 that characterize the AOD distribution in autumn–winter and spring–summer, respectively.

The SSA frequency of occurrence plot also allows the fitting by a bimodal lognormal distribution with the larger amplitude mode peaked at 0.974±0.003 and the lower amplitude mode at 0.94±0.01. It is shown that the mode peaked at 0.94±0.01 that spans the 0.86–0.99 range is mainly representative of spring–summer SSAs. Then, the comparison with literature data of Lecce's spring–summer AODs and SSAs has led to the assumption that moderately-absorbing urban–industrial aerosols dominate in spring– summer at Lecce. On the contrary, the comparison of autumn-winter AODs and SSA with literature data (Smirnov et al., 2003) has led to the assumption that polluted-maritime aerosols dominate in autumn-winter at Lecce.

The seasonal dependence of the Angstrom coefficient (873 nm/441 nm), whose frequency distribution plot allows the fitting by a bimodal lognormal distribution with the larger amplitude mode peaked at 1.58±0.03 and the lower amplitude mode at 0.7±0.1, furthermore supports the above conclusions: the latter mode can represent sea-salt and water soluble particles (the main components of maritime aerosols) affected by water uptake, besides dust particles.

The seasonal dependence of the particle chemical composition is revealed by n and k temporal plots: k takes 15-day averaged values $\cong 0.007$ in summer and $\cong 0.002$ in autumn–winter, whereas n 15-day averaged values span the range 1.40–1.47 and 1.48– 1.54 in spring–summer and autumn–winter, respectively. Then, the trimodal lognormal distribution fitting the n frequency of occurrence plot allows recognition of the main aerosol constituents: sea-salt and water soluble particles quite affected by water uptake by the mode peaked at 1.32±0.01, soot and minerals by the mode peaked at 1.58±0.08, water soluble particles by the mode peaked at 1.44±0.03.

The k frequency of occurrence plot reveals that moderately-absorbing aerosols dominate over south–east Italy: 70% of k daily averaged values span the range $0.0005<k<0.005$. However, the k trimodal lognormal distribution fitting curve reveals two lower amplitude modes at $(2.51\pm0.08)\times10^{-3}$ and $(5.0\pm0.1)\times10^{-3}$, that maybe are due to wet and dry water-soluble aerosol components, besides the larger amplitude and broader mode peaked at $(0.11\pm0.04)\times10^{-3}$.

It is also shown that the comparison with literature data of sunphotometry retrievals along dust events supports experimental findings showing that moderately absorbing ($0.005<k<0.05$) dust particles with a high content of illite are mainly advected over the central-east Mediterranean basin during Sahara dust storms.

Average, maximum, and minimum values of all investigated aerosol parameters are also provided to facilitate comparison with literature data and it is shown that

Lecce's data are in satisfactory accordance mainly with those found in south–east Mediterranean sites away from major sources of anthropogenic aerosols.

It is also shown that the aerosol volume size distributions referring to high-AOD-days that are affected by urban–industrial aerosols from Central and Eastern Europe, and from the Atlantic Ocean, are rather similar to the ones observed at GSFC (USA) and Creteil- Paris (France) by Dubovik et al. (2002a): the total volume of fine-mode particles is clearly larger than the total volume of coarse mode particles and both increase with AODs. On the contrary, the daily-averaged volume size distributions of dust-days reveal that the coarse mode volume distribution is predominant.

In conclusion, we believe that these results, based only on 1 year of measurements, may have contributed to the aerosol characterization over the Mediterranean basin providing indicative data on the seasonal evolution of aerosol load, particle size distribution, and chemical composition, and on the aerosol parameters and/or types with larger frequency of occurrence. These indicative results will also be used to validate satellite retrievals of aerosol parameters in chapters 5, 6 and 7 and to incorporate aerosol particles into climate models and evaluate climate forcing effects produced by aerosols of different origin and type.

CHAPTER 4

CORRELATION BETWEEN ADVECTION PATTERNS AND AEROSOL OPTICAL AND MICROPHYSICAL PROPERTIES IN THE CENTRAL MEDITERRANEAN BASIN

The Mediterranean region, the largest enclosed basin of the Earth, is certainly one of the most interesting regions in terms of atmospheric particulate and various model studies predicted maximum net direct radiative forcing by aerosols for this region (e.g. Charlson et al. 1991; Hatzianastassiou et al., 2004; Giorgi, 2006). The Mediterranean Sea that is bounded to the north by the European continent and to the south by North Africa, is largely affected by different classes of particles: desert dust, from the Sahara desert and surrounding arid regions; anthropogenic particles, produced mainly in urban and industrial areas of Europe; marine aerosol, from the Mediterranean itself or transported from the North Atlantic; and biomass burning particles, often produced in forest fires (e.g. Lelieveld et al., 2002; Barnaba et al., 2004; G. Pace et al., 2006; Barnaba et al, 2007). The strength of dust outbreaks over the Mediterranean tends to facilitate the Saharan dust detection by both ground and space based observations, allowing the quantification of its transport and of its optical and microphysical properties (e.g. De Tomasi et al., 2003; Tafuro et al., 2006). In contrast, the export of particulate matter from the industrialized countries surrounding the Mediterranean is complicated by the fact that an extremely large number of species and gas precursors contribute to it (e.g. Formenti et al., 2002; Barnaba et al., 2004). The Mediterranean Intensive Oxidant Study (MINOS) Project, that highlighted the important role of pollutants in the summertime Mediterranean atmosphere, is representative of the international effort to quantify the impact of anthropogenic emissions on the natural background of the Mediterranean environment (Lelieveld et al., 2002). Barnaba and Gobbi (2004), for the sole Mediterranean basin and for the whole 2001, implemented a method (aerosol mask) to separate, on the basis of MODIS data, the contribution to the total aerosol optical depth (AOD) of the three aerosol types prevailing over the Mediterranean basin: maritime, continental and desert dust aerosol. In the paper of Barnaba and Gobbi (2004) the application of an

aerosol mask showed that in urban/industrial conditions, optical properties are dominated by fine particles while, in the presence of desert dust, these are strongly dominated by coarse particles. In maritime conditions, the relative contribution of coarse particles, although variable, is generally higher than in urban/industrial conditions and lower than for desert dust.

Models were also usefully employed to investigate the export pathways of air pollution from Europe (Stohl et al., 2002; Duncan and Bey, 2004). The cluster analysis that appeared at the end of the 80's (Kalkestein et al., 1987; Moody, 1986; Moody and Galloway, 1988) represents a valuable tool to reduce the subjectivity of the atmospheric aerosol classification. Cluster analysis is a multivariate statistical technique which is finding increasing application in scientific research (Andenberg, 1973). The approach involves splitting data set into a number of groups which are distinct in terms of typical group values of the variables.

Four-day back trajectories categorized in five major clusters were used by Kazadzis et al. (2007) to assess the influence to the aerosol load over Thessaloniki (Greece) of long-range transport from various regions. Nine years (1997-2005) of direct sun spectral measurements were used for the determination of the spectral aerosol optical depth (AOD) in the UV , as well as of the Angstrom exponent. The analysis of the origin of aerosols at Thessaloniki showed that in addition to the boundary layer aerosol originating mainly from local sources, transport of aerosols at higher altitudes contribute to the total AOD column, especially in the summer months. The cluster analysis showed that the contribution of air masses coming from the North and North Eastern directions result in high aerosol loads over Thessaloniki, while minimum aerosol optical depth is associated with air masses originating from the Atlantic ocean.

Five-day backtrajectories were used by Pace et al. (2006) to characterize at Lampedusa (Central Mediterranean) aerosol optical properties retrieved from multi filter rotating shadowband radiometer (MFRSR) observations (July 2001-September 2003). The backtrajectory analysis revealed that in cloud-free conditions, 36% of the air masses came from Africa, 25% from Central-Eastern Europe, and 19% from Western France, Spain and the North Atlantic. In almost all cases, African aerosols displaied high values of AOD and low values of Angstrom exponent Å (average values of AOD and Å were 0.36 and 0.42, respectively). Particles originating from Central-Eastern Europe showed relatively large average values of AOD and Å (0.23 and 1.5, respectively), while particles from Western France, Spain and the North Atlantic showed the lowest average values of AOD (0.15), and relatively small values of Å (0.92). Clean marine conditions were rare at Lampedusa , and were generally associated with subsidence of the air-masses reaching the island. Average values of AOD and Å for clean marine conditions reached 0.11 and 0.86, respectively. Intermediate values of Å were often connected with relatively fast changes of the air-masses originating sector, suggesting the contemporary presence of different types of particles in the air column.

Four-day backtrajectories were used by Fotiadi et al. (2006) to characterize the aerosol physical and optical properties over the eastern Mediterranean basin using a complete series of two-year (2003-2004) measurements from the FORTH-AERONET station in Crete. Maximum values of AOD were found primarily in spring, which together with small values of Å indicate dust transported from African deserts, whereas the minimum values of AOD occurred in winter. In autumn, large AOD values observed at near-infrared wavelengths arised also from dust transport. In summer, large AOD values at ultraviolet (340 nm) and visible wavelengths (500 nm), together with large values of Å, were associated with transport of fine aerosols of

urban/industrial and biomass burning origin. In conclusion, the broad frequency distributions of AOD and Å values together with the backtrajectory analysis revealed the presence of a great variety of aerosol types over the study region including dust, urban-industrial and biomass-burning pollution, and maritime, as well as mixed aerosol types.

Several experimental studies on aerosols were focused on the Eastern Mediterranean area in the last decade (Mihalopolulos et al., 1997; Papayannis et al., 1998, 2005; Formenti et al., 2001, 2002; Lelieveld et al., 2002; Gerasopoulos et al., 2003; Balis et al., 2003, 2004; Amiridis et al., 2005). In contrast, only few studies were conducted to characterize aerosol properties in the Central Mediterranean.

In this chapter, aerosol measurements from the AERONET station in Lecce (40º 20' N, 18º 06' E) combined with five-day backtrajectories are analyzed to characterize aerosol properties over the Central Mediterranean basin, to assess the impact on the aerosol load of long-range transport from various regions, and to study the mixing of different aerosol types. The aerosol data include AOD, single scattering albedo (SSA), asymmetry factor (g), Angstrom coefficient (Å), fine-mode fraction (η), and lidar ratio (Lr) retrieved from measurements performed in the period March 2003 – October 2004. The location of the Lecce-AERONET station offers a good opportunity to monitor aerosols from different sources and distinguish among various aerosol load scenarios. Lecce is on a narrow peninsula of south-east Italy away from large cities and industrial areas, ~20 km away from both the Ionic and the Adriatic Sea, ~ 100 km away from the Balcan peninsula coast, and ~800 km away from the North Africa coast. Satellite images and data from the MODerate resolution Imaging Spectroradiometer (MODIS) were also used to better assess the effects of forest-fires (http://maps.geog.umd.edu/default.asp) and dust outbreaks (http://modis.gsfc.nasa.gov) on aerosol properties.

4.1 Aerosol source regions by 5-day backtrajectories

Analytical backtrajectories provide information on the aerosol origin observed at a particular location and on the dynamical patterns governing the air mass transport (Kazadzis et al, 2007). In this thesis, 5–day analytical backtrajectories were used to characterize main advection patterns over Lecce AERONET site. The trajectories are based on the trajectory Code 613.3 developed at NASA/Goddard - The Atmospheric Chemistry and Dynamics Branch (http://croc.gsfc.nasa.gov/aeronet/index.html) and are provided for distinct arrival pressure levels and for two arrival times (12:00 and 24:00 UTC) on a day-by-day basis. Figure 4.1 shows the 5-day back trajectories of all available measurement days within March 2003 – October 2004, for the arrival time of 12:00 UTC and for arrival pressure levels of 950, 850, 700, 500, 400, 300, 250 and 200 hPa. In particular, in this study trajectories with arrival pressure levels over Lecce of 950, 850, 700 and 500 hPa have been used. To this purpose, as told in Chapter 1, it worth mentioning that Lidar measurements at Lecce revealed that the aerosol load extends up to ~ 5 km from ground (De Tomasi et al., 2006). One can observe from figure 4.1 that most of the measurement days are characterized by air masses coming from North, North-West Europe, while few of them are characterized by air masses coming from Southern regions.

Considering figure 4.1 and hence the main advection patterns over south-east Italy (Perrone et al., 2005; De Tomasi et al., 2006), three broad geographical sectors, shown in Figure 4.2, were defined as aerosol source regions: Sector A, which includes all continental European sources with the exception of Spain that is generally crossed by air masses from the west Atlantic Ocean; Sector B, which includes the Southern Mediterranean Sea and the Africa continent; Sector C, which includes the Western Mediterranean, the Iberian Peninsula, and the Atlantic Ocean. Air masses from Sector A have the common property to travel across several industrialized

European areas before reaching Lecce (De Tomasi et al., 2003). African deserts are instead the main sources of the Sector B aerosol. Marine and to lesser extent anthropogenic particles from the Atlantic Ocean (http://ww.esrl.noaa.gov/csd/ICARTT/) and/or the Western Mediterranean regions are expected to be advected from Sector C. A degree of arbitrariness in the definition of the sectors exists, due to the effective distribution of the sources. Hence, a different identification of the sectors could also be possible.

The aerosol origin Sector can be identified by considering the time spent in the different sectors along with the trajectory pathway (di Sarra et al., 2001, Gerasopoulos et al., 2003) or by more sophisticated correlation methodologies (Formenti et al., 2001). Previous analysis have demonstrated that a good identification of the aerosol source Sector Could also be obtained by identifying the properties of particles originating from different geographical sectors. A sensitivity study was performed in this work in order to properly relate aerosol properties to source sector.

4.1.1 Global aerosol properties

Figure 4.3a shows the behaviour of AERONET Angstrom coefficient calculated from AOD values at 870 and 440 nm, versus the AERONET AOD at 440 nm retrieved

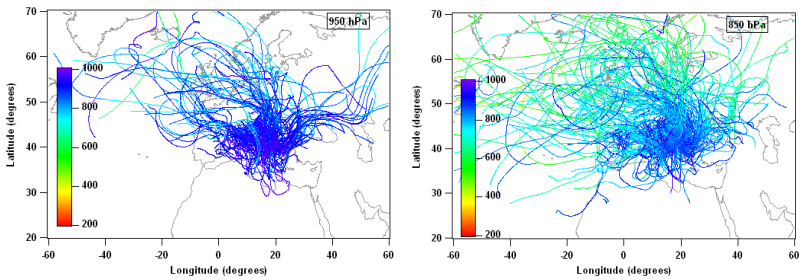

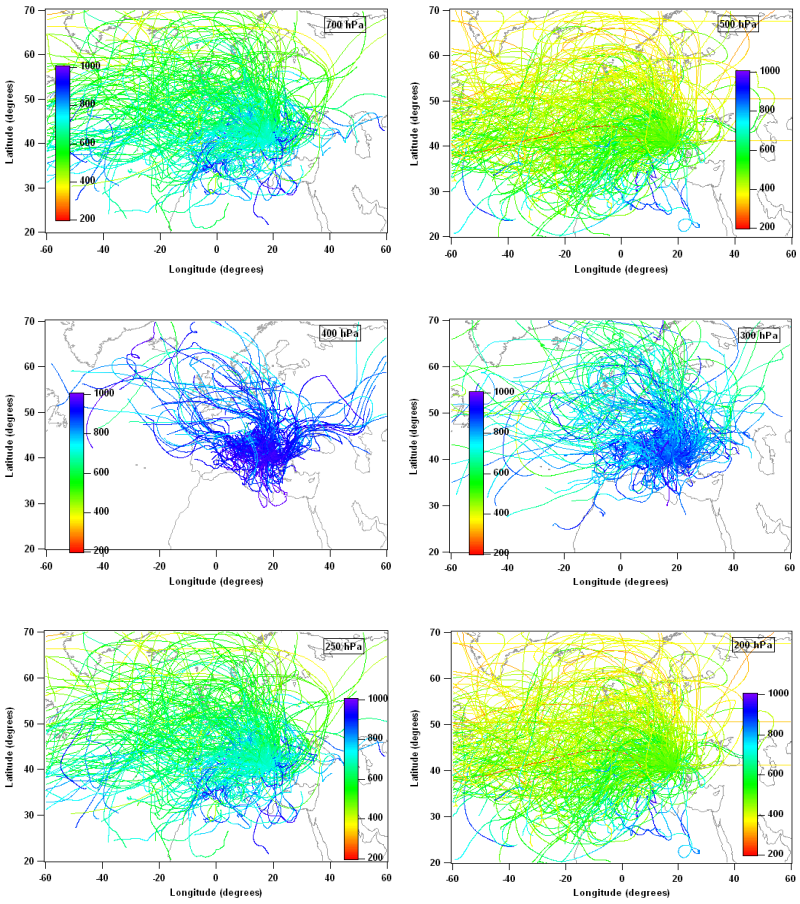

Figure 4.1. The 5-day back trajectories of all measurement days within March 2003 – October 2004, for the arrival time of 12:00 UTC and for arrival pressure levels of 950, 850, 700, 500, 400, 300, 250 and 200 hPa. Different colors are used to characterize pressure levels of each backtrajectory as a function of the time.

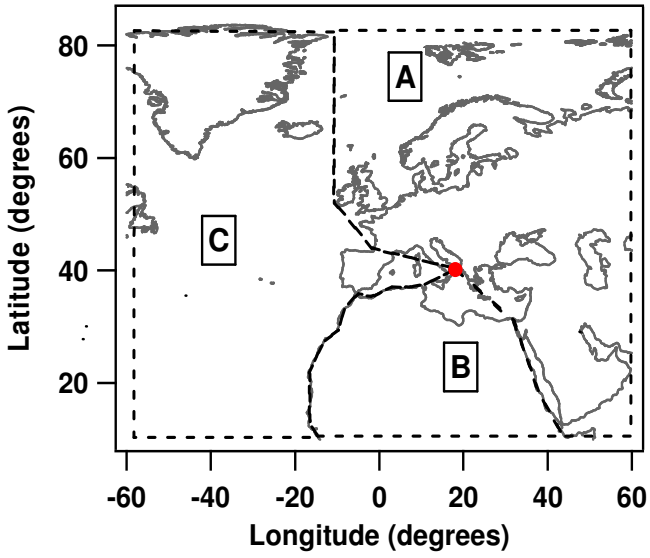

Figure 4.2. Aerosol source sectors.

from AERONET measurements performed in the period March 2003 – October 2004. In particular, quality assured (automatically cloud cleared and manually inspected) level 2 AERONET data from the V1 algorithm (Smirnov et al., 2000) have been used in this study.

It worth noting that AODs depend on aerosol load, while Å depends on the aerosol size distribution: typical values range from Å >2.0 for fresh smoke particles, which are dominated by accumulation mode aerosols to nearly zero for large dust particles (Dubovik and King, 2000a). Therefore, the Å-AOD scatterplot gives us a qualitative indication on the aerosol load due to particles of different size: particles of different size (type) tend to concentrate in different areas of the plot and this can allow inferring aerosol of different origin. This method has been used in a large number of studies and is based on the sensitivity of the AOD and the Å to different, somewhat independent, microphysical aerosol properties. Low and high values of Å are due to the dominant presence of large and small particles, respectively, i.e. the preponderance of the coarse or the accumulation mode (Pace et al., 2006).

A total of 658 measurements derived from 240 measurement days are reported in Figure 4.3a showing that Å and AOD values vary within the 0.1-2.2 and the 0.1-1.0 range, respectively. In addition, Figure 4.3a reveals either that small particles ($1.2 < Å < 2$) leading to AODs within the 0.1-0.4 range are predominant and that highest AOD values (>0.6) are due to fine mode particles.

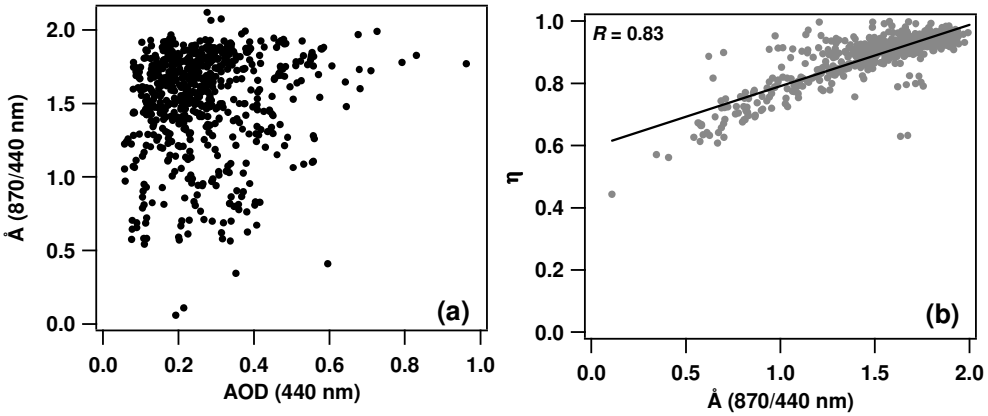

Figure 4.3. a) Scatter plot of the Angstrom coefficient (Å) calculated from AOD values at 870 and 440 nm and the AOD at 440 nm retrieved from 240 AERONET measurements days between March 2003 and October 2004; b) scatter plot of the fine mode fraction η at 440 nm versus Å.

Aerosol size is a key parameter to separate natural from man-made aerosol. The anthropogenic aerosol is dominated by fine-mode particles, while natural aerosol contains a substantial component of coarse-mode particles (e.g. Kaufman et al., 2001). The AERONET inversion algorithm allows retrieving volume particle size distributions and all particles with radius 0.06 μm ≤ r < 0.6 μm are considered fine, while those with 0.6 μm ≤ r ≤ 8.8 μm are considered coarse. The predominant role of fine-mode particles over south-east Italy is better revealed by Figure 4.3b showing the fine mode fraction η at 440 nm versus Å. η is the ratio between the fine-mode and the total optical depth at 440 nm. We observe that η values, which are quite correlated to Å values (correlation coefficient = 0.83), vary within the 0.5-1.0 range. In particular, η values within the 0.8-1.0 range are predominant (88%). Hence, anthropogenic particles are predominant over south-east Italy and are responsible of the highest AODs.

It is worth comparing Figure 4.3a of this paper with Figure 2 of the paper by Pace et al. (2006), and Figure 5 of the paper by Fotiadi et al. (2006), which are reported in this paper as figures 4.4 and 4.5, respectively. In particular, figure 4.4

shows the behaviour of the Angstrom exponent (α) versus the AOD (τ) at 495.7 nm from July 2001 to September 2003 retrieved by multi filter rotating shadowband radiometer (MFRSR) observations, carried out at the island of Lampedusa. Figure 4.5 represents the scatterplots of α versus τ per season obtained using spectral measurements from the AERONET station in Crete for the period 2003-2004. The comparison provides a quite significant indication on the dependence of the Å -AOD scatter plot, on the location of the monitoring site in the central-east Mediterranean basin.

The data reported by Pace et al. (2006) show, despite the results of this paper, that large-size particles characterized by Å values within the 0.5 - -0.3 range and by AOD values at 496 nm within the 0.2-0.8 range are predominant at Lampedusa that is ~ 140 km away from the Africa coast. Coarse mode particles are also responsible of the highest AOD values.

According to Pace et al. (2006), the particles advected at Lampedusa from European countries, are responsible of Å and AOD values within the 1-2 and the 0.1-0.6 range, respectively.

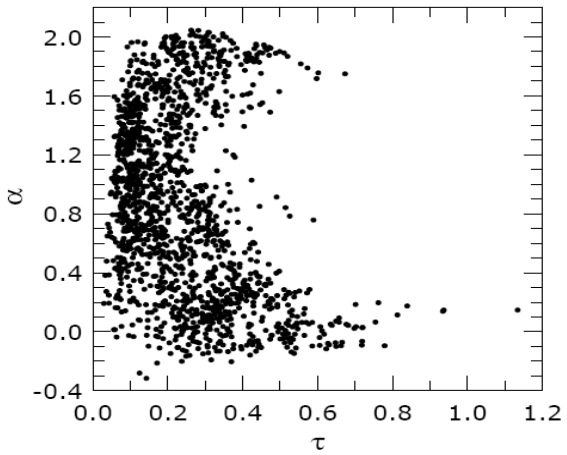

Figure 4.4. Behaviour of the Angstrom exponent, α, as a function of the aerosol optical depth, τ, during July 2001 – September 2003, reported as figure 2 in the paper by Pace et al., 2006.

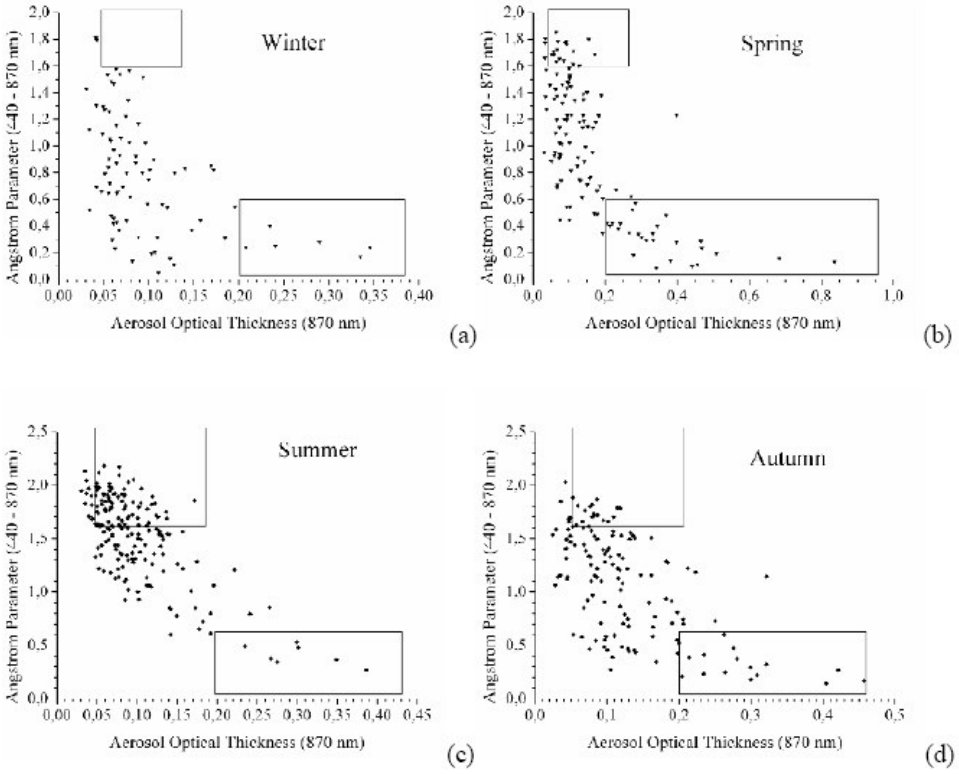

Figure 4.5. Scatterplot of Angstrom parameter (440 – 870 nm) versus the aerosol optical thickness at 870 nm per season reported in the paper by Fotiadi et al., 2006 as Figure 5.

The amount and properties of aerosols in the eastern Mediterranean island of Crete were found by Fotiadi et al. (2006) (figure 4.5) to be strongly determined by the marine environment involving significant concentrations of sea-salt aerosols produced by sea-spray, which constitute the background conditions. Å and AOD values were also influenced by dust aerosols mainly from African deserts, and secondarily from the Middle-East and Anatolian plateau. As a consequence, coarse mode particles also are predominant at Crete and are responsible of the highest AOD values. The transport of pollution fine aerosols from Europe and Turkey is responsible at Crete of the particles with Å values within the 1- 2 range, in

accordance to the results of Lampedusa and Lecce. However, fine-mode particles and hence, the aerosol of anthropogenic origin is responsible at Crete of AODs < 0.2. The larger distance of Crete from continental polluted regions is responsible of latter results. In conclusion, the above reported discussion highlights that, despite Lampedusa and Crete that are more affected by coarse mode particles mostly of natural origin, south-east Italy is more affected by fine-mode particles and hence by anthropogenic aerosol particles

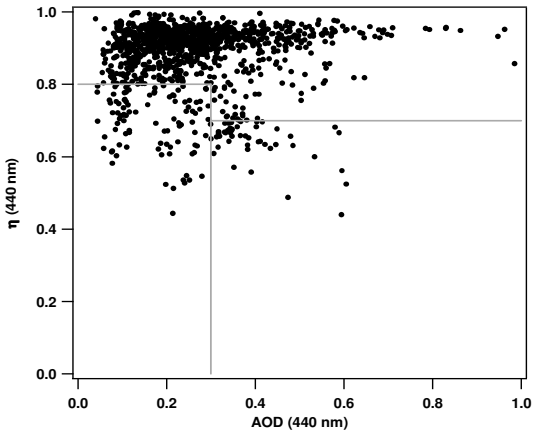

Figure 4.6 Scatterplot between AERONET fine mode fraction η and aerosol optical depth AOD at 440 nm retrieved at Lecce from March 2003 to September 2004.

Figure 4.6 shows the scatterplot of η versus the AOD at 440 nm retrieved at Lecce during the studied period. Likewise the Å-AOD plot, the η vs AOD plot also allows the discrimination of different aerosol types: η depends (mainly) on size distribution, while AOD depends mainly on the aerosol column density.

It is interesting to compare figure 4.6 with figure1 of the paper by Barnaba and Gobbi, 2004, here reported as figure 4.7. Barnaba and Gobbi implemented a simple method (aerosol mask) to separate the contribution of the three main aerosol types: maritime, continental and desert dust over the Mediterranean. In particular, they used based AOD and η values retrieved by MODIS measurements during the-year 2001.

Applying the aerosol mask method of figure 4.7 to figure 4.6 (grey lines) one can observe that most of the data points retrieved at Lecce are concentrated in the area of the plot characterized by η and AOD values that span the range 0.8 -1 and 0.05 -1, respectively. According to Barnaba and Gobbi (2004), continental aerosols were predominant over south-east Italy during the studied period.

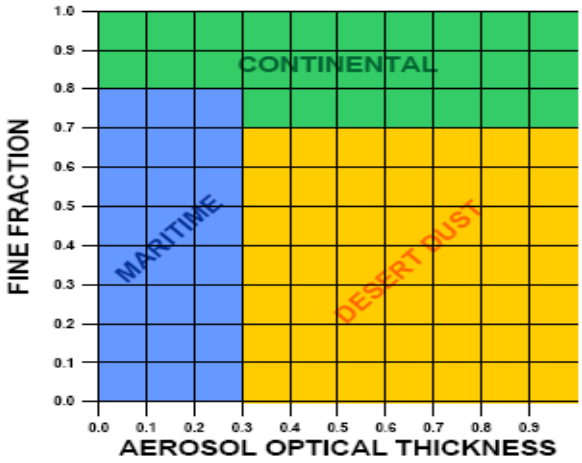

Figure 4.7 Aerosol mask defining the η – AOD regions corresponding to continental (green), desert dust (yellow) and maritime aerosol (blue) as reported in the paper of Barnaba and Gobbi, 2004.

4.1.2 Tested criteria to define sources sectors

The peculiar geographical location of south-east Italy determined the use of different constraints on the number and time spent by each back-trajectory in a sector, to properly define an aerosol source sector. The performed sensitivity tests are outlined below. The trajectories referring to the air masses confined at altitudes ≤ 5 Km have been used in these studies. In fact, aerosols have been detected by the lidar only up to about 5 km (De Tomasi et al., 2006)

4.1.2a *Definition of Sector A as source – region according to back trajectories pathways*

The different criteria implemented in this work to define the constraints required to define Sector A as source – region, are outlined below. We believe that Sector A could be considered source sector:

a) if at least one of the back-trajectories has spent more than 80% of the last 5-day period inside the Sector A before reaching the sampling site.
b) if at least two of the four back-trajectories have spent more than 80% of the last 5-day period inside the Sector A before reaching the sampling site.
c) if at least three of the four back-trajectories have spent more than 80% of the last 5-day period inside the Sector A before reaching the sampling site.
d) if all the back-trajectories spent more than 80% of the last 5-day period inside the Sector A, before reaching the sampling site.

Figures 4.8 shows the η vs the AOD plot obtained according to the a) criterion.

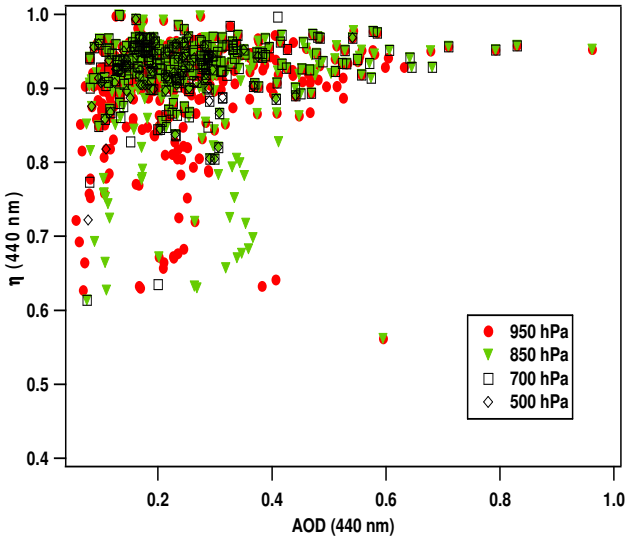

Figure 4.8. η vs AOD at 440 nm for the aerosol source Sector A selected using the following criterion: all the 5-day back-trajectories are attributed to the Sector A when at least one of them has spent more than 80% of the last 5-day period inside the sector

Different symbols in the figure 4.8 represent data points for different back-trajectory arrival pressure levels (950 hPa, 850 hPa, 700 hPa, 500 hPa). Figure 4.8 shows that η vary between 0.5 – 1 and AOD vary between 0.05 and 1: the variability range is close to that of figure 4.6. We believe that the results of figure 4.8 indicate that the a) criterion is not good to discriminate different aerosol types.

The η versus AOD plot obtained according to the b) criterion is shown in figure 4.9. The wide variability range of η and AOD also indicates that the b) criterion doesn't allow discriminating aerosol coming from Sector A.

Figure 4.10 shows the η – AOD plot for the aerosol source Sector A selected according to the c) criterion.

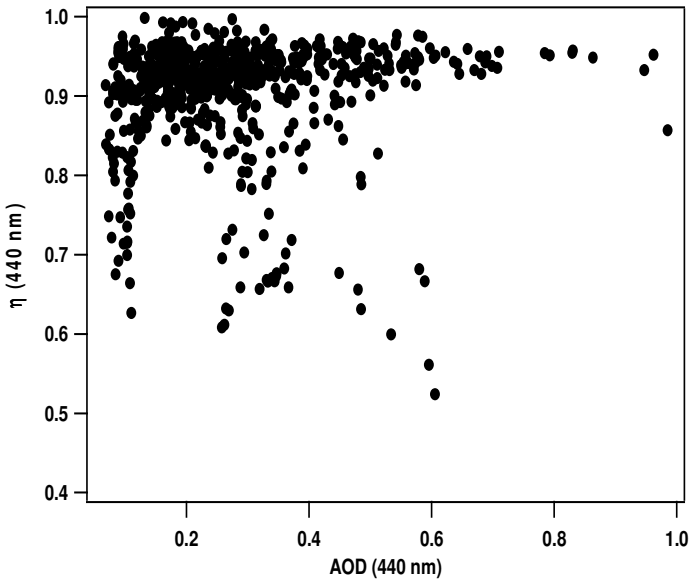

Figure 4.9. η vs AOD at 440 nm for the aerosol source Sector A selected using the following criterion: all the 5-day back-trajectories are attributed to the Sector A when at least two of them have spent more than 80% of the last 5-day period inside the sector

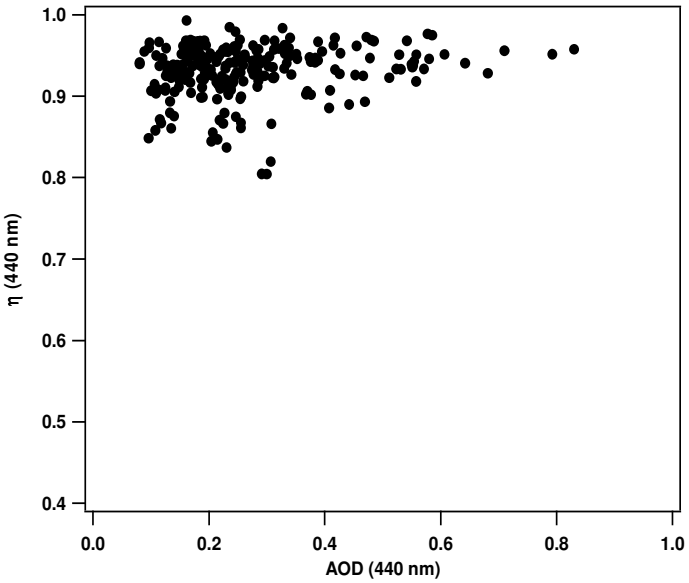

Figure 4.10. η vs AOD at 440 nm for the aerosol source Sector A selected using the following criterion: all the 5-day back-trajectories are attributed to Sector A when at least three of them have spent more than 80% of the last 5-day period inside the sector

One observe from figure 4.10 that, the fine fraction parameter assume values in the range 0.8-1 if at least three of the four back trajectories have spent at least 80% of the time inside Sector A. We believe that the c) criterion is well suited to characterize

Sector A as source sector. In fact this last criterion allow discriminate particle with η values varying within the 0.8 – 1 range and characterized by AOD > 0.1. Barnaba and Gobbi (2004) found that continental aerosol originating in the industrialized countries surrounding the Mediterranean Sea assumes η and AOD values that vary in the range 0.7 -1 and 0-1, respectively. Last results, suggest us that the last criterion is probably satisfactory to properly classify aerosol particles from Sector A.

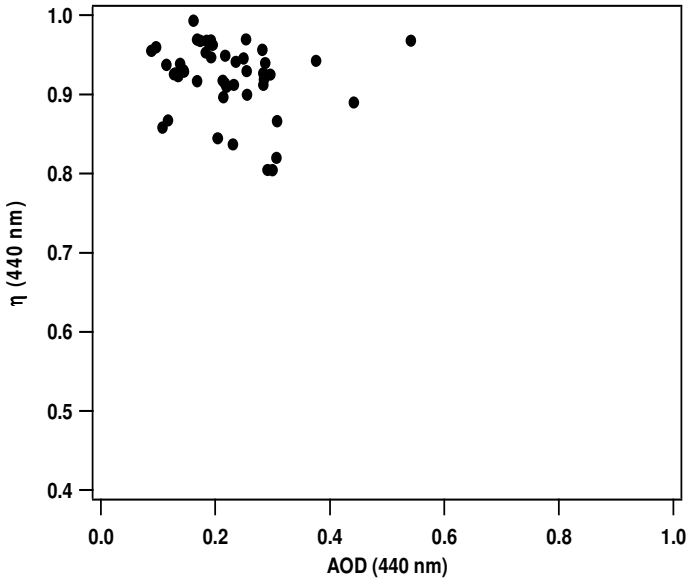

Figure 4.11. η vs AOD at 440 nm for the aerosol source Sector A selected using the following criterion: all the 5-day back-trajectories are attributed to the Sector A when all of them spent more than 80% of the last 5-day period inside the sector

Figure 4.11 shows the scatter plot obtained according to the d) criterion.

Comparing figure 4.10 to figure 4.11 one can observe that the d) criterion significantly reduces the number of data points without affecting the η variability range. η that is quite correlated to particle size is a good parameter to discriminate the different particle's type.

4.1.2b. ***Definition of Sector A as source – region according to the altitude of the back trajectories***

In addition to the time spent by each back-trajectory in a sector, the role of the back-trajectory altitude in a sector is tested in this section.

As a consequence, Sector A is considered the aerosol source region:

e. if at least three of the 950, 850, 700 and 500 hPa 5-day back trajectories have at least 80% of the data points at pressures $p > 480$ hPa within the Sector A before reaching the sampling site.

f. if all four of the 950, 850, 700 and 500 hPa 5-day back trajectories have at least 80% of the data points with a pressure $p > 480$ hPa within the Sector A before reaching the sampling site.

AERONET η – AOD plots referring to e) and f) criteria are plotted in figures 4.12a and 4.12b, respectively.

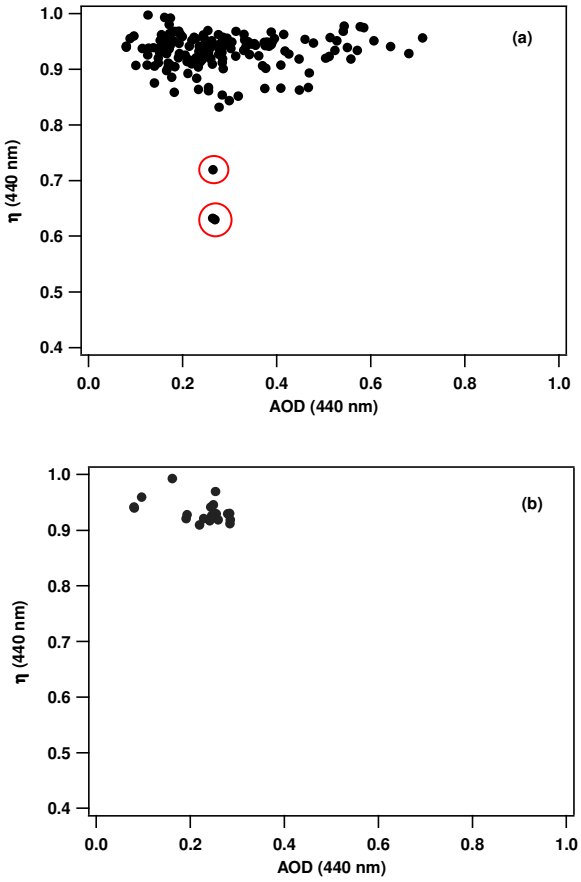

Figure 4.12 η vs AOD at 440 nm for the aerosol source Sector A selected using the following criterion: A is the aerosol source region if at least (a) three or (b) four of the 950, 850, 700 and 500 hPa 5-day back trajectories have 80% of the data points with a pressure p > 480 hPa within the sector.

One can observe that the f) criterion that has led to figure 4.12b is very restrictive. Moreover, comparing the results of figures 4.10 and 4.12a one can observe that, with the restriction p>480 hPa, the number of data points in the plot increases a little, but we have three data points, indicated in figure 4.12a with the red circle, that we believe are not representative of continental aerosol particle. In conclusion, we have decided that the c) criterion is the best suited to define Sector A as source sector.

4.1.2c. ***Definition of Sector B as source – region according to back trajectory pathways***

The different criteria implemented in this work to define Sector B as source – region according to back pathways are outlined below.

1) We believe that Sector B could be considered source sector:

a1) if at least one of the four back-trajectories has spent more than 80% of the last 5-day period before reaching the sampling site, inside the Sector B.

b1) if at least two of the four back – trajectories have spent more than 80% of the last 5-day period before reaching the sampling site, inside the Sector B.

c1) if at least three of the four back-trajectories have spent more than 80% of the last 5-day period before reaching the sampling site, inside the Sector B.

d1) if all the 5-day back-trajectories have spent more than 80% of the last 5-day period before reaching the sampling site, inside the Sector B.

Figure 4.13 shows the AERONET η – AOD plot for the aerosol source Sector B selected by the a1) criterion. Different symbols are referred to the four different arrival pressure levels (950 hPa, 850 hPa, 700 hPa, 500 hPa).

One can observe from figure 4.13 that η values span a rather wide range Therefore, we believe that a1) criterion doesn't allow to discriminate aerosols from Sector B.

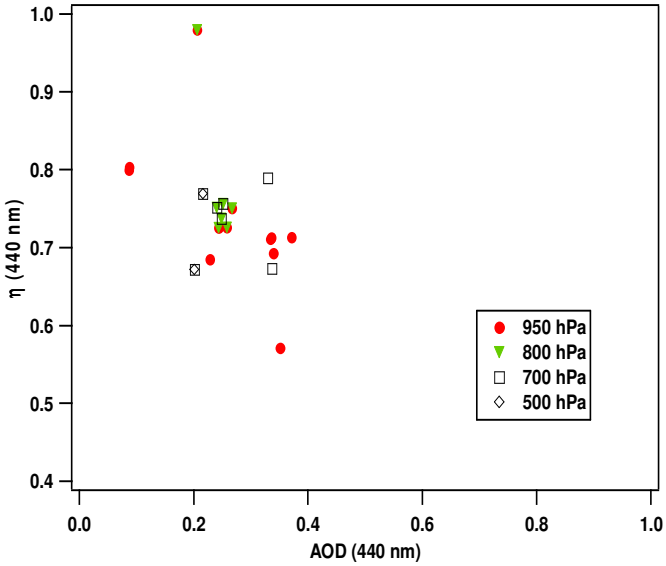

Figure 4.13. η vs AOD at 440 nm for the aerosol source Sector B selected using the following criterion: all the 5-day back-trajectories are attributed to the Sector A when at least one of them has spent more than 80% of the last 5-day period inside the sector.

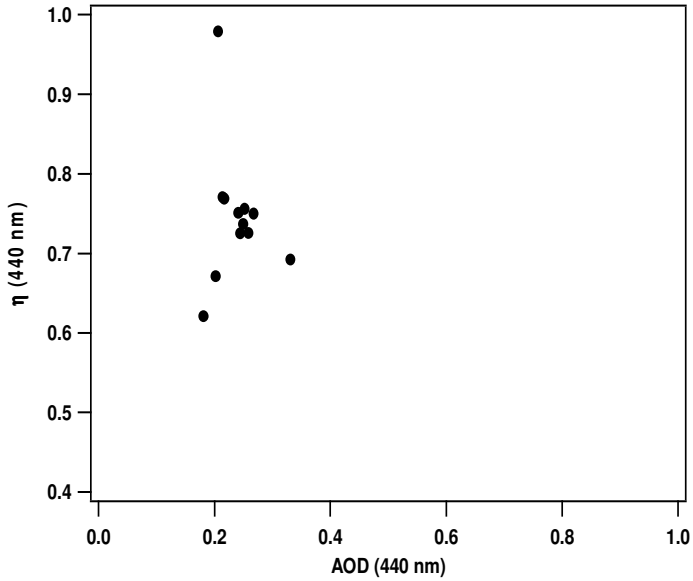

Figure 4.14. η vs AOD at 440 nm for the aerosol source Sector B selected using the following criterion: all the 5-day back-trajectories are attributed to the Sector A when at least two of them have spent more than 80% of the last 5-day period inside the sector.

Figure 4.14 shows the η – AOD plot obtained according to the b1) criterion.

The η variability range is similar to that of figure 4.13 .The η – AOD plots referring to c1) and d1) criterion are not shown since there are no data points that satisfy both criteria.

2) Criteria different than those used for Sector A have hence tested. In particular, we have assumed that sector B could be considered source sector:

a2) if at least one of the 5-day back-trajectories has spent more than 70% of the last 5-day period before reaching the sampling site, inside the Sector B.

b2) if at least two of the 5-day back-trajectories have spent more than 70% of the last 5-day period before reaching the sampling site, inside the Sector B.

c2) if at least three of the 5-day back-trajectories have spent more than 70% of the last 5-day period before reaching the sampling site, inside the sector B.

d2) if all four the 5-day back-trajectories have spent more than 70% of the last 5-day period inside Sector B.

Figure 4.15 a-c shows the η versus AOD plot obtained according to the a2), b2) and c2) criteria. From figures 4.15a and 4.15b one can observe that there is a η value, indicated by the grey arrows, that is characterized by a rather low and high AOD and η values, respectively. As a consequence, one can suppose that a2) and b2) criteria do not allow a good discrimination.

In contrast, one can observe from figure 4.15c that the c2) criterion quite discriminant

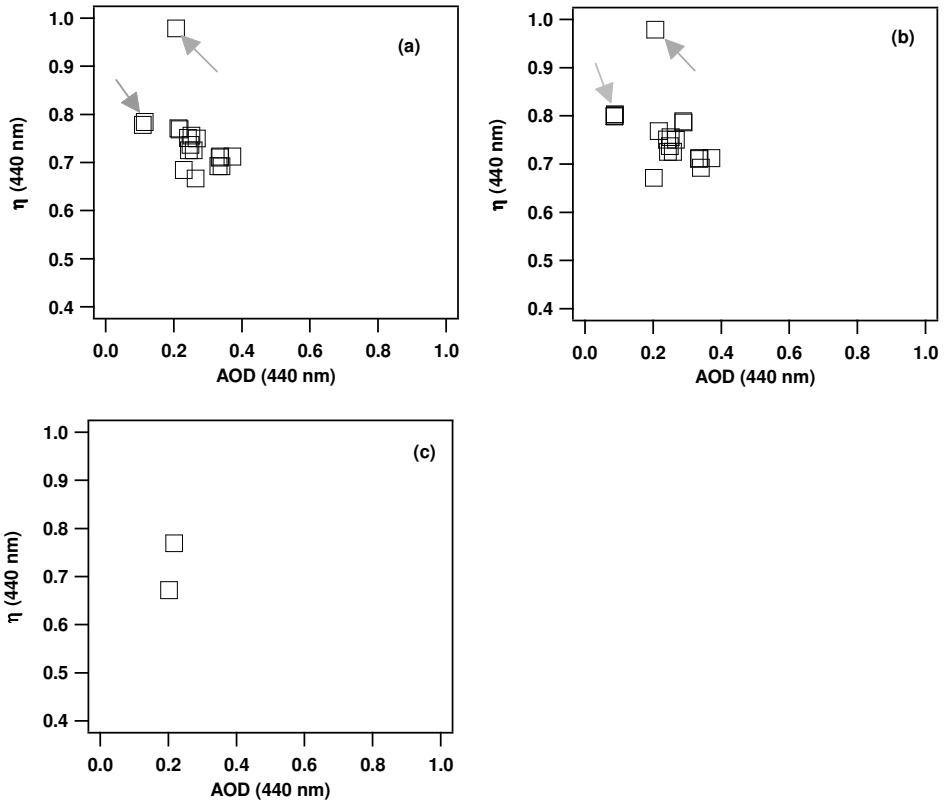

Figure 4.15. η vs AOD at 440 nm for the aerosol source Sector B selected using the following criterion: all the 5-day back-trajectories are attributed to the Sector B when at least one (a), two (b) or three (c) of them have spent more than 70% of the last 5-day period inside the sector.

3) Then we have assumed that Sector B could be considered source sector:

a3) if at least one of the 5-day back-trajectories has spent more than 60% of the last 5-day period before reaching the sampling site, inside the Sector B.

b3) if at least two of the 5-day back-trajectories have spent more than 60% of the last 5-day period before reaching the sampling site, inside the Sector B.

c3) if at least three of the 5-day back-trajectories have spent more than 60% of the last 5-day period inside the Sector B.

d3) if all the four 5-day back-trajectories have spent more than 60% of the last 5-day period inside the Sector B.

Figure 4.16a represents the η vs AOD plot of the data points that satisfy the a3) criterion.

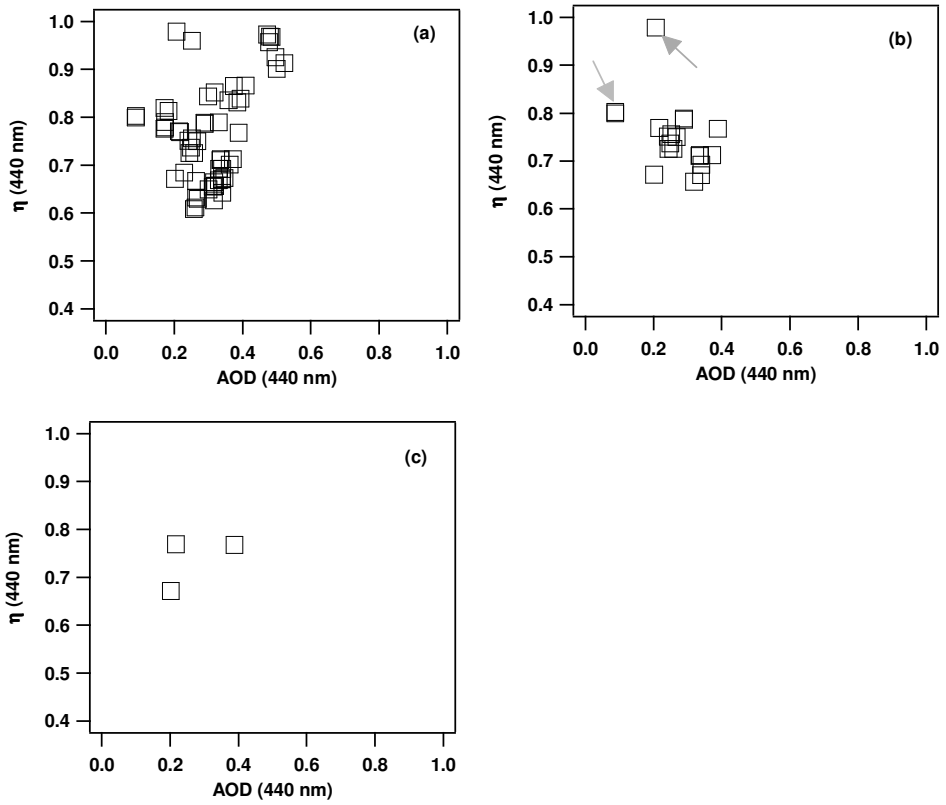

Figure 4.16. η vs AOD at 440 nm for the aerosol source Sector B selected using the following criterion: all the 5-day back-trajectories are attributed to the Sector B when at least (a) one, (b) two or (c) three of them have spent more than 60% of the last 5-day period inside the sector.

One observe from figure 4.16a that the η values span the 0.8 -1 range, and, as it was mentioned previously, this latter wide range doesn't allow discriminating aerosol of a particular type.

The η-AOD plot obtained according to the criterion b3) is reported in figure 4.16b. According to the results in figure 4.16a, we believe that b3) doesn't represent a good criterion to classify aerosols from Sector B.

The η-AOD plot retrieved in accordance with the c3) criterion is shown in figure 4.16c. We have decided to exclud this latter criterion since it is very restrictive. Finally, we have found that the d3) criterion does not allow getting data points.

4.1.2d. *Definition of Sector B as source – region according to the back trajectories permanence's time inside the Sector.*

We have assumed that Africa deserts could be considered responsible of the advection of particles over south-east Italy:

e. if at least two of the four back-trajectories have spent 10%, 20%, 30% or 40% of the time inside the border of the African continent.

f. if at least three of the four back-trajectories have spent 10%, 20%, 30% or 40% of the time inside the border of the African continent.

Figure 4.17 shows the AERONET η – AOD plots in accordance with the e) (black open boxes) and f) (full grey dots) criteria. In particular, figures from 4.17a to 4.17d are obtained for the back-trajectories that have spent 10%, 20%, 30% and 40% of time inside the Africa continent, respectively.

The results obtained in figure 4.17 show that, considering only the percentage of time spent by the back trajectories inside the Africa continent, we obtain data points that are characterized by η values between 0.4 and 1 that are not representative of dust particles. However, these latter results suggested us that the percentage of time spent by the back trajectories inside the border of Africa, in addition to another condition, could allow making a suitable selection of the particles coming from Sector B.

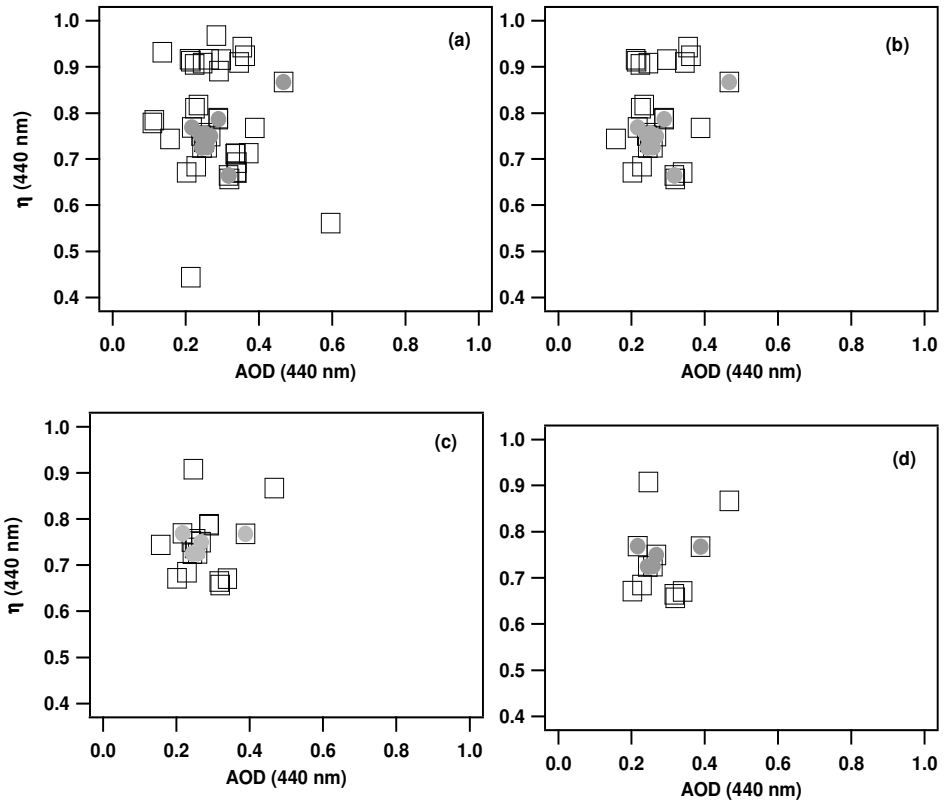

Figure 4.17. η vs AOD at 440 nm for the aerosol source Sector B selected using the following criterion: all the 5-day back-trajectories are attributed to the Sector B when at least two (black open boxes) or three (full grey dots) back trajectories have spent (a) 10%, (b) 20% , (c) 30% and (d) 40% of time inside the Africa.

4.1.2e. *Definition of Sector B as source – region according to back trajectory altitude*

Analogously to the criteria tested in the section 4.1.2b for Sector A, we believe that it is useful to define some constraints on the back-trajectories altitude in addition to the time spent by the back-trajectories in the Sector B.

We suppose that Sector B could be considered source sector:

g. If at least one of the 950, 850, 700 and 500 hPa 5-day back trajectories has at least ~ 40% of the data points with a pressure p > 800 hPa within the Sector B before reaching the sampling site.

h. if at least two of the four 5-day back trajectories have at least ~ 40% of the data points with a pressure p > 800 hPa within the Sector B.

i. if at least three of the four 5-day back trajectories have at least ~ 40% of the data points with a pressure p > 800 hPa within the Sector B.

Figure 4.18a represents the η versus AOD plot in accordance with the g) criterion.

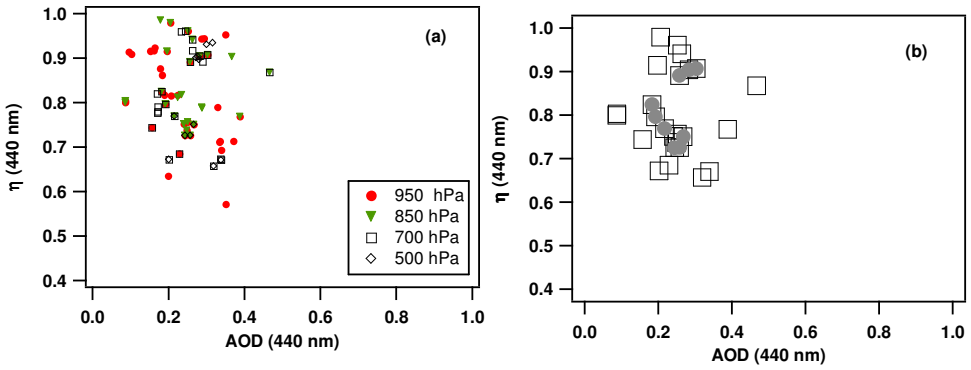

Figure 4.18. η vs AOD at 440 nm for the aerosol source Sector B selected using the following criterion: all the 5-day back-trajectories are attributed to the Sector B when at least (a) one, (b) two (open black boxes) or three (full grey dots) of the 5- day back trajectories have at least ~ 40% of the data points with a pressure p > 800 hPa inside the sector.

In the figure the different arrival pressure levels of 950, 850, 700 and 500 hPa are represented by different symbols. The η – AOD plot for the data points that satisfy the h) (open black boxes) and i) (full grey dots) criteria is reported in figure 4.18b. Figure 4.18 demonstrates that the latter above reported g), h) and i) criteria are not good enough classify aerosol from Sector B.

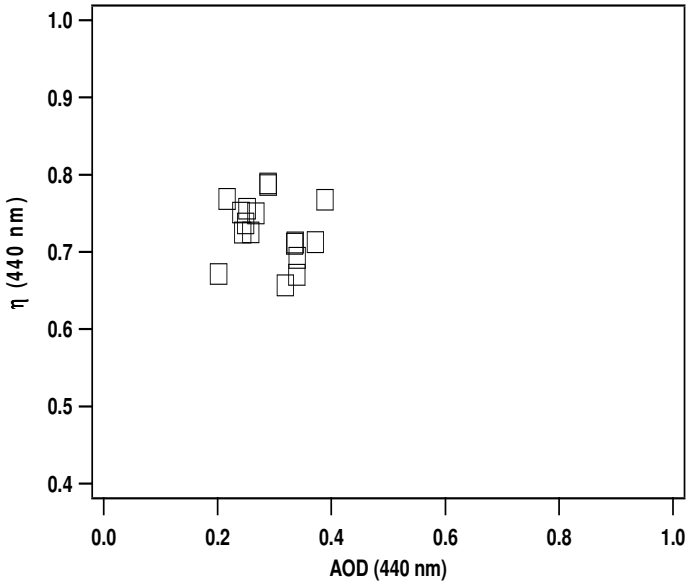

Figure 4.19. η vs AOD at 440 nm for the aerosol source Sector B selected using the following criterion: all the 5-day back-trajectories are attributed to the Sector B when at least two of the four back trajectories spent more than 10% of time inside the border of the African continent and more than 60% of the time inside the Sector B before getting to the monitoring site.

In conclusion, the study implemented in this thesis to define Sector B as source – region, has revealed that the better criterion to define the aerosol origin for Sector B could be obtained considering both the results of figures 4.16b and 4.17a. In particular, we believe that Africa can be considered responsible for the advection of particles over south-east Italy if at least two of the four back trajectories have spent more than 10% of time inside the border of the African continent and more than 60% of the time inside the Sector B before getting to the monitoring site. Figure 4.19 shows the η – AOD plot obtained by AERONET measurements at 440 nm considering the above reported criterion.

4.1.2f *Definition of Sector C according to back trajectory pathways*

The identification of cases of clean marine aerosols is particularly complex in the Mediterranean, due to the influence of surrounding continents and the limited dimension of the basin (Pace et al., 2006). The criteria implemented in this work to properly define Sector C as source – region according to pathways are outlined below.

We suppose that Sector C could be considered source sector:

a) if at least one of the four 5-day back-trajectories has spent more than 80% of the last 5-day period before reaching the sampling site, inside the Sector C.

b) if at least two of the 5-day back-trajectories have spent more than 80% of the last 5-day within Sector C.

c) if at least three of the 5-day back-trajectories have spent more than 80% of the last 5-day within Sector C.

d) if all the four 5-day back-trajectories have spent more than 80% of the last 5-day within Sector C.

Figure 4.20a shows η versus AOD plot obtained by AERONET measurements according to the a) criterion. Different symbols are referred to the four different arrival pressure levels (950 hPa, 850 hPa, 700 hPa, 500 hPa). One can observe from figure 4.20a that the variability range of η and AOD is the same of that of figure 4.6 in which aerosols from all the Sectors are considered.

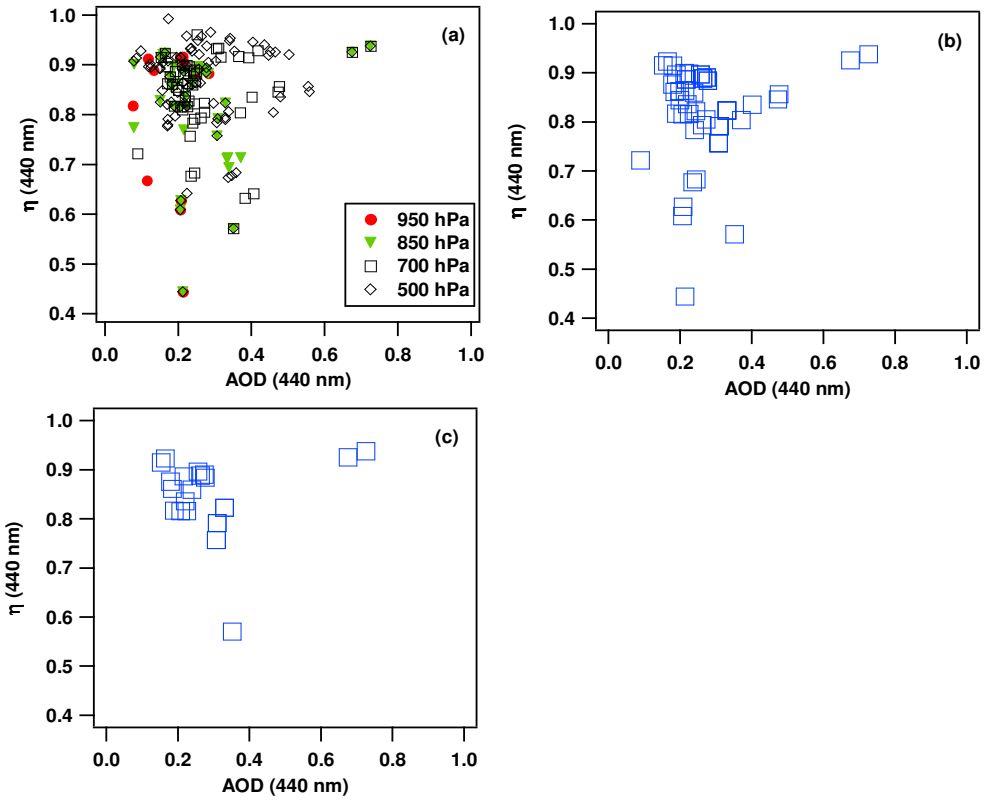

Figure 4.20. η vs AOD at 440 nm for the aerosol source Sector C selected using the following criterion: all the 5-day back-trajectories are attributed to the Sector C when at least (a) one, (b) two and (c) three of them have spent more than 80% of the last 5-day period inside the sector.

Then, we believe that the a) criterion doesn't allow discriminating marine aerosols from Sector C.

The η – AOD plot referred to the days that respect the b) criterion is reported in figure 4.20b. Likewise to the results of figure 4.20a, the data points show η and AOD variability range that doesn't allow us to properly classify aerosols from Sector C.

Figure 4.20c represents the η – AOD plot obtained following the c) criterion. This latter criterion was also excluded because the variability range of η and AOD is rather wide.

Finally, the d) criterion was excluded because there are no data points that satisfy it.

4.1.2g Definition of Sector C as source – region according to back trajectory the permanence's time inside the Sector

Although marine aerosol is expected to contribute significantly to the optical properties of the air-masses classified as Sector C, additional analyses was required in this study to isolate the clean marine cases. The analysis was based on the identification of the effective time that the back trajectories spent over the ocean. To this purpose, a more detailed mask of the European continent was applied, defining a new small oceanic Sector C that includes only the Atlantic Ocean and the Mediterranean. According to the last new geographical definition of Sector C, we suppose that Sector C could be considered source sector:

e. if at least two of the four 5-day back trajectories have spent 10%, 20%, 30% , 40% or 50% of time inside the Sector C.
f. if at least three of the four 5-day back trajectories have spent 10%, 20%, 30% , 40% or 50% of time inside the Sector C.
g. if all of the four 5-day back trajectories have spent 10%, 20%, 30% , 40% or 50% of time inside the Sector C.

In figures 4.21 are reported the η – AOD plots obtained following the e) (blue open diamonds), f) (red open boxes) and g) (black full dots) criterion. In particular, figures from 4.21a to 4.21e are obtained for the back-trajectories that have spent 10%, 20%, 30% and 40% of time inside Sector C defined.

An accurate analysis of the results in figure 4.21 has let us to conclude that the f) criterion is the best suited to define Sector C as source sector.

In conclusion, the study implemented in this paragraph to define source sectors has demonstrated that less restrictive criteria favor the inclusion of "mixed" advection patterns. On the contrary, more restrictive criteria tend to exclude significant data points.

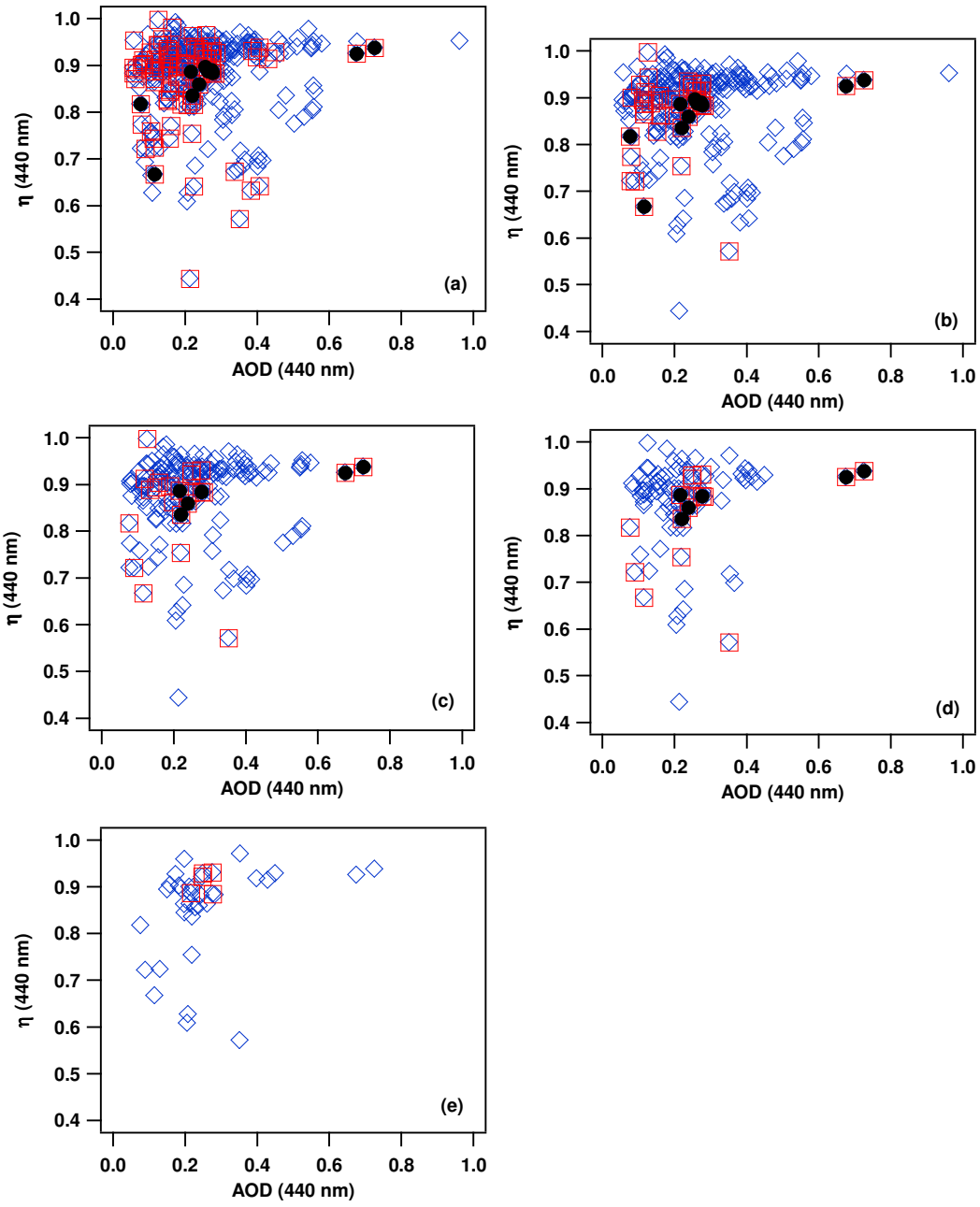

Figure 4.21. η vs AOD at 440 nm plot at 440 nm for the data points that satisfy the condition that at least two (blue open diamonds), three (red open boxes) and four (black full dots) of the 5-day back trajectories spent (a) 10%, (b) 20%, (c) 30% , (d) 40% and (e) 50% of time inside the new large oceanic Sector C

4.1.3 Selected criteria for the final identification of the aerosol source sector

The sensitivity study performed in the previous paragraph suggested us the better criteria to properly infer optical and microphysical properties of particles advected from the three broad geographical sectors, shown in figure 4.2, and defined in this study as aerosol source regions. In particular, to define Sector A as aerosol source region we have chosen the following criteria:

- A is the aerosol source region if at least three of the 950, 850, 700, and 500 hPa 5-day back trajectories have spent at least 80% of the time within the Sector before reaching the sampling site.
- Sector B, and hence Africa deserts, have been considered responsible of the advection of dust particles over south-easy Italy if at least two of the four back trajectories have spent more than 10% of time inside the border of the African continent and more than 60% of the time inside the Sector B before getting to the monitoring site.
- Finally, we assumed Sector C as aerosol source region, if at least three of the 950, 850, 700, and 500 hPa back trajectories spent more than 40% of the time within the Sector before reaching the sampling site.

Considering the above reported criteria, we found that 32% of the 240 measurement days were characterized by air masses coming from Sector A, while 3% of the measurement days were characterized by air masses coming either from Africa deserts (Sector B) or from the Atlantic and Mediterranean Sea (Sector C). Figures 4.22a-d show for different arrival pressure levels, the back-trajectories of the measurement days with Sector A as aerosol source region. 5-day back-trajectories of the measurement days with Sector B and C as aerosol source region are shown in figure 4.23 and 4.24, respectively. We mention that 62% of the measurement days

were characterized by back-trajectories that do not allow defining the aerosol source sector. The aerosol monitored on these days are considered due mostly to mixed source regions (Sector M). Figures 4.25a and 4.25b show as example, the 950 and 700 hPa backtrajectories, respectively for the Sector M measurement days. Different colors are used in Figs. 3.22-3.25 to characterize pressure levels of each back-trajectory as a function of the time.

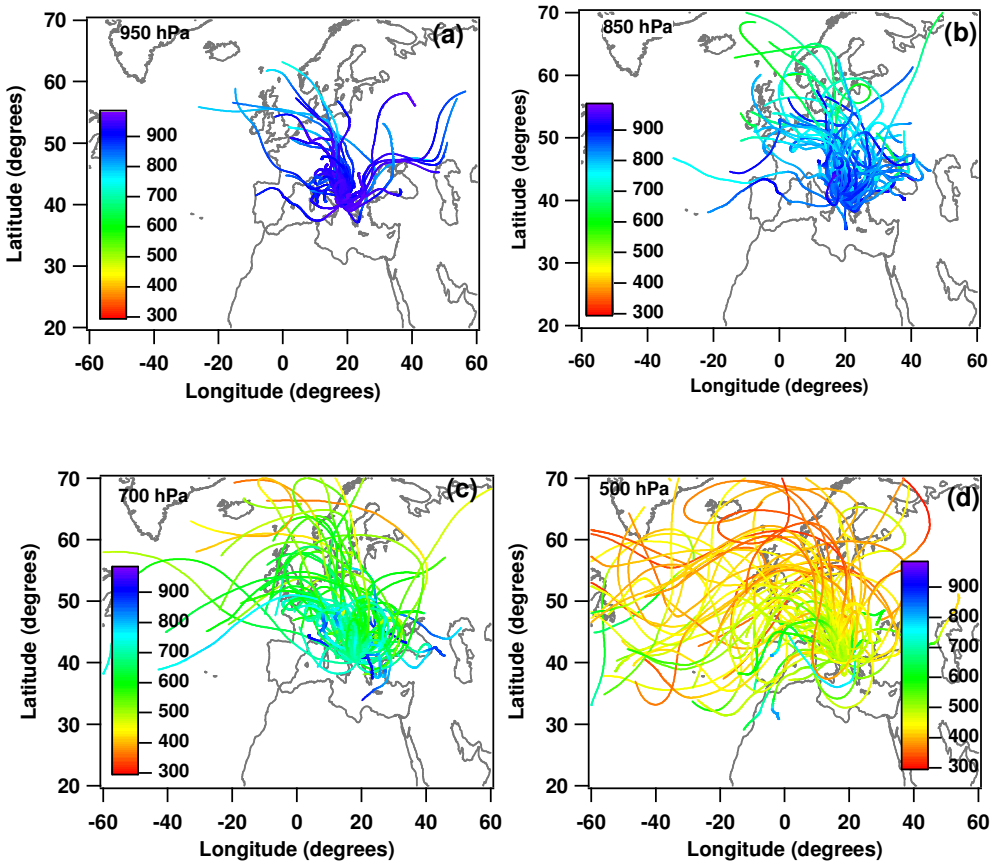

Figure 4.22. The 5-day back trajectories of the measurement days with Sector A as aerosol source region and for arrival pressure levels of (a) 950, (b) 850, (c) 700 and (d) 500. Different colors are used to characterize pressure levels of each back-trajectory as a function of the time.

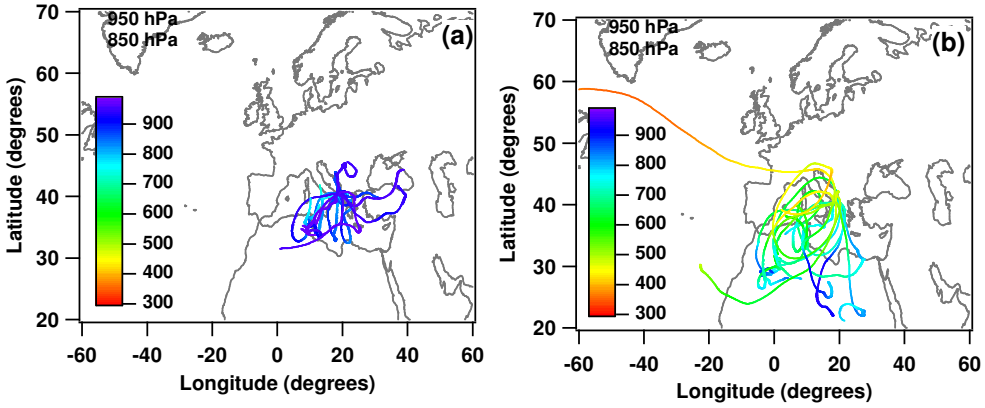

Figure 4.23. The 5-day back-trajectories of the measurement days with Sector B as aerosol source region and for arrival pressure levels of (a) 950 – 850 hPa, (c) 700 – 500hPa. Different colors are used to characterize pressure levels of each backtrajectory as a function of the time.

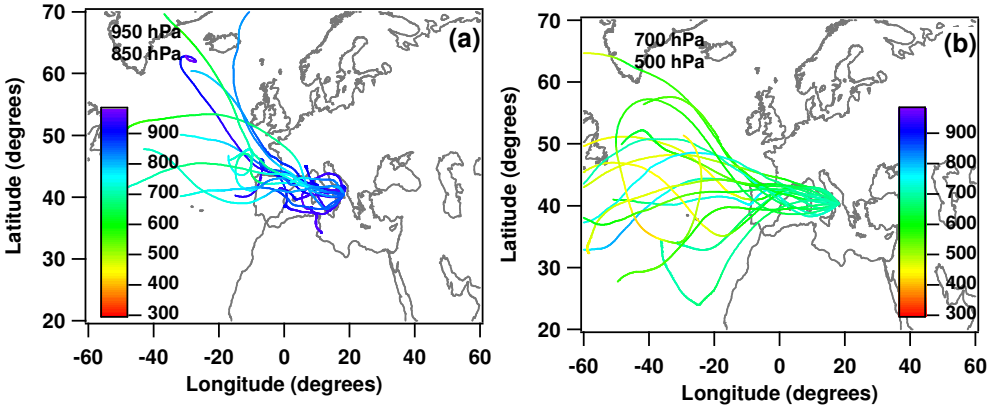

Figure 4.24. The 5-day back-trajectories of the measurement days with Sector C as aerosol source region and for arrival pressure levels of (a) 950 – 850 hPa, (c) 700 – 500hPa. Different colors are used to characterize pressure levels of each back-trajectory as a function of the time

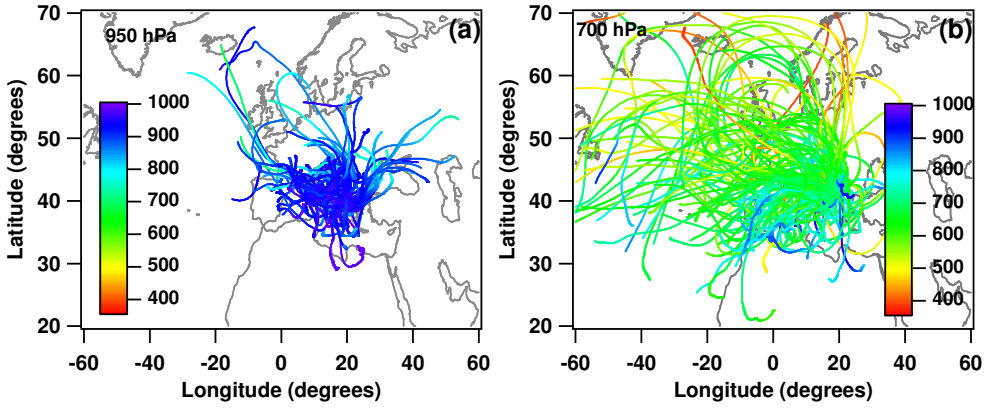

Figure 4.25. The 5-day back-trajectories of the measurement days with Sector M as aerosol source region and for arrival pressure levels of (a) 950 hPa, (c) 700 hPa. Different colors are used to characterize pressure levels of each back-trajectory as a function of the time

4.2 Aerosol parameter analysis: study of correlation

The study performed in this thesis, to properly characterize aerosol properties of different source regions, is based on the analyses of the correlation between different AERONET parameters, such as the fine fraction η, the single scattering albedo SSA, the Lidar Ratio LR, the fine r_{vf} and coarse r_{vc} effective radius and the aerosol optical depth AOD retrieved from March 2003 to October 2004.

Figures 4.26 shows the correlation between the fine-fraction parameter η and the aerosol optical depth AOD obtained by AERONET measurements at 440 nm. Symbols of different colours indicate measurements classified as originating from different sectors following the classification implemented in the section 4.1.3. Both black grey open and full dots represent in figure 4.26a data referring to Sector A, full black triangles represent particle properties from Sector C, open black boxes represent aerosol properties from Sector B. In figure 4.26b full black dots represent data referring to Sector M. We mention that, in figure 4.26a grey open dots represent the parameters of aerosol loads advected from urban/industrial Sector A regions. In contrast, grey full dots represent the parameters of aerosol loads also affected by the advection of biomass burning particles from Sector A regions. In addition to back trajectories, fire maps retrieved by MODIS satellite images were used (http://maps.geog.umd.edu/d) to infer the advection of biomass burning particles over south-east Italy.

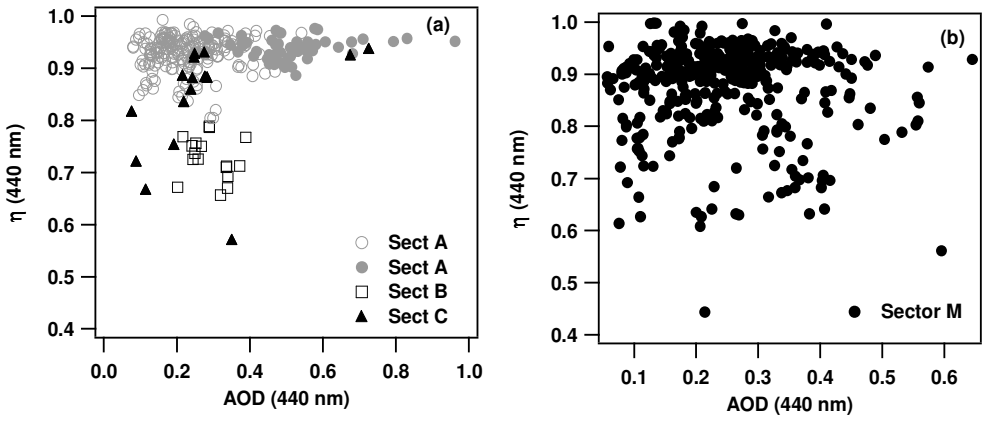

Figure 4.26. η versus AOD at 440 nm for aerosol of different source Sectors: both grey open and full dots represent data referring to Sector A aerosol. In particular, grey full dots represent data that could be affected by the advection of biomass burning particles (BB). Open boxes and full triangles represent data of Sector B and C aerosol, respectively; b) η versus AOD of the Sector M aerosol.

As we told before, the combined use of the optical depth and the fine-fraction parameter give us a qualitative indication about the size and the amount of particles in atmosphere. Figure 4.26 shows, at first, that, particles of different type tend to concentrate in different areas of the plot and this allows to locate aerosols of different origin. Moreover, we can observe from figure 4.26 that particles from Sector A (continental) and from Sector M (mixed) are predominant during all the analyzed period.

According to previous results (Remer and Kaufman, 1998; Dubovik et al., 2002a) figure 4.26a shows that, on average, η values are largest for Sector A and smallest for Sector B (Sahara desert), indicating that the particles of Sector A are mainly fine while those from the Sector B are the largest. Infact, we can see from figure 4.26a that the continental aerosol (grey open dots) are characterized by high η values > 0.8 and by AOD values that span the range 0.1-0.6, while dust particles (black open boxes) assume η values in the range 0.6-0.8 and aerosol optical depth values ranging from 0.2 to 0.6. Moreover, one can observe that biomass burning aerosols from

Sector A are characterized by relatively larger η (~0.9-1) and AOD (~0.3-1) values. From figure 4.26a one can see also that the particles coming from Sector C, represented by black full triangles, are characterized by values of η and AOD between 0.5 and 1 and between 0 and 0.3, respectively, while figure 4.26b shows that particles of mixed origin have values that span within the whole range of both values. The latter results are in good accordance with the results obtained in the previous study of Barnaba and Gobbi (2004). They have observed that the distribution of points relative to dust and continental particles have a tendency to concentrate in the region characterized by η values that span the 0-0.7 and 0.7-1 range, respectively, (figure 4.26) in accordance with the data of figure 4.26 of this paper. Moreover, Barnaba and Gobbi have classified maritime aerosols with AOD < 0.3 and η < 0.8. In contrast to the results of Barnaba and Gobbi (2004), in our study we obtain for the marine aerosols values of η ~1. One can suppose that this last result may indicate that Sector C particles are more continentally-affected over south-east Italy .

Figure 4.27a shows Å versus AOD at 440 nm for the selected aerosol source Sectors: both grey open and full dots represent data referring to the Sector A aerosol referred to aerosol affected and not-affected by biomass burning, respectively. Å values have been retrieved by AOD values at 870 and 440 nm. Open boxes and full triangles in figure 4.27a represent aerosol data of the Sector B and C aerosol, respectively. We observe from figure 4.27a that fine-mode particles (0.94 <Å<2.0) that are also responsible of the highest AODs are advected over south-east Italy from Sector A. In contrast, large size particles (0.57 < Å < 0.96) are advected from Sector B. Particles of variable size that are on average responsible of rather low AODs are advected from Sector C. The results of Figure 4.27a are in accordance with previous studies (e.g. Pace et al., 2006; Fotiadi et al., 2006). The aerosol from Sector A, which travels over urban/industrial environments before getting to the monitoring site, is dominated by

fine-mode particles (Remer and Kaufman, 1998; Dubovik et al., 2002a), while the one advected from desert regions (Sector B) is strongly dominated by coarse-mode particles. Sector C data (Figure 4.27a, full triangles) show that in maritime conditions, the relative contribution of coarse particles, although variable (Smirnov et al., 2002), is generally higher than that in urban/industrial environments and lower than that for desert dust (Dubovik et al., 2002a). The results reported in figure 4.27 also are in good accordance with those reported in the paper of Pace et al. 2006: they demonstrate that African aerosols are characterized by high values of AOD (average values of 0.37) and by low values of Angstrom exponent Å (average values of 0.42) and, therefore, by coarse particles. Moreover, they show that particles originating from Central-Eastern Europe are characterized by relatively large average values of AOD and Angstrom exponent Å (0.23 and 1.50 respectively), and, therefore, they are mainly fine-mode particles. Finally, they show that average values of AOD and Å for clean marine conditions are 0.11 and 0.86, respectively.

Figure 4.27b shows Å (calculated by AOD at 870 and 440 nm) versus AOD for aerosol loads monitored on measurement days for which it was not possible to infer the aerosol source sector in accordance to the criteria defined in Section 3.1.3 (Sector M). Variability ranges of both Å and AOD values are rather similar to those of figure 4.3a. Latter observation confirms that the Sector M aerosol properties represented in figure 4.27b are rather close to the properties of the total aerosol load from Sector A, B, and C. Sector M back-trajectories (figure 4.25) support last comment.

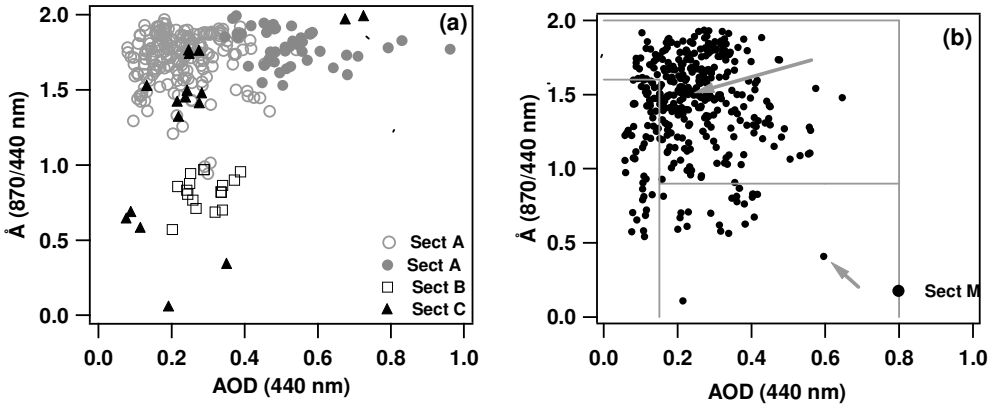

Figure 4.27. Å versus AOD at 440 nm for aerosol of different source Sectors: both grey open and full dots represent data referring to Sector A aerosol. In particular, grey full dots represent data that could be affected by the advection of biomass burning particles (BB). Open boxes and full triangles represent data of Sector B and C aerosol, respectively; b) Å versus AOD of the Sector M aerosol.

To better highlight peculiarities of mixed advection patterns we have analyzed as an example, the aerosol parameters retrieved on August 29, 2003. Grey arrows indicate in figure 4.27b the data points retrieved on August 29. Figure 4.28 showing the back trajectories of August 29 at 12:00 UTC, reveals that the 950 and 850 hPa air masses are advected from Sector A, while the 700 and 500 hPa air masses are advected from Sector C and B, respectively. AERONET retrievals indicate that the aerosol monitored on the early morning (05:24 UTC) was characterized by Å = 1.5 and AOD = 0.24.

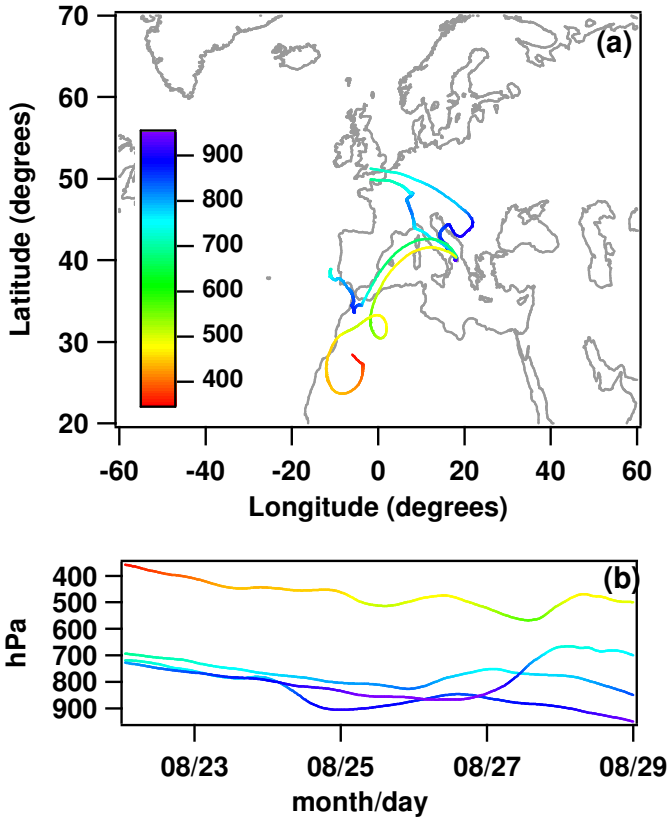

Figure 4.28. a) 5-day analytical back-trajectories of August 29, 2003 at 12:00 UTC arrival time; b) altitude change as a function of time of each back-trajectory.

In contrast, aerosol properties were characterized by Å = 0.4 and AOD = 0.4 in the early afternoon (14:45 UTC). Latter results indicate that fine-mode particles probably advected from north-east Europe were present over south-east Italy on the early morning. In contrast, coarse-mode particles (probably from north-west Africa) determining a quite large aerosol load were predominant on the afternoon. In addition to back trajectories, MODIS images by Terra and Aqua satellites (http://rapidfire.sci.gsfc.nasa.gov) were used to support last comments: the image by Terra reveals that a dust plume was present over the Tyrrhenian Sea at 09:45 UTC (figure 4.29a), while the image by Aqua indicates that the dust plume was rather close to south-eat Italy at 11:20 UTC (figure 4.29b).

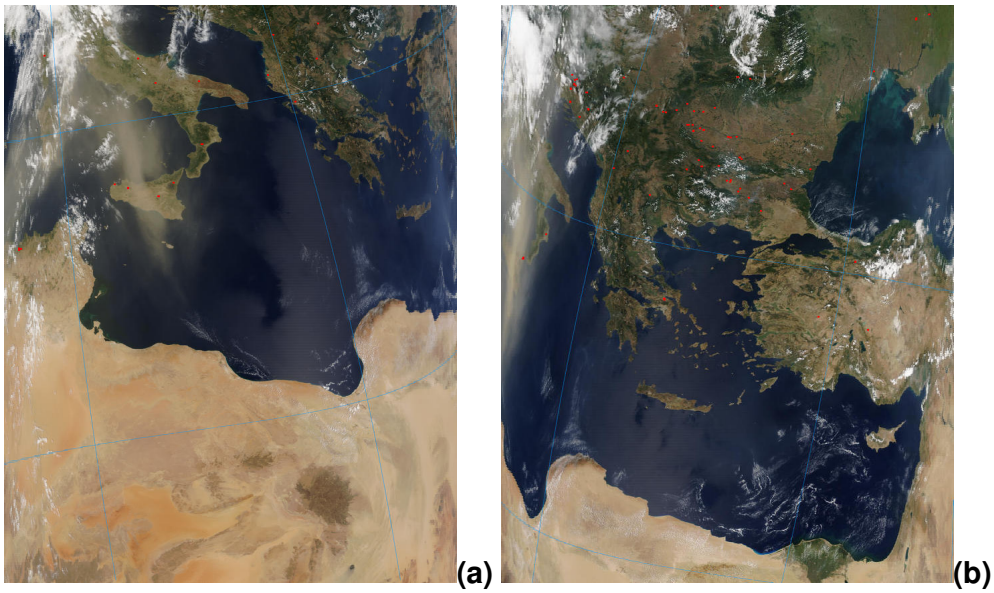

Figure 4.29. True color images on 29 August 2003 provided by MODIS Sensor on board the NASA EOS (a) Terra Spacecraft at 09:45 UTC, (b) Aqua Spacecraft at 11:20 UTC.

The above reported discussion besides revealing the ability of the AERONET inversion algorithm to follow aerosol property changes, shows the importance of using single measurements instead of daily averaged data, to properly characterize aerosol properties of different source regions.

In figure 4.30 are reported the AERONET single scattering albedo SSA and AOD scatter plot for the different selected aerosol source sectors. In particular, 1.5 level SSA data were plotted in figure 4.30 since level 2 data were not available.

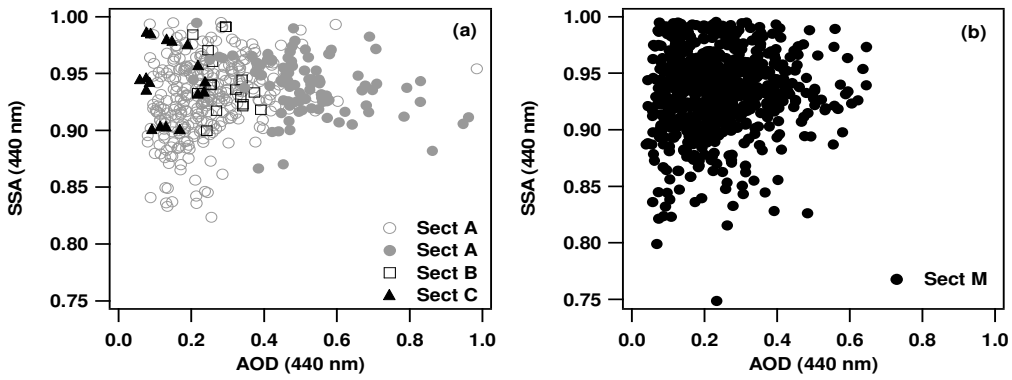

Figure 4.30. SSA versus AOD at 440 nm for aerosol of different source Sectors: both grey open and full dots represent data referring to Sector A aerosol. In particular, grey full dots represent data that could be affected by the advection of biomass burning particles (BB). Open boxes and full triangles represent data of Sector B and C aerosol, respectively; b) SSA versus AOD of the Sector M aerosol.

Figure 4.30 reveals that particles from Sector A and M assume SSA values in the range ~ 0.8 – 1, while particles from Sector B and C assume higher values of SSA between 0.9 and 1. Then, this result allows inferring that the Mediterranean is dominated by moderately-absorbing particles. Finally, it worth observing from figure 4.30a that SSA values are not very sensitive to source sectors.

The plot between the AERONET asymmetry factor *g* and AOD for the different aerosol source areas are shown in figure 4.31.

One can observe from figure 4.31a that, at first, the variability range of *g* is nor dependent on AOD values. In addition, the *g* variability range is not dependent on the particle source sector.

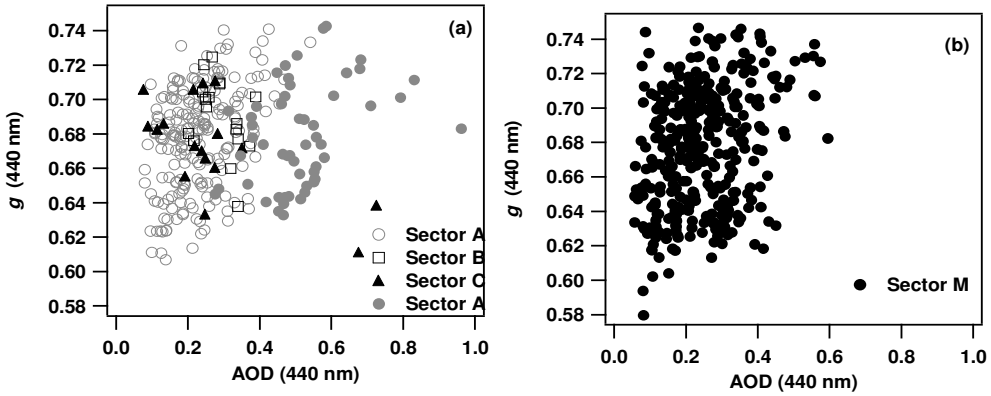

Figure 4.31. *g* versus AOD at 440 nm for aerosol of different source Sectors: both grey open and full dots represent data referring to Sector A aerosol. In particular, grey full dots represent data that could be affected by the advection of biomass burning particles (BB). Open boxes and full triangles represent data of Sector B and C aerosol, respectively; b) *g* versus AOD of the Sector M aerosol.

Figure 4.32 shows the correlation between *g* and the fine fraction η. The symbols used in figure 4.32 to indicate particles from different sectors are reported in the figure. Figure 4.32 reveals that, despite *g,* η is quite sensitive to particle source regions, as it has been told.

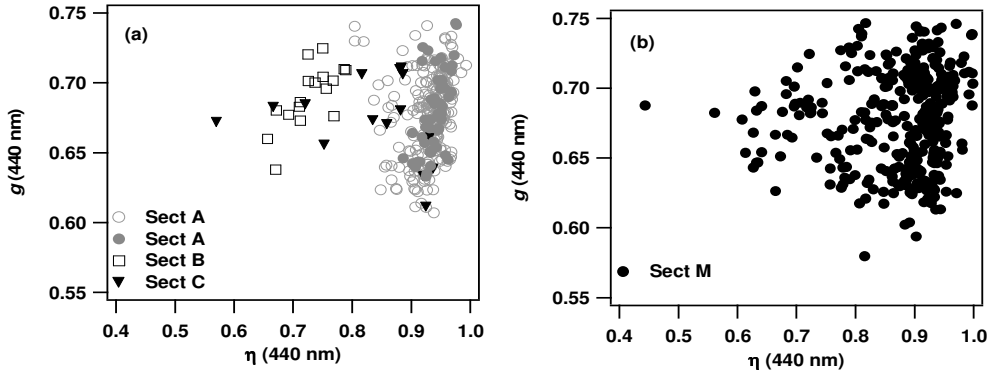

Figure 4.32. *g* versus η at 440 nm for aerosol of different source Sectors: both grey open and full dots represent data referring to Sector A aerosol. In particular, grey full dots represent data that could be affected by the advection of biomass burning particles (BB). Open boxes and full triangles represent data of Sector B and C aerosol, respectively; b) *g* versus η of the Sector M aerosol.

The correlation between the Lidar Ratio *Lr* and the aerosol optical depth AOD at 440 nm has also been investigated in this study (figure 4.33). The Lidar Ratio *Lr* is calculated from AERONET measurements according to the following equations (Muller et al., 2003):

$$Lr(\lambda) = \frac{4\pi}{SSA(\lambda)P(\lambda,180^{\circ})} \qquad (4.1)$$

where $SSA(\lambda)$ represents the single-scattering albedo and $P(\lambda,180^{\circ})$ describes the phase function at 180° derived from the inversion of Sun photometer data. One can see from figure 4.33a that particles of different type tend to concentrate in different areas of the plot.

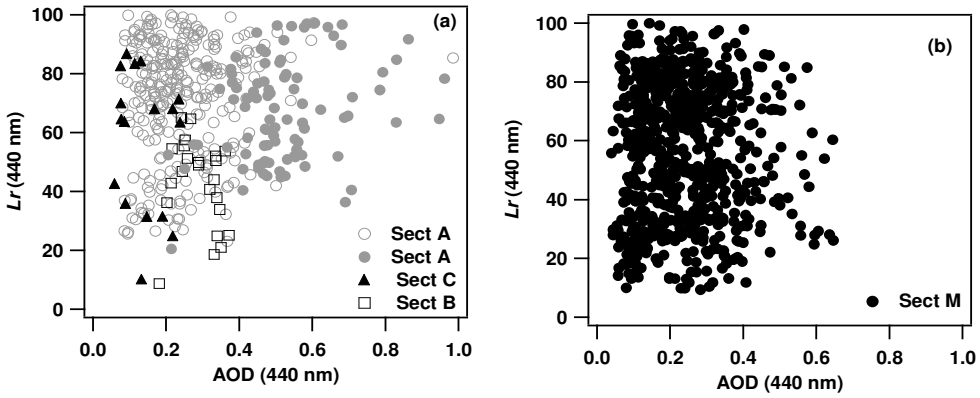

Figure 4.33. *Lr* versus η at 440 nm for aerosol of different source Sectors: both grey open and full dots represent data referring to Sector A aerosol. In particular, grey full dots represent data that could be affected by the advection of biomass burning particles (BB). Open boxes and full triangles represent data of Sector B and C aerosol, respectively; b) *Lr* versus η of the Sector M aerosol.

In particular, figure 4.33a shows that aerosols from Sector A (grey open dots) are characterized by values of *Lr* that vary between ~ 20 and 100 sr (averaged values of 73 sr), while particles from Sector C (black triangles) show two different groups of values: one characterized by *Lr* values that vary in the ~ 10-40 sr range and one characterized by *Lr* values that vary in the ~ 50-90 sr range. Previous studies on the aerosol properties characterization have demonstrated that marine aerosols are characterized by a lidar ratio of *Lr* ~ 20 sr (Ackerman, J, 1998). Cattral et al., 2005 have found for marine aerosols a value of *Lr*~ 27 sr at 550 nm computed on the basis of selected retrievals of aerosol properties from 26 Aerosol Robotic Network (AERONET) sites across the globe. According to these latter results, we believe that in figure 4.33 the group of particles with *Lr* up to 40 sr can be ascribed to pure marine aerosols, while the group of particles characterized by higher values have resulted from a mixture of maritime and continental aerosols, which lead to high lidar ratio values. Infact, usually, high lidar ratio values are associated to continental aerosols: average lidar ratios ranging from 40 to 80 sr have been reported by

Matthias and Boesenberg (2002) for Raman-lidar measurements at 351 nm performed in Germany along three years. In the numerical study of Ackermann (1998) the lidar ratio calculated at 351 nm for continental aerosols varies from 42 to 70 sr. According to the previous results, we can observe in figure3.32 that most of the continental particles are concentrated at high *Lr* values ranging from ~ 60 to 110 sr. Aerosols from Sector A affected by the advection of biomass-burning particles and represented in figure 4.33 by grey full dots are characterized by values of *Lr* that vary from ~35 to 100 sr, with a mean value of 67 sr. In accordance with our results, Cattral et al. (2005) have found a mean value for biomass burning of about 60 sr.

Black open boxes in figure 4.33a represent *Lr* vs AOD values relative to the particles originated in Sector B (dust particles). One can see that *Lr* assume values ranging from ~10 to 65 sr (averaged values of ~ 43 sr). Our latter results are consistent with those reported by Ackermann et al. (1998) that have found for desert aerosols values of *Lr* between 42 and 48 sr, while Balis et al.(2004) have found that the lidar ratio of the desert dust particles retrieved at Thessaloniki, Greece, using a Raman lidar system at 355 nm during the years 2000-2001 is about 40 sr.

Finally, figure 4.33b shows that particles from Sector M are characterized by a variability range of *Lr* that are similar to that of figure 4.33a and this result confirms that particles from Sector M are a mixing of different particle types coming from the Sector A, B and C.

Figure 4.34 shows the plot of the fine $r_{eff\,fine}$ and coarse $r_{eff\,coarse}$ effective radius versus the aerosol optical depth AOD at 440 nm. Symbols of different colour correspond to measurements classified as originating from the different sectors.

Open grey and red dots represent in figure 4.34a $r_{eff\,fine}$ and $r_{eff\,coarse}$ vs AOD, respectively, for Sector A particles, while green and grey open dots represent $r_{eff\,fine}$

and $r_{eff_{coarse}}$ vs AOD, respectively, for particles from Sector A affected by the advection of biomass-burning. Open light blue and black boxes represent $r_{eff_{fine}}$ and $r_{eff_{coarse}}$ vs AOD, respectively, for Sector B particles, blue and black triangles correspond to $r_{eff_{fine}}$ vs AOD and $r_{eff_{coarse}}$ vs AOD, respectively, for Sector C. Moreover, red and black symbols in figure 4.34b are referred to $r_{eff_{fine}}$ and $r_{eff_{coarse}}$ vs AOD, respectively, for Sector M particles.

The effective radius (r_{eff}) is defined by Hansen and Travis (1974) as:

$$r_{eff} = \frac{\int_0^\infty \pi r^3 \frac{dN}{dr} dr}{\int_0^\infty \pi r^2 \frac{dN}{dr} dr} \qquad (4.2)$$

where N is the total columnar number density and *r* is the particle radius. The effective radius is a parameter that is related to the magnitude of the diffuse radiation effect measured by the sunphotometer and it is dependent on the aerosol size distribution (Eck et al., 1999). We can see from figure 4.34 that the aerosols from Sector A assume $r_{eff_{fine}}$ (open red and full green dots) and $r_{eff_{coarse}}$ (open and full grey dots) values that vary between 0.09-0.17 μm and between 1.5 – 3.2 μm, respectively.

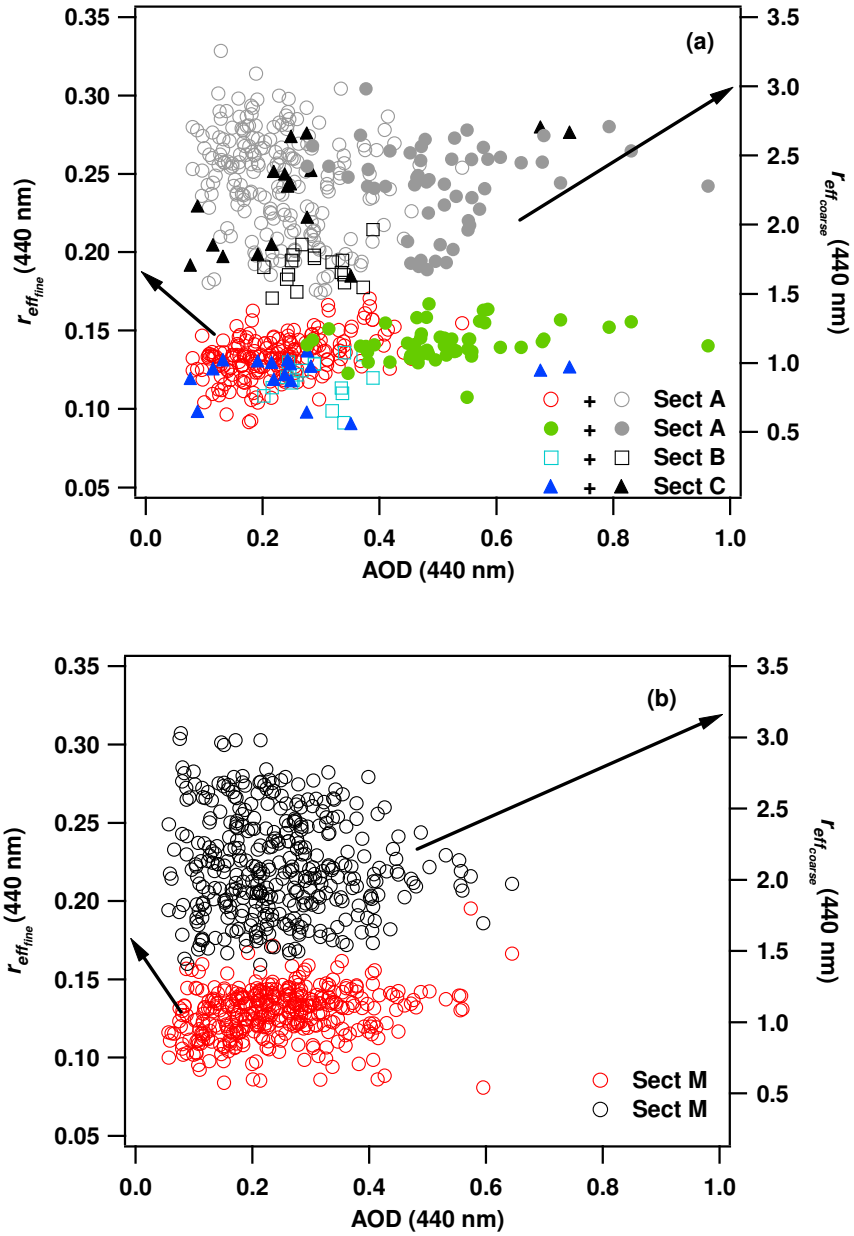

Figure 4.34. (a) $r_{eff\ fine}$ and $r_{eff\ coarse}$ versus AOD at 440 nm for aerosol of different source Sectors: both grey and red open and grey and green full dots represent data referring to Sector A aerosol. In particular, grey and green full dots represent data that could be affected by the advection of biomass burning particles (BB). Open black and light blue boxes and full black and blue triangles represent data of Sector B and C aerosol, respectively; b) $r_{eff\ fine}$ and $r_{eff\ coarse}$ versus η of the Sector M aerosol

In particular, we observe that aerosols from Sector A affected and not-affected by biomass burning, are characterized by a great variability of $r_{eff\ coarse}$ values while the aerosols coming from other sectors tend to concentrate in a smaller region of the plot.

Infact, particles from Sector B in are characterized by a $r_{eff\,fine}$ and $r_{eff\,coarse}$ values varying within the ~ 0.09 – 0.13 (light blue boxes) and the ~ 1.46 – 1.96 range (black open boxes), respectively, with a mean values of $r_{eff\,fine}$ = 0.12 µm and $r_{eff\,coarse}$ = 1.68 µm. Aerosols from Sector C assume $r_{eff\,fine}$ and $r_{eff\,coarse}$ values that vary in the 0.1 – 0.13 µm range (blue triangles) and 1.7- 2.6 µm range(black triangles), respectively. This latter result is comparable with size distributions reported in the literature. Infact, Smirnov et. al 2003 found that the maritime component in the columnar size distributions retrieved from AERONET at 500 nm in three island locations is bimodal with a fine mode at an effective radius $r_{eff\,fine}$ ~ 0.11-0.14 µm and a coarse mode $r_{eff\,coarse}$ ~1.8-2.1 µm. In figure 4.33b the plots $r_{eff\,fine}$ vs AOD (red open boxes) and $r_{eff\,coarse}$ vs AOD (black open boxes) for the Sector M show that the variability range of $r_{eff\,fine}$ and $r_{eff\,coarse}$ is the same of that of figure 4.34a. This latter result highlighted that the correlation plot r_{eff} – AOD do not help us to discriminate significant differences between aerosols coming from Sector M and from other different sectors.

The correlation study performed in this paragraph shows that this methodology of analysis don't allow clearly individuating specific properties of the particles originated from different sectors. Then it was necessary to develop a different method based on the study of the frequency of occurrence plots of the investigated parameters. The frequency of occurrence analysis is reported in the next paragraph.

4.3 Aerosol parameter analysis by frequency of occurrence plots

The frequency distribution analysis of the AERONET products including AOD, single scattering albedo, asymmetry factor, Angstrom coefficient, fine-mode

fraction, and lidar ratio is used in this section to characterize aerosol properties of different source regions. We mention that AOD, η, SSA, *g*, are the main parameters needed to incorporate aerosol particles into global climate models and evaluate aerosol direct radiative effects (Lyamani et al., 2004).

4.3.1 *Sector A: aerosol parameter analysis*

Figure 4.35a (grey line) shows the AOD frequency of occurrence plot of the total Sector A aerosol, and for summer (black dashed line), spring (black full line), and autumn (black dotted line) measurements. Data points of winter months were not available for the lack of AERONET measurements. We observe from Figure 4.35a (grey line) that AOD values vary within the 0.08-0.96 range with a yearly average of 0.29±0.15 and a main peak at ~ 0.2. The summer-AOD frequency plot (Figure 4.35a, dashed line), which vary within the 0.08-0.96 range, is bimodal with a main peak at ~ 0.2 and a secondary peak at ~ 0.5. Figure 4.27a indicates that AOD values larger than 0.4 are mostly due to aerosol affected by biomass burning particles. In fact, most of forest fires occur on summer. Hence, AODs < 0.4 are mostly due to continental urban/industrial aerosol. Figure 4.35a shows that AOD values of autumn (dotted line) and spring (solid black line) measurements are smaller (0.08-0.5) than those retrieved on summer, as it is generally observed over the Mediterranean basin (e. g. Gerasopoulos, 2005), where the aerosol load is on average larger in summer for the lack of rainy days, which favor the accumulation of aerosol particles and for the larger solar irradiance that favors the production of photochemical smog. Figure 4.35b shows for comparison the AOD frequency plot of the Sector B- (dotted line), C- (full black line), and M-aerosol (dashed grey line). We observe from figure 4.35b that particles from Sector C and M are responsible of AODs varying up ~ 0.7. In

contrast, Sector B AODs vary within the 0.2-0.4 range with a yearly average of 0.29±0.05.

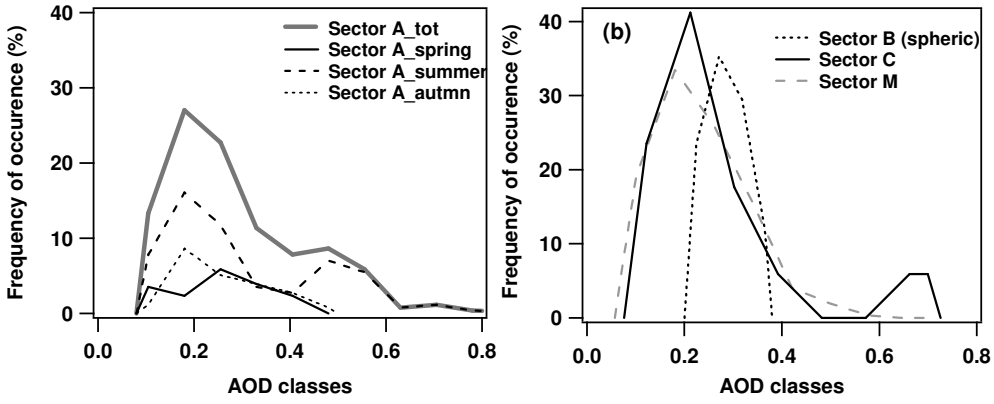

Figure 4.35. a) AOD frequency of occurrence plot for Sector A aerosol (grey line), and for summer (black dashed line), spring (black full line), and autumn (black dotted line) AOD data; b) AOD frequency plot of Sector B (dotted line), C (full black line), and M (dashed grey line) aerosol.

Figure 4.36 (grey line) shows the η frequency of occurrence plot of the total Sector A aerosol. Black and dotted lines represent in figure 4.36 the η frequency distribution plot due to the aerosol affected and not-affected by biomass burning particles, respectively (figure 4.27a). Figure 4.36 reveals that Sector A η-values span the 0.8-1.0 range and are peaked at ~0.94. Hence, fine mode particles are mostly advected from Sector A. In addition, it is worth noting that according to previous studies (e.g. Dubovik et al., 2002a) figure 4.36 (solid line) reveals that the contribution of fine-mode particles is larger for the aerosol affected by biomass burning particles.

The SSA- and the *g*-frequency distribution plot of the total Sector A aerosol are shown in figure 4.37 (grey line) and 4.36 (grey line), respectively. Black and dotted lines represent in both figures data referring to aerosol affected and not-affected by biomass burning particles, respectively. 1.5 level SSA data were plotted in figure 4.37, since level 2 data were not available.

We observe from figure 4.37 (grey line) that SSA values vary between 0.8 and 1 with a yearly average of 0.93±0.03.

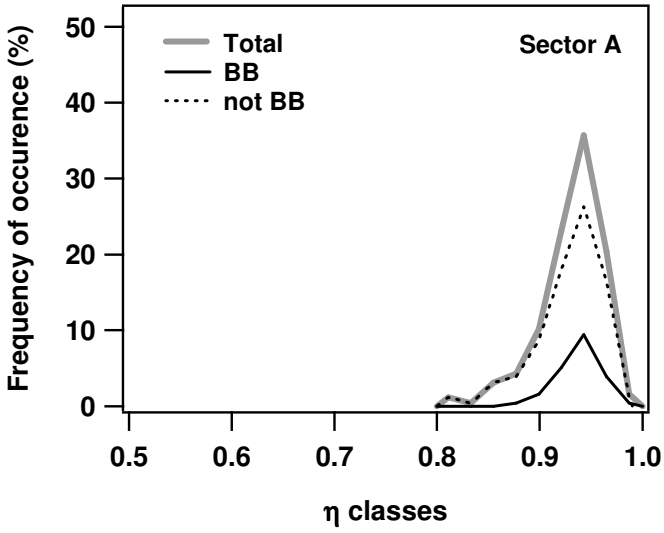

Figure 4.36. η frequency of occurrence plot of Sector A aerosol (grey line). Black and dotted lines represent in the figure data referring to aerosol affected (BB) and not-affected (not BB) by biomass burning particles, respectively.

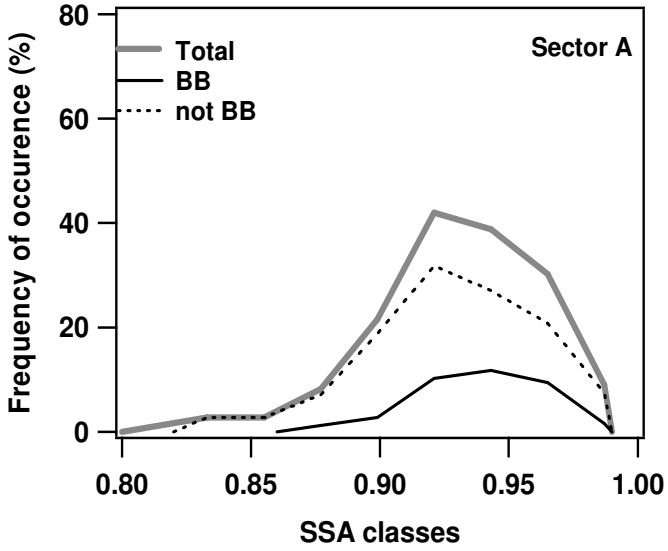

Figure 4.37. SSA frequency of occurrence plot of Sector A aerosol (grey line). Black and dotted lines represent in the figure data referring to aerosol affected (BB) and not-affected (not BB) by biomass burning particles, respectively.

Figure 4.38 (grey line) reveals that *g* values vary within the 0.6-0.74 range with a yearly average of 0.67±0.03.

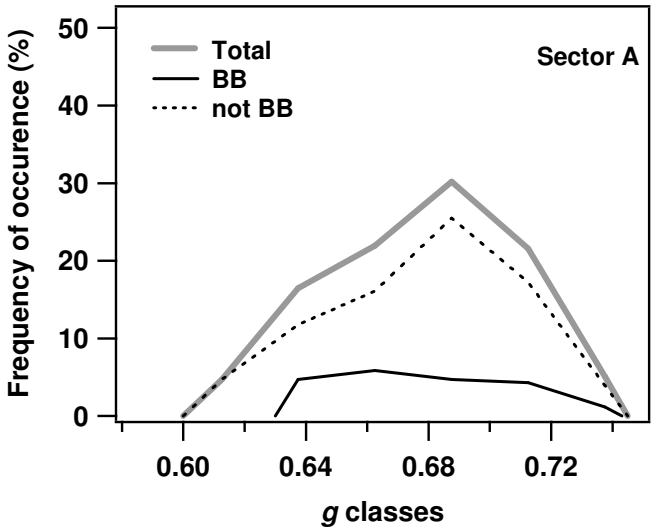

Figure 4.38. *g* frequency of occurrence plot of Sector A aerosol (grey line). Black and dotted lines represent in the figure data referring to aerosol affected (BB) and not-affected (not BB) by biomass burning particles, respectively

The comparison between the solid- and the dotted-black line both in figure 4.37 and 4.38, indicates that the variability range of SSA and *g* values extends toward lower and higher values, respectively for the aerosol not affected by biomass-burning particles, as a consequence of the higher presence of larger-size, more-absorbing particles. In conclusion, figs. 4.35a-4.38 show that the Sector A aerosol affected by biomass burning particles is mostly made of smaller-size particles that also are responsible of the highest AOD values and on average of higher (smaller) SSA (*g*) values. Variability ranges and yearly average values of the aerosol parameters above analyzed are given in Table 4.1.

According to d'Almeida et al. (1991) and Hess et al. (1998), AOD, η , SSA, and *g* frequency distribution plots (figs. 4.35a-4.38) indicate that the Sector A aerosol can be considered representative of "continental average aerosol", mostly made of water soluble and a small amount of soot and insoluble components. To this end, it is worth mentioning that a closure study between a 2.5-year data set of Raman lidar measurements (performed in Lecce within the European Aerosol Research Lidar Network) and a numerical model, also indicated that rather clean continental aerosols, with water-soluble fine-mode aerosol accounting for 98-99% of the total number of particles, characterized the aerosol load advected over souht-east Italy from north and east European countries (Barnaba et al., 2007).

The lidar ratio *Lr* that is mainly retrieved from Raman lidar measurements (e.g. De Tomasi et al., 2006) also is used to characterize aerosols of different type.

Figure 4.39 (grey solid line) shows the *Lr* frequency of occurrence plot for λ = 440 nm and for the total Sector A aerosol. Black and dotted lines represent in figure 4.39 the *Lr* frequency of distribution plot due to aerosol affected and not-affected by biomass burning particles, respectively. Figure 4.39 (grey solid line) reveals that total *Lr* values vary between 20 and 120 sr and are peaked at $\cong$ 80 sr. These data are in satisfactory accordance with those retrieved by Raman lidar measurements at 351 nm performed in Lecce during 2.5 year measurements, which provided lidar ratios spanning the 5-130 sr range (Barnaba et al., 2007) for air masses advected from north and east-European countries. Figure 4.39 (black solid line) indicate that 70% of the *Lr* values due to aerosol affected by biomass burning particles vary within the 40 - 80 sr range.

To this end, it is worth mentioning that Cattrall et al. (2005) analyzing AERONET measurements from 26 sites across the world, revealed that lidar ratios at 550 nm of biomass-burning aerosol varied within the 40-80 sr range and were peaked

at 60 sr, in accordance with the results of this paper. In addition, Cattrall et al. (2005) found that the urban-industrial aerosol was characterized by *Lr* values varying within the 40-100 sr range and peaked at 71 sr.

Figure 4.39 (black dotted line) showing *Lr* values of urban/industrial aerosol not affected by biomass burning particles, reveals that *Lr* values vary within the 20-120 sr range and that 70% of the *Lr* values vary within the 85-120 sr range, in accordance with the results by Cattrall et al. (2005) for urban/industrial aerosol. In conclusion, the above reported analysis indicates that air masses carrying moderately-absorbing ($0.8<SSA<1.0$ and $20\ sr<Lr<120\ sr$), fine-mode ($0.8<\eta<1.0$ and $0.6<g<0.8$) particles are advected over south-east Italy and hence over the central Mediterranean basin, from the urban/industrial European countries. In addition, these air-masses are responsible mostly in summer of rather high aerosol loads (AOD>0.5) for the contribution of biomass burning aerosol.

Table 4.1: Variability ranges, yearly average with standard deviations and number of data points (*N*) of the investigated parameters for air-masses originating from different sectors.

Sector A	Sector B (Spheric)	Sector B (Spheroid)	Sector C	Sector M
		N		
255	**17**	**17**	**17**	**369**
		AOD Aver		
0.29±0.15	**0.29±0.05**	**0.29±0.05**	**0.27±0.17**	**0.24±0.11**
		AOD Min		
0.08	**0.20**	**0.20**	**0.07**	**0.05**
		AOD Max		
0.96	**0.38**	**0.39**	**0.72**	**0.64**
		η Aver		
0.93±0.03	**0.73±0.04**	**0.72±0.05**	**0.8±0.1**	**0.87±0.09**
		η Min		
0.80	**0.65**	**0.61**	**0.57**	**0.44**
		η Max		
0.99	**0.78**	**0.79**	**1.0**	**1.0**

		SSA Aver		
0.93±0.03	**0.94±0.04**	**0.94±0.03**	**0.94±0.03**	**0.93±0.03**
		SSA Min		
0.82	**0.84**	**0.89**	**0.90**	**0.75**
		SSA Max		
0.99	**0.99**	**0.99**	**0.98**	**0.99**
		***g* Aver**		
0.67±0.03	**0.69±0.02**	**0.69±0.02**	**0.67±0.03**	**0.68±0.03**
		***g* Min**		
0.60	**0.64**	**0.65**	**0.61**	**0.58**
		***g* Max**		
0.74	**0.72**	**0.72**	**0.71**	**0.75**
		***Lr* Aver**		
72±20	**43±15**	**56±13**	**58±24**	**57±23**
		***Lr* Min**		
20.48	**8.7**	**37**	**10**	**9.3**
		***Lr* Max**		
120	**65**	**80**	**87**	**107**

According to the number of data points/Sector (*N*), Table 4.1 reveals either that 289 data points of Figure 4.3a can be ascribed to well defined source Sectors and that 88% of the data points are representative of the "continental average aerosol" advected from Sector A source regions. Hence, the aerosol advected from Sector A is predominant over that advected from Sector B and C.

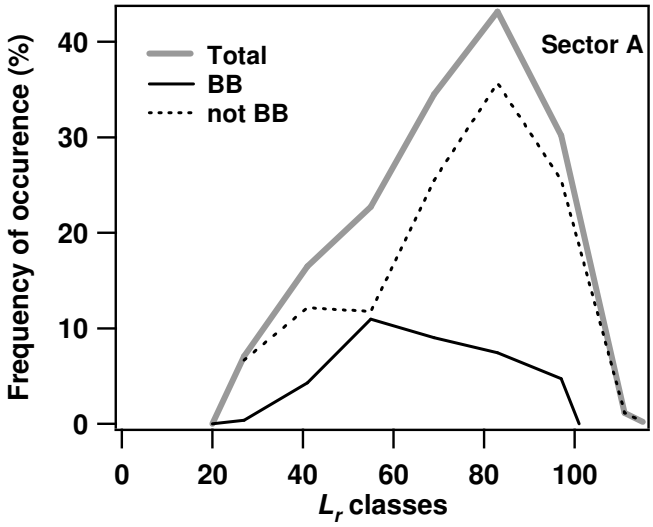

Figure 4.39. *Lr* frequency of occurrence plot for λ = 440 nm of Sector A aerosol (grey line) and for aerosols affected (black solid line) (BB) and not-affected (black dotted line) (not BB) by biomass burning particles, respectively.

4.3.2 *Sector B: aerosol parameter analysis*

The frequency distribution plot of figure 4.35b (black dotted line) indicates that the particles advected from Africa deserts (Sector B) are characterized by AOD values varying within the 0.2-0.4 range with a yearly average of 0.29± 0.05. The larger contribution of coarse mode particles to the Sector B aerosol is revealed by the η-frequency distribution plot of figure 4.39 (black dotted line), which indicates that η values span the 0.65-0.78 range.

Figures 4.41-4.43 show by black dotted lines SSA-, *g*-, and *Lr*-frequency distribution plots for aerosol particles from Sector B. Variability ranges and yearly average values of the investigated parameters are given in Table 4.1.

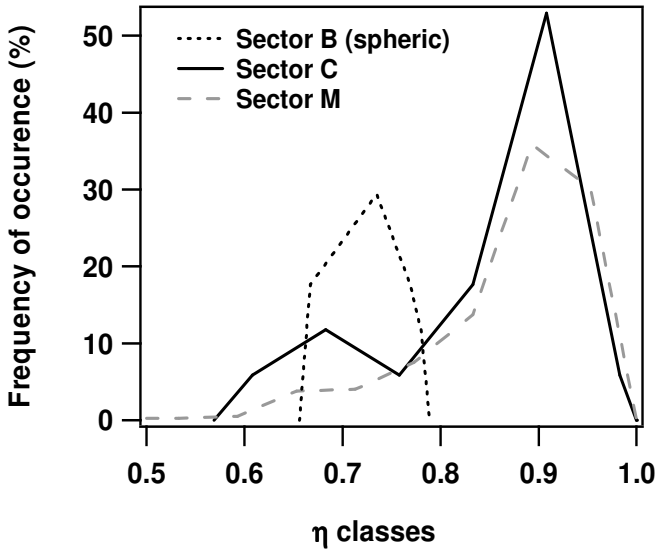

Figure 4.40. η-frequency distribution plot for particles advected from Sector B (black dotted line), from Sector C (black line), and from Sector M (grey dashed line).

All data of figs. 4.40-4.43 were retrieved for aerosol particles that are assumed to be polydisperse homogeneous spheres with the same complex refractive index. However, it is well known that latter assumption misleads AERONET inversion products when the aerosol load is significantly affected by non-spherical particles and aerosols from Sector B are significantly affected by desert type particles, which are flattened and irregular in shape (Dubovik and King, 2000a). It was shown by Dubovik et al. (2002b) that in dust dominated environments the use of polydisperse, randomly oriented spheroids leads to a significant improvement in retrieving the size distribution and real refractive index .

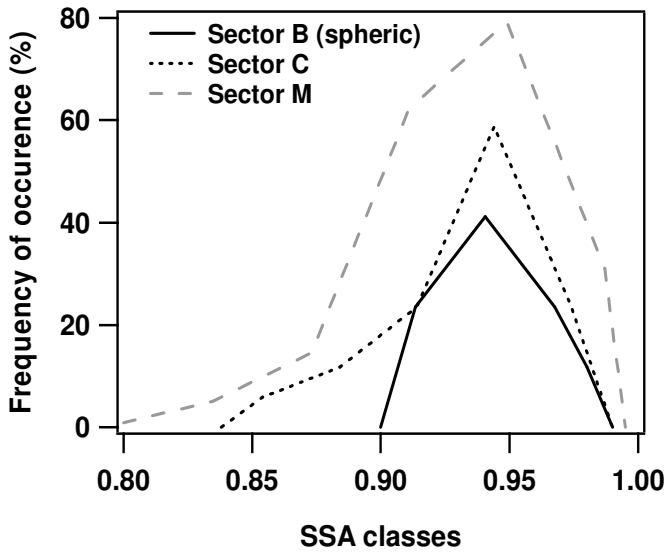

Figure 4.41. SSA-frequency distribution plot for particles advected from Sector B (black dotted line), from Sector C (black line), and from Sector M (grey dashed line).

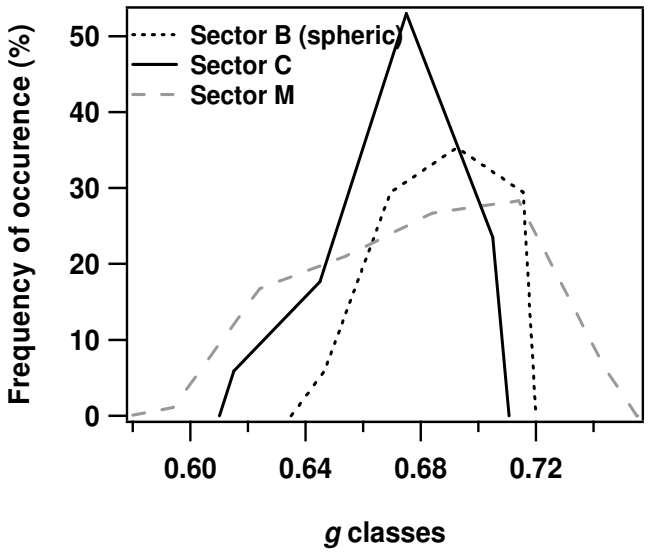

Figure 4.42. *g*-frequency distribution plot for particles advected from Sector B (black dotted line), from Sector C (black line), and from Sector M (grey dashed line).

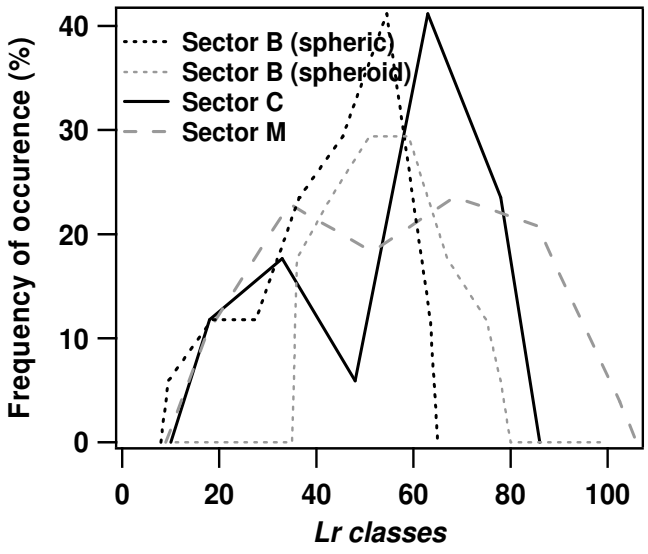

Figure 4.43. *Lr* -frequency distribution plot for particles advected from Sector B (black dotted line), Sector C (black line) and Sector M (grey dashed line). The grey dotted line represents the - *Lr* frequency distribution plot of the Sector B *Lr* values calculated by the spheroid model.

Variability ranges and yearly average values of the Sector B aerosol parameters retrieved by the spheroid model are given in Table 4.1. The comparison between η-, SSA-, and *g*-values by the spheroid and the spherical model revealed that the percentage variations were lower than 5%. In contrast, lidar ratio values by the spheroid model were significantly larger than the values provided by the spherical model: percentage variations of the values provided by the two models were as high as 100%. Figure 4.43 shows by grey dotted line the frequency distribution plot of *Lr* values by the spheroid model and we observe that the lidar ratio values vary within the 37-80 sr range with a yearly average of 55±13 sr. Last results are in satisfactory accordance with those reported by Cattrall et al. (2005). Analyzing AERONET aerosol products of Africa and Saudi Arabia sites significantly affected by desert dust, they found at 550 nm that lidar ratio values by the spherical model varied within the 10-20 sr range and were peaked at 15 sr. In contrast, lidar ratios by the spheroid model were peaked at 42 sr and varied within the 20-60 sr range. The results of figure 4.43 (grey dotted line) are also in satisfactory accordance with *Lr* values retrieved over south-east Italy by Raman-lidar measurements at 351 nm (e.g. De Tomasi et al., 2003), which combined with model calculations, revealed that an average lidar ratio of 47 sr could be used to characterize Sahara dust particles over south-east Italy (Barnaba et al., 2004).

Table 4.1 reveals that η values of the Sector B aerosol vary within the 0.61-0.79 range with a yearly average of 0.72 ± 0.05. Latter results indicate that the Sector B aerosol advected to south-east Italy is also quite affected by the contribution of fine-mode particles. In fact, a recent Sahara dust event study by complementary remote sensing measurements and ground observations revealed that the anthropogenic fine mode aerosol was over south-east Italy more than 50% of the total aerosol load

during a dust outbreak (Bellantone et al., 2007). η values smaller than 0.5 were generally retrieved both at Lampedusa and Crete during dust outbreaks. The larger η values retrieved over south-east Italy may be partially due to the sedimentation of large-size dust particles, being south-east Italy more away from desert source regions than Lampedusa and Crete. However, the contribution of polluted particles from marine and continental areas crossed by the desert air masses before reaching south-east Italy can represent a significant contributing factor. SSA and *g* variability ranges and yearly average values support last comment. According to Dubovik et al., (2002a) desert dust at Cape Verde was characterized at 440 nm by SSA = 0.93±0.01 and *g* = 0.73±0.04. In contrast, Table 4.1 shows both that SSA values span the 0.89-0.99 range with a yearly average of 0.94±0.03, and that *g* values span the 0.65-0.72 range with a yearly average of 0.69±0.02. The larger (smaller) SSA (*g*) mean value found over south-east Italy with respect to that of Cape Verde can be explained by assuming that desert dust particles advected over south-east Italy were also affected by the contribution of moderately-absorbing, fine-mode particles as those due to water soluble species: the predominant component of the "continental average aerosol" that is advected over the Mediterranean basin from continental European countries. Finally, we mention that according Table 4.1, only 6% of the 289 Sector A-C data points were representative of polluted desert-dust aerosol advected from Sector B source regions. As a consequence, desert-dust is a minor aerosol component over south-east Italy.

4.3.3 *Sector C: aerosol parameter analysis*

Figure 4.35b (black line) shows the AOD-frequency distribution plot for Sector C aerosol that is expected to be significantly affected by marine particles.

Black lines represent in figs. 4.40-4.43 η-, SSA-, *g*-, and *Lr*-frequency distribution plots of Sector C aerosol. Variability ranges and yearly average values of the investigated parameters are given in Table 4.1. The frequency distribution plot of figure 4.35b (black line) shows that AODs span the 0.07-0.72 range with a yearly average of about 0.3±0.2. According to Hess et al. (1998) and Smirnov et al. (2003) clean maritime particles are responsible of AODs at 440 nm smaller than 0.2. Hence, the Sector C aerosol is expected to be maritime polluted. SSA- and *g*-variability ranges support last comment. In fact, according to d'Almeida et al. (1991), sea-salt and oceanic particles are characterized at 450 nm by SSA and *g* values close to 1 and 0.79, respectively. In addition, Dubovik et al. (2002a) showed that the oceanic aerosol is characterized at 440 nm by AOD ≤ 0.15, SSA = 0.98 ± 0.03, and *g* = 0.75 ± 0.04. Despite the results by d'Almeida et al. (1991) and Dubovik et al. (2002a), figure 4.41 (solid line) shows that SSA values span the 0.90-0.98 range with a yearly average of 0.94±0.03 and figure 4.42 reveals that *g* values peaked at ~ 0.69, span the 0.61-0.71 range with a yearly average of 0.67±0.03. The smaller SSA and *g* values of this paper with respect to the ones reported by d'Almeida et al. (1991) and Dubovik et al. (2002a) for marine aerosol can be explained by assuming that fine-mode and moderately-absorbing particles of non-marine origin affect the Sector C aerosol. To this end, we mention that the rather high AOD values indicated by the arrow in figure 4.27a are possibly due to contamination by biomass burning particles. In fact, the two AOD values were retrieved on September 9, 2003 at 15:37 UTC and 14:07 UTC, respectively and according to bactrajectories (http://croc.gsfc.gov/aeronet/) and satellite fire maps (http://maps.geog.umd.edu/default.asp), the air masses advected from the Atlantic crossed fire affected sites before reaching south east Italy. In addition, the marked bimodal structure of both the η- and the *Lr*-frequency distribution plot (figs. 4.40 and 4.43, solid line), indicates that the Sector C aerosol is

made at least of two main classes of particles. Figure 4.44 showing the *Lr* versus η scatterplot for the Sector C aerosol, allows inferring the two main aerosol classes that contribute to the Sector C aerosol. We observe from Figure 4.44 that *Lr* values span the 10-36 sr range when η values vary within the 0.57-0.75. In contrast aerosol loads characterized by η values spanning the 0.8-1.0 range are characterized by *Lr* values varying within the 42-86 sr range.

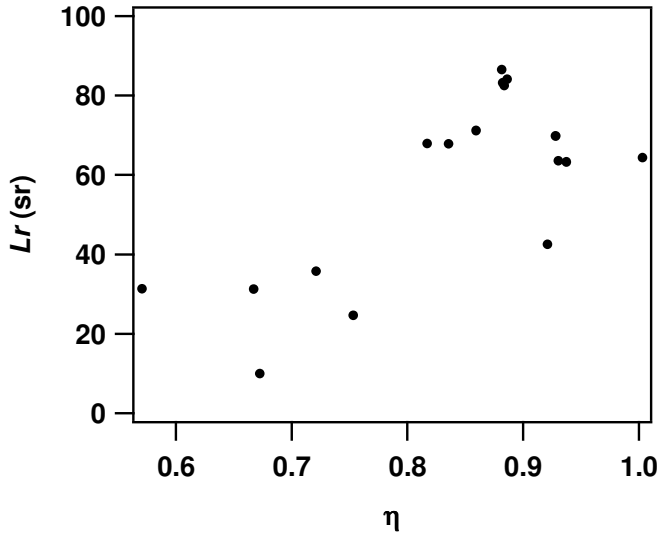

Figure 4.44. *Lr* versus η values for the Sector C aerosol.

According to Ackerman (1998), the maritime aerosol is characterized at 355 nm by *Lr* values varying within the 17-24 sr range, while the continental aerosol, which consists of insoluble, soot, and water soluble components, is characterized by lidar ratios spanning the 43-70 sr range. In addition, the studies by Cattrall et al. (2005) revealed that at 550 nm, lidar ratio values of oceanic particles spanned the 20-40 sr range, while *Lr* values of urban/industrial aerosol varied within the 40-100 sr range. Cattrall et al. (2005) also showed that oceanic particles were characterized by Angstrom coefficient values spanning the 0.3-1.2 range, while Å values of

urban/industrial aerosol varied within the 1.6-2.0 range. Finally, lidar measurements over south-east Italy by an elastic-Raman lidar operating at 351 nm, combined with model calculations, revealed that an average lidar ratio of 29 sr can be used to characterize maritime aerosols (Barnaba et al., 2004) over south-east Italy. In conclusion, the comparison between the results of this paper and those reported by several authors (Ackerman, 1998; d'Almeida et al., 1991, Dubovik et al., 2002a, Barnaba et al., 2004; Cattrall et al., 2005) indicates that the Sector C aerosol characterized by *Lr* and η values spanning the 10-36 sr and the 0.57-0.75 range, respectively can be considered of maritime type. In contrast, the Sector C aerosol characterized by *Lr* and η values spanning the 42-86 sr and the 0.8-1.0 range, respectively can be considered of maritime-polluted type. Hence, Sector C air masses are responsible over south-east Italy of the advection of maritime-polluted air masses. Last results are mostly determined by the geographical location of south-east Italy: oceanic particles generally cross urban/industrial area and the Mediterranean basin before reaching south-east Italy. We mention that Barnaba et al. (2004) showed that the classification of cases of clean marine aerosols was particularly complex in the Mediterranean, due to the influence of the surrounding continents and the limited dimension of the basin.

4.3.4 *Sector M: aerosol parameter analysis*

According to the backtrajectory analysis and the criteria defined in the paragraph 4.1.3, 62% of the 240 measurements days analyzed in this study were characterized by advection patterns that do not allow defining the aerosol source sector (Sector M). Frequency distribution plots of AOD, η, SSA, *g*, and *Lr* values of the Sector M aerosol are plotted in figs. 4.35b and 4.40-4.43 by grey dashed lines.

Variability ranges and yearly average values of Sector M aerosol parameters are given in Table 4.1. The comparison of Sector M aerosol properties with the corresponding ones referring to Sectors A-C and in particular the comparison of figure 4.27a with figure 4.27b, indicate that Sector M aerosol properties are rather close to the properties of the total aerosol load from Sector A, B, and C. Back trajectory pathways of figure 4.25 support last comment. Externally mixed aerosol populations from Sector A, B, and C, respectively are also expected to affect the Sector M aerosol load. The mixing of different particle types is mainly expected to occur when the advection pattern changes with time of the day. A typical example of measurement day characterized by a mixed advection pattern was analyzed in the paragraph 4.2, where it was shown that the aerosol properties significantly varied within few hours as a consequence of the advection pattern change.

The aerosol mask method (Barnaba and Gobbi, 2004), which represents a valuable tool to classify aerosol of different type, was applied to the Sector M data points of figure 4.27b to separate the contribution of maritime, continental and desert dust aerosol to the total Sector M aerosol. Maritime, continental and desert dust particles are the main aerosol components over the Mediterranean basin. According to Dubovik et al. (2002a), we assumed that maritime particles were represented in the Å versus AOD scatterplot of figure 4.27b by the data points with AOD < 0.15 and Å $\leq$ 1.6. In contrast, the data points of figure 4.27b characterized by AOD $\geq$ 0.15 and Å $\leq$ 0.9 were considered representative of desert dust particles. All the data points that could not be ascribed to maritime and desert dust particles were considered representative of continental urban/industrial particles. Solid lines in figure 4.27b define the aerosol mask and hence the regions of the Å versus AOD scatterplot that are representative of different aerosol types. The used aerosol mask criteria are in satisfactory accordance with the previously reported results of this paper. According

to the aerosol mask criteria, it was found that 6%, 14%, and 80% of the 369 data points of figure 4.27b were representative of desert dust, maritime and continental aerosol particles, respectively. Latter results are in satisfactory accordance with the percentage values obtained by analyzing back trajectories to infer the aerosol contribution from Sector A, B, and C source regions, respectively. Hence, the aerosol mask results further more show that Sector M aerosol properties are rather close to the properties of the total aerosol load from Sector A, B, and C. In particular, they also reveal that the contribution of continental urban/industrial aerosol was predominant over south-east Italy. Finally, we mention that the comparison between the Sector M AOD frequency of occurrence plot with the AOD frequency of occurrence plot due to the total aerosol load from Sector A, B, and C, revealed that the differences were lower than 5%.

4.4 Conclusions

In this chapter aerosol measurements from the AERONET station in Lecce over south-east Italy, combined with five-day back trajectories were analyzed to characterize aerosol properties over the Central Mediterranean basin, to assess the influence to the aerosol load of long-range transport from various regions, and to study the mixing of different aerosol types. The aerosol data include AOD, single scattering albedo, asymmetry factor, Angstrom coefficient, fine-mode fraction, and lidar ratio retrieved from measurements performed in the period March 2003-October 2004. 5–day analytical back trajectories were used to characterize main advection patterns over Lecce AERONET site. In particular, three broad geographical sectors were defined as aerosol source regions: Sector A, which includes all continental European sources with the exception of Spain; Sector B, which includes the Southern Mediterranean Sea and the Africa continent; Sector C,

which includes the Western Mediterranean, the Iberian Peninsula, and the Atlantic Ocean. The time spent by the trajectories in a sector up to the measurement day was also considered to better define the aerosol origin sector. We found that 32% of the 240 measurement days were characterized by air masses coming from Sector A, while 3% of the measurement days were characterized by air masses coming either from Africa deserts (Sector B) or from the Atlantic and Mediterranean Sea (Sector C). 62% of the measurement days were characterized by backtrajectories that did not allow defining the aerosol source Sector According to the criteria adopted in this paper. The aerosol monitored on these days was considered due to mixed source regions (Sector M).

Air masses from Sector A have the common property to travel across several urban and industrialized European areas before reaching Lecce. As a consequence, it was shown that Sector A air masses could be considered responsible of the transport of urban/industrial and biomass burning aerosols. In particular, the comparison of the Sector A aerosol parameter mean values (AOD = 0.29±0.15, η = 0.93±0.03, SSA = 0.93±0.03, g = 0.67±0.03, and Lr = 72±20 sr) with previous investigations revealed that a "continental average aerosol", mostly made of water soluble and a small amount of soot and insoluble component was advected over south-east Italy from Sector A source regions. The analysis of the Sector B aerosol parameters, which were characterized by AOD=0.29±0.05, η = 0.72±0.05, SSA = 0.94±0.03, g = 0.69±0.02, and Lr = 56±13 sr, revealed that desert dust particles advected over south-east Italy were also affected by the contribution of moderately-absorbing, fine-mode particles as those due to water soluble species: the predominant component of the "continental average aerosol" that is advected over the Mediterranean basin by the European continent. Hence, it was shown that polluted-desert dust particles were

advected over south east Italy from Sector B source regions. It was also found that Sector C air masses were responsible of the advection over south-east Italy of maritime-polluted aerosol due to marine and to lesser extent anthropogenic particles from the Atlantic Ocean and/or the Western Mediterranean regions crossed by the Sector C air masses before reaching Lecce. Sector C aerosol parameter mean values (AOD = 0.27±0.17, η = 0.8±0.1, SSA = 0.94±0.03, g = 0.67±0.03, and Lr = 58±24 sr) were compared to the values reported by previous studies to reach the above mentioned conclusion.

The results obtained by the application of an aerosol mask to the data points of Sector M, showed that 80% of the 369 Sector M data points were representative of "continental average aerosol", while 14% and 6% of the data points were representative of maritime and desert-dust aerosol, respectively.

The geographical location of south-east Italy that is rather close to continental European regions is considered responsible of the predominant contribution of the "continental average aerosol" to the aerosol load of south-east Italy. To this end, it is worth mentioning that maritime-polluted and desert dust-polluted particles were advected over south-east Italy from Sector C and B air masses, respectively.

In conclusion, the results of the work presented in this chapter beside revealing that the aerosol characterization over the Mediterranean is complicated by the fact that a large number of sources and hence of aerosol species contribute to it, have contributed to the aerosol characterization over the Mediterranean, providing valuable data for future studies devoted to the evaluation of the direct radiative forcing by aerosols for this region.

CHAPTER 5

THE MODERATE RESOLUTION IMAGING SPECTRORADIOMETER (MODIS)

Measurements of high spatial and temporal coverage are important to characterize aerosol properties because of the large variability (close to sources) and short lifetime (a few hours to a few weeks) of aerosol particles. The aerosol remote sensing from long-term operation satellites, provides a means to achieve a global and seasonal characterization of aerosols. Satellite sensors provide global images of the entire Earth and allow resolving the spatial patterns resulting from the spatial inhomogeneeties of aerosol sources and the temporal patterns resulting from the short lifetimes of aerosols, which are on the order of a few days to a week (Remer et al., 2005). The last generation of satellites carrying instruments such as the Moderate Resolution Imaging Spectroradiometer (MODIS), the Multiangle Imaging Spectroradiometer (MISR), and the wide field of view imaging radiometer POLDER (POLarization and Directionally of the Earth's Reflectances) reveal the big interest of the scientific community in getting worldwide aerosol characterizations. The Moderate Resolution Imaging Spectroradiometer (MODIS) unlike previous satellite sensors, has the unique ability to retrieve aerosol optical thickness with greater accuracy and to retrieve parameters characterizing aerosol sizes. MODIS aerosol products have recently been validated with ground-based sunphotometer data, particularly those of AERONET (e.g. Chu et al., 2002; Chu et al., 2003; Ichoku et al., 2004; Levy et al., 2005; Remer et al., 2005).

The correlation of MODIS aerosol products and corresponding AERONET data retrieved by sunphotometer measurements performed at the Physics Department of Lecce's University (40º, 20' N, 10º, 6' E), to contribute to the validation of MODIS retrievals over south-east Italy and hence over the eastern Mediterranean basin,

represents one of the main activities performed during my PhD research activity. As mentioned, aerosols from different sources converge to the Mediterranean basin: urban/industrial aerosols and seasonal biomass burning from Central and Eastern Europe, maritime and long-range transported polluted air masses from the Atlantic Ocean, mineral dust from North Africa, and sea spray from the Mediterranean sea itself (De Tomasi et al., 2006). As a consequence, this area can be well suited to test the performance of MODIS retrieval algorithms. A brief description of the MODIS Instrument Design Concept is given in paragraph 5.1. The MODIS retrieval algorithms are described in paragraph 5.2 and aerosol products are given in Section 5.3.

5.1. MODIS Design Concept

The Moderate Resolution Imaging Spectroradiometer (MODIS) is a key instrument launched aboard the EOS Terra and Aqua polar-orbiting satellites since December 1999 and May 2002, respectively (figure 5.1). Terra's orbit around the Earth is timed so that it passes from north to south across the equator in the morning (approximately on 10:30 am), while Aqua passes south to north over the equator in the afternoon (approximately on 1:30 pm). Terra and Aqua MODIS are viewing the entire Earth's surface every 1 to 2 days, acquiring data in 36 spectral bands, ranging from 0.4 to 14.4 μm wavelengths. In particular, two bands (0.66 and 0.86 μm) are imaged at a nominal resolution of 250 m, with five bands (0.47, 0.55, 1.24, 1.64 and 2.13 μm) at 500 m, and the remaining 29 bands at 1 km. A ±55-degree scanning pattern achieves a 2,330-km swath and provides global coverage every one to two days.

These data will allow improving our understanding of global dynamics and processes occurring on the land, in the oceans, and in the lower atmosphere.

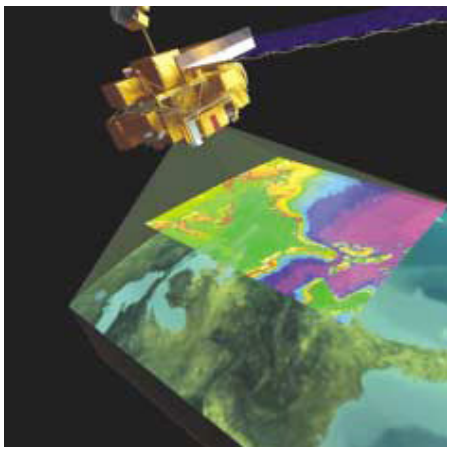

Figure 5.1. Image of MODIS Sensor

The main components of the MODIS Instrument are (figure 5.2):

- The Scan Mirror Assembly, that is the core of the MODIS Instrument, consists of a continuously rotating double-sided scan mirror, driven by a motor encoder that directs light from the Earth's surfaces onto the Optical System.
- The Optical System consists of a two-mirror off-axis afocal telescope, which directs energy to four refractive assemblies (Focal Plane Assemblies, FPAs).
- The Focal Plane Assemblies (FPAs) design includes 36 distinct spectral bands broken into four separate FPAs: Visible (VIS), Near Infrared (NIR), Short and Mid-Wave Infrared (SWIR/MWIR) and Long-Wave Infrared (LWIR). Each FPA focuses light onto a certain section of detector pixels, which are relatively large – ranging from 135 μm to 540 μm square. When light hits a detector pixel, it will generate a distinct signal depending on the type of light it is sensitive to. The signals that the pixels generate are what scientists process and study to learn about Earth's land surfaces, water surfaces, and atmosphere.

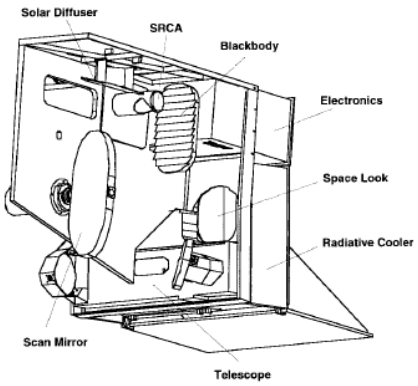

Figure 5.2. MODIS Sensor subsystems

The system also includes four on-board calibrators that provide the spatial, spectral and radiometric calibration.

MODIS data are transferred to ground stations in White Sands, New Mexico, via the Tracking and Data Relay Satellite System (TDRSS). The data are then sent to the EOS Data and Operations System (EDOS) at the Goddard Space Flight Center.

There are 44 standard MODIS data products that scientists are using to study global change. Most users will obtain data products by ordering them through an ordering system (http://modis-atmos.gsfc.nasa.gov./MOD04_L2/acquiring.html).

5.2. MODIS Algorithms

The MODIS aerosol algorithm is actually two entirely indipendent algorithms, one to derive aerosol properties over land surfaces (Kaufman et al. 1997a), the second for over the ocean (Tanre'et al., 1997). Both algorithms were conceived and coded prior to Terra launch (Kaufman et al., 1997a, Tanre' et al., 1997), and scientifically have changed little since then.

Both the land and ocean aerosol algorithms rely on calibrated, geolocated reflectance from the first seven MODIS bands (between 0.47 and 2.1 μm) provided by the MODIS Characterization Support Team (MCST). These reflectance data are first

corrected for trace gas and water vapor columns and final aerosol properties are retrieved for 10 km x 10 km boxes. Using results by geolocation and cloud mask data, individual pixels of 10 km x 10 km boxes are classified as ocean or land. If all pixels in the 10 km x 10 km box are determined to be "ocean", then the ocean algorithm is performed. If any pixel is land, then the land retrieval is applied. After the land or ocean branch is concluded, the algorithm merges some parameters into combined land and ocean products for convenience (Levy et al., 2005). The main combined land-ocean products are the AOD and the fine fraction η (the fraction of the total AOD that was contributed by smaller particles) at 0.55μm.

5.2.1. *MODIS over ocean*

If all pixels in the 10x10 km box are identified as water pixels, the ocean algorithm is chosen. First, "obstructed" pixels (cloudy or otherwise unsuitable for retrieval) are removed, including those within the glint mask (within 40º of the specular reflection angle), those flagged as cloudy (Platnick et al., 2003, Martins et al., 2003, Gao et al., 2002) and those that contain sediments (Li et al., 2003). The remaining good pixels are sorted by their near-infrared (0.86 μm) brightness. Of these, the darkest and brightest 25% are removed, thereby leaving the middle 50% of the data and eliminating residual cloud and/or surface contamination. If at least 10 pixels remain in the 10x10 km box, the reflectance statistics for all seven channels are calculated and used for inversion. As introduced by Tanre' et al.(1997) and updated by Levy et al. (2003) and Remer et al. (2005), the MODIS inversions attempts to minimize the difference between the observed spectral radiance in six MODIS channels and radiance precomputed in a look up table (LUT). The look up table models the total reflectance observed by satellite, which includes not only aerosol contributions, but also spatially and temporally constant atmospheric

(Rayleigh) and ocean surface contributions. The aerosol radiance contribution is computed for five total aerosol loadings, for four fine modes and five coarse modes (Levy et al., 2003 and Remer et al., 2005). The inversion assumes that the total aerosol contribution is composed of a single fine and single coarse mode. The modes from the LUT are combined using the fine fraction parameter η as the weighting parameter:

$$\rho_\lambda^{LUT}(AOD_{0.55}^{tot}) = \eta\rho_\lambda^{f}(AOD_{0.55}^{tot}) + (1-\eta)\rho_\lambda^{c}(AOD_{0,55}^{tot}) \qquad (5.1)$$

Equation 5.1 means that the spectral reflectance calculated from the LUT values, $\rho_\lambda^{LUT}(AOD_{0.55}^{tot})$ for the determined values of η and $AOD_{0.55}^{tot}$, is a weighted average of the reflectance values for an atmosphere with a pure fine mode "f" and optical thickness $\tau_{0.55}^{tot}$ and the reflectance of an atmosphere with a pure coarse mode with the same $\tau_{0.55}^{tot}$. For each of the 20 combinations of one fine mode and coarse mode, the inversion finds the pair of $AOD_{0.55}^{tot}$ and $\eta_{0.55}$ that minimizes the error (ε) defined as:

$$\varepsilon = \sqrt{\frac{\sum_{\lambda=1}^{6} N_\lambda \left(\frac{\rho_\lambda^m - \rho_\lambda^{LUT}}{\rho_\lambda^m + 0.01} \right)^2}{\sum_{\lambda=1}^{6} N_\lambda}} \qquad (5.2)$$

Where N_λ is the sum of good pixels at wavelength λ, ρ_λ^m is the measured MODIS reflectance at wavelength λ, and ρ_λ^{LUT} is calculated from the combination of modes in the lookup table and is defined by equation (5.1).

The 20 solutions are then sorted according to values of ε. The "best" solution is the combination of modes with the accompanying $AOD_{0.55}^{tot}$ and $\eta_{0.55}$ that minimizes ε. The solution may not be unique. The "average" solution is the average of all

solutions with ε<3% (Remer, 2005), or the average of the three best solutions if all ε>3%.

The volume size distribution is determined by the following relationship:

$$\frac{dV(r)}{d\ln r} = \eta_M \sum_{i=1}^{npixel} \frac{1}{\sigma_{i,fine}\sqrt{2\pi}} \exp\left\{\frac{-[\ln(r/r_{v_{i,fine}})]^2}{2\sigma_{i,fine}^{\ 2}}\right\} + (1-\eta_M) \sum_{i=1}^{npixel} \frac{1}{\sigma_{i,coarse}\sqrt{2\pi}} \exp\left\{\frac{-[\ln(r/r_{v_{i,coarse}})]^2}{2\sigma_{i,coarse}^{\ 2}}\right\} \quad (5.3)$$

where $r_{v_{i,fine}}$ ($r_{v_{i,coarse}}$) and $\sigma_{v_{i,fine}}$ ($\sigma_{v_{i,coarse}}$) are volume modal radius and standard deviation of fine (coarse) mode particles at the MODIS retrieval pixel *i*. The four and five discrete values of $r_{v,fine}$ and $r_{v,coarse}$, respectively are within the 0.11-0.29 μm and 1.17-2.35 μm range, respectively. MODIS derived aerosol properties have been validated before (Tanré et al., 1999) and after (Remer et al., 2001) the launch of Terra. The aerosol optical thickness is derived over ocean with an error ΔAOD_M = ±0.03 ± 0.05AOD_M (Tanré et al., 1997). The errors were found to be mostly random with very little bias remaining for large statistics of data (Kaufman et al., 2005a). Remer et al. (2002) indicate the particles size-dependent parameters (as η_M) to be retrieved with an accuracy within ± 25%.

A variety of parameters can be inferred from the chosen size distribution including spectral optical thickness, effective radius, concentration, etc.

5.2.2. *MODIS over land*

Like the over-ocean algorithm, the theoretical retrieval over land has not changed much since its inception (Kaufamnn et al., 1997b).

Not all pixels in the 10x10 km box need to be detected as land for the land retrieval to continue. First, cloudy pixels are removed by combining cloud mask tests (Platnick et al., 2003, Martins et al., 2002, Gao et al., 2002). The Normalized

Difference Vegetation Index (NDV1) discards large water bodies (lakes, rivers) and most snow or ice pixels. The NDVI products are produced by the Bureau of Meteorology for the Australian region using measurements from the Advanced Very High Resolution Radiometer (AVHRR) on board the USA's NOAA polar orbiting meteorological satellites. The reflectance measured from two channels, Channel 1 (visible: 0.58 - 0.68 microns) and Channel 2 (near infrared: 0.725 - 1.0 microns) are used to calculate the index.

From the remaining pixels, the algorithm selects “dark” surface pixels based on reflectance at 2.1 μm. These dark pixels are discarded to eliminate pixels contaminated by clouds, cloud shadows, or odd surfaces. The remaining 30% of the pixels are used in the aerosol retrieval.

If at least 12 pixels remain in the 10x10 km box, the algorithm calculates the mean measure reflectance at the three land wavelengths (0.47, 0.66 and 2.1 μm). Using empirical relationships proposed by Kaufman et al. (1997b) the surface reflectance in the two visible (VIS) wavelengths are estimated from the reflectance at 2.1 μm. The difference between the surface reflectance and the Rayleigh (standard atmosphere)-corrected satellite reflectance is known as the aerosol “path reflectance”. Assuming a generic, mostly fine mode “continental” model (which includes three mode, Kaufamn et al., 1997b), the MODIS-measured path reflectance is compared with reflectance found in precomputed lookup tables. AOD is derived at 0.47 and 0.66 μm. The spectral dependence of the path reflectance, determined from the preliminary use of continental aerosol model, determines whether to add coarse dust (Kaufamn et al., 1997b). Then, the fine model is rederived using a specific aerosol model, depending on the season and location. All models are described in Remer et al., (2005).

Like over –ocean algorithm, a number of aerosol products are inferred, including AOD at 0.55μm that is derived over land with an error $\Delta AOD_M = \pm 0.05 \pm 0.15 AOD_M$ (Kaufman et al., 1997a)

5.4. MODIS Products

MODIS – derived aerosol properties are reported in level 2 (L2) granule-based (granule: 5-minute segment one orbit of data) and level 3 (L3) global, 8-day and monthly gridded products. Examples of the two main aerosol products retrieved during a dust event occurred on 16 July 2003: the aerosol optical thickness, AOT and the fine fraction parameter η at 0.55μm are shown in figure 5.3a and 5.3b, respectively.

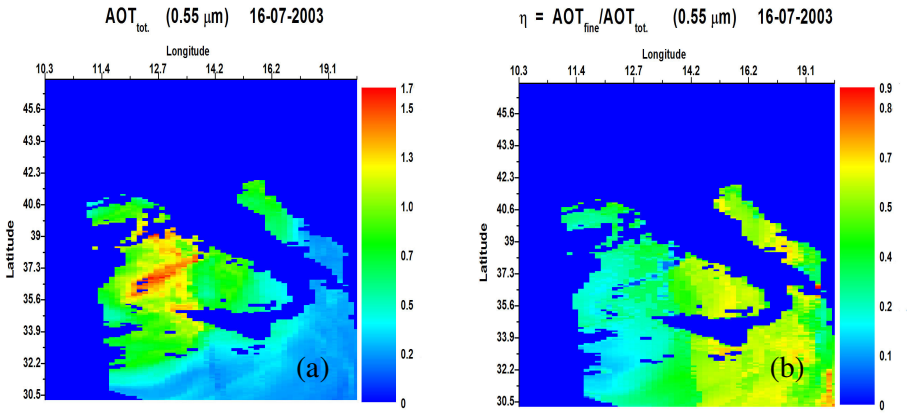

Figure 5.3. Examples of MODIS aerosol products at level 2 stage (MOD04).The data represent daily averaged values of (a) AOD, (b) fine fraction parameter η, at 0.55 μm collected on 16 July 2003 during a Sahara dust outbreak.

Figure 5.3a shows that on 16 July 2003 the aerosol load over the Mediterranean basin is very high since the AOTs assume values in the range 0.5 -1.7. Moreover, figure 5.3b shows that onh 16 July the Mediterranean is dominated by larger particles

since the fine fraction parameter assume in this area lower values between 0.1 and 0.6.

The level 2 products, designated as MOD04 files, contain 64 separate products, all connected to aerosol retrievals. The level 2 files are produced every day and represent the first level of MODIS aerosol retrieval. In addition, statistics based on the level 2 aerosol retrievals can also be found in level 3 files, designated as MOD08. These level 3 files contain parameters produced from the entire MODIS atmospheres team and include such parameters as water vapor and cloud characteristics along with the aerosol information.

All together there are 64 aerosol products at level 2: 9 products describe geometry and location, 3 products are joint land and ocean products, 23 are land-only products, and 29 are ocean-only products. Tables 5.1- 5.4 list all 64 products.

Table 5.1. Contents of MODIS aerosol level 2 hdf file (MOD04): Time and geometric information. Two-dimensional arrays of 204 *135 are indicated.

Name of product	Dimension	Status
Longitude	2D	Diagnostic
Latitude	2D	Diagnostic
Scan_Start_Time	2D	Diagnostic
Solar_Zenith	2D	Diagnostic
Solar_Azimuth	2D	Diagnostic
Sensor_Zenith	2D	Diagnostic
Sensor_Azimuth	2D	Diagnostic
Scattering_Angle	2D	Diagnostic
Cloud_Mask_QA	2D	Diagnostic

Table 5.2. Contents of MODIS aerosol level 2 hdf file (MOD04): Global land and ocean products, at 550 nm.

Name of product	Dimension	Status
Optical_Depth_ Land_And_Ocean	2D	Validated
Optical_Depth_Ratio_ Small_Land_And_Ocean	2D	Not yet validated
Reflected_Flux_ Land_And_Ocean	2D	Derived

The three joint land and ocean products are simple two-dimensional arrays of one wavelength (table 5.2). The land-only and ocean-only products contain an additional dimension. In many cases this additional dimension is wavelength. Tables 5.3–5.4 list the wavelengths for each product where applicable.

The additional dimension in the ocean-only products can designate either the "best" solution or the "average" solution from the ocean retrieval as described above in paragraph 5.3.1. Both solutions are reported for some parameters, although they are often identical.

Tables 5.3-5.4 also list whether the product is "validated," "not yet validated," "derived," "experimental," or "diagnostic." A validated product indicates that substantial comparison was made to ground-based data and that the retrieval is well characterized so that error bars can be defined and comfortably applied to the retrieval product (Ichoku et al. 2002; Chu et al. 2002; Remer et al. 2002). "Not yet validated" indicates that the retrieved parameter has not yet been well characterized, but that data are being collected and analysis is underway.

"Derived" is a parameter that follows from the retrieval's choice of aerosol model and the magnitude of the retrieved optical thickness. A derived parameter is not directly retrieved and there are no expectations of ever validating a derived

parameter with independent data. “Experimental” is a scientific product that may have future applications but, as of now, is too innovative to be well characterized. “Diagnostic” refers to output that is either an auxillary or intermediate parameter. Diagnostic parameters are meant to aid in understanding the final product, but will never themselves become validated.

In particular, the MODIS aerosol products used in this thesis and analyzed in the chapters 6 and 7 are retrieved from MOD04_L2 Scientific Data Set and are:

- over ocean: the aerosol optical thickness AOD (“Effective_Optical_Depth_Average_Ocean”), the fine fraction parameter η (“Optical_depth_ratio_small_ocean_055micron”) and the volume size distribution $\frac{dV(r)}{d\ln r}$ obtained by “Solution_index_Ocean_Large” and Solution_index_Ocean_Small” at 0.55 μm;
- over land-ocean: the aerosol optical thickness AOD (Optical _Depth_Land_And_Ocean

Table 5.3. Contents of MODIS aerosol level 2 hdf file (MOD04): Land products.

Name of product	Dimension	Status
Corrected_Optical_Depth_Land	0.47, 0.55, 0.66 μm	Validated
Optical_Depth_Ratio_Small_Land	0.55 μm	Not yet valid
Mass_Concentration_Land	2D	Derived
Ångström_Exponent_Land	0.66/0.47	Not yet valid
Reflected_Flux_Land	0.47, 0.55, 0.66 μm.	Derived
Transmitted_Flux_Land	0.47, 0.66 μm	Derived
Aerosol_Type_Land	2D	Diagnostic
Continental_Optical_Depth_Land	0.47, 0.66 μm	Diagnostic
Estimated_Uncertainty_Land	0.47, 0.66 μm	Diagnostic
Mean_Reflectance_Land_All	0.47, 0.66, 2.13 μm	Diagnostic
Standard_Deviation_Reflectance_Land_All	0.47, 0.66, 2.13 μm	Diagnostic
Cloud_Fraction_Land	2D	Diagnostic
Number_Pixels_Percentile_Land	0.47, 0.66 μm	Diagnostic
Mean_Reflectance_Land	0.47, 0.66, 0.87, 2.13, 3.75 μm	Diagnostic
STD_Reflectance_Land	0.47, 0.66, 0.87, 2.13, 3.75 μm	Diagnostic
Quality_Assurance_Land	See QA plan Diagnostic (http://modis-atmos.gsfc.nasa.gov)	
Path_Radiance_Land	0.47, 0.66 μm	Experimental
Error_Path_Radiance_Land	0.47, 0.66 μm	Diagnostic
Critical_Reflectance_Land	0.47, 0.66 μm	Experimental
Error_Critical_Reflectance_Land	0.47, 0.66 μm	Diagnostic
Quality_Weight_Path_Radiance	0.47, 0.66 μm	Experimental
Quality_Weight_Critical_Reflectance_Land	0.47, 0.66 μm	Experimental
Quality_Assurance_Crit_Ref_Land	0.47, 0.66, 0.87, 2.13, 3.75 μm	Diagnostic

Table 5.4. Contents of MODIS aerosol level 2 hdf file (MOD04): Ocean products.

Name of product	Dimension	Status
Effective_Optical_Depth_Average_Ocean	0.47, 0.55, 0.66, 0.87 1.24, 1.63, 2.13 μm	Validated
Optical_Depth_Small_Average	0.47, 0.55, 0.66, 0.87 1.24, 1.63, 2.13 μm	Not yet validated
Optical_Depth_Large_Average	0.47, 0.55, 0.66, 0.87 1.24, 1.63, 2.13 μm	Not yet validated
Effective_Radius_Ocean Best,	average	Validated
Optical_Depth_Ratio_Small_Ocean_0.86micron	Best, average	Not yet validated
Mass_Concentration_Ocean	Best, average	Derived
Cloud_Condensation_Nuclei_Ocean	Best, average	Derived
Ångström_Exponent_1_Ocean	0.55/0.87	Not yet validated
Ångström_Exponent_2_Ocean	0.87/2.13	Not yet validated
Reflected_Flux_Average_Ocean	0.47, 0.55, 0.66, 0.87 1.24, 1.63, 2.13 μm	Derived
Transmitted_Flux_Average_Ocean	0.47, 0.55, 0.66, 0.87 1.24, 1.63, 2.13 μm	Derived
Asymmetry_Factor_Average_Ocean	0.47, 0.55, 0.66, 0.87 1.24, 1.63, 2.13 μm	Derived
Backscattering_Ratio_Average_Ocean	0.47, 0.55, 0.66, 0.87 1.24, 1.63, 2.13 μm	Derived
Solution_Index_Ocean_Small	Best, average	Diagnostic
Solution_Index_Ocean_Large	Best, average	Diagnostic
Least_Squares_Error_Ocean	Best, average	Diagnostic
Optical_Depth_by_models_Ocean	Nine models	Diagnostic
Effective_Optical_Depth_Best_Ocean	0.47, 0.55, 0.66, 0.87 1.24, 1.63, 2.13 μm	Diagnostic
Optical_Depth_Small_Best	0.47, 0.55, 0.66, 0.87 1.24, 1.63, 2.13 μm	Diagnostic
Optical_Depth_Large_Best	0.47, 0.55, 0.66, 0.87 1.24, 1.63, 2.13 μm	Diagnostic
Reflected_Flux_Best_Ocean	0.47, 0.55, 0.66, 0.87 1.24, 1.63, 2.13 μm	Diagnostic
Transmitted_Flux_Best_Ocean	0.47, 0.55, 0.66, 0.87 1.24, 1.63, 2.13 μm	Diagnostic
Asymmetry_Factor_Best_Ocean	0.47, 0.55, 0.66, 0.87 1.24, 1.63, 2.13 μm	Diagnostic
Backscattering_Ratio_Best_Ocean	0.47, 0.55, 0.66, 0.87 1.24, 1.63, 2.13 μm	Diagnostic
Cloud_Fraction_Ocean	2D	Diagnostic
Number_Pixels_Used_Ocean	2D	Diagnostic
Mean_Reflectance_Ocean	0.47, 0.55, 0.66, 0.87 1.24, 1.63, 2.13 μm	Diagnostic
STD_Reflectance_Ocean	0.47, 0.55, 0.66, 0.87 1.24, 1.63, 2.13 μm	Diagnostic
Quality_Assurance	See QA plan	Diagnostic

CHAPTER 6

AERONET VERSUS MODIS AEROSOL PARAMETERS AT DIFFERENT SPATIAL RESOLUTIONS OVER SOUTH-EAST ITALY

As told in the chapter 5, the Moderate Resolution Imaging Spectroradiometer (MODIS) is a new sensor with the ability to characterize the spatial and temporal characteristics of the global aerosol field. In fact, daily global images from satellites resolve the temporal patterns resulting from the short life times of aerosols, which are on the order of a few days to a week. In particular, the Moderate Resolution Imaging Spectroradiometer (MODIS) is a new sensor with the ability to characterize the spatial and temporal characteristics of the global aerosol field.

In this chapter, aerosol parameters retrieved by AERONET sunphotometer measurements at the Physics Department of Lecce's University (40º, 20' N, 10º, 6' E), are compared to similar MODIS data retrieved at different spatial resolutions co-located in space and time. In particular, MODIS aerosol products retrieved for window sizes of 50x50, 100x100, and 300x300 km^2 centered on the AERONET monitoring site (figure 6.1), are correlated with corresponding AERONET retrievals co-located in time, to contribute to the validation of MODIS aerosol products over south-east Italy and to investigate the dependence of correlation on spatial resolution and hence to understand to what extent the Lecce's AERONET site can be considered representative of a larger area and locally-derived aerosol parameters can be of use in General Circulation and Chemical Transport Models (e.g. Kinne et al., 2003; Guibert et al., 2005). MODIS and AERONET aerosol retrievals from March 2003 to September 2004 are used for the correlation studies reported in this chapter.

A brief overview of the methodology employed for the correlation studies is reported in paragraph 6.1. Results are presented in Section 6.2 and conclusions are given in paragraph 6.3.

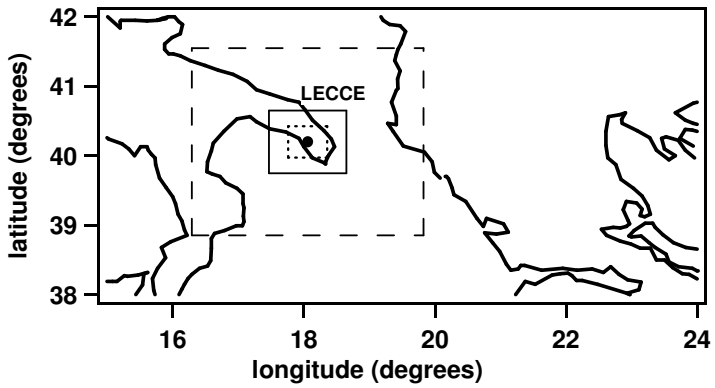

Figure 6.1. Geographic location of the AERONET monitoring site. Full dot represents Lecce's location, dotted, solid, and dashed boxes represent the 50x50, 100x100, and 300x300 km^2 window centered on the AERONET site.

6.1. Methodology and results

In this chapter we use level 2 aerosol products from MODIS onboard the EOS-Terra satellite that are operationally derived at 10-km spatial resolution. In order to take into account both spatial and temporal variability of the aerosol distribution, the MODIS retrievals at 10-km spatial resolution and the AERONET direct sun measurements at 15-minutes intervals (Holben et al., 1998) need to be co-located in space and time (Chu et al., 2002). The methodology adopted in this work to compare temporal statistics from AERONET to spatial statistics from MODIS is the same to the one described by Ichoku et al. (2002). We require that at least 2 out of the possible 5 AERONET measurements are within ± 30 min of MODIS overpasses and that at least 5 out of the possible 25 MODIS retrievals are in a square box of 50 km x 50 km centered over the AERONET site (Chu et al. 2003). Accordingly, sunphotometer retrievals between ± 60 min and ± 90 min of the satellite overpass are compared with MODIS products in a square box of 100 km x 100 km and of 300 km x 300 km (figure 6.1), respectively centered on the sunphotometer site. The mean values of the co-located spatial and temporal ensemble are then used to investigate the correlation between AERONET and MODIS aerosol

products. Aerosol optical depths and fine fraction parameters provided by MODIS at 550 nm are used for the correlation study of this paper. MODIS and AERONET wavelengths do not match exactly except at 870 nm. According to Remer et al. 2005, the interpolation of AERONET data is done on a log-log plot assuming linearity between 0.44 and 0.87 μm. The error in the interpolation varies between 0% and ~ 10% depending on the aerosol type (due to nonlinear spectral dependence), with fine-mode-dominated aerosol at high optical thickness introducing the most error, and a mixed- or coarse-dominated aerosol introducing the least (Eck et al., 1999; Ichoku et al., 2005). As told in chapter 5, in agreement with theoretical error analysis *AOD* is derived with an error of $\Delta AOD = \pm 0.03 \pm 0.05 AOD$ over ocean (Tanre' et al., 1997) and with an error of $\Delta AOD = \pm 0.05 \pm 0.15 AOD$ over land (Chu et al.1998, King et al. 1999), while the fine fraction parameter η over ocean is retrieved with accuracy of ±25%.

6.2. Results

In this section aerosol parameters retrieved by AERONET sunphotometer measurements at the Physics Department of Lecce's University (40º, 20' N, 10º, 6' E) from March 2003 to September 2004, are compared to similar MODIS data retrieved at different spatial resolutions co-located in space and time. In particular, the correlation study is made in terms of the aerosol optical depth AOD and the fine fraction parameter η at 550 nm.

6.2.1. AERONET versus MODIS –ocean AODs

The data analysis that follows uses aerosol products retrieved over oceans from MOD04_L2 Scientific Data Set: Effective_Optical_Depth_Average_Ocean

files, which can be found at the web site http//:modis-atmos.gsfc.nasa.gov/. Figures 6.2a-6.2c show the scatterplot (open dots) of the mean values of MODIS-ocean aerosol optical depths at 550 nm, AOD_M, retrieved for window sizes of (a) 50x50, (b) 100x100, and (c) 300x300 km^2 centered on the AERONET site, versus the corresponding mean values of sunphotometer aerosol optical depths, AOD_A, co-located in time. The total number of data points *N* of each plot is also given in Figures 6.2a-6.2c. MODIS standard deviations σ_M, referring to the data points of figures 6.2a-6.2c versus the corresponding sunphotometer standard deviations σ_A, are plotted on figures 6.2d-2f for window sizes of 50x50, 100x100, and 300x300 km^2, respectively.

σ_M values are representative of both the retrieval uncertainties and the spatial variability of aerosol optical depths: aerosol spatial distributions may vary significantly even within few kms. Besides retrieval uncertainties σ_A values are also representative of the temporal variability of the atmospheric aerosol distribution. We observe from figures 6.2d-6.2f that both σ_M and σ_A increase with window size. It is possible that the dependence of σ_M and σ_A on window size is mainly determined by the higher spatial and temporal variability of the aerosol distribution as averaging area and time are increased. σ_M and σ_A reach values up to ~0.05 when the window size is 50x50 km and up to ~0.2 when the window size gets 300x300 km. In addition, figures 6.2d-6.2f indicate that σ_M are on average larger than σ_A. Latter results can be due either to the larger aerosol variability with space than with time and to the larger uncertainties of AOD_M ($\Delta AOD = \pm 0.03 \pm 0.05 AOD$) with respect to the uncertainties of AOD_A values ($\pm$ 0.01).

The solid line of each plot of figures 6.2a-6.2c represents the regression line fitting the data points. Regression line parameters and correlation coefficients (R) are reported on the top of each plot. We observe that correlation coefficients vary from 0.86 to 0.83. The regression line slope decreases from 0.85 down to 0.7 as the window size area increases from 50x50 km^2 up to 300x300 km^2. While, the regression line intercept increases from 0.03 up to 0.05 as the window size area is varied from 50x50 km^2 up to 300x300 km^2.

The dashed lines of each plot of figures 6.2a-6.2c represent the MODIS "expected errors" to contain the mean and the first standard deviation (66%) of all points (i.e. $\Delta AOD = \pm 0.03 \pm 0.05 AOD$) when the ocean algorithm is used. The constant term represents the estimated error due to the surface reflectance assumption, while the second term that is proportional to AOD, represents the error due to aerosol model assumptions. The data analysis of figures 6.2a, 6.2b and 6.2c shows that 70%, 67%, and 70% of the AOD values, respectively meet the pre-specified accuracy conditions. It is worth noting that the percentage of AOD values within pre-specified accuracy conditions does not appear significantly affected by the window size.

Figure 6.2a also reveals that the regression line obtained by fitting the data points of the 50x50 km^2 window size, fits inside the expected error lines at least up to AOD_A values of about 0.6 The regression line parameters of each plot of figures 6.2a-6.2c indicate either that MODIS overestimates aerosol optical depths at low aerosol loadings and that MODIS underestimates aerosol optical depths at higher aerosol loadings. In addition, the aerosol optical depth underestimation gets more significant as the window size is increased.

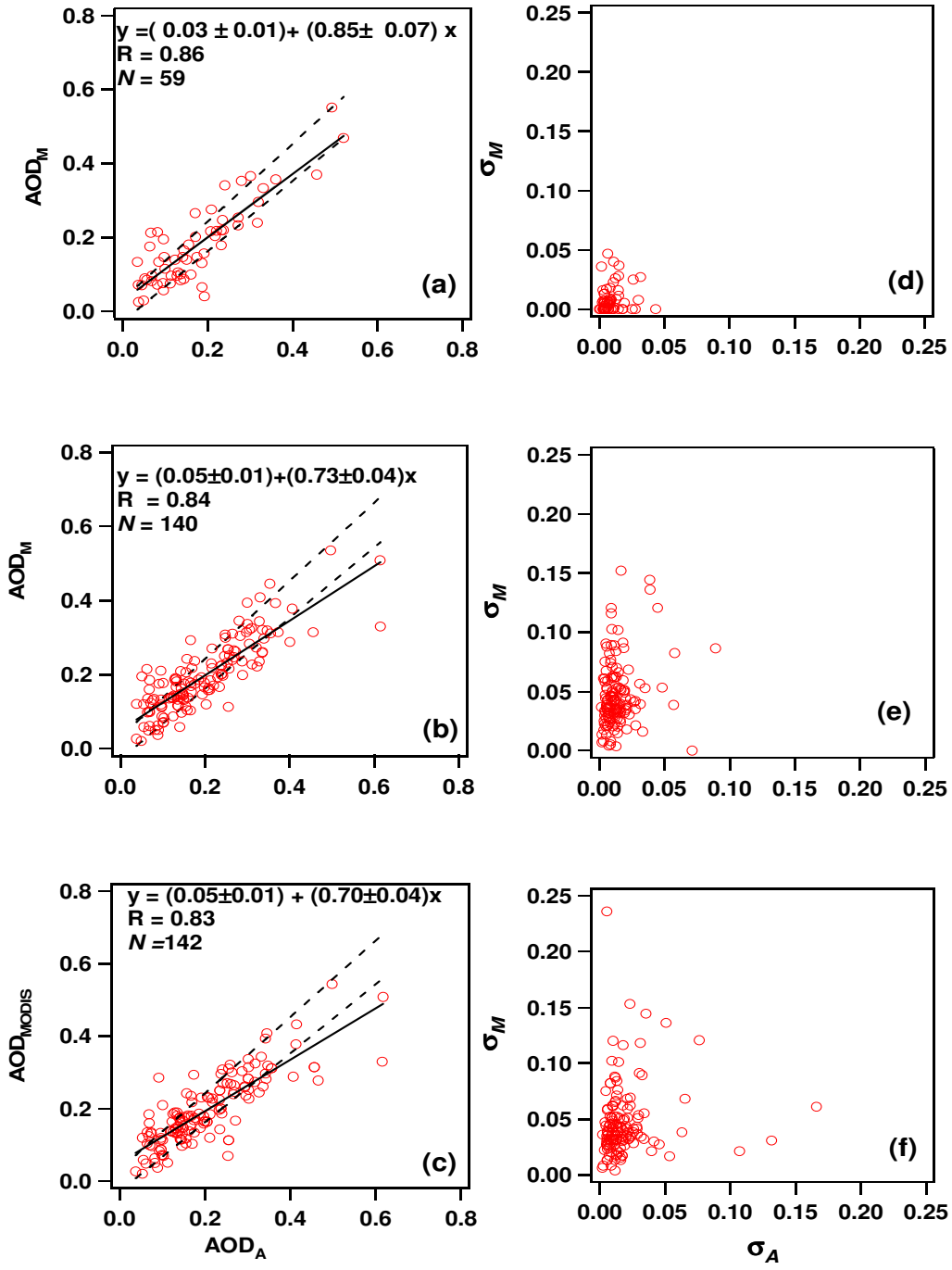

Figure 6.2. Scatter plots of MODIS-ocean AOD_M values referring to the (a) 50x50, (b) 100x100, and (c) 300x300 km^2 window size versus AOD_A mean values co-located in time; solid lines represent the regression lines fitting the data points. Regression line parameters and correlation coefficients (R) with the total number of data points N are shown on the top of each panel. Dashed lines represent on each panel MODIS pre launch expected uncertainties; (d)-(f) scatter plots of MODIS-ocean standard deviations versus corresponding AERONET standard deviations referring to the data points of a-c scatter plots, respectively

Aerosol optical depths retrieved at low aerosol loadings are expected to be more affected by the assumed surface reflectivity. While, *AOD* values retrieved at high aerosol loadings are expected to be more dependent on the aerosol model. Besides the spatial variability of the aerosol characteristics, the surface reflectivity underestimation whose effects get more significant with the increase of the averaging area and hence of *N*, can also be responsible of the intercept positive value of the regression line, which increases with the window size. While, the MODIS aerosol model assumption can be responsible of the regression line slope values that are always smaller than unity and take smaller values as the window size is increased. According to Zhao et al. (2002), a slope that is different from unity indicates that there may be some inconsistency between aerosol microphysical and optical properties used in the MODIS retrieval algorithm and those in the real situation.

The Chesapeake Lighthouse and Aircraft Measurements for Satellites (CLAMS) experiment has recently been designed in part to examine and validate MODIS retrievals over coastlines (e.g. Smith et al., 2005; Levy et al., 2005). The measurements that have been performed during July-August 2001, have revealed that the optical depths over the ocean retrieved from MODIS compared well to those measured by the sun photometers: 86% of all individual ocean retrievals at 550 nm were within the expected error lines. However, it is worth noting that the scatterplot of MODIS versus sunphotometer aerosol optical depths at 550 nm, has been fitted by a regression line with a positive intercept value (equal to 0.02) and a slope different from unity and equal to 0.92 (Levy et al., 2005). The scatterplot of 2052 MODIS aerosol optical depths at 550 nm co-located with AERONET aerosol optical depths retrieved at different stations either on the coast or on an island, has also revealed either that the MODIS ocean algorithm leads to a slight under prediction at high

optical depths (Remer et al., 2005) and that 62% of all retrievals over ocean at 550 nm were within the defined expected uncertainty. The quality of the aerosol optical depth data retrieved over ocean by MODIS from 2000 to 2003 has also been evaluated by Ichoku et al. (2005) by investigating the correlation of MODIS and AERONET data co-located in time and referring to several worldwide sites. Despite the results of Remer et al. (2005) and Levy et al (2005), the Ichoku et al. (2005) study has provided results similar to those of this paper.

Figure 6.3a shows the AOD_M frequency distribution referring to the 50x50 km^2 (solid blue line), 100x100 km^2 (dashed line), and 300x300 km^2 (red solid line) window size. Figure 6.3b shows the frequency distribution of the mean aerosol optical depths calculated by averaging sunphotometer *AOD* values retrieved between ± 30 min (solid line), ± 60 min (dashed line), and ± 90 min (red solid line) of the Terra satellite overpass.

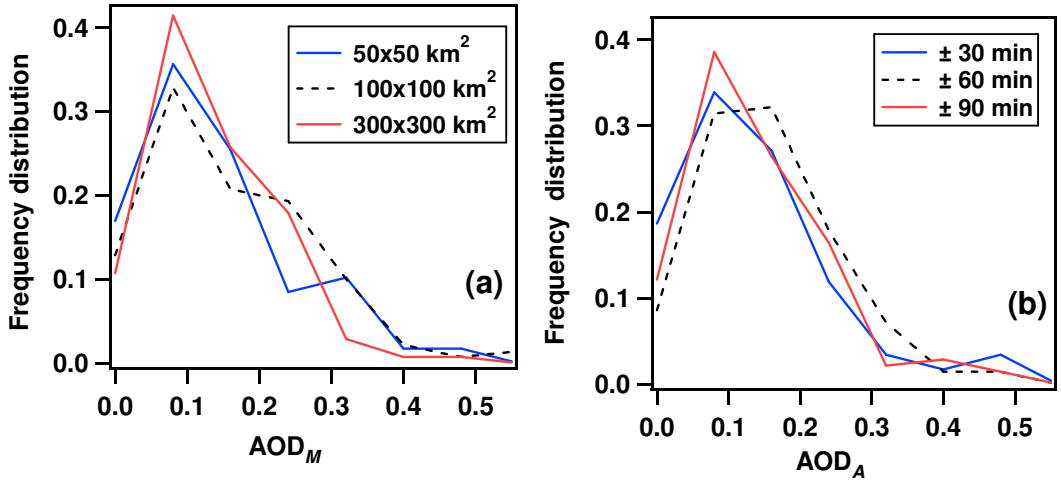

Figure 6.3. Frequency distribution of (a) MODIS-ocean AOD_M values, (b) AOD_A values co-located in time with MODIS-ocean AOD_M values.

We observe from figure 6.3a that the AOD_M frequency distribution is not significantly affected by window size and that all frequency distributions are peaked

at about 0.08. In addition, figure 6.3b reveals that the AOD_A frequency distribution is not significantly affected by the averaging time and that the plots of figure 6.3b are similar to those of figure 6.3a.

Mean optical depths $\overline{AOD_M}$ and $\overline{AOD_A}$ and corresponding standard deviations for different spatial and temporal resolutions, respectively are summarized on Table 6.1 to facilitate comparison between MODIS and AERONET data.

In order to investigate if the correlation between MODIS and AERONET aerosol optical depths is dependent on the time of the year, we have plotted in figures 6.4a-6.4c AOD_M (red dots) and co-located in time AOD_A (blue dots) values as a function the time of the year and for the (a) 50x50, (b) 100x100, and (c) 300x300 km^2 window size. Open blue and open red dots represent monthly average values of AOD_M and AOD_A, respectively.

Figures 6.4a-6.4c reveal that AOD_M closely follows the temporal evolution of AOD_A at all tested window sizes.

Table 6.1: Mean AODs and corresponding standard deviations for different spatial resolutions by MODIS and for different temporal resolutions by AERONET. $\overline{AOD_M}$ represent mean MODIS-ocean AODs and $\overline{AOD_A}$ represent corresponding mean AERONET AODs co-located in time. $\overline{AOD_M^*}$ represent mean MODIS land-ocean AODs and $\overline{AOD_A^*}$ represent corresponding mean AERONET AODs co-located in time.

Spatial resolution	$\overline{AOD_M}$	$\overline{AOD_M^*}$	$\overline{AOD_A}$	$\overline{AOD_A^*}$
50x50 km^2	0.2 ± 0.1	0.3 ± 0.1	0.2 ± 0.1	0.2 ± 0.1
100x100 km^2	0.19 ± 0.09	0.3 ± 0.1	0.2 ± 0.1	0.2 ± 0.1
300x300 km^2	0.19 ± 0.09	0.3 ± 0.1	0.2 ± 0.1	0.2 ± 0.1

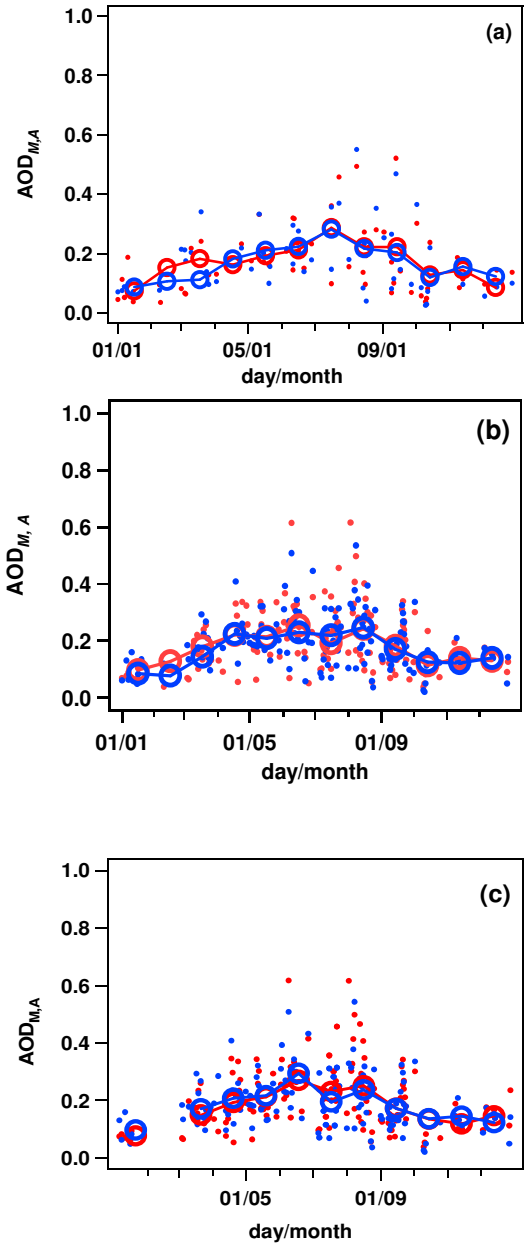

Figure 6.4. Temporal evolution of MODIS-ocean (blue dots) and AERONET (red dots) aerosol optical depths referring to the (a) 50x50, (b) 100x100, and (c) 300x300 km^2 window size, open blue and red dots represent monthly average values of MODIS-ocean and AERONET optical depths co-located in time, respectively.

Latter comment is further supported by figures 6.5a-6.55c showing the differences ΔAOD_{M-A} (grey full dots) between monthly average values of AOD_M and AOD_A. The solid black line represents $\Delta AOD_{M-A} = 0$, while dotted lines

represent MODIS "expected errors". Figures 6.5a-6.5c show that most of the ΔAOD_{M-A} values fit inside the expected error lines at all tested window sizes.

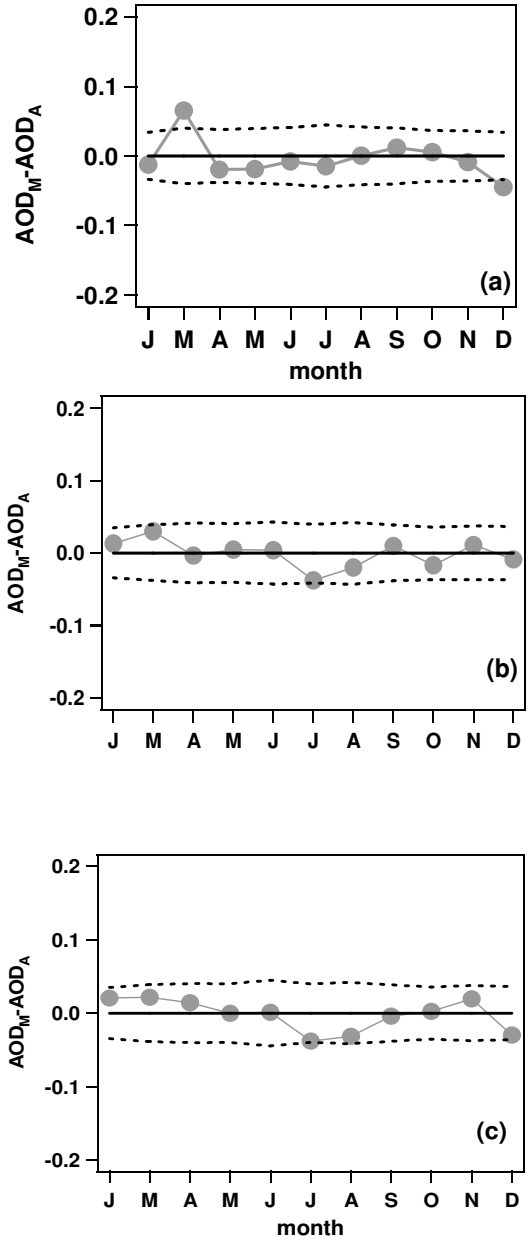

Figure 6.5. Differences between monthly average values of MODIS–ocean and AERONET aerosol optical depths (grey full dots) at (a) 50x50, (b) 100x100, and (c) 300x300 km^2 window size. On each panel dotted lines represent MODIS expected errors uncertainties.

Grey full dots above or below the solid black line, represent MODIS overestimation or underestimation, respectively with respect to AERONET values. Latter results indicate that over south-east Italy, the differences ΔAOD_{M-A} are not significantly affected by the time of the year at all tested window sizes.

In conclusion, the results of this section at first show that the correlation of MODIS and AERONET aerosol optical depths is weakly affected by window size: 70%, 67%, and 70% of *AOD* values retrieved at 50x50 km^2, 100x100 km^2, and 300x300 km^2 window sizes, respectively meet pre-specified accuracy conditions. In addition, aerosol optical depth frequency distributions (figure 6.3a) and temporal evolutions (figures 6.4a-6.4c) do not appear significantly affected by the window size.

As a consequence, we believe that the AERONET aerosol optical depths retrieved at Lecce can be considered representative of an area of at least 300x300 km^2: the sunphotometer continues to describe the evolution of regional aerosol characteristics, but it begins to lose predictive capabilities since slopes and intercepts get worse as the window size is increased.

It is possible that the dependence on window size of intercept and slope values (figures 6.2a-6.2c) is weakly determined by the larger spatial and temporal variability of aerosol properties with window size and that it is mostly due to the MODIS surface reflectance underestimation and to some inconsistency of the MODIS ocean-algorithm: last two effects are also expected to increase with window size and hence with the number of data point increase.

We believe that the data reported by Levy et al. (2005), Remer et al. (2005), and Ichouku et al. (2005) can demonstrate that the ground surface reflectance and the aerosol properties of the sites chosen for the correlation study affect intercept and

slope values of the regression lines fitting the scatterplots of sunphotometer and MODIS aerosol optical depths.

6.2.2. *AERONET and MODIS land-ocean AODs*

Considering the peculiar location of the Lecce's University AERONET site that is on a narrow peninsula of south-east Italy (figure 6.1), we consider rather meaningful in this section to investigate the correlation of AERONET and MODIS land-ocean aerosol optical depths (MOD04_L2 Scientific Data Set: Optical_Depth_Land_And_Ocean) co-located in time and space. Figures 6.6a-6.6c show the scatterplot (open dots) of the mean values of MODIS land-ocean aerosol optical depths AOD_M^* retrieved for window sizes of (a) 50x50, (b) 100x100, and (c) 300x300 km^2 centered on the AERONET site, versus the mean values of corresponding sunphotometer aerosol optical depths AOD_A^* co-located in time. Solid lines represent regression lines fitting the data points while dashed lines represent pre-launch expected uncertainties over land that are given by the relationship $\Delta AOD = \pm 0.05 \pm 0.15 AOD$ (Chu et al.1998, King et al. 1999). It is worth noting that there are no quantified expected uncertainties for land-ocean aerosol optical depths. Scatterplots of standard deviations of land-ocean data points σ_M^* versus corresponding σ_A^* values are plotted on figures 6.6d-6.6f.

The comparison of figures 6.2a-6.2c and figures 6.6a-6.6c at first reveals that the data point dispersion is larger on figures 6.6a-6.6c. In addition, figures 6.6d-6.6f reveal a small trend of σ_M^* to increase with window size and that that the σ_M^* variability range is nearly twice larger than that of $\sigma_A^* : \sigma_M^*$ values up about 0.25 are retrieved at 50x50 km^2 and at 300x300 km^2 window size. Besides the larger

uncertainties of aerosol optical depths retrieved over land, the larger surface heterogeneity can be responsible of latter results: the land-ocean retrievals are not required to meet at the shoreline, and may be discontinuous. Correlation coefficients of the plots of figures 6.6a-6.6c vary from 0.88 to 0.84 as the window size is increased from 50 x 50 km^2 to 300x300 km^2 and the percentage of data points within expected uncertainties is 85%, 88%, and 82% for the 50x50 km^2, 100x100 km^2, and 300x300 km^2 window size, respectively.

As the window size increases the proportion of land and ocean contribution varies and this may also account for latter results.

In accordance to the results of figures 6.2a-6.2c, regression line parameters of figures 6.6a-6.6c also indicate that MODIS overestimates and underestimates aerosol optical depths at low and high aerosol loadings, respectively and that both effects get more significant as the window size is increased.

However, regression line slopes values of figures 6.6a-6.6c are closer to unity than those of figures 6.2a-6.2c and this result may indicate that the MODIS-land-ocean aerosol optical depths are best suited to represent the aerosol properties over south-east Italy.

On the contrary the higher intercept values of the regression lines of figures 6.6a-6.6c with respect to those of figures 6.2a-6.2c, likely indicate that the ground reflectivity underestimation is larger for the MODIS-land retrieval algorithm over south-east Italy. Intercept values of figures 6.6a-6.6c are also greater than expected offset of 0.05 for all tested window sizes.

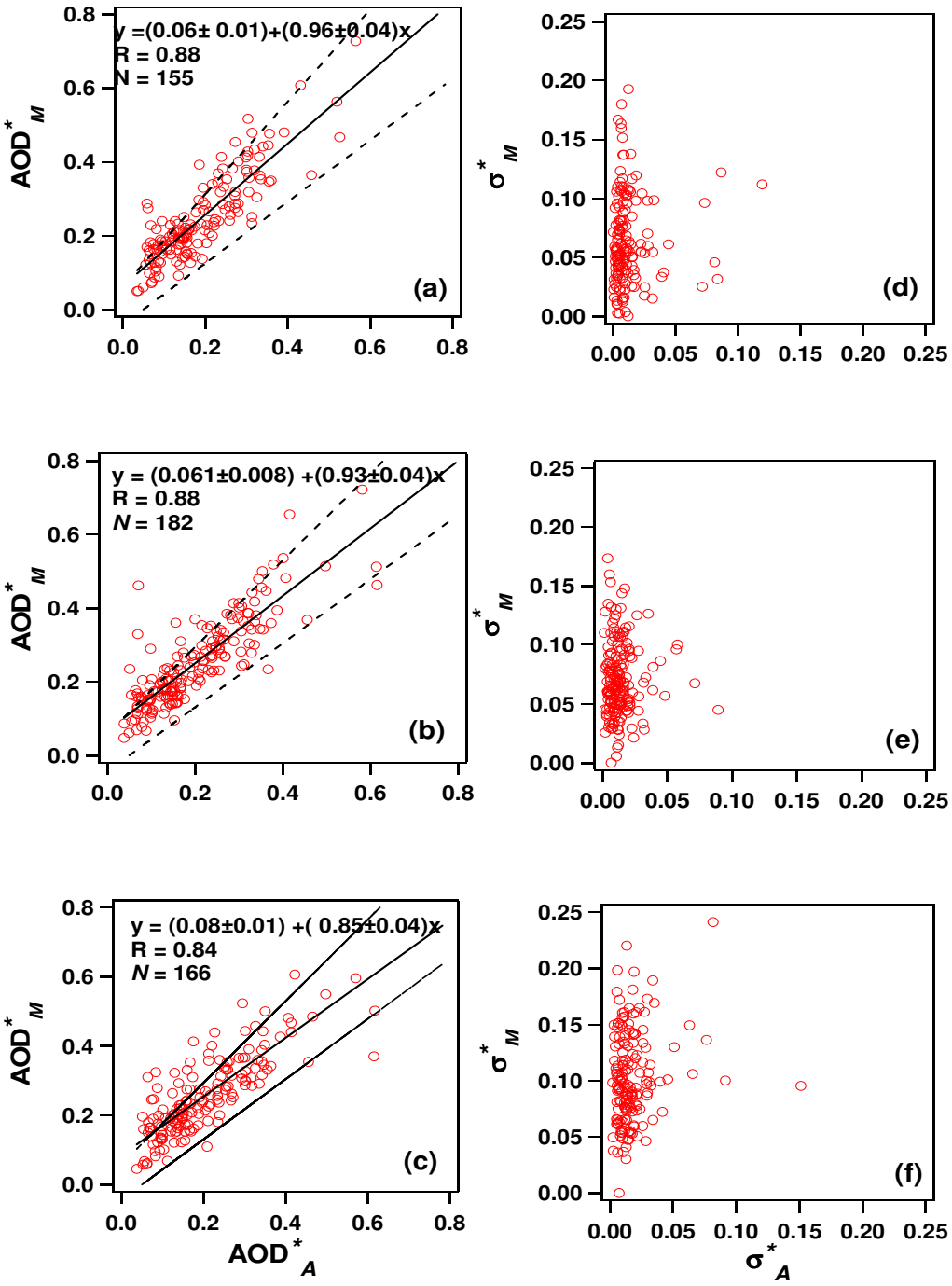

Figure 6.6. Scatter plots of MODIS-land-ocean values referring to the (a) 50x50, (b) 100x100, and (c) 300x300 km^2 window size versus AOD_A^* mean values co-located in time. (d)-(f) scatter plots of MODIS-land-ocean standard deviations versus corresponding AERONET standard deviations referring to the data points of a-c scatter plots, respectively

Figures 6.7a-6.7c showing AOD_M^* (blue dots) and AOD_A^* (red dots) and the corresponding monthly means (open dots) as a function the time of the year reveal that AOD_M^* closely follows the temporal evolution of AOD_A^* at all tested window sizes, but AOD_M^* monthly means are larger than AOD_A^* during all the year of almost a constant amount.

Latter comment is further supported by figures 6.8a-6.8c showing the differences ΔAOD^*_{M-A} (grey full dots) between monthly average values of AOD_M^* and AOD_A^* corresponding values.

The solid black line represents $\Delta AOD^*_{M-A} = 0$, while dotted lines represent MODIS "expected errors". ΔAOD^*_{M-A} values mostly fit inside expected error lines at all tested window sizes, but they are almost above solid black lines since MODIS overestimate aerosol optical depths with respect to AERONET values.

The land validation study of Remer et al. (2005) also reveals that the plot of 5906 MODIS aerosol optical depths at 550 nm co-located with AERONET measurements at different sites, shows a positive offset of 0.068 that is larger than expected.

In addition, the correlation study reported by Ichouku et al. (2005) shows that over land and at 550 nm, the scatterplot of level-1.5-AERONET data and Terra-MODIS aerosol optical depths (T004), is fitted by a regression line with 0.72 slope value, 0.128 intercept value, and 0.68 linear correlation coefficient and that only 53.5% of 9740 data points were within expected error bounds.

The correlation at 550 nm of MODIS versus sunphotometer aerosol optical depths over land during CLAMS (Levy et al., 2005) is disappointing: the regression line intercept and slope are equal to 0.21 and 0.64, respectively and the correlation coefficient takes the value of 0.36. The land algorithm deduces ground reflectivity from the radiance measured at 2.13 μm.

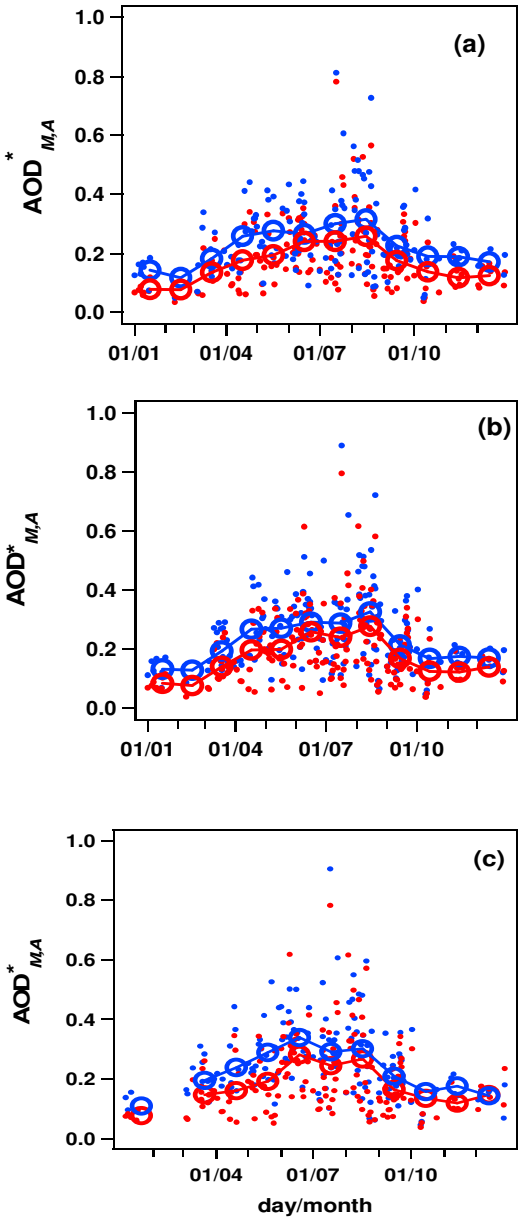

Figure 6.7. Temporal evolution of MODIS-land-ocean (blue dots) and AERONET (red dots) aerosol optical depths referring to the (a) 50x50, (b) 100x100, and (c) 300x300 km^2 window size, open blue and red dots represent monthly average values of MODIS-land-ocean and AERONET optical depths co-located in time, respectively.

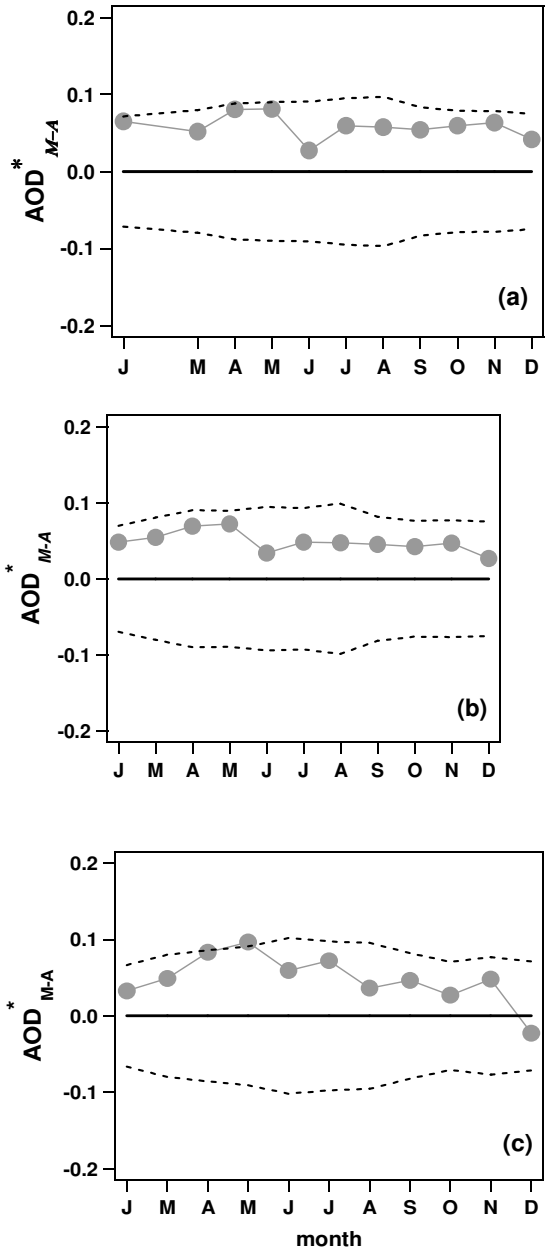

Figure 6.8. Differences between monthly average values of MODIS-land-ocean and AERONET aerosol optical depths at (a) 50x50, (b) 100x100, and (c) 300x300 km^2 window size. On each panel dotted lines represent MODIS expected errors uncertainties.

Both measurements (Kaufman and Remer 1994; Kaufman et al. 1997a) and theoretical studies (Kaufman et al. 2002) have demonstrated that for certain vegetated surfaces throughout the globe, the surface reflectance at 0.47 μm and 0.66

μm can be derived from the mean radiance at 2.13 μm by empirical relationships. However, it has also been shown that these relationships do not hold for specific regions and it is possible that they are responsible of the positive bias revealed either by the scatterplots of figures 6.6a-6.6c and observed worldwide (Remer et al., 2005; Levy et al., 2005, Ichouku et al. 2005).

Finally, figures 6.9a and 6.9b that show the AOD_M^* and AOD_A^* frequency distribution, respectively reveal that the AOD_M^* and AOD_A^* frequency distributions are not significantly affected by the window size.

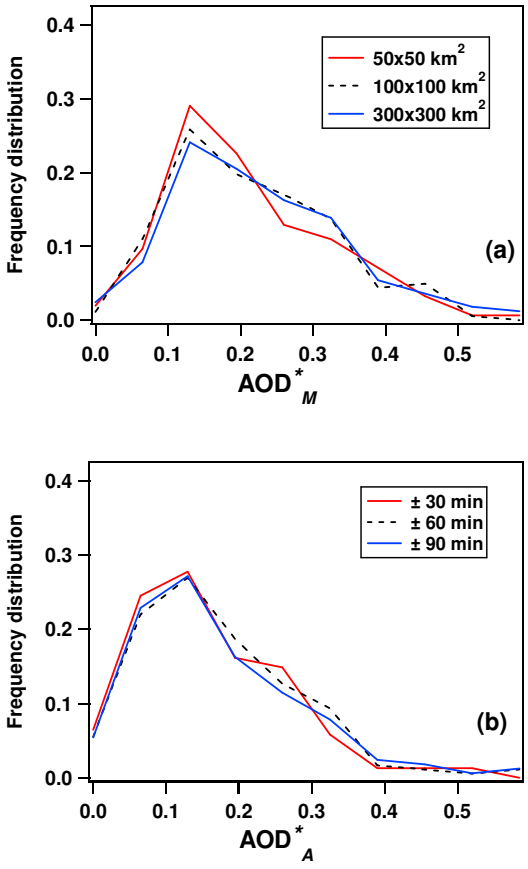

Figure 6.9. Frequency distribution of (a) MODIS-land-ocean AOD_M^* values, (b) AOD_A^* values co-located in time with MODIS-land-ocean AOD_M^* values.

In accordance to the comments of the previous paragraph, the results of this section also show that the AERONET aerosol optical depths retrieved at Lecce can be considered representative of an area of at least 300x300 km^2.

Table 6.1 provides mean optical depths $\overline{AOD_M^*}$ and $\overline{AOD_A^*}$ and corresponding standard deviations for different spatial and temporal resolutions, respectively.

6.2.3. *AERONET and MODIS-ocean fine fraction parameters*

According to Tanre' et al. (1997), Levy et al. (2003), and Remer et al. (2005), the six reflectances measured from MODIS in the 0.55- 2.13 μm spectral range and used in the ocean retrieval, upon finding best fits to modeled reflectances, allow getting the total optical depth at one wavelength and the fine fraction parameter η_M at that wavelength. As we told, η_M represents the ratio between fine mode and total optical thickness.

Figures 6.10a-6.10b show versus the time of the year the available η_M values at 550 nm (red dots) from March 2003 to September 2004 (MOD04_L2 Scientific Data Set: Optical_depth_ratio_small_ocean_055 micron) for the 50 km x 50 km and the 300 km x 300 km window size centered on the AERONET site, respectively. For comparison figure 6.10c provides η_A versus the time of the year. η_A is the ratio between fine mode and total optical thickness at 550 nm (red dots) retrieved from March 2003 to September 2004 AERONET measurements. The AERONET inversion algorithm allows retrieving aerosol volume distributions and all particles with the radius smaller than 0.6 μm are considered fine, while those with the radius larger than 0.6 μm are considered coarse. Therefore, the AERONET fine mode optical thickness represents the aerosol optical depth due to particles with the radius smaller than 0.6 μm. Hence, η_M and η_A do not represent the same aerosol parameter,

but they are comparable parameters and we believed that is more meaningful to compare the temporal evolution of both parameters instead of plotting simultaneous data in a scatterplot. In addition, Remer et al. (2005) have shown that rather few simultaneous η_M and η_A data can be available if one or two years of AERONET and MODIS aerosol products are used for comparison. η_A is retrieved from sky radiance measurements that are taken less often than direct sun measurements in the AERONET protocol (Dubovik et al. 2000a). The monthly distribution of data points *n* (grey lines) is also shown on each plot of figure 6.10. Black full dots and error bars represent in figure 6.10 monthly average values of the fine fraction optical parameter and corresponding standard deviations: the latter indicate the fine fraction parameter variability range.

The fine fraction contribution to the total optical thickness is an important parameter to assess the climate impact of anthropogenic aerosols (Kaufmann et al., 2002): it helps us to discriminate natural aerosols (largely, mechanically-generated dust and sea salt) from anthropogenic ones (largely, combustion-generated sulfates, organics, and black carbon). The comparison of figure 6.10a and 6.10b at first reveals that the η_M temporal evolution is not affected by the window size: monthly average values of the 50 km x 50 km window size are rather similar to those of the 300 km x 300 km window size. In addition, one can observe that η_M takes values in the 0.7-0.8 and 0.4-0.6 range from April to September and from October to March, respectively. On the contrary, η_A monthly means (figure 6.10c) span the 0.7-0.8 range during all year and are not significantly affected by seasons.

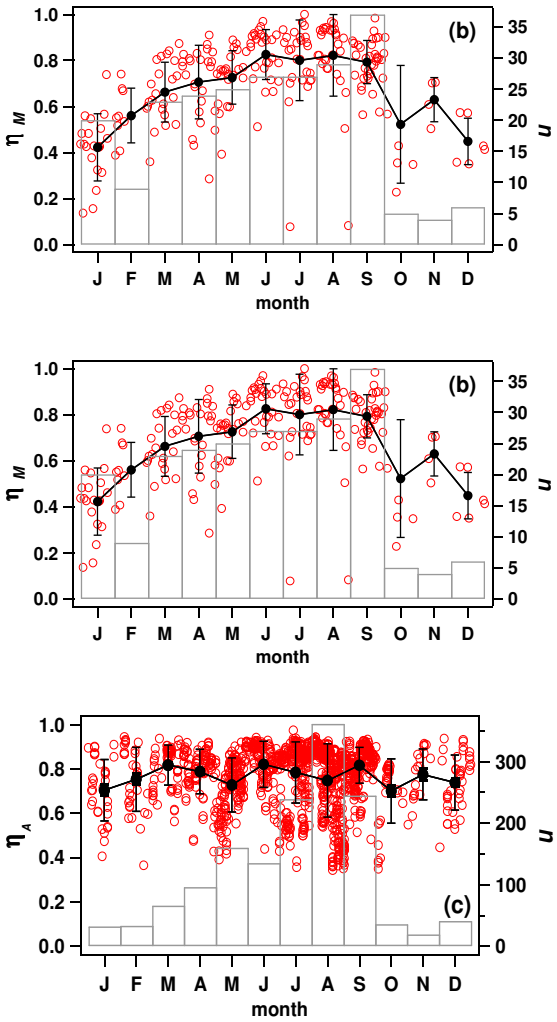

Figure 6.10. Temporal plot (red dots) of MODIS-ocean η_M values referring to the (a) 50x50 km^2 and (b) 300x300 km^2 window size, (c) temporal plot (red dots) of the AERONET fine fraction parameter. Black full dots and error bars represent monthly average values and corresponding standard deviations. Grey boxes show on each panel the monthly distribution of data points.

Perrone et al.(2005) allow understanding the η_A temporal evolution. In figure 9 of that paper is given the temporal plot of the ratio between fine and coarse number of particles per cross section of the atmospheric column (N_f/N_c). The plot shows that the N_f/N_c ratio is characterized by a marked seasonal evolution: fine particles dominate during the year and mainly on spring-summer: N_f/N_c monthly means reach values larger than ~ $3x10^3$ from June to September. Therefore, if the aerosol optical

depth due to fine mode particles is significantly larger than that due to coarse mode particles, η_A that is defined as the ratio between the fine particle aerosol optical depth and the total (fine + coarse particles) optical depth, is expected to not be significantly affected by season.

The differences $\Delta\eta_{M-A}$ between η_M and η_A monthly means for the 50x50 and 300x300 km window size are shown on figures 6.11a and 6.11b, respectively. Dashed lines are the pre launch estimated uncertainties: ±30% (Remer et al., 2005). Figure 6.11 reveals that spring-summer $|\Delta\eta_{M-A}|$ values are within pre launch estimated uncertainties and are lower than 14%, from April to September. On the contrary, $|\Delta\eta_{M-A}|$ takes values larger than pre launch estimated uncertainties on winter months. These differences may either be physically real and caused by problems comparing temporal data with spatial data or may merely be an artifact of problems associated with the MODIS retrieval algorithm as it is explained below.

The data point distribution of figures 6.10a and 6.10b show that η_M monthly values of autumn-winter months are determined by averaging rather few data points, mainly in November and December. In addition, aerosol optical depths are smaller on autumn-winter months (figure 6.4) and according to Remer et al (2005), at low aerosol optical depths, because of less signal, there is greater susceptibility to all algorithmic and sensor uncertainties. In accordance to the above discussion, it is possible to assume that the autumn-winter η_M values are affected by larger uncertainties and in particular that the MODIS-ocean algorithm underestimates the fine fraction contribution on autumn-winter. However, the autumn-winter regional variation of the aerosol properties may also be responsible of latter results. It could be possible that especially on winter, when the wide spread of regional haze is probably not developed, the aerosol load over the sea seen by MODIS is more

affected by oceanic aerosols than the aerosol load on land monitored by AERONET, being the latter probably more affected by local land sources.(De Tomasi et al, 2006).

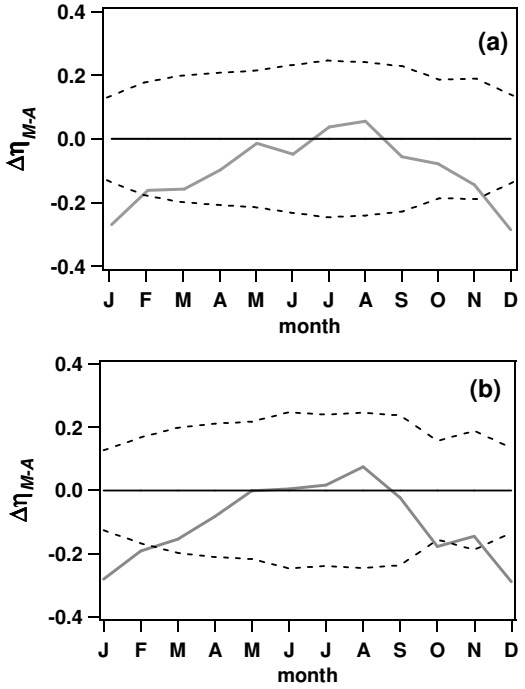

Figure 6.11 Differences between η_M and η_A monthly means $\Delta\eta_{M-A}$ at (a) 50x50 and (b) 300x300 km^2 window size as a function of the time of the year. On each panel solid black lines represent $\Delta\eta_{M-A} = 0$, while dashed lines are the pre launch estimated uncertainties: ± 30 %.

Remer et al. (2005) have recently reported comparisons of monthly means of MODIS- and AERONET-derived fine fraction values for different worldwide sites. They show that for some sites, such as GSFC, Anmyon, and Male, η_A and η_M agree to within 20% for much of the year. For Bermuda, Midway Island, and Lanai, the agreement is sustained for the first six months of the year until η_M drops down to much lower values. Latter results have been ascribed by Remer et al. (2005) to the larger uncertainties of aerosol size parameters retrieved at low aerosol loads.

However, it is worth noting from the data reported by Remer et al. (2005) that $|\Delta\eta_{M-A}|$ takes values much larger than the expected accuracy at the sites where the temporal evolution of η_A is not significantly affected by seasons, like Bermuda, Midway Island, Lanai and Rome-Tor-Vergata.

6.3. Conclusions

Aerosol parameters retrieved by AERONET sunphotometer measurements at the Physics Department of Lecce's University from March 2003 to September 2004, are compared in this chapter to corresponding MODIS data retrieved at different spatial resolutions co-located in space and time, to contribute to the validation of MODIS aerosol products over south-east Italy, to investigate the correlation dependence on spatial resolution, and to identify regional biases of Lecce's AERONET data. Despite most of the studies on the validation of MODIS retrievals, the results of this thesis refer to a single site on south-east Italy where different aerosol types may converge during the year and many aerosol types can superimpose mainly in summer as a consequence of weather stability (Perrone et al., 2005). Then, the area can be well suited to test the performance of MODIS retrieval algorithms. Averaged values of ocean- and land-ocean-MODIS aerosol optical depths retrieved at 550 nm for window sizes of 50x50, 100x100, and 300x300 km^2 centered on Lecce, have been correlated to AERONET aerosol optical depths co-located in time. We have observed that correlation factors of linear regressions span the 0.88-0.83 range and weakly tend to reduce with the window size increase. In addition, MODIS aerosol optical depths meet expected uncertainties. 70%, 67%, and 70% of AOD_M values of the 50x50 km^2, 100x100 km^2, and 300x300 km^2 window size, respectively

is within expected uncertainties. While, 85%, 88%, and 82% of AOD_M^* values retrieved at 50x50 km^2, 100x100 km^2, and 300x300 km^2 window size, respectively meets pre-specified accuracy conditions. In addition, we have observed that frequency distributions and temporal evolutions of ocean and land-ocean mean aerosol optical depths are not dependent on window size. All these results can allow inferring that AERONET aerosol optical depths retrieved at Lecce can be considered representative at least of a 300x300 km^2 area centered on Lecce and hence that locally-derived aerosol parameters can be of use in General Circulation and Chemical Transport Models based on spatial resolutions of few hundred kms. This represents one of the main issues of the chapter and it can be mainly due to the geographical location of Lecce's AERONET site that is on a flat area away from large sources of local pollution.

We have also found that slopes and intercepts of the linear regressions fitting the aerosol optical depth scatterplots are dependent on MODIS retrieval algorithm and window size. But regression lines fitting ocean- and land-ocean-MODIS optical depths values are all characterized by a positive intercept value, which weakly increases with window size and by a slope value smaller than unity that decreases as the window size increases. As a consequence, we have observed that MODIS overestimates *AOD* at low aerosol loadings and it is possible that this result is due to the fact that both the MODIS-ocean and mainly the MODIS-land algorithm underestimate the ground surface reflectance. Similar results have been reported in several papers. We have also found that the slopes of the regression lines fitting the scatterplots with ocean- and land-ocean-MODIS aerosol optical depths vary within the 0.85-0.70 and 0.95-0.85 range, respectively. As it has been told MODIS aerosol model assumptions are considered responsible of regression line slope values

different from unity. Then, being the slopes of the regression lines fitting the scatterplots with land-ocean-MODIS aerosol optical depths closer to unity, the results can indicate that the land-ocean-MODIS aerosol optical depths better represent the aerosol properties over south-east Italy.

Finally, it is shown that the monthly evolution of MODIS and AERONET aerosol optical depths is rather similar and it is characterized by a significant seasonal dependence. The temporal evolution of the MODIS fine fraction parameter η_M and of AERONET η_A values has instead revealed that η_M monthly means depend on seasons and take values in the 0.7-0.8 and 0.4-0.6 range in spring-summer and autumn-winter, respectively. On the contrary, η_A monthly means span the 0.7-0.8 range during all year. It has been shown that it is possible that the marked seasonal evolution of η_M is due either to the autumn-winter regional variation of the aerosol properties and to the MODIS-ocean algorithm that underestimates the fine fraction contribution on autumn-winter months because of the lower aerosol loads and hence the less signal and greater susceptibility to all algorithmic and sensor uncertainties .

In conclusion, we believe that the results found in this chapter can contribute to the validation of MODIS aerosol retrievals over coastal sites of south-east Italy and hence of the eastern Mediterranean sea.

CHAPTER 7

MODIS AND AERONET RETRIEVALS DURING DUST OUTBREAKS OVER THE MEDITERRANEAN

Mineral dust play an important role in climate forcing by altering the radiation balance in the atmosphere trough the scattering and absorption of radiation (Sokolik et al., 2001) and by affecting cloud nucleation and cloud optical properties (Wurzler et al., 2000). On a global scale, the dominant sources of mineral dust are all located in the Northern Hemisphere, mainly in North Africa, the Middle East, central Asia, and the Indian subcontinent (Prospero et al., 2002). North-west Africa is the most important source of mineral aerosols over the Mediterranean basin and very large quantities of African dust (60-200 x 10^8 tons yr^{-1}) are carried into the Mediterranean basin every year (Prospero and Carlson, 1972; Jaenicke and Schutz, 1978). Large-scale atmospheric circulation spreads Saharan dust particles both across the Mediterranean (e.g. De Tomasi et al., 2003), Northern Europe (Ansmann et al., 2003), and the Atlantic (Husar et al., 1997).

One of the main objectives of this chapter is to contribute to the validation of MODIS retrievals by comparing MODIS-ocean aerosol products and corresponding AERONET data retrieved during Sahara dust outbreaks over the Mediterranean. The validation of aerosol optical depths (AODs) is well advanced for all major aerosol types but, fewer studies have been performed to validate MODIS fine-mode fractions, η_M. MODIS and AERONET products retrieved at Lecce, Lampedusa, Oristano and Etna during Sahara dust outbreaks occurred from 2003 to 2005, are analyzed in this chapter. The methodology adopted in this work to compare temporal statistics from AERONET with spatial statistics from MODIS, is the same to the one described by Ichoku et al (2002) and reported in paragraph 6.1.

Aerosol optical depths, fine-mode fractions, and volume size distributions are the main parameters of the correlation study of this chapter. In particular, we use level 1.5 AERONET data from version 1 (V1) algorithm, which are cloud screened

(Smirnov et al., 2000) and on the average provide aerosol optical depths at 15-minutes intervals. In addition, AERONET products by the spheroidal model are generally used to characterize dust events (Dubovik et al., 2002b and 2006). However, in this study we used AERONET retrievals by the spherical model, because of the lack of a spheroidal MODIS-ocean inversion algorithm and hence to properly investigate the correlation of AERONET and corresponding MODIS products (Chu et al., 2005).

AERONET data from Lecce, Lampedusa, Oristano and Etna only are analyzed here, because these sites are expected to be less affected by aerosols of local origin, due to their location. In addition, MODIS-ocean aerosol products only are considered, being less affected by surface reflectance values, because of the minimum spatial variability of the ocean surface reflectance (Tripathi et al., 2005).

A brief description of the studied area is provided in Section 7.1. The 19 July, 2005 dust event monitored over Lecce and Lampedusa is analyzed in Section 7.2. Correlation studies of AERONET and MODIS data are presented and discussed in Section 7.3. Summary and conclusion are in Section 7.4.

7.1 Location of the selected Mediterranean AERONET sites

The Mediterranean Sea, the largest enclosed basin of the Earth, is a region characterized by a great variety of different aerosol types. Due to its location, this area is affected by desert dust originated from the Sahara desert and from arid regions in the Iberian Peninsula. This peculiarity makes the Mediterranean rather suitable for monitoring desert type aerosols advected from African deserts.

Figure 7.1 shows the geographical location of the four Mediterranean AERONET sites selected for this study: Oristano, Lampedusa, Etna and Lecce.

Oristano is on the west coast of Sardinia, at about 400 km north from the African coasts. The sunphotometer is located on the roof of the building of the International Marine Center (IMC, 39.91 °N, 8.5 ºE, 10 m asl). Lampedusa is a small Italian island located in the middle of the Sicilian Channel, about 130 km east of the coast of Tunisia. The sunphotometer is located in the area of the Military base LORAM (35.52 ºN, 12.63 °E, 45 m asl). The Etna AERONET site is located in Nicolosi (37.61 ºN, 15.02°E, 736 m asl), a small village on the southern flank of Mt. Etna, 400 km far from the African coasts. The sunphotometer is situated on the roof of the building of the Italian Institute of Geophysics and Vulcanology (INGV). As told in chapter 1, Lecce's sunphotomer is located on the roof of the Physics Department of Salento University (40.33º n, 18.10° E, 27 m asl) that is on the suburb of Lecce, about 900 km away from the North African coast (Tafuro et al., 2006). We have used in this study only AERONET data from the above mentioned sites since they appear more suitable to characterize aerosol properties during dust outbreaks from Sahara, with respect to other Mediterranean AERONET sites such as Rome, Ispra, and Venice that we believe are more affected by local anthropogenic pollution considering their proximity to a large city and/or a large industrial area.

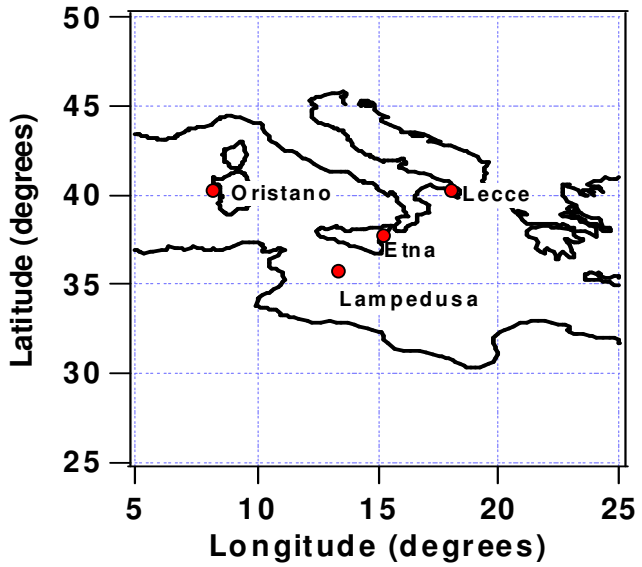

Figure 7.1. Selected AERONET sites

7.2. Case study: dust event of 19 July, 2005

In this section, we analyze in detail as an example, AERONET and MODIS products retrieved during the dust outbreak occurred on 19 July, 2005 over the Mediterranean. Data from Lecce and Lampedusa only are available for this case study.

7.2.1 *Satellite images and analytical backtrajectories of July 19, 2005*

In order to provide an overview of the Saharan dust outbreak occurred over the Mediterranean on July 19, 2005, Figure 7.2 shows the true colour image provided at 09:30 UTC by the MODIS Sensor (http://modis-atmos.gsfc.nasa.gov./) on board the NASA EOS Terra spacecraft. Figure 7.2 shows that the dust plume from North-west Africa mainly affects Lampedusa. Besides MODIS images, analytical backtrajectories also support the advection of African dust particles over the Mediterranean on July 19, 2005. The 7-day analytical backtrajectories are provided by NASA GSFC (http://www.aeronet.gsfc.nasa.gov/) for two arrival times (00:00 UTC and 12:00 UTC) and for four distinct arrival height levels (950, 850, 700, and

500 hPa). Figures 7.3a and 7.3b show that air masses mainly from north-west Africa were advected over Lecce and Lampedusa on July 19, 2005 at 12:00 UTC. The pressure level change as a function of time of each back trajectory is shown in figures 7.3c and 7.3d for Lecce and Lampedusa, respectively. It is worth noting from figure 7.3c that the air masses reaching Lecce at 500 and 700 hPa were at altitudes even lower than 950 hPa over north-west Africa. On the other side, the air masses reaching Lampedusa at 850 and 950 hPa were over north-west Africa at altitudes even lower than 950 hPa.

Figure 7.2. True-color image provided by the MODIS Sensor (http://modis-atmos.gsfc.nasa.gov./) on board the NASA EOS Terra Spacecraft on 19 July 2005 at 09:30 UTC.

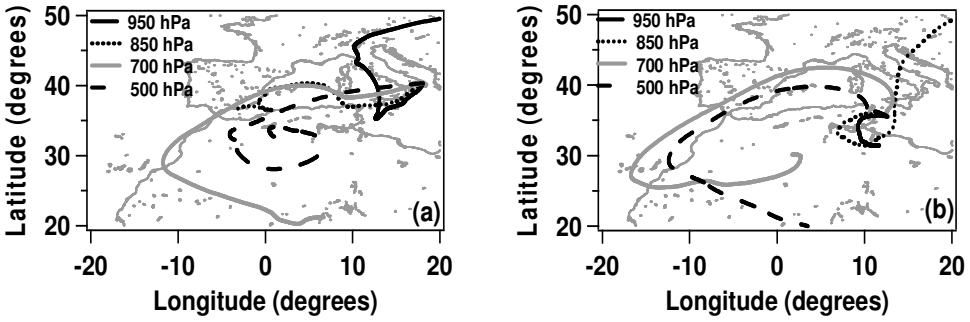

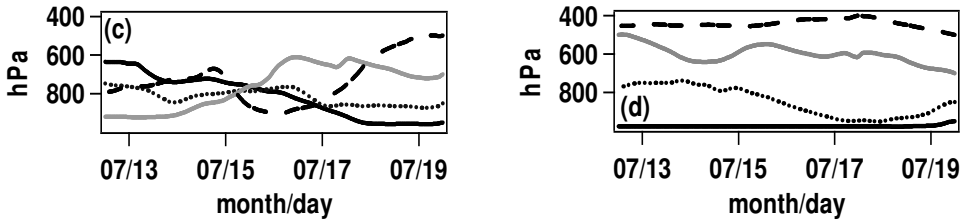

Figure 7.3. 7-day analytical backtrajectories (for the 12:00 UTC arrival time) of July 19 , 2005 over (a) Lecce and (b) Lampedusa. Pressure level change as a function of time of each backtrajectory at (c) Lecce and (d) Lampedusa.

7.2.2 *AERONET and MODIS-ocean aerosol retrievals on July 19, 2005*

In order to have a global view of the aerosol load over the Mediterranean on July 19, three MODIS-ocean AOD_M maps at 550 nm are at first shown in Figure 7.4. The maps are relative to different day-hours: a) 09:30 UTC (Terra satellite), b) 11:10 UTC (Aqua satellite) and c) 12:45 UTC (Aqua satellite). We can observe that at 09:30 UTC (figure 7.4a) MODIS AODs are of about 0.2 both over Lecce and Lampedusa. Later on, when the dust event become stronger (figures 7.4b and 7.4c), AODs reach values of about 0.5 - 0.6 over Lecce and Lampedusa.

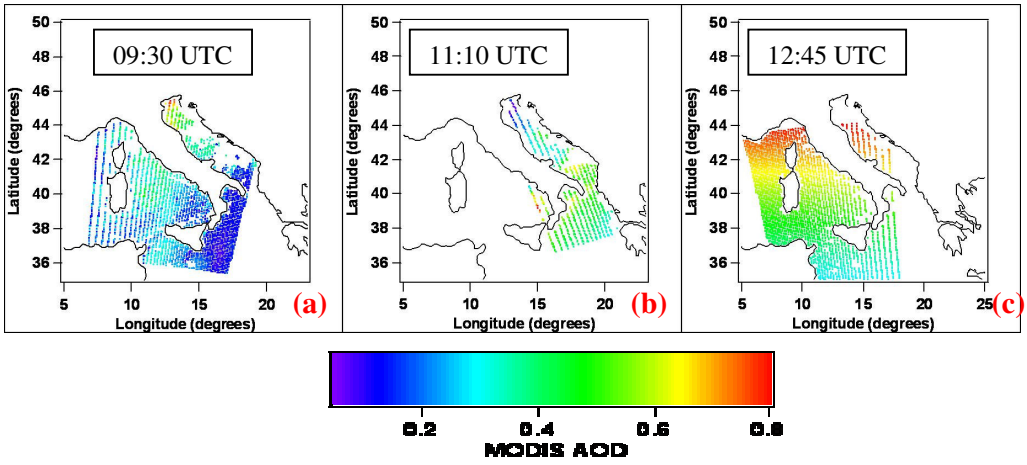

Figure 7.4. Aerosol's map outcome from MODIS AODs data of 19 July, 2005 at (a) 09:30 UTC (MODIS –Terra), (b)11:10 UTC (MODIS-Aqua) and (c)12:45 UTC (MODIS-Aqua).

7.2.2a. Analysis of the aerosol products over Lecce

To better highlight the intrusion of dust particles on July 19, the temporal evolution of the AERONET AOD at 550 nm (AOD_A) retrieved from July 18 to July 21 is reported in figure 7.5a (red symbols). The temporal evolution of the fine-mode fraction η_A that is the ratio between fine-mode and total optical depth at 550 nm is shown in figure 7.5b (red open boxes).

It worth mentioning, as we told in chapter 6, that η_M and η_A do not represent the same aerosol parameter but, they are comparable parameters

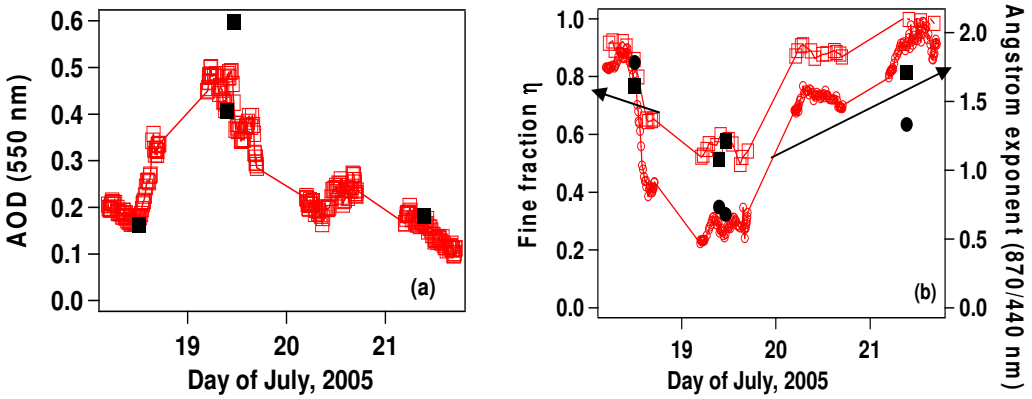

Figure 7.5. Lecce's temporal evolution of AERONET (a) AODs (red boxes) and (b) fine-mode fractions (red boxes) at 550 nm, and Angstrom coefficients (red open dots) from July 18 to July 21, 2005. Black symbols are corresponding MODIS-ocean aerosol products.

The temporal evolution of the Angstrom exponent $Å_A$ (computed from AERONET AODs at 440 and 870 nm) is also reported in figure 7.5a (red open dots)

to show the strong correlation between η_A and $Å_A$ values. As we told, for its sensitivity to the aerosol particle size, Å is a good marker to trace the temporal evolution of particle size distribution changes during pollution events such as dust outbreaks. Figure 7.5b reveals that $Å_A$ takes values smaller than one when η_A values are smaller than 0.6.

The fast AOD_A increase and the decrease of both η_A and $Å_A$ occurring on the afternoon of July 18, suggest that a significant advection of large dust particles over Lecce started to occur on the afternoon of July 18. AOD_A reaches maxima values and both η_A and $Å_A$ reach minima values on July 19. Then, figure 7.5 suggests that the dust outbreak was already over on July 20, as suggested by the rather low AOD_A values and the fast increase of both η_A and $Å_A$ values. Black boxes in figure 7.5a represent mean values of MODIS-ocean AODs, while full black dots and boxes in figure 7.5b represent $Å_M$ and η_M, values, respectively, retrieved for window sizes of 50x50 km^2 centered on Lecce's AERONET site. In accordance with AERONET data, AOD_M takes larger values, while η_M and $Å_M$ take smaller values during the dust event. We observe from figure 7.5a that the accordance between the AERONET and MODIS AOD co-located in space and time (Ichoku et al., 2002) is rather good (percentage difference lower than 10%) on July 18, at 12:03 UTC. In contrast, percentage differences are of 32% on July 19 at 09:30 UTC. AOD, η and Å values by MODIS and AERONET, respectively, co-located in space and time are given in Table 7.1 with corresponding percentage differences.

Table 7.1: AOD, Å, and η values over Lecce by MODIS and AERONET, respectively, co-located in space and time from July 18 to July 21st, 2005.

Aerosol parameters	July 18 12:03 UTC	July 19 09:30 UTC	July 19 11:10 UTC	July 21 09:18 UTC
AOD_M	0.162 ± 0.004	0.60 ± 0.01	0.41 ± 0.02	0.182 ± 0.004
AOD_A	0.177 ± 0.003	0.45 ± 0.03	0.43 ± 0.05	0.166 ± 0.004
$\frac{AOD_M - AOD}{AOD_A}$ %	8%	32%	4%	28%
$\mathring{A}_M$	1.78 ± 0.09	0.73 ± 0.01	0.68 ± 0.03	1.33 ± 0.01
$\mathring{A}_A$	1.63 ± 0.03	0.62 ± 0.03	0.54 ± 0.03	1.91 ± 0.03
$\frac{\mathring{A}_M - \mathring{A}_A}{\mathring{A}_A}$ %	9%	18%	26%	30%
η_M	0.770 ± 0.004	0.51 ± 0.01	0.580 ± 0.004	0.813 ± 0.004
η_A	0.8 ± 0.1	0.6 ± 0.03	0.58 ± 0.04	1 ± 0.1
$\frac{\eta_M - \eta_A}{\eta_A}$ %	10%	15%	0%	18%

MODIS and AERONET volume size distributions have been analyzed to better understand the difference between η_A and η_M values. Figures 7.6a-7.6c (dashed lines) show the normalized AERONET volume size distributions retrieved on July 19 at 9:30 and 11.55 UTC, and on July 21st at 8:55 UTC, respectively.

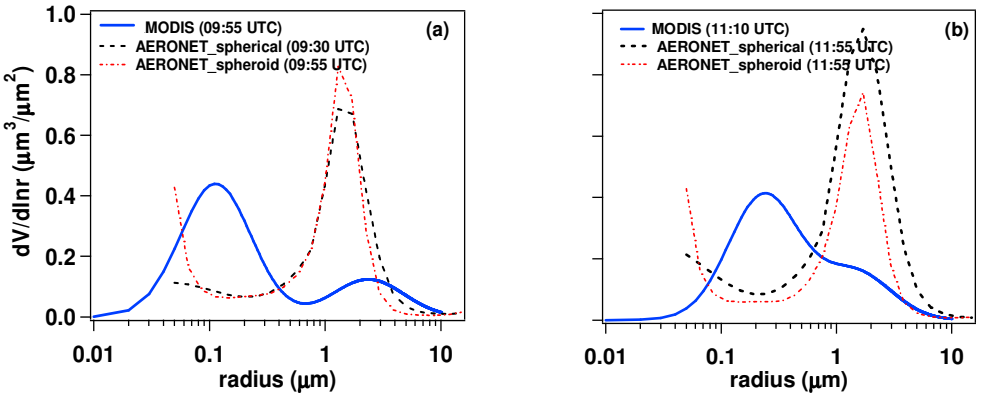

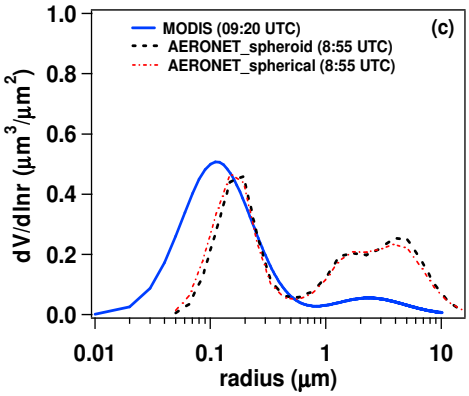

Figure 7.6 Comparison between AERONET volume size distributions by the spherical- (dashed red lines) and the spheroid-model (dotted black lines), and MODIS-ocean (solid blue lines) volume size distributions retrieved at Lecce: (a) and (b) on July 19, 2005 at different day hours and (c) on July 21, 2005.

AERONET volume size distributions retrieved by the spheroid almucantar retrieval model are also plotted in figure 7.6 (black dotted lines) for comparison. According to Dubovik et al. (2006) the spheroid model significantly improves the performance of aerosol retrievals for desert dust observations. In particular, it allows getting a decrease of the residual of fitting AERONET observations compared to the residual achieved by using the Mie scattering theory. We note from figure 7.6c that spherical and spheroid model provide rather close volume size distributions on July 21st, being the dust event already over. In contrast, volume size distributions by the spherical model are different than those retrieved by the spheroid model during dusty days. Solid blue lines in figures 7.6a -7.6c show the MODIS volume size distribution retrieved on July 19, at 9:55 and 11:10 UTC, and on July 21st at 9:20 UTC, respectively. According to the AOD temporal evolution, both MODIS and AERONET volume size distributions show that the contribution of coarse mode particles increases from the morning up to midday on July 19, while it is significant lower on July 21st, being the dust event already over. However, it is worth noting from figure 7.6 that MODIS volume size distribution profiles differ significantly

from corresponding AERONET volume size distribution profiles retrieved by the spherical (red dashed line) and the spheroid model (black dotted line). It appears that the MODIS-ocean algorithm is not able to properly catch the larger contribution of coarse-mode particles during dust outbreaks as opposed to AERONET inversion algorithms. The different numerical procedure by MODIS and AERONET to retrieve volume size distributions is responsible of latter results: AERONET volume size distributions are calculated from standard inversions of observed sky radiance (Dubovik and King, 2000a), while MODIS aerosol volume size distributions are calculated by an inversion procedure based on a Lookup Table (Tanré et al., 1997).

7.2.2b *Analysis of the aerosol products over Lampedusa's sunphotometer site*

Figure 7.7a (red symbols) shows the temporal evolution of the AERONET AOD at 550 nm retrieved at Lampedusa from July 18 to July 21. There are rather few η_A values available from 18 to 21st July and are plotted in figure 7.7b (red symbols). Black full symbols represent in figures 7.7a and 7.7b mean values of AOD_M and η_M, respectively retrieved for a window size of 50x50 km^2 centered on Lampedusa's AERONET site. Figure 7.7a shows that both AERONET and MODIS AODs take larger value during the dust event of July 19.

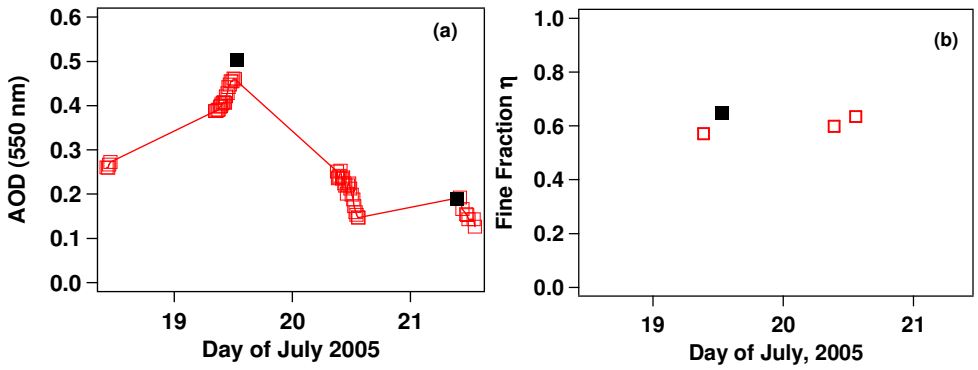

Figure 7.7: Temporal evolution of (a) AERONET AODs (red boxes) and (b) AERONET fine-mode fractions (red boxes) at 550 nm at Lampedusa's site during July 19-21, 2005. Black symbols are MODIS-ocean aerosol products.

The percentage difference between MODIS and AERONET AODs co-located in space and time is about 10% on July 19 and less of 3% on July 21st. Again figure 7.7b may indicate that MODIS overestimates the fine-mode fraction during the dusty day: η_M at 12:43 UTC is 12% higher than η_A at 9:18 UTC. However, latter difference may also be ascribed to the fact that η_M and η_A values refer to different day hours, by considering the strong spatial and temporal variability of aerosol particles mainly during dust outbreaks (e.g. Tafuro et al., 2006). Figure 7.8 shows AERONET (dashed line) and MODIS (solid line) volume size distributions retrieved on July 19 at 9:18 and 12:43 UTC, respectively. The AERONET volume size distribution retrieved by the spheroid model at 9:55 UTC is also plotted in figure 7.8 (grey dotted line). Again, the significant differences between AERONET and MODIS profiles could be due to the fact that they are referred to different hours of the day. However, we believe that they are also due to the differences between MODIS and AERONET inversion algorithm. The discrepancy between the two profiles of figure 7.8 is rather similar to that found by comparing MODIS and AERONET size distribution profiles retrieved at closer day hours (e.g. figure 7.6).

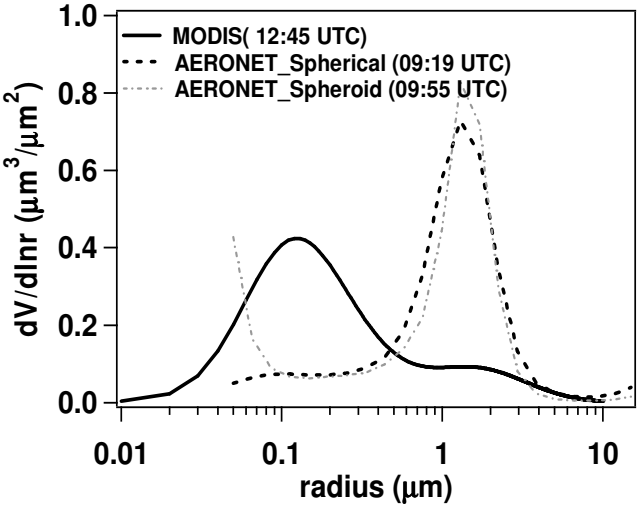

Figure 7.8. Comparison between the AERONET volume size distribution by the spherical- (dashed black line) and the spheroid-model (dotted grey lines), and the MODIS-ocean (solid line) volume size distribution retrieved on July 19 at Lampedusa.

7.3. Correlation of AERONET and MODIS data and discussion

In this section we report the results on the correlation between MODIS-ocean and AERONET aerosol products retrieved over four selected Mediterranean sites (figure 7.1) during dust events occurred from 2003 to 2005. MODIS true color images, analytical backtrajectories and AERONET data rather sensitive to the advection of dust particles such as the Angstrom exponent (Tafuro et al., 2006) have been used in this study to classify dusty days.

7.3.1 *Correlation study of AERONET and MODIS-ocean AODs*

We correlate in this section spatial statistics of MODIS-ocean AODs with corresponding temporal statistics of AERONET AODs at 550 nm retrieved during Saharan dust outbreaks. It would be inappropriate to compare single MODIS pixel values directly to AERONET point measurements because air masses are constantly in motion, therefore, an air mass captured by MODIS across a certain horizontal span

over a sunphotometer site, is sampled by the sunphotometer during a certain time period (Ichoku et al., 2002). The methodology adopted in this work to compare temporal statistics from AERONET with spatial statistics from MODIS is the same of paragraph 6.1 and requires that at least 2 out of the possible 5 AERONET measurements are within ± 30 min of MODIS overpasses and that at least 5 out of the possible 25 MODIS retrievals are in a square box of 50 km x 50 km centered over the AERONET site (Ichoku et al., 2002; Chu et al., 2003). As we have mentioned, the choice to analyze only MODIS-ocean retrievals is due the minimum spatial variability of the ocean surface reflectance (Tripathi et al., 2005). MODIS-land aerosol products are expected to be also affected by uncertainties due to the land surface reflectance (Santese et al., 2007).

The scatter plot of mean MODIS-ocean AODs retrieved for window sizes of 50x50 km^2 centered at the selected AERONET sites, versus the corresponding AERONET AODs co-located in time and space, is shown in figure 7.9. In the figure, data points referring to different sites are represented by different symbols. Error bars represent one standard deviation of mean values. The dashed line in figure 7.9 represents the regression line fitting data points, while solid lines are MODIS-ocean pre-launch "expected errors" (i.e. $\Delta AOD_M = \pm 0.03 \pm 0.05 AOD_M$). Total number of data points N=50, regression line parameters and correlation coefficient R are given at the top of the figure 7.9.

We observe from figure 7.9 that AOD_M and AOD_A are quite well correlated being the correlation coefficient R = 0.86, the slope equal to 1.04±0.04 and the bias within the estimated bias. Regression line fits inside expected error lines. However, only 42% of the data points meets the pre-specified accuracy range. By doubling bias and

slope of the expected uncertainty lines, the percentage of the data points within pre-specified accuracy conditions increases up to 72%.

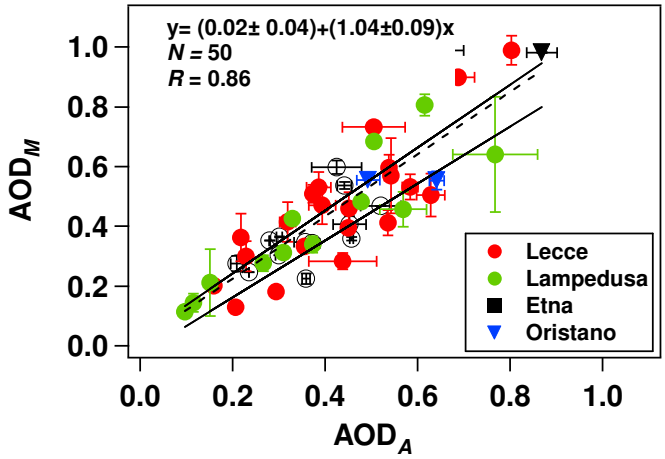

Figure 7.9 Scatter plot between mean values of MODIS-ocean AODs retrieved for 50x50 km² window sizes centered on the selected Mediterranean sites and corresponding mean values of AERONET AODs co-located in space and time.

MODIS standard deviations σ_M referring to the data points of figure 7.9 versus the corresponding AERONET standard deviations σ_A are plotted in figure 7.10a. As we told in chapter 6, σ_M values are representative of both the retrieval uncertainties and the spatial variability of aerosol optical depths. In contrast, σ_A values are mainly representative of the temporal variability of the atmospheric aerosol distribution (Santese et al., 2007).

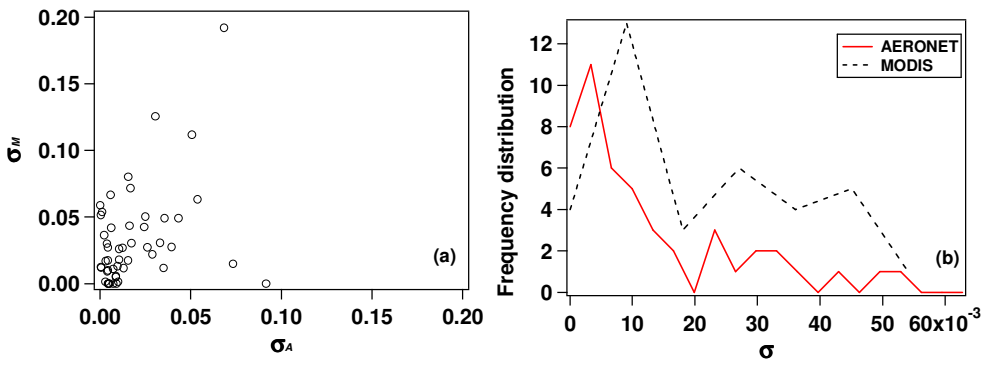

Figure 7.10. (a) Scatter plot of MODIS-ocean standard deviations versus corresponding AERONET standard deviations referring to the data points of figure 7.9; (b) frequency distribution of MODIS-ocean (black dashed line) and AERONET (red line) standard deviations of figure 7.10a.

Figure 7.10a reveals that σ_M reaches values up to 0.2, while σ_A assumes values lower than 0.1. σ_M (black dashed line) and σ_A (red line) frequency distributions are shown in figure 7.10b. We observe that the σ_M frequency distribution is peaked at 0.009, while the σ_A frequency distribution is peaked at 0.003. Latter results may indicate that the spatial variability of dust particles into an area of about 50x50 km^2 centered at the AERONET site is larger than the aerosol temporal variability that occurs in ± 30 min of the satellite overpass.

Figure 7.11 shows the frequency distribution of the MODIS and AERONET AODs plotted in figure 7.9. Error bars are standard deviations of mean values.

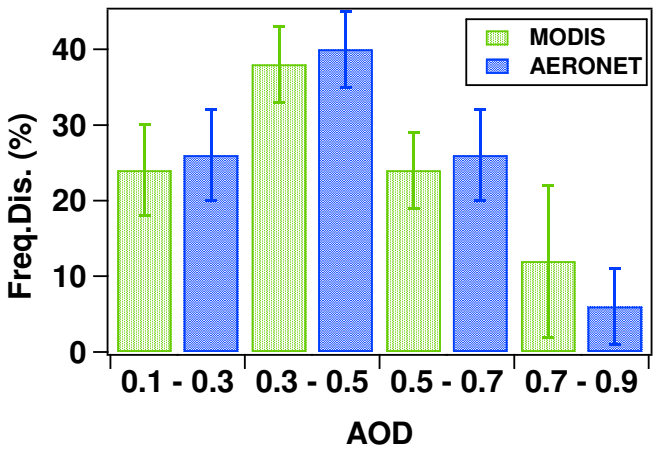

Figure 7.11. Frequency distributions of MODIS-ocean and AERONET AODs. Error bars represent standard deviations of mean values.

We observe that AOD_M and AOD_A frequency distributions are in satisfactory accordance. However, the difference between AOD_M and AOD_A frequency

distribution mean values is lower than 2% for AOD bin intervals < 0.7, while is of 6% for the 0.7-0.9 AOD bin interval. Figure 7.12 shows the differences AOD_M - AOD_A versus AOD_A. It is worth noting that the differences are almost positive and increase with AOD_A: (AOD_M - AOD_A) values vary within the -0.03-0.14 range at AOD_A < 0.4 and within the 0.08-0.33 range at AOD_A > 0.6. The solid line in figure 7.12 represents the regression line of data points and it is characterized by a positive slope value (0.17±0.05) even if the correlation coefficient takes a small value (R=0.45). Latter results may indicate that MODIS overestimates AODs mainly at high dust loads in accordance to the plots of figures 7.5a and 7.7a.

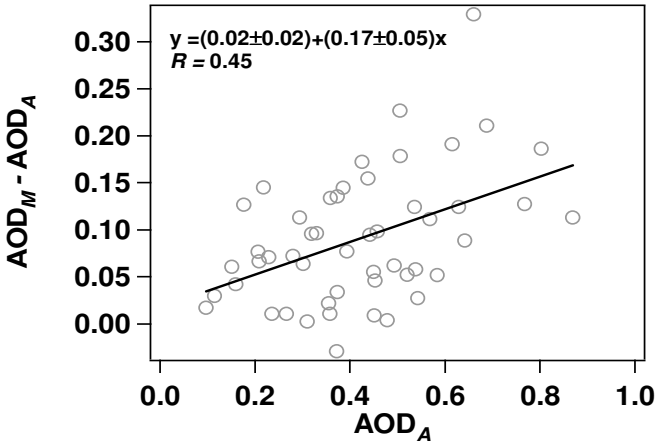

Figure 7.12. Differences between MODIS-ocean and AERONET AODs as function of AERONET AODs

Latter results are in agreement with those reported by Tripathi et al. (2005) over Kampur (India), which have revealed that MODIS overestimates AODs during the dust loading period, while underestimates AODs during the dust-free periods. However, it is worth noting that the results by Tripathi et al. (2005) are based on MODIS-land aerosol products. Recent studies performed by the authors over Lecce

(Santese et al., 2007) have also revealed that MODIS-ocean underestimates AODs during dust-free days characterized by high aerosol loads. Intercomparison studies by Kaufman et al. (2005a) at Capo Verde have shown that though some differences were due to spatial inhomogeneity or differences of AERONET to MODIS, on annual average MODIS-ocean AODs were higher than AERONET AODs by 4% in 2001 and lower than AERONET AODs by 5% in 2002.

In order to test if the correlation between MODIS and AERONET AODs is affected by the time of the year, figure 7.13a shows AOD_M (blue dots) and co-located in space and time AOD_A (red dots) values as a function of the time of the year.

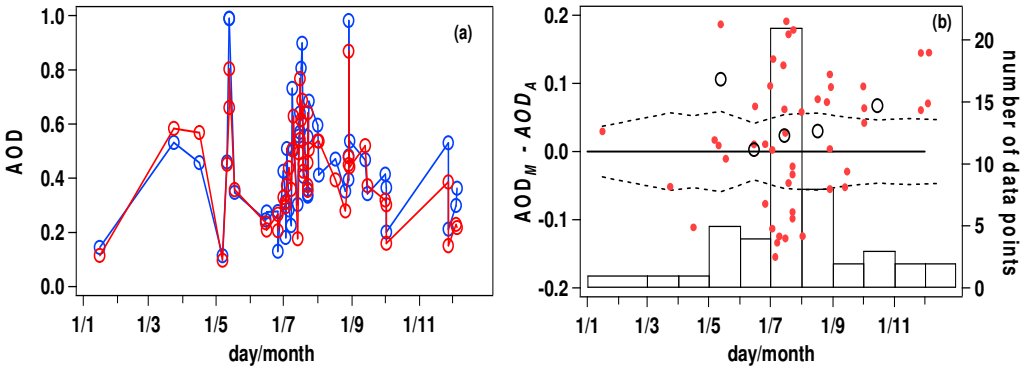

Figure 7.13. (a) Temporal evolution of MODIS-ocean (blue open dots) and AERONET (red open dots) AODs values collected during dust events occurred over the selected Mediterranean sites from 2003 to 2005; (b) Temporal evolution of the differences (full dots) between MODIS and AERONET AODs. Open dots represent monthly averaged values calculated for months with at least four data points. Black bars are the monthly number of data points.

All 2003-2005 available data for the selected Mediterranean sites are plotted in figure 7.13a, which as expected, shows that both MODIS and AERONET AODs are on the average larger on spring-summer (e.g. De Tomasi et al., 2006; Santese et al., 2007). The differences between MODIS and AERONET AODs versus the time

of the year are given in figure 7.13b (full dots) with monthly averaged values (open dots). Monthly means have only been calculated for months with four or more dust events. Black bars in figure 7.13b represent the monthly number of data points while dashed lines represent the MODIS-ocean pre-launch "expected errors". Figure 7.13b does not reveal any seasonal dependence: ~55% of data points are within expected error lines and monthly mean values vary within the 0.0 – 0.1 range.

The effects of unresolved clouds on MODIS measurements of the AOD have recently been investigated by Kaufman et al. (2005b). They found that the main cloud effect is from residual cirrus that increases the AOD by 0.015 ± 0.003 at 0.55 μm over cloud-free oceans. In addition, they found that an additional 0.010 ± 0.005 of excess optical thickness was associated with lower level clouds. According to the results by Kaufman et al. (2005b), the cloud contamination may also be responsible of the differences between MODIS and AERONET AODs revealed by Figures 7.11, 7.12, and 7.13b.

7.3.2. *AERONET versus MODIS-ocean fine-mode fractions*

Figure 7.14a shows the yearly temporal evolution of η_M (blue open dots) and η_A (red open dots) at 550 nm, retrieved during dust events occurred over the Mediterranean from 2003 to 2005 years.

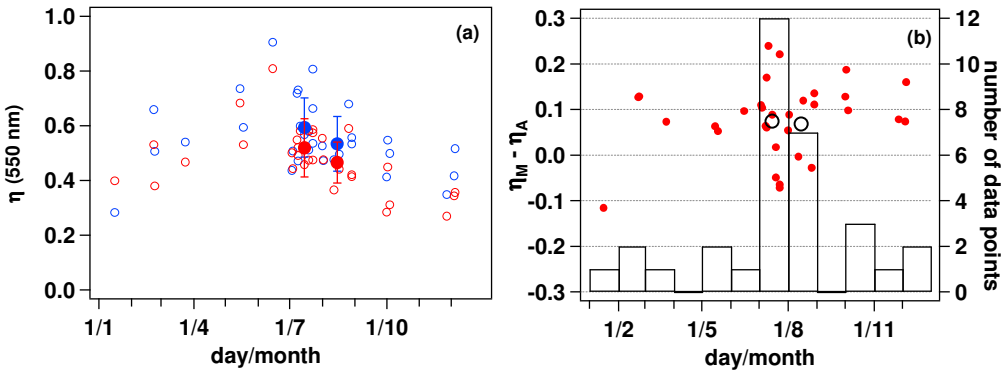

Figure 7.14. (a) Temporal evolution of MODIS-ocean (blue open dots) and AERONET (red open dots) fine-mode fractions retrieved during dust events occurred from 2003 to 2005. Full blue and red dots represent monthly mean values of η_M and η_A calculated for months with at least four data points. (b) Temporal evolution (red full dots) of the differences $\eta_M - \eta_A$. Black open dots are monthly averaged values and black bars are the number of data points for each month.

The Ichoku et al. (2002) criteria for co-location of the data are no longer used for the data reported in this section. In fact, η_M values are co-located in space with η_A values, but even though have been retrieved during the same dust days, they may refer to different day-hours and thus they may not be co-located in time. Indeed, rather few η_M and η_A data points co-located in space and time have been available for the studied period. This is mainly due to the fact that η_A is retrieved from sky radiance measurements that are taken less often than direct sun measurements in the AERONET protocol (Santese et al., 2007). In addition, the prevalence of inhomogeneous sky conditions in dust-dominated regimes represents a contributing factor. O'Neill et al. (2001, 2003) recently proposed a spectral deconvolution method for using AERONET solar extinction data to optically derive the fine to coarse mode optical depth ratio. This last method allows retrieving a larger amount of η_A data points. Nevertheless, we decided to only compare MODIS and AERONET Dubovik inversion fine fraction retrievals since both methods have been in operational use for several years. Monthly averaged values of η_M (blue full dots) and η_A (red full dots) and corresponding standard deviations for the months with at least four data points, are also reported in figure 7.14a, which reveals that both η_M and η_A have a similar seasonal evolution. Both MODIS and AERONET fine mode fractions reveal that the contribution of fine mode particles is higher on spring-summer over the selected monitoring sites.

Figure 7.14a shows that most of the η_M values are larger than the η_A values. The temporal evolution of the (η_M - η_A) differences (full red dots) is plotted on figure 7.14b with the monthly mean differences (open dots), if at least four data points are available within a month, and the monthly number of data points (black bars). It is worth mentioning that the comparison of MODIS with AERONET O'Neill fine fraction retrievals also revealed that MODIS tends to slightly overestimate fine fraction for dust-dominated aerosols (Kleidman et al., 2005).

To better investigate the dependence of fine-mode fractions on corresponding AODs, figures 7.15a and 7.15b show the correlation between η_M and AOD_M and the correlation between η_A and AOD_A, respectively. The different sites are represented by different symbols in figure 7.15 revealing that both MODIS and AERONET fine-mode fractions are not dependent on aerosol optical depths. In addition, figure 7.15 clearly shows that both MODIS and AERONET fine-mode fractions are on the average larger at Lecce than at Lampedusa, even though they vary within a different variability range. The latter result can be ascribed to the fact that Lampedusa is closer to the African continent than Lecce. Hence, a major impact of large dust particles is expected at Lampedusa.

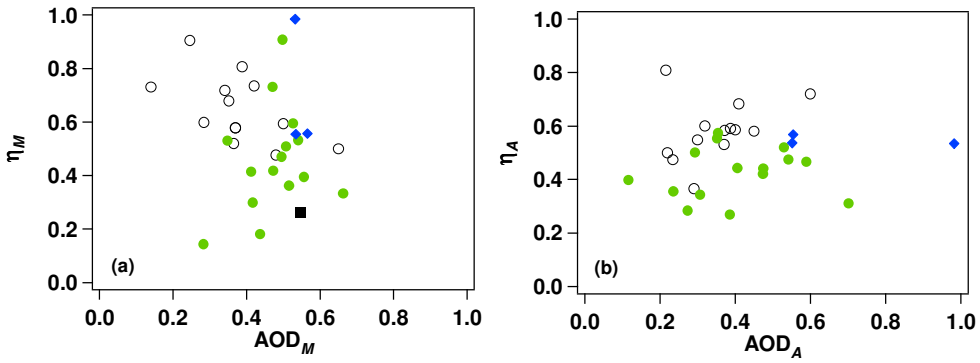

Figure 7.15. Correlation between (a) MODIS-ocean and (b) AERONET fine-mode fractions and corresponding AODs values at 550 nm retrieved at Lecce (black open

dots), Lampedusa (green full dots), Oristano (black full boxes) and Etna (blue full diamonds).

In agreement with the results of this section, several studies revealed that MODIS slightly overestimates the fine-mode fraction for dust-dominated aerosols (Chu etal., 2005; Anderson et al., 2005; Kleidman et al., 2005) and according to Kleidman et al. (2005), MODIS overestimation in dust-dominated aerosol conditions should decrease significantly with the inclusion of a nonspherical model. However, the differences between MODIS and corresponding AERONET retrievals may not only due to the lack of assumption about dust non-sphericity in the MODIS aerosol model, unless the MODIS algorithm is more affected by the non-spherical assumption than the AERONET inversion algorithm. AERONET products retrieved by the inversion algorithm for spherical particles have been used in this study and the plots of figures 7.6 and 7.8 provide some indications on the effects of the AERONET spheroid model on volume size distributions.

7.3.3 *AERONET and MODIS-ocean particle size distributions*

To better understand the differences between η_M and η_A, we have investigated in this section the correlation between MODIS and AERONET volume size distributions corresponding to the data points of figure 7.14a. In particular, results on the size distribution profiles retrieved during dusty days characterized by fine-mode fractions within the 0.4-0.6 range are analyzed: 78% of the data points of figure 7.14 are within that range. According to figure 7.7b, $Å_A$ takes values smaller than one when η_A values are smaller than 0.6. Equation 5.3 is used to retrieve MODIS volume size distributions. AERONET volume size distributions are provided for 22 equal log-radius size bin intervals between 0.05 and 0.15 μm

(Dubovik and King, 2000a). Figure 7.16 (solid lines) shows the normalized mean MODIS volume size distributions calculated for (a) Lecce, (b) Lampedusa and (c) Oristano, by averaging 6, 10 and 2 volume size distribution profiles, respectively retrieved during different dusty days. Corresponding mean AERONET profiles obtained by the inversion spherical model are plotted in figure 17.6 by dotted lines. Despite the fair accordance between η_M and η_A revealed by figure 7.13b, the plots of figure 7.16 appear to indicate that the MODIS inversion algorithm is not able to catch the significant contribution of large dust particles during dust events. AERONET profiles of figure 7.16 clearly show that Lampedusa, being the closest (~200 km) site to the African continent, is also the site characterized by a mean size distribution profile with the smaller and larger contribution of fine- and coarse-mode particles, respectively with respect to Lecce and Oristano that are ~ 900 and 400 km away, respectively from the northern Africa coast.

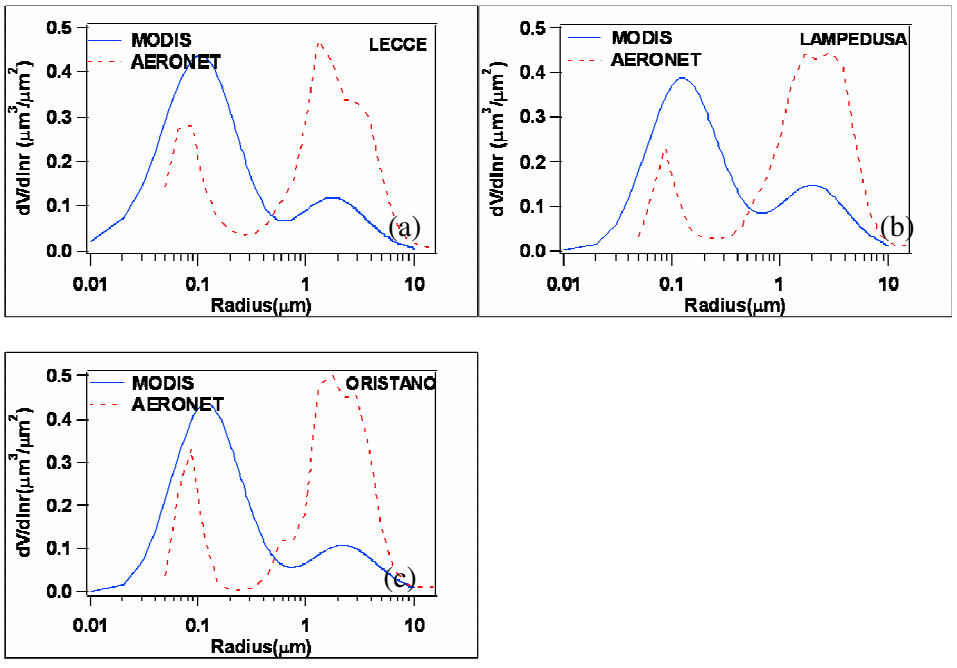

Figure 7.16. Comparison between mean MODIS-ocean (solid line) and AERONET (dotted line) volume size distributions retrieved at (a) Lecce, (b) Lampedusa and (c)

Oristano sites. The profiles have been calculated by averaging at each site all available profiles with fine mode fraction values between 0.4 and 0.6. AERONET profiles have been retrieved from the spherical inversion procedure.

In addition, the mean peak-value of the coarse-mode volume distribution that is at 1.3 μm and at 1.7 μm at Lecce and Oristano, respectively, is at 2.94 μm at Lampedusa. We believe that the last observations further more support the goodness of AERONET retrievals by the spherical inversion algorithm. MODIS size distribution profiles allow only inferring that the peak value of the coarse-mode distribution is slightly higher at Lampedusa with respect to Lecce and Oristano.

Figures 7.17a and 7.17d show fine- and coarse-volume modal radii versus η_M for all MODIS size distributions used to get mean size distribution profiles of figures 7.16a-7.16c. The fine- and coarse-volume modal radii versus η_M for all AERONET size distributions used to get the mean dashed profiles of figures 7.16a-7.16c are plotted in figures 7.17b and 7.17e as a function of η_A. Figures 7.17c and 7.17d show the frequency distribution of MODIS and AERONET fine- and coarse-volume modal radii, respectively.

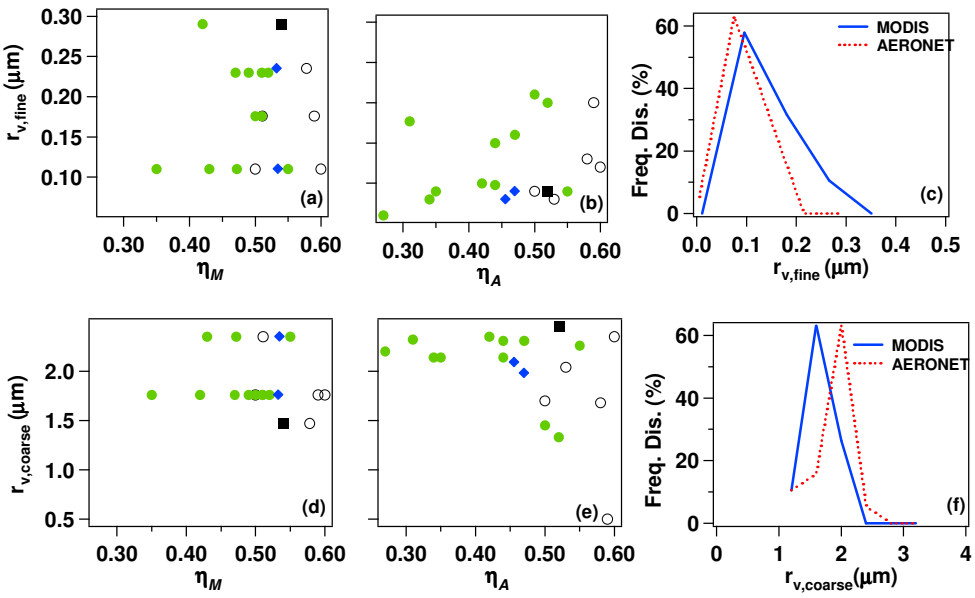

Figure 7.17. MODIS-ocean (a) fine and (d) coarse volume modal radii versus η_M and AERONET (b) fine and (e) coarse volume modal radii versus η_A. Different symbols refer to different sites: Lecce (black full dots), Lampedusa (black open boxes), Oristano (grey open diamonds) and Etna (grey full dots). Frequency distribution of MODIS (solid lines) and AERONET (dotted lines) (c) fine and (g) coarse volume modal radii.

Figures 7.17a and 7.17d reveal that fine- and coarse-volume modal radii are not dependent on η_M and span the 0.11-0.29 μm and the 1.17-2.35 μm range, respectively in accordance to the variability range for fine and coarse volume modal radii set by the MODIS inversion procedure. In contrast, figures 7.17b and 7.17e indicate that on average fine- and coarse-volume modal radii take larger and smaller values, respectively as η_A increases. The higher sensitivity of AERONET $r_{v,fine}$ and $r_{v,coarse}$ values to η_A revealed by figures 7.17b and 7.17e, may be due to the larger variability range set by the AERONET inversion algorithm. In fact, the AERONET inversion algorithm allows aerosol particles to have the radius within the 0.05-15 μm range without setting $r_{v,fine}$ and $r_{v,coarse}$ values, and all particles with the radius smaller than 0.6 are considered fine, while all the others are considered coarse. In contrast, four $r_{v,fine}$ and $\sigma_{v_{i,fine}}$ values and five $r_{v,coarse}$ and $\sigma_{v_{i,coarse}}$ values are only allowed by the MODIS inversion algorithm. However, it is worth noting from figures 7.17c and 7.17e that AERONET and MODIS frequency distributions of both of $r_{v,fine}$ and $r_{v,coarse}$ are similar: the frequency distribution of MODIS and AERONET fine-volume modal radii is peaked at 0.096 μm and 0.075 μm, respectively. While, the frequency distribution of MODIS and AERONET coarse-volume modal radius is peaked at 1.6 μm and 2 μm, respectively. Hence, we believe that the results of the previous and of this section suggest that the differences between MODIS and AERONET fine mode fractions can be due to the lower sensitivity of the MODIS-

ocean inversion algorithm to the number concentration of dust particles with respect to the AERONET spherical inversion algorithm.

7.4. Conclusions

Sahara dust outbreaks occurred over the central Mediterranean basin from 2003 to 2005 have been analyzed in this chapter to contribute to the validation of MODIS retrievals in dust dominated aerosol conditions. In particular, MODIS-ocean aerosol products and corresponding AERONET data from the spherical model retrieved at Lecce, Lampedusa, Oristano and Etna have been analyzed and correlated. Thanks to their location, away from large cities and industrial areas, the selected AERONET sites are expected to be less affected by aerosols of local origin and hence are better suited to investigate the validation of MODIS retrievals in dust dominated aerosol conditions.

A specific dust outbreak occurred on July 19, 2005 over the central Mediterranean has been studied by analyzing MODIS-ocean AODs, fine-mode fractions, and size distributions and corresponding AERONET products retrieved over Lecce and Lampedusa. This study has been reported to provide preliminary results on the main differences between MODIS and corresponding AERONET aerosol products. Furthermore, all MODIS-ocean and AERONET products retrieved at the four selected Mediterranean sites during dust events occurred from 2003 to 2005 have been analyzed. We found that MODIS-ocean AODs are quite correlated to AERONET AODs co-located in space and time: correlation factor and slope of the linear regression are 0.86 and 1.04, respectively. In addition, 42% of the data points are within the pre-specified accuracy range. However, the plot of the differences (AOD_M - AOD_A) versus AOD_A has clearly revealed that (AOD_M - AOD_A) values are

mostly positive and increase with AOD_A: (AOD_M - AOD_A) values vary within the -0.03-0.14 range at $AOD_A < 0.4$ and within the 0.08-0.33 range at $AOD_A > 0.6$. Latter results have led assuming that MODIS overestimates AODs mainly during high dust load conditions, in accordance to the results provided by other authors and referring to different geographical areas. However, according to Kaufman et al. (2005b), the differences between MODIS and AERONET AODs revealed by figures 7.11, 7.12, and 7.13b could also be due to cloud contamination.

The temporal evolution of MODIS-ocean and AERONET fine-mode fractions co-located in space has been also analyzed. We observed that the MODIS-ocean inversion algorithm overestimates the contribution of fine-mode particles for dust-dominated aerosols. Similar results have been reported by several authors and have been ascribed to the lack of assumption about dust non-sphericity in the MODIS aerosol model. AERONET products retrieved by the inversion algorithm for spherical particles have been used in the correlation study of this work. We believe that the differences between η_M and η_A are not only due to the use of a spherical MODIS inversion algorithm. However, it might be possible that MODIS retrievals will be more affected by the use of a non-spherical inversion algorithm than AERONET products. The different definition of fine and coarse mode by the MODIS-ocean and AERONET inversion algorithm could also be responsible of the positive mean values of the (η_M - η_A) differences.

The dependence of η_M and η_A on corresponding AODs has been also analyzed. The plot of η_M versus AOD_M and that of η_A versus AOD_A has at first revealed that both MODIS and AERONET fine-mode fractions are not dependent on AODs.

MODIS-ocean and corresponding AERONET volume size distributions have been analyzed in order to better understand the differences between η_M and η_A values. The comparison of MODIS and AERONET mean volume size distributions co-located in space has shown that the MODIS-ocean inversion algorithm underestimates the contribution of coarse mode particles. Indeed, it appears that the MODIS-ocean algorithm is not able to catch the larger contribution of coarse-mode particles during dust outbreaks. To this end, it is also worth mentioning that frequency distributions of MODIS fine and coarse volume modal radii are rather close to corresponding AERONET frequency distributions, despite the quite different variability range of $r_{v,fine}$ and $r_{v,coarse}$ set by the MODIS and AERONET inversion algorithm.

In conclusion, the presented results contribute to the validation of MODIS retrievals providing further details about the correlation between MODIS and corresponding AERONET products. In particular, we believe that the existing MODIS-ocean inversion algorithm in dust-dominated aerosol conditions should be improved, in accordance to previous studies. The poor sensitivity to the concentration of coarse-mode particles of the MODIS inversion algorithm, with respect to the spherical AERONET inversion algorithm appears mainly responsible for the differences between MODIS and AERONET aerosol products.

CHAPTER 8

SIMULATION OF DUST OUTBREAKS OVER THE MEDITERRANEAN BASIN WITH THE *Regional Climate Model* (RegCM3)

The spatial and temporal distributions of aerosols tend to be highly inhomogeneous on regional scales due to their relatively short lifetimes. Moreover, measurements of atmospheric aerosol concentrations (both horizontally and vertically) in non-urban areas are scarce. For these reasons, three-dimensional chemical transport models that simulate emissions, transport, conversion and removal process of different aerosol species are important tools to characterize the aerosol spatial distributions on global/regional scales, and to assess their climate effects (Schimel et al., 1996). General circulation models (GCMs) with global coverage have been the primary tool used in climate studies since the 1960's. GCMs that run at current resolutions of 200-500 km appear to be capable of simulating the global mean climate states. Because of the coarse resolution of these global models, however, they can produce biases in simulated regional climate and variability with apparent errors of as much as ±5 ºC in temperature, and -40% to +60% in precipitation (Leung et al., 2003: IPCC, 2001). Therefore, different modeling approaches have been developed to regionally enhance the GCM information (Giorgi ad Means, 1991). The idea that limited area models (LAMs) could be used for regional studies was originally proposed by Dickinson et al., 1989. The development of a regional climate model began at the National Center for Atmospheric Research (NCAR). The NCAR Regional Climate Model (RegCM) was initially built upon the NCAR-Pennsylvania State University (PSU) Mesoscale Model version 4 (MM4) with modifications and augmentations of various parameterizations to make it appropriate for longer-term climate simulations and to make it capable of being nested inside the NCAR Community Climate Model (CCM). In subsequent years, the RegCM model has been updated and further improved at the Abdus Salam International Centre for Theoretical Physics (ICTP), Trieste, (Giorgi et al., 1993, 1999, 2002), and modules have been added to make it possible to study climate-chemistry interactions.

In the past, a number of efforts have been made to simulate the desert dust cycle in climate models, particularly at the global scale (Joussame, 1990; Cakmur et al., 2004, 2005; Miller et al., 2004, 2006; Zender et al., 2004; Luo et al., 2003). Fewer studies are available on the inclusion of dust processes in regional climate models (Gong et al., 2003; Song and Carmichael, 2001; Nickovic et al.,2001). Dust radiative effects on climate are likely to be especially important at the regional scale, thus RCMs can be particularly useful tools to investigate the regional climate effects of dust outbreaks (Zakey et al., 2006).

In this thesis, preliminary results obtained over the Mediterranean Basin by the implementation of a dust module within the regional climate modeling framework RegCM (Version 3.1), developed at the Abdus Salam International Centre for Theoretical Physics (ICTP), Trieste, are presented. In particular, for the test simulation we have considered two strong Saharan dust outbreaks that occurred in the second half of July 2003, which have spread large tongues of dust particles all over the central Mediterranean basin. In particular, a first simulation was done for a Mediterranean domain of 10010 km * 4542 km centered at latitude of 30º and longitude of 5º and a horizontal spacing of 50 Km. Then, we made a second simulation for a Mediterranean domain that is smaller than the first (of ~ 4995km*2227km) but centered at the same point (at a latitude of 30º and a longitude of 5º), with a horizontal spacing of 50 Km. We believe that the two simulations should allow us understanding how the choice of the run simulation's domain may influence model results. Model simulations are compared with experimental data to test the RegCM model performance in order to contribute to the establishment of models more dependent on measurements.

In particular, AODs from AERONET sunphotometer and MODIS satellite measurements over four sites of the Mediterranean Basin (Lecce, Lampedusa,

Oristano and Etna), extinction coefficient profiles α_{ext} retrieved from Lidar measurements at Lecce and Etna and PM_{10} and total suspended particulate (PTS) matter concentrations measured at Lecce are compared with the corresponding parameters provided by the RegCM.

It worth noting that, to fully assess the climatic effects of aerosols, long-term multi-year simulations are required. However, the results presented in this thesis are only preliminary and they allow us to evaluate the model performance from the scale of individual episodic events. The evaluation of individual dust events is a necessary step in order to assess the realism of emission and transport processes inside the model.

8.1 Model Description

The Regional Climate Model (RegCM3) used in this thesis, is the third-generation grid-point limited area model developed by Giorgi et al., 1993 a,b, Giorgi and Mearns, 1999 and Pal et al., 2000. It is a hydrostatic, sigma vertical coordinate model whose dynamics is essentially the same as the hydrostatic version of the mesoscale model MM5 (Grell et al., 1994). The modeling system usually gets and analyzes its data on pressure surfaces, but these have to be interpolated to the model's vertical coordinate before input to the model. The vertical coordinate is terrain-following meaning that the lower grid levels follow the terrain while the upper surface is flatter. Intermediate levels progressively flatten as the pressure decreases toward the top of the model. A dimensionless σ coordinate is used to define the model vertical levels, which is defined as:

$$\sigma = \frac{p - p_t}{p_s - p_t} \tag{8.1}$$

where p is the pressure, p_t and p_s is the top and surface pressure of the model, respectively. It can be seen from equation 8.1 that σ is zero at the top and one at the surface, and each model level is defined by a value of σ. The model vertical resolution is defined by a list of values between zero and one that do not necessarily have to be evenly spaced.

The horizontal grid has an Arakawa-Lamb B-staggering of the velocity variables with respect to the scalar variables. This is shown in figure 8.1 where it can be seen that the scalars, like temperature T, pressure p, etc..are defined at the center of the grid box, while the eastward (u) and northward (v) velocity components are collocated at the corners.

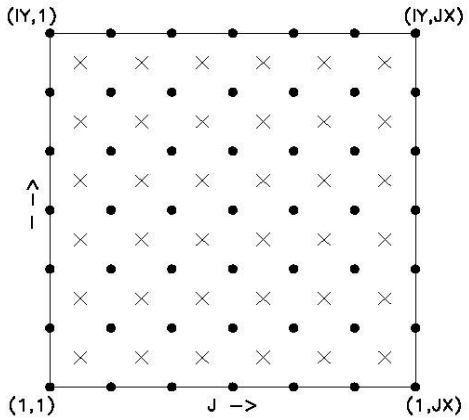

Figure 8.1: Schematic representation showing the horizontal Arakawa B-grid staggering of the dot and cross grid points.

The center points of the grid squares will be referred to as cross points, and the corner points are dot points. Hence horizontal velocity is defined at dot points. Data is input to the model, the preprocessors do the necessary interpolation to assure consistency with the grid (http://users.ictp.it/RegCNET/regcm.pdf).

Typical horizontal resolutions for climate application range from 20 to 80 km.

Surface processes are represented via the Biosphere-Atmosphere Transfer Scheme (BATS, Dickinson et al., 1993) and boundary layer physics is formulated following the non-local scheme of Holtslag et al., 1990. Resolvable scale (larger scale) clouds and precipitation are represented via the simplified explicit scheme described by Giorgi and Marinucci (1996) and Giorgi and Shields (1999), which includes a prognostic equation of cloud water content; while non-resolvable (small scale) convective clouds and precipitation are represented by the simplified form of the Kuo-type scheme of Anthes (1997) and Anthes et al. (1987). Radiative transfer calculations are carried out using the radiation package of the NCAR Community Climate Model, version CCM3 (Kiehl et al., 1996). Detailed descriptions of the RegCM3 ca be found in Giorgi et al. (1993a, 1993b, and 1999a) and at http://users.ictp.it/RegCNET/regcm.pdf.

8.2. Dust parameterization in the RegCM3

The representation of dust emission processes is a key element in a dust model and depends on the wind conditions, the soil characteristics and the particle size. Following Marticorena and Bergametti (1995) and Alfaro and Gomes (2001), here the dust emission calculation is based on parameterizations of soil aggregate saltation and sandblasting processes. The main steps in this calculation are: the specification of soil aggregate size distribution for each model grid cell, the calculation of a threshold friction velocity leading to erosion and saltation processes, the calculation of the horizontal saltating soil aggregate mass flux, and finally the calculation of the vertical transportable dust particle mass flux generated by the saltating aggregates. In relation to the BATS interface, these parameterizations become effective in the

model for cells dominated by desert and semi desert land cover. A brief description of the main steps used for dust parameterization in the RegCM is given below, but a detailed discussion is reported in the paper of Zakey et al., 2006.

8.2.1. *Soil aggregate distribution*

In order to characterize the erodible fraction of different types of soils, soil aggregate distributions are provided to the model. In the model, a three-mode lognormal soil aggregate diameter distribution $n(D_p)$ (in cm^{-3}) is associated to each texture class following Zobler (1986): the mass mean diameter (MMD, μm), standard deviation (σ), and soil texture composition used to characterize each textural class are reported in the paper of Zakey et al., 2006. The geographical distribution of this soil information is based on the geographical distribution of soil texture categories widely used in global and meso-scale modeling which are accessible to the public (at ftp://ttp.ucar.edu/mesouser/MM5V3/TERRAIN_DATA). The global texture index distributed at 10 min resolution is aggregated over the simulation domain at the model resolution according to the dominant texture type of a given grid cell.

8.2.2. *Minimum threshold friction velocity and horizontal saltating mass flux*

Soil aggregates can be mobilized if the wind shear at the surface, represented by the wind friction velocity, is sufficiently strong. Marticorena and Bergametti (1995, 1997a,b) showed that the mobilization of a given aggregate size D_p becomes effective above the minimum threshold friction velocity $u^*_t(D_p)$ that is given from the equation:

$$u^*_t(D_p) = u^*_{ts}(D_p) * f_{eff} * f_w \qquad (8.2)$$

where $u^*_{ts}(D_p)$ represents an ideal minimum threshold friction velocity, f_{eff} is a correction factor accounting for the effect of surface roughness. $u^*_{ts}(D_p)$ and f_{eff} follow the parameterization of Marticorena and Bergametti (1995), while f_w is a factor that accounts for the effect of soil moisture content on the threshold friction velocity and it is parameterized according to Fecan et al., 1999.

The horizontal flux (Kg/m*s) change dH_F associated to a given saltating aggregate of size D_p is obtained by the size-dependent expression of the threshold friction velocity and is given by the following equation:

$$dH_F(D_p) = E \cdot \frac{\rho_a}{g} \cdot u^{*3} \cdot (1 + R(D_p)) \cdot (1 - R^2(D_p)) \cdot dS_{rel}(D_p) \qquad (8.3)$$

where E is the ratio of erodible to total surface, ρ_a is the surface air density calculated by the model, g is the gravitational acceleration, $dS_{rel}(D_p)$ is the relative surface of soil aggregate of diameter D_p to the total aggregate surface, determined from the above defined soil aggregate distribution. Finally $R(D_p)$ is the ratio of the threshold friction velocity defined in Eq. (8.2) to the friction velocity u^* calculated within each grid cell from the model prognostic surface wind and the surface roughness height.

The total horizontal particle flux is then obtained by the integration of Eq. (8.3) over D_p.

8.2.3. *The vertical transportable dust particle mass flux*

In the sandblasting process, the fine dust transportable particles are released either from saltating soil aggregate disintegration or from surface bombardment by

aggregates. In the model, the distribution of such emitted transportable dust particles is fixed according to a three mode lognormal "emission distribution". The corresponding parameters have been taken from Alfaro and Gomes (2001) and are based on specific studies of Saharan aerosols (table 8.1):

Table 8.1: Dust emission lognormal size distribution parameters.

	Mode 1	Mode 2	Mode 3
D_i (μm)	1.5	6.7	14.2
σ_i	1.7	1.6	1.5

D_i represents the median diameter associated to the i_{th} emission mode and σ_i is the standard deviation. According to Alfaro and Gomes (2001) for a given saltating soil aggregate of diameter D_p, the vertical mass emission flux (Kg/m²*s) corresponding to each emission mode *i* is obtained by:

$$F_{dust,i}(D_p) = \left(\frac{\pi}{6}\right) \cdot \rho_{p\cdot} \cdot D_i^{\,3} \cdot N_i \qquad (8.4)$$

where ρ_p is the aggregate density taken to 2.65 g/cm^3, N_i is the elementary vertical dust particle number flux integrated over the soil aggregate size range, and D_i is given in table 8.1.

The above defined dust emission flux is partitioned in a number of size bins that are effectively transported by the model. In the basic configuration adopted in this work this number is set to 4 and each transport-bin is considered as a distinct tracer and is transported according to the tracer transport equation defined in Salomon et al., 2006. The transport bin sizes considered in the model are reported in table 8.2.

Table 8.2: Transport bin sizes in the standard model. α^*_{ext} is the bin specific extinction coefficients

Transport bin sizes (μm)	0.01-1	1-2.5	2.5-5	5-20
$\alpha^*_{ext}(m^2 g^{-1})$	2.85	0.86	0.37	0.13

The bin specific extinction coefficients $\alpha^*_{ext}(m^2 g^{-1})$ obtained from Mie calculations and characteristic of the 350-640 nm model spectral band. The specific extinction coefficient $\alpha^*_{ext}(m^2 g^{-1})$ (mass extinction cross section) is defined in OPAC as the ratio of extinction coefficient $\alpha_{ext}(km^{-1})$ to the aerosol mass M ($\mu g * m^{-3}$):

$$\alpha^*_{ext} = \frac{\alpha_{ext}}{M} \qquad (8.5)$$

8.2.4. *Dust specific extinction coefficient*

Dust optical properties are computed for each size bin and each spectral band of the RegCM radiation scheme (18 wavelength bands) using the Mie theory.

The refractive index, which depends on wavelength, has been taken from the OPAC database (Hess et al., 1998) for the band 350-640 nm, centered around 500 nm. In particular, the refractive index has been set to 1.55-0.0055i. The above defined three mode emission distribution (Table 8.1) has been considered as the sub-bin particle size distribution for Mie calculation. To estimate representative optical properties, a Mie scattering code has been used considering a set of 16 typical emission particle distributions representing different arid soil component/wind speed combinations given by Alfaro and Gomes 2001. The different specific extinction coefficient $\alpha^*_{ext}(m^2 g^{-1})$ are obtained from each of these combinations ranges, for example from 1.87 $m^2 g^{-1}$ for a friction velocity of 35 cm s^{-1} over alumino-silicated

silts to 2.99 $m^2 g^{-1}$ for a friction velocity of 80 cm s^{-1} over coarse sand (Zakey et al., 2006). "Climatic" specific extinction coefficients have been obtained by averaging the results of the 16 different combinations for each of the transport bins reported in table 8.2. The aerosol optical depth AOD is calculated from the extinction coefficient $\alpha_{ext}(km^{-1})$ (8.5) of the chosen aerosol type in combination with the distribution of aerosol particles with height $N(h)$ which is predefined in OPAC (Hess et al., 1998):

$$AOD = \sum_j \alpha_{ext,j} N_j(h) = \sum_j \alpha_{ext,j} N_j(0) \int_{H_{j,\min}}^{H_{j,\max}} e^{-\frac{h}{Z_j}} dh \qquad (8.6)$$

where $\alpha_{ext,j}$ is the extinction coefficient of the *j* aerosol in layer with a thickness of $H = (H_{i,\max} - H_{j,\min})$, normalized to 1 particle cm^{-3}, $N_j(0)$ is the number density of the aerosol type at sea level in the aerosol layer *j*, *h* is the altitude above ground in kilometers and *Z* the scale height in kilometers, which describes the slope of the profile.

8.3. Comparison of model and experimental data

A particularly intense dust storm occurred over the central Mediterranean basin from 15 to 26 July 2003. In order to provide an overview of the July 2003 Saharan dust outbreaks, the true-colour images obtained between July 15 and July 26, 2003, from the Sea Wide Field-of-view Sensor (http://www.nrlmry.navy.mil/aerosol/) on board the NASA SeaStar spacecraft, are shown in figure 8.2. One picture per day is shown for the whole Mediterranean region, as a composite of the data collected between 11 and 13 UTC along the spacecraft polar orbit. In addition to satellite images, horizontal and vertical

displacement of the dust plumes based on lidar data (Tafuro et al., 2006), support the presence of the dust storm during the analyzed period.

8.3.1 *Comparison between experimental and RegCM model data for the 10010 km * 4542 km domain*

As told before, the first simulation for the dust event of July 2003 was made using a domain (figure 8.3) of ~ 10010 km * 4542 km centered at a latitude of 30º and a longitude of 5º, with a horizontal spacing of 50 Km.

The sand sources inside the chosen domain for the model simulation are shown in figure 8.3. The colors scale represents percentages sand source.

AODs, extinction coefficients α_{ext}, PM_{10} and PTS concentrations, obtained from the RegCM model and from the available observations over the central Mediterranean are compared in this section.

8.3.1a *Comparison between RegCM , AERONET and MODIS AODs at 550 nm*

Figures 8.4, 8.5, 8.6 and 8.7 show daily simulated AODs by the RegCM model at 550 nm and daily AODs estimated from MODIS Land_Ocean algorithm at 550 nm for the period 15-17 July, 18-20 July, 21-23 July and 25– 26 July, 2003, respectively.

Figure 8.4a shows that on 15 July the modeled dust plume starts to move from the Western Africa. Analogously, the available data obtained by MODIS Land-Ocean products show that on 15 July satellite AODs assume higher values (~0.5 – 0.8) in the Western part of Mediterranean (figure 8.4d).

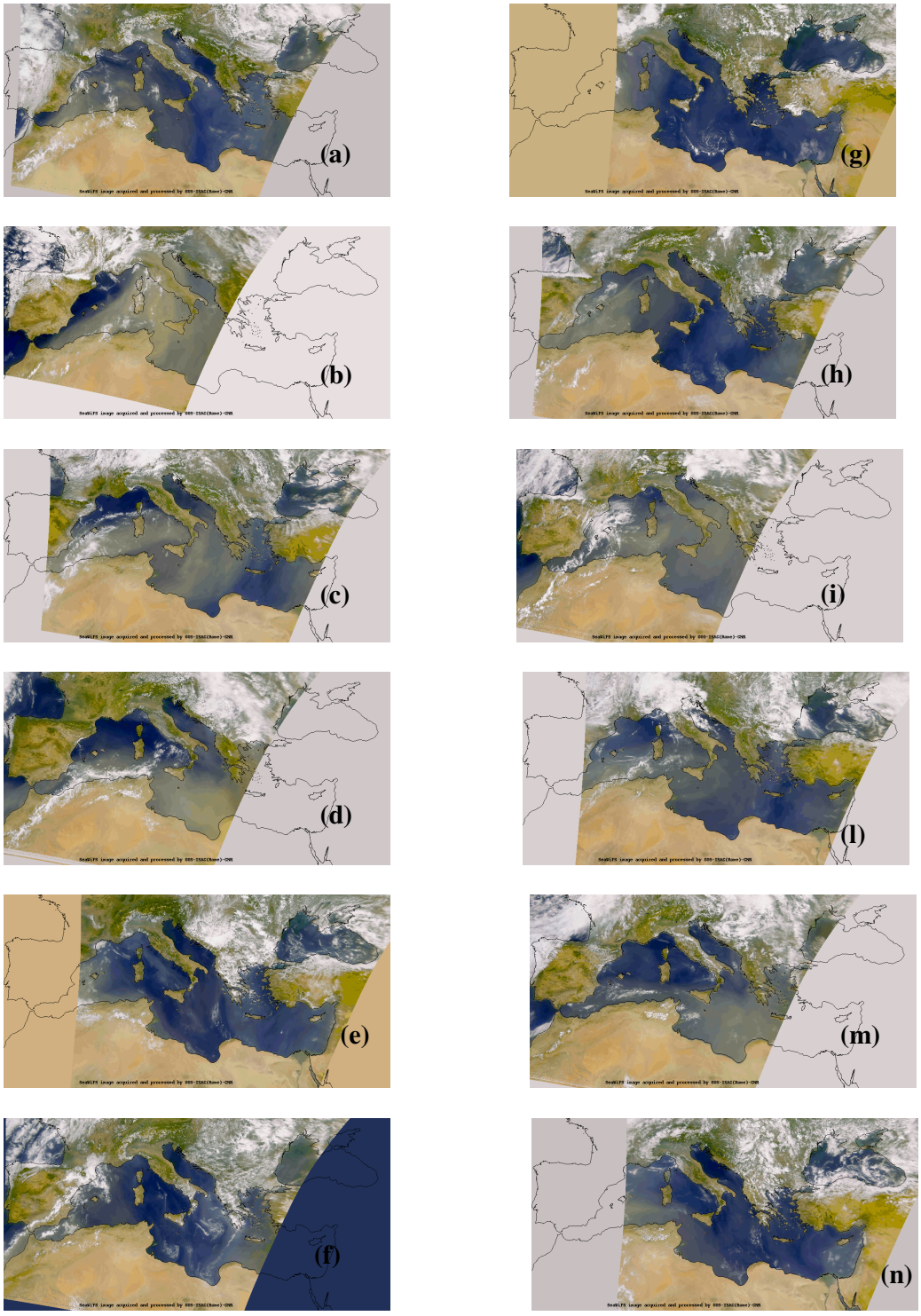

Figure 8.2: SeaWifs true-colour images of (a) 15 (11:57 UTC), (b) 16 (12:39 UTC), (c) 17 (11:40 UTC), (d) 18 (12:21 UTC), (e) 19 (11:23 UTC), (f) 20 (12:04 UTC), (g) 21(11:07 UTC), (h) 22 (11:48 UTC), (i) 23 (12:29 UTC), (l) 24 (11:31 UTC), (m) 25 (12:11 UTC), and (n) 26 (11:14 UTC), July 2003.

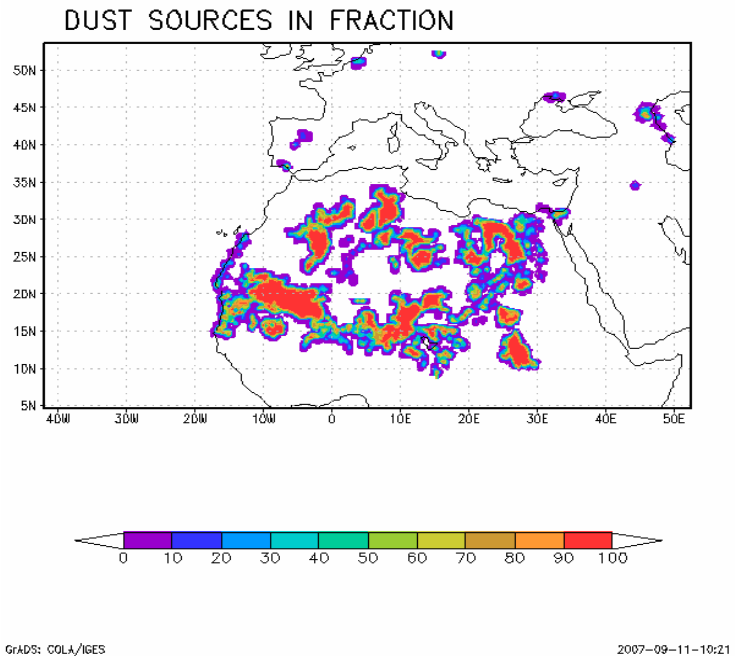

Figure 8.3. Model domain of ~ 10010 km * 4542 km centered at a latitude of 30º and a longitude of 5º, with a horizontal spacing of 50 Km

Moreover, figure 8.4b shows that on 16 July the simulated dust plume moves toward the Western Mediterranean reaching the Sicily and covering all the Sardinia. In accordance with model data, figure 8.4e shows that on 16 July MODIS AODs assume higher values over the Sardinia (≥ 1) and over the Sicily (~ 0.5 – 1).

Model data show that the dust plume extension over the central Mediterranean Basin on July 17 (figure 8.4c). This latter result is also consistent with that obtained from the MODIS satellite reported in figure 8.4f. In fact, figure 8.4f shows that the dust

plume on 17 July covers Sicily and south Italy where MODIS aerosol optical depths reache higher values, ranging from ~ 0.8 -1.

Model data show that the dust plume on 18 July (figure 8.5a) extends over the Southern Mediterranean. Analogously, we observe from figure 8.5d that on 18 July MODIS AODs take higher values (in the range 0.6 -1) over the southern Mediterranean and the Sicily.

Figures 8.5b, 7.5c reveal the lack of dust plumes indicate that over the central Mediterranean on July 19 and 20. Analogously, figures 8.5e and 8.5f reveal that MODIS AOD values assume rather low values (AOD $\leq$ 0.5) over the Mediterranean from 19 to 20 July. This latter result allows to suppose, in accordance with the model's results, that on 19 and 20 July, the central Mediterranean was not affected by Saharan dust. These latter results are confirmed by the satellite images of figures 8.2e and 8.2f

In addition, figures 8.6a and 8.6d show that on July 21 the central Mediterranean is not affected by dust plume. On 22 July figures 8.6b shows a modeled dust plume that resides in the eastern part of the Mediterranean, reaching the Sicily and the south of Italian peninsula. Analogously, MODIS AODs assume on 22 July higher values of about 0.5-1 over the east part of the Mediterranean basin (figure 8.6e).

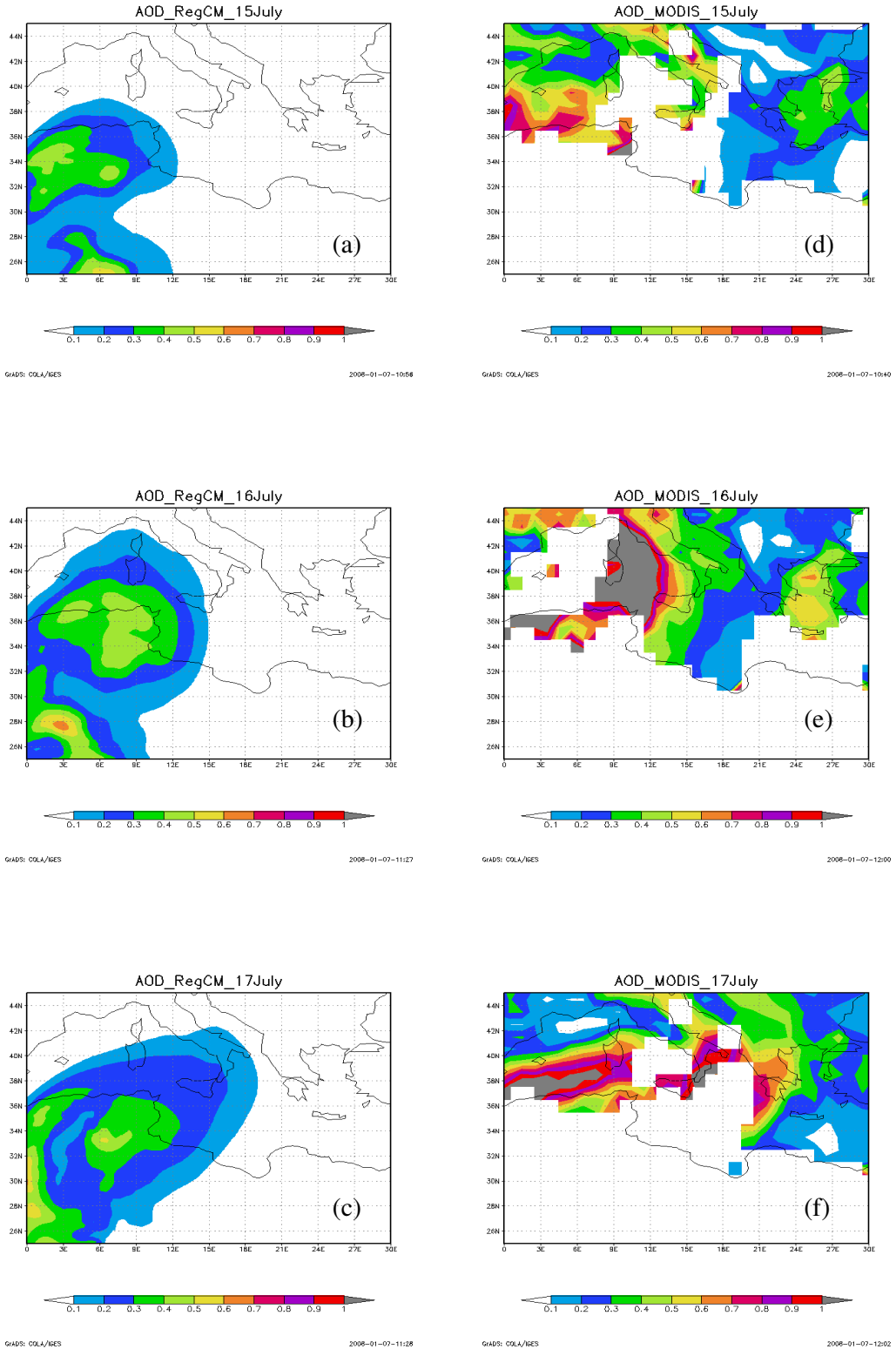

Figure 8.4. (a)-(c) RegCM simulated AOD at 550 nm on (a) 16, (b)17 and (c) 18 July 2003; (d)-(f) MODIS Land-Ocean AOD at 550 nm on (d) 16, (e)17 and (f) 18 July 2003.

The 23 and 24 July also are characterized by the advection of dust plume towards the central Mediterranean, as illustrated by the satellite images (figures 8.2i, 8.2l). In particular, the simulated desert dust plume covers almost completely the central Mediterranean on 23 (figure 8.6c) and on July 24 (figure 8.7a). In accordance with the last results, the MODIS data reveal the presence of a dust plume predominates over the central Mediterranean Basin and that appears more intense in the western part of the Basin closed to the Sardinia on 23 July. On 24 July (figure 8.7c) the available MODIS AOD values show that the dust plume persists over south Italy.

Finally, on 25 (figure 8.7b) and 26 July (figure 8.7c) the model shows a less intense dust plume that doesn't affects the central Mediterranean basin. Analogously, satellite images of figures 8.2m and 8.2n indicate that the 25 and 26 July are dust-free days over the central Mediterranean basin. In accordance with model's simulations maps and SeaWifs satellite images, figures 8.7e and 8.7f show that on 25 and 26 July MODIS AODs assume values ≤ 0.7 over the central Mediterranean and – Italy.

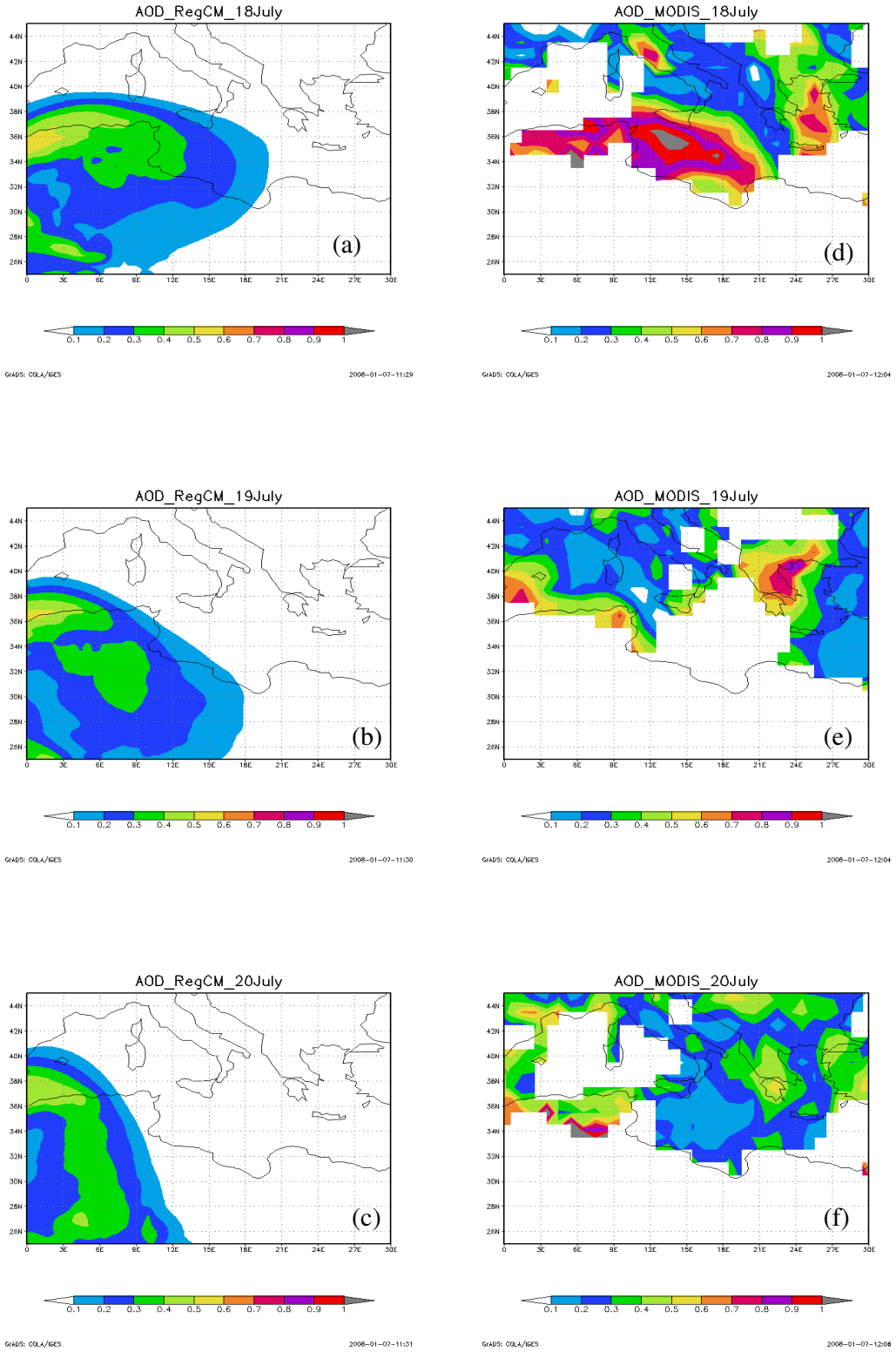

Figure 8.5. (a)-(c) RegCM simulated AODs at 550 nm on (a) 18, (b)19 and (c) 20 July 2003; (d)-(f) MODIS Land-Ocean AODs at 550 nm on (d) 18, (e)19 and (f) 20 July 2003.

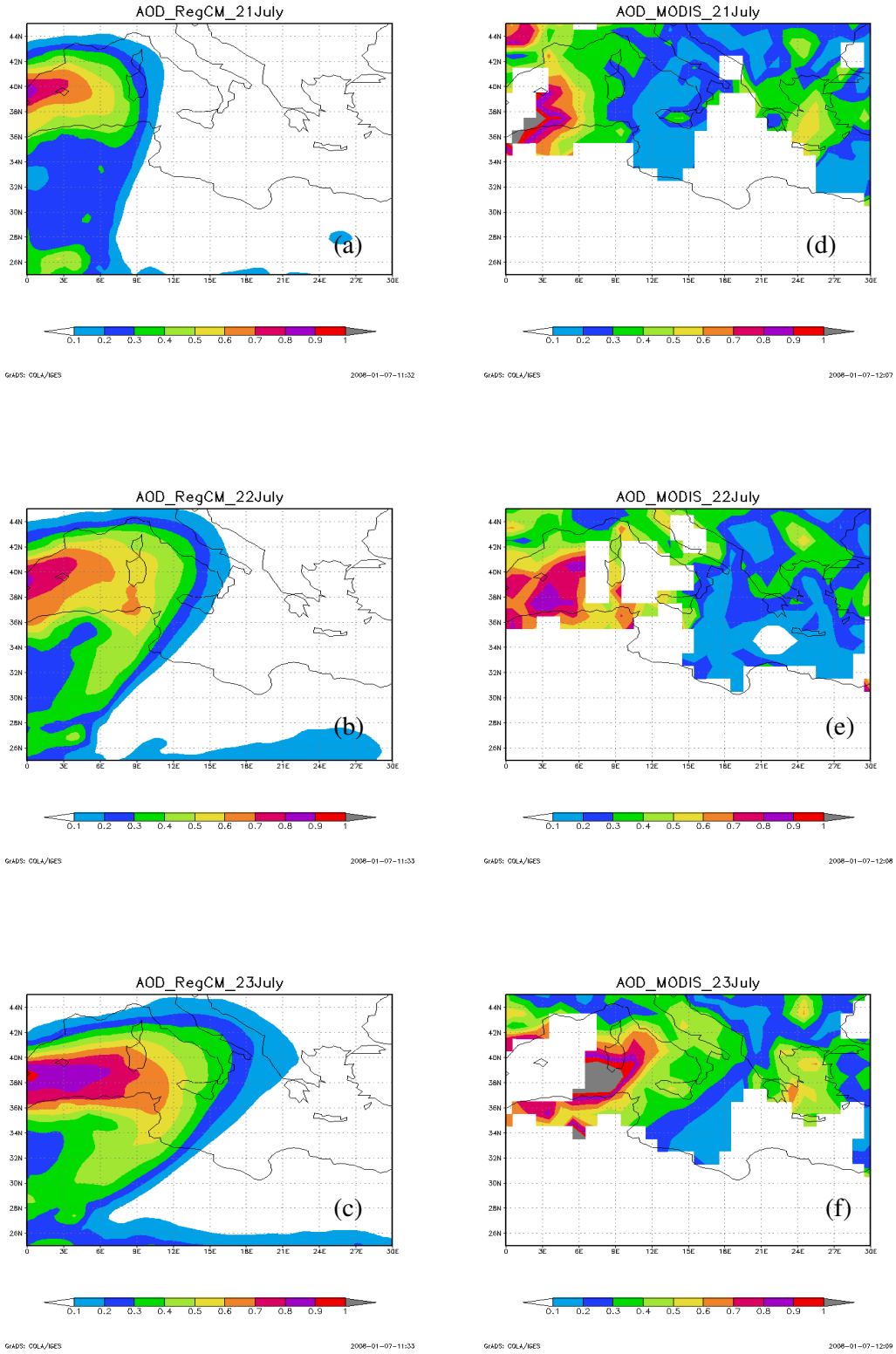

Figure 8.6. (a)-(c) RegCM simulated AODs at 550 nm on (a) 21, (b) 22 and (c) 23 July 2003; (d)-(f) MODIS Land-Ocean AODs at 550 nm on (d) 21, (e) 22 and (f) 23 July 2003.

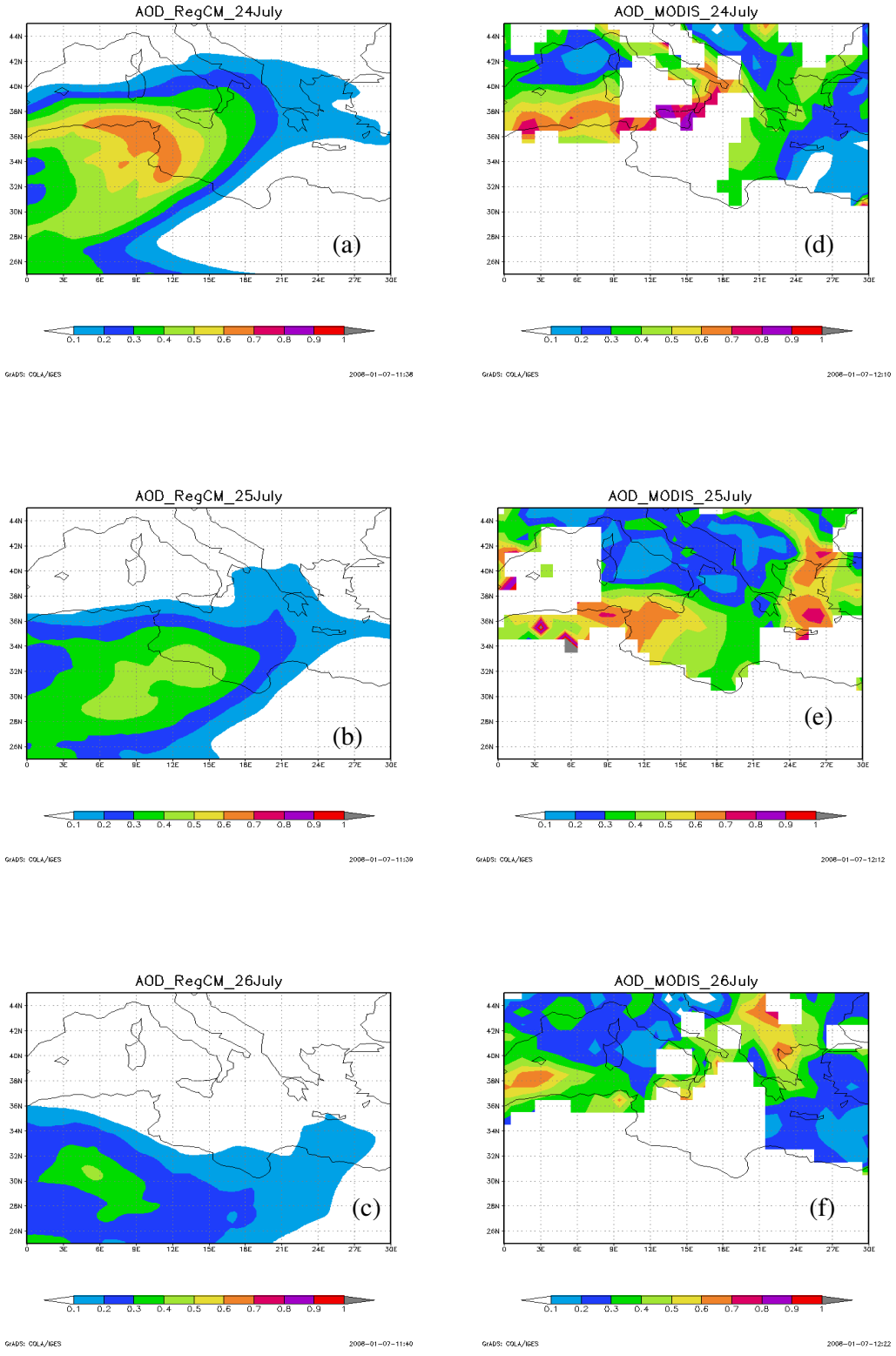

Figure 8.7. (a)-(c) RegCM simulated AODs at 550 nm on (a) 24, (b) 25 and (c) 26 July 2003; (d)-(f) MODIS Land-Ocean AODs at 550 nm on (d) 24, (e) 25 and (f) 26 July 2003.

In order to test the RegCM performance for the studied dust outbreak over the central Mediterranean basin, model daily AODs obtained from 15 to 26 July 2003 are compared in figure 8.8 to daily AERONET and MODIS Land-Ocean AOD at 550 nm over four Mediterranean sites: Lecce (figure 8.8a), Lampedusa (figure 8.8b), Etna (figure 8.8c) and Oristano (figure 8.8d). In particular, in figure 8.8 the black, red and blue lines represent RegCM, AERONET and MODIS daily temporal plots. MODIS Land-Ocean AODs, retrieved by MODIS Atmosphere Parameter Subset Statistics (MAPSS) (http://modis-atmos.gsfc.nasa.gov/validation_corrdata.html), and the RegCM AODs are obtained for a window size of 50x50 km^2 centered on the four Mediterranean sites.

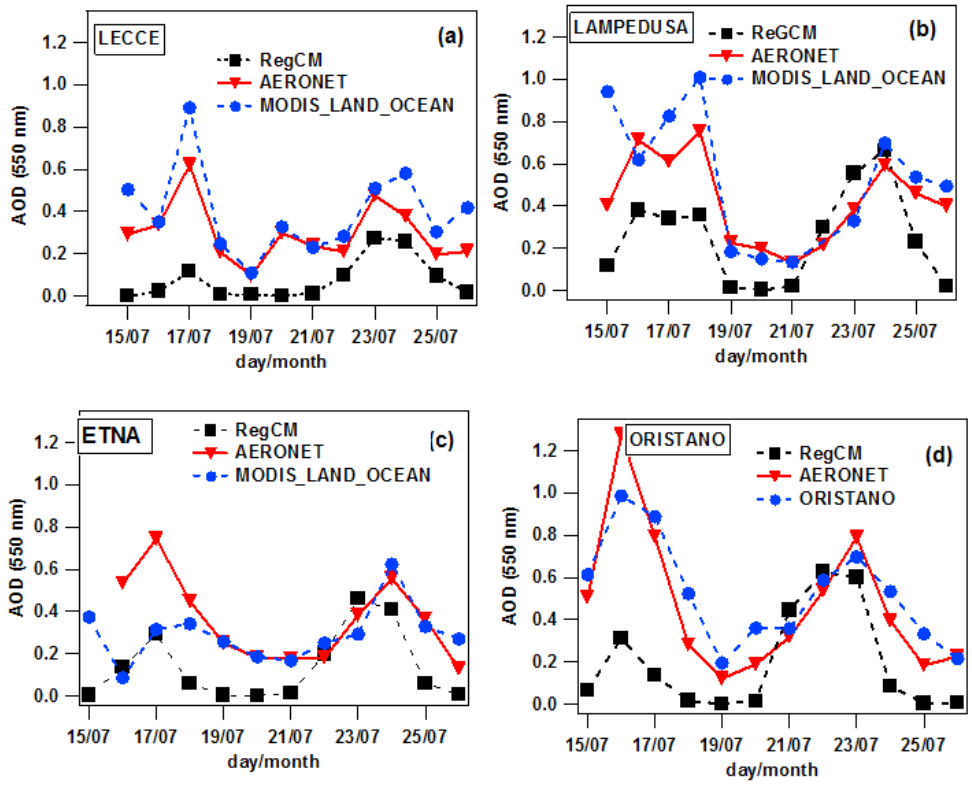

Figure 8.8. Temporal plots of AODs at 550 nm obtained by RegCM model (black line), MODIS Land-Ocean (blue line) and AERONET (red line) over (a) Lecce, (b) Lampedusa, (c) Etna and (d) Oristano.

We can observe from figure 8.8 that AOD data show a strong temporal variability linked to the two specific dust outbreaks of 17 and 22-23-24 July 2003. This variability is well reproduced by the model outputs (black line).

In particular, we can see from figure 8.8a that the RegCM simulated AOD follows at Lecce the same temporal evolution obtained by AERONET and MODIS measurements. However, the RegCM model tends to underestimate the AOD along all the analyzed period.

Figure 8.8b shows that at Lampedusa modeled AODs reproduce very well the temporal evolution obtained from AERONET, but assume lower values than those obtained from both AERONET and MODIS Land-Ocean measurements. On the contrary, during the dust event of 24 July, the RegCM AODs are better correlated to the available observations.

Moreover, on figure 8.6c we observe that Etna simulated AODs are consistent only with that obtained by MODIS observations on 17 July. In contrast, we observe a better correlation between observed and modeled data during the event of 22-23-24 July.

Finally, figure 8.8d shows that simulated AODs catch the dust event of 17 July of Oristano site, but assume lower values with respect to the corresponding AERONET and MODIS values. In contrast, modeled AOD values of 21, 22 and 23 July are consistent with those obtained by the observations.

In conclusion, the results presented in this section have demonstrated that the RegCM- model was able to simulate the occurrence of strong dust outbreaks over the four studied Mediterranean sites. However, the comparison with AERONET and MODIS Land-Ocean AOD shows that the simulated AOD intensities are not always well represented. In fact, the accordance between the simulated and the AERONET and MODIS AODs is quite significant on 22, 23 and 24 July at the Lampedusa, Etna

and Oristano sites while on 17 July the intensity of dust event appears smaller that the real. We believe that this latter result may be due to the fact that the model AOD obtained by the RegCM model is proportional only to the dust burden, neglecting the contribution of aerosol of different types, AERONET and MODIS AODs are representative of the total aerosol load.

8.3.1b *Comparison between Lidar and RegCM simulated extinction profiles*

In this paragraph, aerosol extinction profiles by lidar measurements at Etna and Lecce are compared to the corresponding profiles provided by the RegCM model. An elastic-Raman lidar employing a XeF excimer laser is routinely used at the Physics Department of Salento's University for the aerosol vertical monitoring at 351 nm and it allows deriving vertical profiles of aerosol extinction α_{ext} coefficients (km^{-1}) (De Tomasi and Perrone, 2003). The vehicle- mounted lidar system (VELIS, Gobbi, 2000), operating at Mount Etna, is a elastic, polarization-sensitive lidar that employs a Nd:Yag laser that provides tropospheric aerosol depolarization and backscatter coefficient profiles at 532 nm.

Figure 8.9 compares RegCM simulated extinction coefficient profiles $\alpha_{ext}(km^{-1})$ at 550 nm and at two different hours (blue and black lines) and lidar (red line) at 351 nm and 550 nm, respectively, at Lecce site on (a) 16 (b) 24 July. As a first order of approximation, one can assume that both the lidar and modeled extinction profiles are proportional to the actual amount of dust in a given atmospheric layer. The simulated values have been interpolated from the original sigma level grid to a regular height grid for comparison (Zakey et al., 2006).

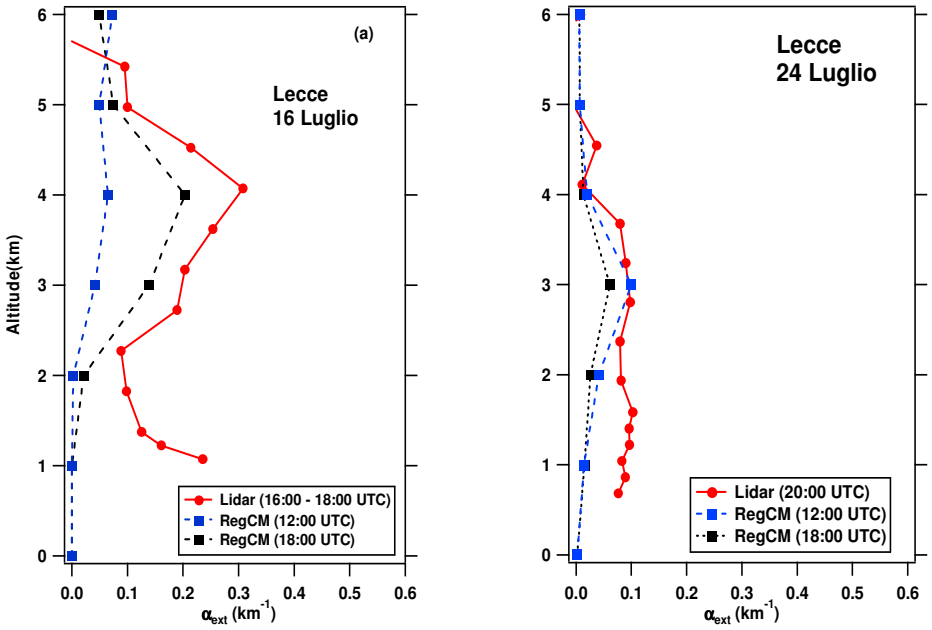

Figure 8.9. Comparison between RegCM (black and blue line) $\alpha_{ext}(km^{-1})$ profiles calculated at two different hours at 550 nm, and lidar (red line) $\alpha_{ext}(km^{-1})$ profiles at 351 nm at Lecce on (a) 16 and (b) 24 July 2003.

In figure 8.9a the red line represent Lidar extinction profile between 16:00 and 18:00 UTC, while blue and black lines are the modeled profiles at 12:00 UTC and 18:00 UTC, respectively. Figure 8.9a shows that on 16 July both the RegCM and the lidar reveal the presence of a dust layer located between 3 – 5 km, and we can observe that the accordance between RegCM and lidar profiles is better for the model profile calculated at 18:00 UTC. In addition, we can see that the simulated α_{ext} assumes lower values than that observed at each altitude. The accordance between lidar and RegCM α_{ext} profiles appears better for the model profile calculated at 12:00 UTC.

Figure 8.9b shows the comparison between Lidar (at 20:00 UTC) (red line) and RegCM α_{ext} profiles at 12:00 UTC (blue line) and at 18:00 UTC (black line) at Lecce on 24 July. We observe that lidar profile shows a dust layer between ~1 and 4 km and a α_{ext} RegCM profile (at 18:00 UTC and 12:00 UTC) characterized by a less intense dust layer between 2 and 4 km.

However, it worth observing that Lidar and RegCM extinction profiles have been calculated at 351nm and 550 nm, respectively. Then, the observed differences in figures 8.9a and 8.9b may be attribute to the different wavelengths. In addition, we can note that the accordance between the Lidar and RegCM $\alpha_{ext}(km^{-1})$ profiles makes worse for altitudes below about 2 km, both in figure 8.9a and 8.9b. This last result may be due to the fact that for altitudes lower than 2 km there is an higher contribution of non dust aerosols.

The comparison between AODs retrieved integrating (between 0 and 6 km) the extinction coefficient α_{ext} values obtained by the RegCM model and by lidar measurements confirms the latter results. In fact, we find that on 16 July over Lecce the AODs calculated by lidar α_{ext} measurements between 16:00 and 18:00 UTC is 0.764, while AODs obtained by RegCM α_{ext} values are 0.019 and 0.46 at 12:00 UTC and 18:00 UTC, respectively. On 24 July, we find AODs calculated from lidar α_{ext} measurements of 0.28 and values of AODs calculated by model α_{ext} of 0.18 and 0.12 at 12:00 UTC and 18:00 UTC, respectively.

The comparison between simulated RegCM at 550 nm(black and blue lines) and lidar at 532 nm (red lines) α_{ext} profiles, referring to Etna site, are reported in figure 8.10 for (a) 17 and (b) 24 July.

We can see from figure 8.10a that on 17 July the lidar profile individuates a dust layer that vary between 1 and 4.5 km and assumes α_{ext} values between 0.5 and 0.15 km^{-1} at 14:04 UTC. Figures 8.10a shows also that the model profiles both at 06:00 UTC and at 12:00 UTC individuates a dust layer for heights between 1 and 5 km, but characterized by a lower α_{ext} intensity than those assumed by the lidar one.

Figure 8.10b shows on 24 July a lidar dust layer at 19:32 UTC between 1 and 6 km. In addition, figure 8.10b shows a dust layer simulated by RegCM model in the range 1- 5km at both 12:00 UTC and 18:00 UTC. However, we can note that the α_{ext} RegCM profile calculated at 18:00 UTC shows a better accordance with the profile provided by the lidar measurements.

Comparisons of AODs calculated integrating α_{ext} values (between 0 and 6 km) retrieved by model and lidar measurements show that on 17 July the lidar-retrieved AOD takes a value of 0.52, while AODs from RegCM assume a value of 0.19 and 0.21 at 12:00 UTC and 18:00 UTC, respectively. On the contrary, on 24 July we find a value of AOD from lidar α_{ext} of 0.33 and values of AODs from RegCM α_{ext} of 0.16 and 0.31 at 12:00 UTC and 18:00 UTC, respectively.

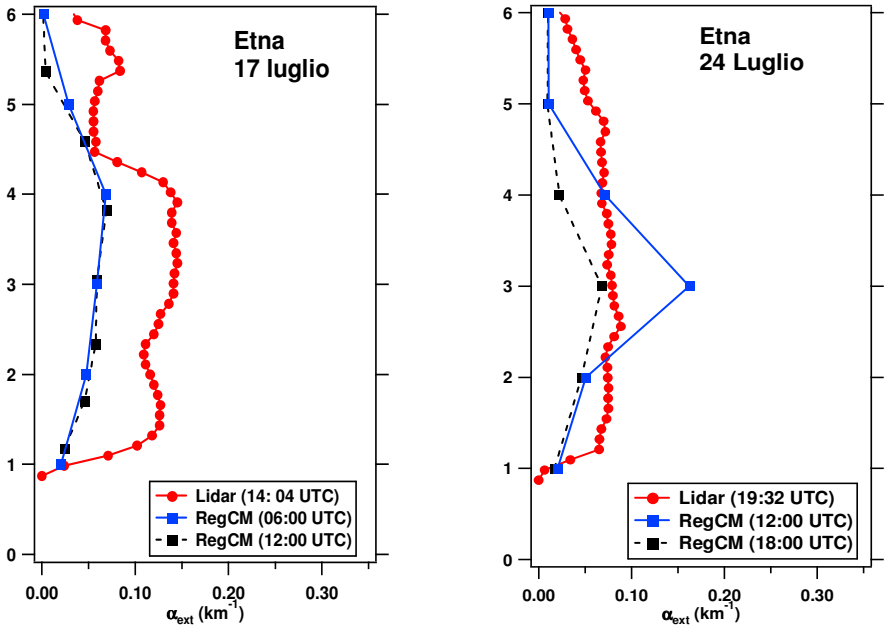

Figure 8.10. Comparison between RegCM (black and blue line) $\alpha_{ext}(km^{-1})$ profiles calculated at two different hours at 550 nm, and lidar (red line) $\alpha_{ext}(km^{-1})$ profiles at 532 nm at Etna on (a) 17 and (b) 24 July 2003.

In conclusion, the results obtained in this paragraph have demonstrated that over the two studied sites (Lecce and Etna) the simulated α_{ext} profiles are able to capture the dust amounts but it is always underestimated by RegCM. This result may be associated to the model dust burden underestimation discussed in paragraph 8.3.1a. In fact, we can note that the better accordance between RegCM and lidar α_{ext} profiles is observed over Lecce and Etna on 24 July when the agreement between simulated and observed AOD was better (figure 8.8).

8.3.1c ***Comparison between mass concentration (PM) by ground-based particulate matter samplers and by RegCM model.***

Ground aerosol parameters as PM mass concentrations ($\mu g/ m^3$) provided by ground-based particulate matter samplers and by RegCM model over two different sites in Lecce, for the period 15-26 July 2003, are compared in this paragraph.

In particular, figure 8.11a shows the comparison between the total suspended particulate matter (PTS) detected by a sampler located at Lecce (site 1) at a latitude of 40.33N and a longitude of 18.179E (red line) and the PTS simulated by the RegCM model over the same site (black line). Figure 8.11b shows the comparison between the PM_{10} (particulate matter with a diameter $\leq$ 10μm) concentrations obtained by a particulate sampler equipped with PM_{10} inlet located at Lecce (site 2) at a latitude of 40.34N and a longitude of 18.159E (red line) and the RegCM simulated PTS concentrations (black line) at the same altitude and longitude.

One can observe from figure 8.11 that model PM mass concentrations follow the time evolution of measured PTS and PM_{10} concentrations and these last data further more show that the model is able to capture the two dust events occurred in the studied period. In particular, figure 8.11 highlights that during the first dust event of

17 July 2003 the model tends to underestimates the PTS mass concentrations, while during the second dust outbreak of 24 July 2003 the model overestimates the PTS mass concentration. We note that the accordance between simulated and observed PM mass concentrations is better in figure 8.11a. In fact, we can note that for the two main peaks of the temporal plot the difference between PTS_LECCE and PTS_RegCM is of about 20% on 17 July and ~70% on 24 July.

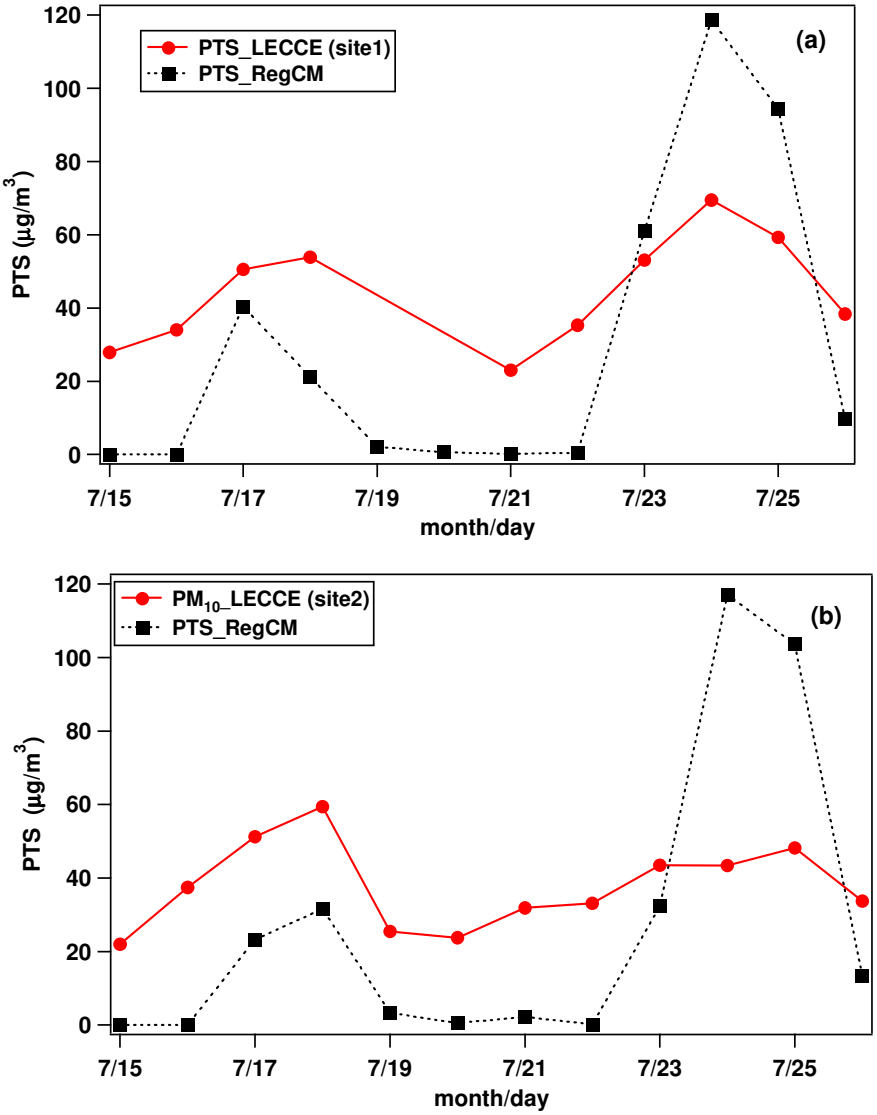

Figure 8.11. (a) Comparison of the temporal plots of the PTS ($\mu g / m^3$) detected by a sampler located at Lecce (site 1) at a latitude of 40.33N and a longitude of 18.179E (red line) and the PTS simulated by the RegCM model over the same site (black line); (b) Comparison of the temporal plots of PM_{10} obtained at Lecce (site 2) at a

latitude of 40.34N and a longitude of 18.159E (red line) and the PTS calculated by the RegCM model (black line).

On the contratry, figure 8.11b shows that the differences between PM_{10}_LECCE and PTS_RegCM is of about 47% on 18 July, while the simulated PTS is about the double of the simulated PM_{10} on 24 July However, this latter result can be ascribed to the fact that the simulated PTS mass concentration is due to the contribution of aerosols of all sizes, while the observed PM_{10} is due to particles with diameter ≤ 10μm.

8.3.2 *Comparison between experimental and RegCM data for the 4995km*2227km domain*

The second simulation performed in this study was made for a domain, shown in figure 8.12, of ~ 4995km*2227km centered at a latitude of 30º and a longitude of 5º with a horizontal spacing of 50 Km. The simulation started on 1 July 2003, 00:00 UTC and ended on 30 July 2003, 18:00 UTC.

In this paragraph, the model data from the two simulation domains are compared with AERONET and MODIS AOD measurements retrieved over four Mediterranean sites (Lecce, Lampedusa, Oristano and Etna) in order to understand how the size of the simulation domain may influence model's results.

Figure 8.13 shows the temporal plot of the AOD at 550 nm obtained by the RegCM model using the big-domain (~ 10010 km * 4542 km) (black line) and the small-domain (~ 4995km*2227km) (grey line) and the AODs from AERONET (red line) and MODIS Land-Ocean (blue line) observations at 550 nm over (a) Lecce, (b) Lampedusa, (c) Etna and (d) Oristano.

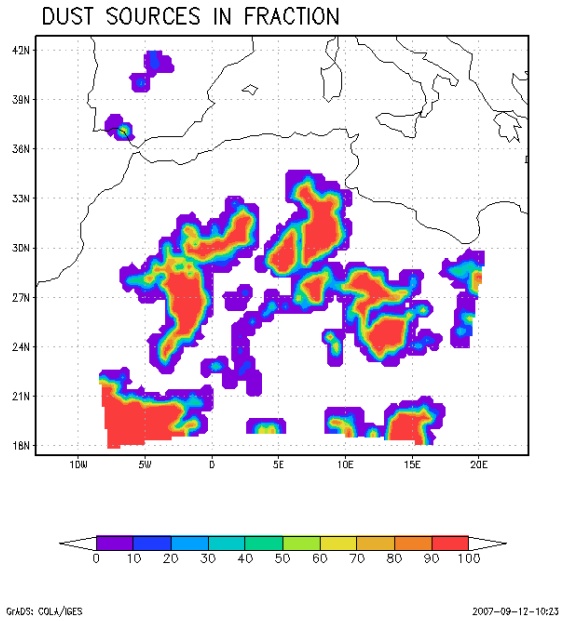

Figure 8.12. Model domain of ~ 4995km*2227km centered at a latitude of 30º and a longitude of 5º with a horizontal spacing of 50 Km

Figure 8.13 clearly shows that the results obtained by the implementation of the model with a small-domain (figure 8.12) appear not in good accordance with the observed AODs values. In particular, over Lecce (figure 8.13a) and Oristano (figure 8.13d) the small-domain simulation gives AOD values that are not in accordance with MODIS and AERONET AODs.

Figure 8.13b shows that at Lampedusa the small-domain simulation (grey line) appears to capture well the first dust outbreak occurred from 16 to 18 July, while tends to underestimate the second dust outbreak of 23-25 July. On the contrary, in figure 8.13c we can observe that the AOD values obtained by the small-domain simulation (grey line) are in good accordance with those retrieved by the big-domain

simulation (black line) and the MODIS observations (blue line) only during the first dust event.

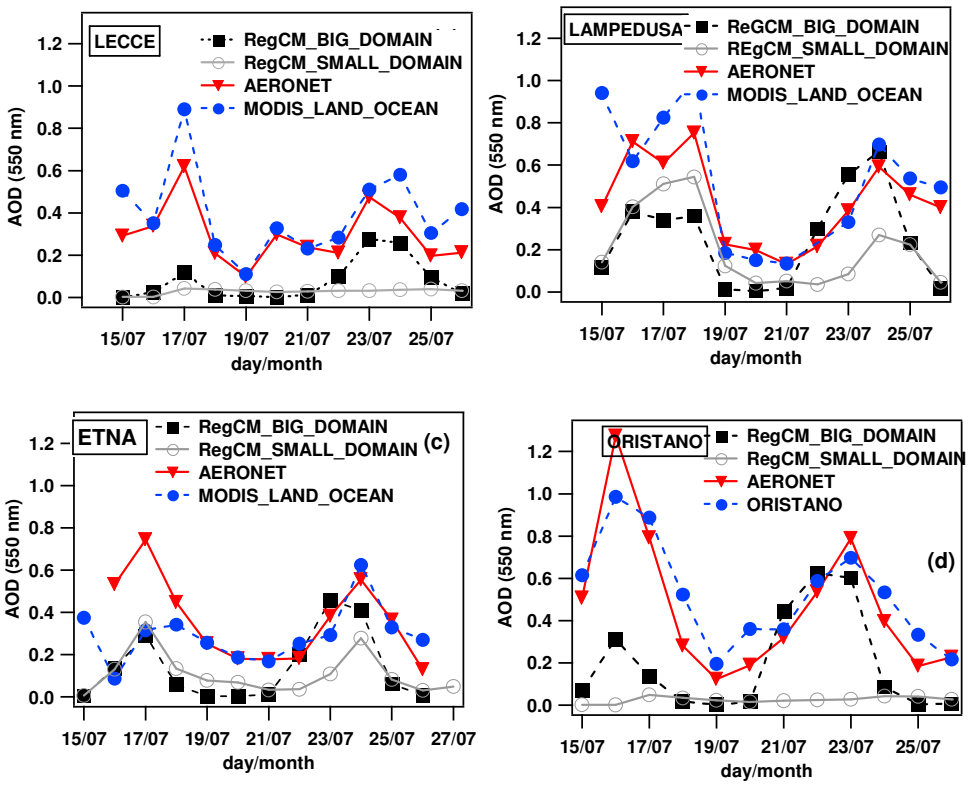

Figure 8.13. Temporal plots of AODs at 550 nm obtained by RegCM model over the 10010 km * 4542 km domain (black line) and over the 4995km*2227km domain (grey line), MODIS Land-Ocean (blue line) and AERONET (red line) over (a) Lecce, (b) Lampedusa, (c) Etna and (d) Oristano.

In summary, the results obtained in figure 8.13 have revealed that the AOD values obtained by the implementation of a model run with a big domain, including a larger part of the Africa continent, are better than those obtained by the model run made for a smaller domain. This latter result can be ascribed to the fact that, reducing the size of the model's domain, we tend to automatically exclude a consistent fraction of dust sources that are present in the African continent. The reduction of the Saharan

sources should affects directly the magnitude of the simulated AOD when compared with the observed AOD.

8.4. Conclusions

In this chapter, preliminary results obtained over the Mediterranean Basin by the implementation of a dust module within the regional climate modeling framework RegCM (Version 3.1), developed at the Abdus Salam International Centre for Theoretical Physics (ICTP), Trieste, are presented. The aim of this study is to test the RegCM model performance in order to contribute to the establishment of models more dependent on measurements. In particular, for the test simulation we have considered two strong Saharan dust outbreaks that occurred in the second half of July 2003. Comparisons with observation have shown that the RegCM model is able to simulate the occurrence of strong dust outbreaks.

In particular, comparisons between model data obtained over a domain of ~ 10010 km * 4542 km, with observation, have revealed that:

- The AODs obtained by the RegCM model follows the same time evolution obtained by AERONET and MODIS Land-Ocean measurements over four investigated sites of the Mediterranean basin. However, the simulated AODs are not always well represented. In fact, at the Lampedusa, Etna and Oristano sites the accordance between the simulated and the AERONET and MODIS AODs is quite significant on 22, 23 and 24 July while on 17 July the intensity of dust event appears smaller that the real.
- The α_{ext} profiles obtained over two Mediterranean sites (Lecce and Etna) by RegCM have shown that the model is able to capture the dust

amounts but it tends to always underestimate the extinction coefficient values. This result may be associated to the model dust burden (AOD) underestimation discussed in the previous point.

- The model follows the time evolution of the measured PTS and PM_{10} for both the investigated locations but it underestimates and overestimates the PTS mass concentrations during the first event of 17 July and the second dust outbreak of 24 July 2003, respectively.

In conclusion, comparisons between experimental and RegCM AODs for a small domain of ~ 4995km*2227km have shown that the AOD values obtained by the implementation of a model run with a small domain are in worse. This last result allows us to suppose that the implementation of a model run with a bigger domain of ~ 10010 km * 4542 km could give better results, closer to the real one.

Overall, the results reported in this chapter have demonstrated the capability of the RegCM model to simulate dust events. We are planning to conduct long term multiyear running including the aerosol sources in addition to dust sources.

CONCLUDING REMARKS

Tropospheric aerosols are responsible of the largest uncertainties in the estimation of the planetary radiative budget because of the high variability of their characteristics and the complex phenomena in which they are involved (Schartz and Andreae, 1996). Some aerosol types, like sulphates (and in particular stratospheric particles after major volcanic eruptions), scatter a significant fraction of the solar radiation (Charlson et al., 1992), producing an increase of the planetary albedo and a cooling of the lower troposphere. On the other hand, strongly absorbing particles, like carbonaceous aerosol and dust, may induce warming effects on the atmosphere (Tegen et al, 1997, Liao and Seinfeld, 1998, Hansen et al., 1993). To estimate the aerosol effects on the radiative budget is necessary to know their concentration, composition, dimensions and physico-chemical properties.

Monitoring of atmospheric aerosol is a fundamental difficult problem. In situ measurements traditionally considered as the most reliable observations are inappropriate for global monitoring of aerosol radiative forcing parameters and usually do not characterize the aerosol in the total atmospheric column (Heintzenberg et al., 1997, Sokoliki et al., 1993 and Toon 1996). Ground-based aerosol remote sensing, with its wide angular and spectral measurements of solar and sky radiation, are suited to reliably and continuosly derive the detailed aerosol optical properties in key locations, but it does not provide global coverage.

On the contrary, satellite remote sensing provide nonintrusive measurements and global coverage. Additionally, refining aerosol optical models is important for improving the accuracy of satellite retrieval algorithms that rely in assumptions of

the optical properties associated with each aerosol type (King et al., 1999, Torres et al., 1998, Stowe et al., 1997). Modeling the aerosol effects on atmospheric radiation, by solving the radiative transfer equation, requires the following aerosol optical properties: aerosol optical depth AOD (loading), phase function (angular dependence of light scattering) and single scattering albedo SSA (ratio of scattering to scattering+absorption). The sensitivity of radiative forcing to observed natural and anthropogenic variations of the above-listed optical properties characterizes the impact of the atmospheric aerosol on climate change (Hansen et al., 1997).

The east Mediterranean basin represents a unique area in terms of suspended particulate matter. Bounded to the north by the European continent and to the south by North Africa it is largely affected by anthropogenic aerosols and seasonal biomass burning from Central and Eastern Europe, maritime and long-range transported polluted air masses from the Atlantic Ocean, mineral dust from North Africa, and sea spray from the Mediterranean sea itself.

The main goal of this work was to contribute to the aerosol properties characterization over the Mediterranean basin using a combination of measurements performed at the University of Salento of Lecce , on south-east Italy, (40.33ºN, 18.10ºE) by a sun/sky photometer, operating in the framework of the AERONET network, and MODIS satellite data. In addition, a regional climate model (RegCM) has been used to simulate the main aerosol properties during a dust event occurred in the Mediterranean and compare modelled data with observations.

The main aims of the research activity of my PhD course were:

- to provide results on the main aerosol optical and microphysical properties (e.g. aerosol optical depth, volume size distribution, real and imaginary refractive index, single scattering albedo,…) retrieved over the Mediterranean analyzing AERONET sunphotometer measurements.

In particular, sunphotometer measurements performed at the Physics Department of University of Salento from March 2003 to March 2004 have been analyzed to get results on the characterization of aerosol load and dominant aerosol types over south-east Italy. Temporal plots of the main aerosol parameters at 441 nm have revealed a significant seasonal variability of aerosol load, size distribution and chemical composition. In particular, it has been found that aerosol optical depth AOD and single scattering albedo SSA day-averaged values span the 0.2-0.4 and 0.93-0.95 range, respectively, in spring-summer and the 0.1-0.2 and 0.97-0.98 range respectively in autumn-winter. In addition, the analysis of the frequency of occurrence plots of AOD values has shown two dominant modes peaked at 0.049±0.008 and 0.20±0.03 that can be considered representative of the autumn-winter and spring-summer, respectively. Analogously, the SSA frequency of occurrence plot showed two mode peaked at 0.974±0.003 and 0.94±0.01 that can be ascribed to autumn-winter and spring-summer, respectively. Then, the comparison with literature data has demonstrated that moderately-absorbing urban-industrial aerosols dominate in spring-summer and polluted-maritime aerosols dominate in autumn-winter in Lecce. The frequency distribution plot of the Angstrom coefficient Å (873/441 nm) confirmed last comment. It worth noting that Å is inversely related to the average size of the aerosol particles: Å >2 indicate the presence of fine mode particles such as sulfates and smoke particles, while Å< 2 indicate the presence of coarse mode particles such as dust. The Å frequency distribution plot has also revealed the presence of two modes,

one peaked at 1.58±0.03 that represents sea-salt and water soluble particles, one peaked at 0.7±0.1 that represents dust particles.

The particle chemical composition has been revealed by real *n* and imaginary *k* refractive index temporal plots and frequency of occurrences. The trimodal lognormal distribution fitting the *n* frequency of occurrence plot has allowed to recognize the main aerosol constituents: sea-salt and water soluble particles by the mode peaked at 1.32±0.01, soot and minerals by mode peaked at 1.58±0.08 and water soluble particles by the mode peaked at 1.44±0.03. In addition the *k* frequency of occurrence has revealed that moderately-absorbing aerosols dominate over south-east Italy. Finally, the study of the aerosol volume size distributions referring to high-AOD days that are affected by urban-industrial aerosols from Central and Eastern Europe and from Atlantic Ocean has shown that the total volume of the fine particles is clearly larger than the total volume of coarse mode particles and both increase with AODs.

- to study the mixing of different aerosol types over the Mediterranean, and hence the different properties related to aerosol of different origin by the combination of measurements from the AERONET station in Lecce and five-day backtrajectories. The combination of aerosol measurements from the AERONET station in Lecce between March 2003 and March 2004 with five-day backtrajectories has revealed that particles of different source origin are characterized by different aerosol properties. In particular, three broad geographical sectors were defined as aerosol source regions: Sector A, which includes all continental European sources with the exception of Spain; Sector B, which includes

the Southern Mediterranean Sea and the Africa continent; Sector C, which includes the Western Mediterranean, the Iberian Peninsula, and the Atlantic Ocean. The time spent by the trajectories in a sector up to the measurement day was also considered to better define the aerosol origin sector. It has been shown that the comparison between Sector A aerosol parameter mean values (AOD = 0.29±0.15, η = 0.93±0.03, SSA = 0.93±0.03, g = 0.67±0.03, and Lr = 72±20 sr) with previous investigations, reveal that a "continental average aerosol", mostly made of water soluble and a small amount of soot and insoluble component, is advected over south-east Italy from Sector A source regions. Then, Sector A air masses could be considered responsible of the transport of urban/industrial and biomass burning aerosols. The analysis of the Sector B aerosol parameters, which were characterized by AOD=0.29±0.05, η = 0.72±0.05, SSA = 0.94±0.03, g = 0.69±0.02, and Lr = 56±13 sr, revealed that desert dust particles advected over south-east Italy were also affected by the contribution of moderately-absorbing, fine-mode particles as those due to water soluble species: the predominant component of the "continental average aerosol" that is advected over the Mediterranean basin by the European continent. Hence, it was shown that polluted-desert dust particles were advected over south east Italy from Sector B source regions.

The comparison of Sector C aerosol parameter mean values (AOD = 0.27±0.17, η = 0.8±0.1, SSA = 0.94±0.03, g = 0.67±0.03, and Lr = 58±24 sr) with values reported by previous studies has shown that Sector C air masses were responsible of the advection over south-east

Italy of maritime-polluted aerosol due to marine and to lesser extent anthropogenic particles from the Atlantic Ocean and/or the Western Mediterranean regions. Finally, the results obtained by the application of an aerosol mask to the data points of Sector M (sector containing the aerosol considered due mostly to mixed source regions) showed that 80% of the 369 Sector M data points were representative of "continental average aerosol", while 14% and 6% of the data points were representative of maritime and desert-dust aerosol, respectively. The results obtained during this study have revealed that the aerosol characterization over the Mediterranean is complicated by the fact that a large number of sources and hence of aerosol species contribute to it

- to compare AERONET sunphotometer measurements performed at Lecce with similar MODIS data (e.g. aerosol optical depth, fine fraction parameter and volume size distribution) retrieved at different spatial resolutions. The aim of this work was to contribute to the validation of satellite's data and to understand when locally-derived aerosol parameters can be of use in General Circulation and Chemical Transport Models. In particular, in this thesis work aerosol parameters retrieved by AERONET sunphotometer measurements at the Physics Department of Lecce's University from March 2003 to September 2004, have been compared to corresponding MODIS satellite data retrieved at different spatial resolutions co-located in space and time, to contribute to the validation of MODIS aerosol products over south-east Italy and to identify regional biases of Lecce's AERONET data.

  Averaged values of ocean- and land-ocean-MODIS aerosol optical depths retrieved at 550 nm for window sizes of 50x50, 100x100, and

300x300 km^2 centered on Lecce, have been correlated to AERONET aerosol optical depths co-located in time. The regression lines parameters fitting ocean- and land-ocean MODIS AODs values have shown that MODIS overestimates *AOD* at low aerosol loadings and it is possible that this result is due to the fact that both the MODIS-ocean and mainly the MODIS-land algorithm underestimate the ground surface reflectance. Moreover, being the slopes of the regression lines fitting the scatterplots with land-ocean-MODIS aerosol optical depths closer to unity, the results could indicate that the land-ocean-MODIS aerosol optical depths better represent the aerosol properties over south-east Italy.

Finally, the temporal evolution of the MODIS fine fraction parameter η_M and of AERONET η_A values has instead revealed that η_M monthly means depend on seasons, while η_A is constant during all the year. It has been shown that it is possible that the marked seasonal evolution of η_M is due either to the autumn-winter regional variation of the aerosol properties and to the MODIS-ocean algorithm that underestimates the fine fraction contribution on autumn-winter months

The results of this research activity have also allowed inferring that AERONET aerosol optical depths retrieved at Lecce can be considered representative at least of a 300x300 km^2 area centered on Lecce and hence that locally-derived aerosol parameters can be of use in General Circulation and Chemical Transport Models based on spatial resolutions of few hundred kms.

- to characterize the main aerosol properties during the dust events. This interest has been due the fact that very large quantities of African dust

(60-200 x 10^8 tons yr^{-1}) are carried into the Mediterranean basin every year To this aim:

1. MODIS-ocean aerosol products and corresponding AERONET data from the spherical model retrieved at Lecce, Lampedusa, Oristano and Etna from 2003 to 2005 have been analyzed and correlated. In particular, we found that MODIS-ocean AODs were quite correlated to AERONET AODs co-located in space and time, but the plot of the differences (AOD_M - AOD_A) versus AOD_A has clearly revealed that (AOD_M - AOD_A) values are mostly positive and increase with AOD_A. Latter results have led assuming that MODIS overestimates AODs mainly during high dust load conditions, in accordance to the results provided by other authors and referring to different geographical areas. The temporal evolution of MODIS-ocean and AERONET fine-mode fractions co-located in space has shown that MODIS-ocean inversion algorithm overestimates the contribution of fine-mode particles for dust-dominated aerosols. Similar results have been reported by several authors and have been ascribed to the lack of assumption about dust non-sphericity in the MODIS aerosol model. The different definition of fine and coarse mode by the MODIS-ocean and AERONET inversion algorithm could also be responsible of the positive mean values of the (η_M - η_A) differences.

   Finally, the comparison of MODIS and AERONET mean volume size distributions co-located in space has shown that the MODIS-ocean algorithm is not able to catch the larger

contribution of coarse-mode particles during dust outbreaks. The result obtained in this section of research activity have suggested that the existing MODIS-ocean inversion algorithm in dust-dominated aerosol conditions should be improved, in accordance to previous studies.

2. A regional climate model (RegCM) has been used to simulate a dust outbreak and the results have been compared with experimental data. In fact, in the last months of my PhD course, my work has been devoted to the study and the implementation of the regional climate model RegCM which has been developed at the Abdus Salam International Centre for Theoretical Physics (ICTP) of Trieste. The RegCM model has been described in chapter 8. The main goal of this last part of my PhD activity has been to test the RegCM model performance in order to contribute to the establishment of models more dependent on measurements. In particular, for the test simulation we have considered two strong Saharan dust outbreaks that occurred in the second half of July 2003. A first simulation was done for a Mediterranean domain of 10010 km * 4542 km centered at latitude of 30º and longitude of 5º and a horizontal spacing of 50 Km, the second simulation for a Mediterranean domain that is smaller than the first (of ~ 4995km*2227km) but centered at the same point (at a latitude of 30º and a longitude of 5º), with a horizontal spacing of 50 Km.

   Comparisons with observation have shown that the RegCM model is able to simulate the occurrence of strong dust

outbreaks. In particular, comparisons between model data obtained over a domain of ~ 10010 km * 4542 km, with observation, have revealed that the AODs obtained by the RegCM model follows the same time evolution obtained by AERONET and MODIS Land-Ocean measurements over four investigated sites of the Mediterranean basin. However, the simulated AODs are not always well represented: the model tends to underestimates the aerosol load mainly on 17 July 2003. The comparison between the extinction coefficient $\alpha_{ext}(km^{-1})$ profiles obtained over two Mediterranean sites (Lecce and Etna) by RegCM and the corresponding profiles calculated by Lidar measurements have shown that the model is able to capture the dust amounts. We believed that the observed differences between Lidar and RegCM $\alpha_{ext}(km^{-1})$ profiles might be also attributed to the different wavelengths. In addition, we have noted that the accordance between the Lidar and RegCM $\alpha_{ext}(km^{-1})$ profiles makes worse for altitudes below about 2 km, both in Lecce and Etna.This last result might be due to the fact that for altitudes lower than 2 km there is an higher contribution of non dust aerosols.

Analogously to the AODs and the $\alpha_{ext}(km^{-1})$, the comparison between the temporal evolutions of the measured PTS and PM_{10} for two locations around Lecce and the RegCM PTS have shown that the model follows the time evolution but it underestimates and overestimates PTS mass concentrations during the first

event of 17 July and the second dust outbreak of 24 July 2003, respectively.

Finally, comparisons between experimental and RegCM AODs for a small domain of ~ 4995km*2227km have shown that the AOD values obtained by the implementation of a model run with a small domain are worse. The results reported in the chapter 8 have demonstrated the capability of the RegCM model to simulate dust events. However, these last results are only preliminary since they allowed us to evaluate the model performance from the scale of individual episodic events. It worth noting that to fully assess the climatic effects of aerosols, long-term multi-year simulations are required and, then, we are planning to conduct in future long term multiyear running including the different aerosol sources in addition to dust sources.

In conclusion, I believe that the results presented in this thesis on aerosol properties retrieved by sunphotometer, satellite, and model data have contributed to the characterization of the different aerosol types present over the Mediterranean. These studies are of great support to improve the understanding of the aerosol effects on the radiative Earth's balance.

APPENDIX

LIST OF SYMBOLS

Symbol	Quantity	Measurement Units
Radiative Quantities		
I	Intensity or Radiance	$W/m^2/sr$
ΔF_{TOA}	Direct Radiative forcing at the top of the atmosphere	W/m^2
ΔF_{BOA}	Direct Radiative forcing at the bottom of the atmosphere	
$\Delta F^{eff}{}_{TOA}$	Direct Radiative forcing efficiency at the top of the atmosphere	
$\Delta F^{eff}{}_{BOA}$	Direct Radiative forcing efficiency at the bottom of the atmosphere	
Aerosol		
α_{ext}	extinction coefficient	km^{-1}
Lr	lidar ratio	sr
AOD	aerosol optical depth	
SSA	single-scattering albedo	
η	Fine fraction parameter	

n	real part of the refractive index	
k	imaginary part of the refractive index	
g	asymmetry parameter	
$dV(r)/d\ln r$	volume size distribution	$\mu m^3/\mu m^2$
Å	Angstrom coefficient	
$P(\theta)$	Phase function	
r_{eff}	Effective radius	μm
PTS	Total suspended particulate matter concentration	$\mu g / m^3$
PM_{10}	Particulate matter concentration with diameter ≤ 10μm	$\mu g / m^3$

Angles

z, ϕ	zenith and azimuth angles
m	secant of the zenith angle

BIBLIOGRAPHY

Ackerman, J., 1998: The extinction-to-backscatter ratio of tropospheric aerosol: A numerical study. J. Atmos. Oceanic Technol., 15**,** 1043-1050.

Alfaro, S.C., and Gomes, L., 2001: Modelling mineral aerosol production by wind erosion: Emission intensities and aerosol size distributions in source areas, J. Geophys. Res., 106, 18075-18084.

Amiridis, V., Balis, D.S., Kazadzis, S., Bais, A., Giannakaki, E., Papayannis, A., and Zerefos, C., 2005 : Four-year aerosol observations with Raman lidar at Thessaloniki, Greece, in the framework of EARLINET, J. Geophys. Res., 110, D21203, doi :10.1029/2005JD006190.

Andenberg, M.R., 1973 : Cluster Analysis for Applications, Academic Press, New York

Anderson, T.L., Wu, Y., Chu, D.A., Schmid, B., Redemann, J., Dubovik, O., 2005: Testing the MODIS Satellite Retrieval of Aerosol Fine – Mode Fraction, J. Geoph. Res – Atmos*., 110***,** doi:10.1029/2005JD005978.

Ansmann, A., Bosemberg, J., Chaikovky, A., Eckhardt, S., Eixmann, R., Freudenthaler, V., Ginoux, P., Komguem, L., Linne, H., Marquez, M.A.L., Matthias, V., Mattis, I., Mitev, V., Muller, D., Music, S., Nickovic, S., Pelon, J., Sauvage, L., Sobolewsky, P., Srivastava, M.K., Stohl, A., Torres, O., Vaughan, G., Wandinger, U., Wiegner, M., 2003: Long-range transport of Saharan dust to northern Europe: the 11-16 October 2001 outbreak observed with EARLINET, J. Geophys Res*,* 108, 4783.

Anthes, R.A., 1977 : A cumulus parameterization scheme utilizing a one-dimensional cloud model, Monthly Weather Review, 105, 270-286.

Anthes, R.A :, Hsie, E.Y., and Kuo, Y.H., 1987 : Description of the Penn State/NCAR Mesoscale Model Version 4 (MM4), NCAR Tech. Note, NCAR/TN-282+STR, National Center for Atmspheric Research, Boulder, Colorado.

Avila, A., Queralt – Mitjans, Alarcon, M., 1997: Mineralogical composition of African dust delivered by red rains over the northeastern Spain, J. Geophys. Res. 102*,* 21,977 – 21,996.

Balis, D., Papayannis, A., Galani, E., Marenco, F., Sanatacesaria, V., Hamonou, E., Chazette, P., Ziomas, I., Zerefos, C., 2000: Tropospheric LIDAR aerosol measurements and sun photometric observations at Thessaloniki. Greece, Atmos. Environ. 34*,* 925 – 932.

Balis, D., Amiridis, V., Zerefos, C., Gerasopoulos, E., Andreae, M., Zanis, P., Kazantzidis, A., Kazadzis, S., Papayannis, A., 2003. Raman lidar

sunphotometric measurements of aerosol optical properties over Thessaloniki, Greece, during a biomass burning episode, Atmos. Environ. 37, 4529 – 4538.

Balis, D.S., Amiridis, V., Nickovic, S., Papayannis, A., and Zerefos, C., 2004 : Optical properties of Sahara dust layers as detected by a Raman lidar at Thessaloniki, Greece, Geophys. Res. Lett., 31, L13104, doi :10.1029/2004GL019881.

Barnaba, F., and Gobbi, G.P., 2004: Aerosol seasonal variability over the Mediterranean region and relative impact of maritime, continental and Saharan dust particles over the basin from MODIS data in the year 2001, Atmos. Chem. Phys., 4, 2367-2391.

Barnaba, F., Tafuro, A.M., De Tomasi, F., and Perrone M.R., 2007: Observed and simulated vertically resolved optical properties of continental aerosols over southeastern Italy: A closure study, J.Geophys. Res., 112, D10203, doi:10.1029/2006JD007926.

Baumgardner, D., G. B. Raga, G. Kok, J. Ogren, I. Rosas, A. Baez, and T. Novakov, 2000: On the evolution of aerosol properties at a mountain site above Mexico City, J. Geophys. Res., 105, 22243-22253.

Bellantone, V., Carofalo, I., De Tomasi, F., Perrone, M. R., Santese, M., Tafuro, A. M., and Turnone, A.: In situ samplings and remote sensing measurements to characterize aerosol properties over south-east Italy, in press.

Blanco, A., De Tomasi, F., Filippo, E., Manno, D., Perrone, M. R., Serra, A., Tafuro, A. M., Tepore, A., 2003: Characterization of African dust over southern Italy, Atmos. Chem. Phys. 3, 2147 – 2159.

Bohren C.F., Huffman D.R., 1998: Absorption and scattering of light by small particles, Wiley.

Cakmur, R. V., Miller, R.L:, and Torres, O., 2004: Incorporating the effect of small scale circulations upon dust emission in an AGCM, J. Geophys. Res., 109, D07201, doi: 10.1029/2003JD004067.

Cakmur, R. V., Miller, R.L., Perliwitz, J., Koch, D., Geogdzhayev, I.V., Ginoux, P., Tegen, I., and Zender, C.S., 2005: Constraining the global dust emission and load by minimizing the difference between the model and observations, available at http://pubs.giss.nasa.gov/authors/rmiller.html, J. Geophys. Res., in press.

Cattral, C., Reagan, J., Thome, K., and Dubovik, O., 2005 :Variability of aerosol and spectral lidar and backscatter and extinction ratios of key aerosol types derived from selected Aerosol Robotic Network locations, J. Geophys. Res., 110, doi :10.1029/2004JD005124.

Charlson, R.J., Langner, J., Rodhe, H., Leovy, C. B. and Warren, S. G., 1991: Perturbation of the northern hemispheric radiative balance by backscattering from anthropogenic surface aerosols, Tellus, 4AB, pp. 152–163.

Chu, D. A., Kaufman, Y. J., Remer, L. A., and Holben, B. N.,1998: Remote sensing of smoke from MODIS airborne simulator during the SCAR – B experiment, J. Geophys. Res., *103*, 31979- 31988.

Chu, D.A., Kaufman, Y.J., Ichoku, C., Remer, L.A., Tanrè, D., and Holben, B.N., 2002: Validation of MODIS aerosol optical depth retrieval over land, Geophys. Res. Lett. 29 (12), 8007, doi: 10.1029/2001GL013205.

Chu, D. A., Kaufman ,Y. J., Zibordi, G., Chern, J.D. , Mao, J., Li, C., and Holben, B., N. 2003: Global monitoring of air pollution over land from the Earth Observing System – Terra Moderate Resolution Imaging Spectroradiometer (MODIS), J. Geophys. Res., 108, 4661, doi:10.1029/2002JD003179.

Chu, D. A., Remer, L. A., Kaufman, Y. J., Schmid, B., Redemann, J., Knobelspiesse, K., Chern, J. – D., Livingston, J., Russel, P., Xiong, X, and Ridgway, W., 2005: Characterization of aerosol properties by MODIS during ACE-Asia experiment., J. Geophys. Res, 110, in press, doi:10.1029/20004JD005208

Colarco, P. R., Toon, O. B., Torres, O., Rash, P. J., 2002: Determining the UV imaginary index of refraction of Saharan dust particles from Total Ozone Mapping Spectrometer data using a three-dimensional model of dust transport, J. Geophys. Res. 107 No. D16, 10.1029/2001JD000903.

D'Almeida, G. A., Koepke, P., Shettle, E. P., 1991: Atmospheric aerosol–global climatology and radiative characteristics, 561 pp. A. Deepak, Hampton, V.

De Tomasi, F., Blanco, A., Perrone, M.R., 2003: Raman lidar monitoring of extinction and backscattering of África dust layers and dust characterization, Appl. Opt., 42, 1699-1709.

De Tomasi, F., Perrone, M. R., 2003. Lidar measurements of tropospheric water vapor and aerosol profiles over southeastern Italy. J. Geophys. Res. 108, 4286 – 4297.

De Tomasi, F., Tafuro, A. M., and. Perrone, M.R., 2006: Height and seasonal dependence of aerosol optical properties over south-east Italy, J. Geophys. Res., 111, D10203, doi;10.1029/2005JD006779.

Di Sarra, A., Di Iorio, T., Cacciani, M., Fiocco, G., and Fua', D., 2001 : Saharan dust profiles measured by lidar at Lampedusa, J. Geophys. Res., 106, 10335-10348.

Dickinson, R.E.R., Errico, M., giorni, F., and Bates G.T., 1989: A regional Climate model for the western U.S., Climate Ch'ange, 15, 383-422

Dickinson, R.E., Henderson-Sellers, A., and P.J. Kennedy, 1993: Biosphere-atmosphere transfer scheme (bats) version 1e as coupled to the NCAR community climate model, Tech. rep., national Center for Atmospheric Research.

Dubovik, O., and King, M. D., 2000a: A flexible inversion algorithm for retrieval of aerosol optical properties from Sun and sky radiance measurements, J. Geophys. Res. 105, 20,673 – 20,696.

Dubovik, O., Smirnov, A., Holben, B.N., King, M.D., Kaufman, Y.J., Eck, T.F., and Slutsker, I., 2000b: Accuracy assessments of aerosol optical properties retrieved from AERONET sun and sky-radiance measurements, J. Geophys. Res., 105, 9791-9806.

Dubovik, O., Holben, B. N., Eck , T. F, Smirnov, A., Kaufman, Y. J., King, M. D., Tanre, D., Slutsker, I., 2002a: Variability of absorption and optical properties of key aerosol types observed in worldwide locations. J. Atmos. Sci. 59, 590 – 608.

Dubovik, O., Holben, B.N., Lapyonok, T., Sinyk, A., Mishechenko, M.I., Yang, P., and Slutsker, I., 2002b: Non-spherical aerosol retrieval method employing light scattering by spheroids, J. Geophys. Res. Lett., 29, 54-1 - 54-4.

Dubovik, O., 2004: Optimization of Numerical Inversion in Photopolarimetric Remote Sensin, in Photopolarimetry in Remote Sensing (G. Videen, Y. Yatskiv and M. Mish-chenko, Eds.), Kluwer Academic Publishers, Dordrecht, Netherlands, 65-106.

Dubovik, O., A. Sinyuk et al., 2006: Ehnanced retrieval of aerosol properties from atmospheric radiation measured by AERONET Sun/sky radiometers. In preparation.

Duncan, B. N., and Bey I., 2004 : A modelling study of the export pathways of pollution from Europe : seasonal and interannual variation (1987-1997), J. Geophys. Res., 109, D08301, doi :10.1029/2003JD004079.

Eck, T.F., Holben, B.N., Reid, J.S., Dubovik, O., Smirnov, A., O'Neill, N.T., Slutsker, I. and Kinne, S., 1999: Wavelength dependence of the optical depth of biomass burning, urban and desert dust aerosols, J. Geophys. Res., 104, 31 333-31 350.

Fecan, F., Marticorena, B., and Bergametti, G., 1999: Parameterization of the increase of aeolian erosion threshold wind friction velocità due to soil misture for arid and semi-arid areas, Ann. Gedophys., 17, 149-157.

Formenti, P., Reiner, O., Sprung, D., Andreae, M.O., Wendisch, M., Wex, H., Kindred, D., Dewey, K., Kent, J., Tzortziou, M., vasaras, A., and Zerefos, C., 2002 : The STAARTE-MED 1998 summer airborne measurements over the Aegean Sea :1. Arosol particles and trace gases, J. Geophys. Res., 107, 4450, doi : 10.1029/2001JD001337.

Formenti, P., Andreae, M.O., Andreae, T.W., Galani, E., Vasaras, A., Zerefos, C., Amidiris, V., Orlovsky, L., Karnieli, A., Wendisch, M., wex, H., Holben, B.N., Maenhaut, W., and lelieveld, J., 2001a : Aerosol optical properties and large scale transport of air masses : Observations at a coastal and a seniarid site in the eastern Mediterranean during summer 1998, J. Geophys. Res., 106, 9807-9826.

Formenti, P., Andreae, M. O., Ichoku, C., Andreae, T. W., Schebeske, G., Kettle, A. J., Maenhaut, W., Cafmeyer, J., Karnieli, A., Lelieveld, J., 2001b: Phisical and chemical characteristics of aerosols over the Negev desert (Israel) during summer 1996, J. Geophys. Res. 106, 4871 – 4890.

Fotiadi, A., Hatzianzstassiou, N., Drakakis, E., Matsoukas, C., Pavlakis, K.G., Hatzidimitriou, D., Gerasopoulos, E., Mihalopoulos N., and Vardavas I., 2006 : Aerosol physical and optical properties in the eastern Mediterranean Basin, Crete, from Aerosol Robotic Network data, Atmos. Chem. Phys., 6, 5399-5413.

Gao, B.C., Kaufman, Y.J., Tanrè, D., and Li., R. –R., 2002 : Distinguishing tropospheric aerosols from thin cirrus clouds for improved aerosol retrieval using ratio of 1.38μm and 1.24 μm channels, Geophys. Res. Lett., 29, 1890, doi :10.1029/2002GL015475.

Gerasopoulos, E., Andreae, M. O., Zerefos, C. S., Andreae, T. W., Balis, D., Formenti, P., Merlet, P., Amiridis, V., Papastefanou, C., 2003. Climatological aspects of aerosol optical properties in Northern Greece. Atmos. Chem. Phys. 3, 2025-2041.

Giorgi, F., marinucci, M.R., and Bates, G.T., 1993a: Development of a second generation regional climate model (RegCM2), Boundary-layer and radiative transfer process, Mon. Weather Rev., 121, 2794-2813, 199a.

Giorgi, F., Marinucci, M.R., Bates, G.T., and De Canio, G., 1993b: development of a second generation climate model (RegCM2), Convective processes and assimilation of lateral boundary conditions, Mon. Weather Rev., 121, 2814-2832.

Giorgi, F., and Marinucci, M.R., 1996: An investigation of the sensitivity of simulated precipitation to model resolution and its implications for limate studies, J. Weath. Rev., 124, 148-166.

Giorgi, F., Huang, Y., Nishizawa, K., and Fu, C., 1999a: A seasonal cycle simulation over eastern Asia and its sensitivity to radiative transfer and surface processes, J. Geophys. Res., 104, D6, 6403-6423.

Giorgi, F., and Mearns, L.O., 1999b: Regional Climate modeling revisited, An introduction to the special issue, J. Geophys. Res., 104, 6335-6352.

Giorgi, F., and Shields, C., 1999: Tests of precipitation parameterizations available in the latest version of the NCAR regional climate model (RegCM) over continental U.S:, J. Geophys. Res., 104, 6353-6375.

Giorgi, F., Bi, X., and Qian, Y., 2002: Direct radiative forcing and regional climate effects of anthropogenic aerosols over East Asia: a regional coupled climate-chemistry/aerosol model study, J. Geophys. Res., 107, AAC7.

Giorgi, F., Bi, X. Q., and Qian, Y., 2003: Indirect vs direct effects of anthropogenic sulphate on the climate of East Asia as simulated with a regional coupled climate-chemistry/aerosol model, Climate Change, 58, 345-376.

Gong, S.L., Zhang, X.Y., Zhao, T.L., McKendry, I.G., j_e, D., A., and Lu, N.M., 2003: Characterization of soil dust aerosol in China and its transport and distribution during 2001 ACE-Asia: 2.tion Model simulation and validation, J. Geophys. Res., 108, 4262, doi:10.1029/2002JD002633.

Grell, G.A., Dudhia, J., and Stauffer, D.R., 1994: description of the fifth generation Penn State/NCAR Mesoscale Model (MM5), Tech. Rep. TN-398+STR, NCAR, Boulder, olorado, pp. 121.

Guibert, S., Matthias, V., Schulz, M., Bosenberg, J., Eixmann, R., Mattis, I., Pappalardo, G., Perrone, M R., Spinelli, N. and Vaughan, G., 2005: The vertical distribution of aerosol over Europe-synthesis of one year of EARLINET aerosol lidar measurements and aerosol transport modeling with LMDzT-INCA, Atmos. Environ, *39*, 2933-2943.

Hansen, J.E., and Travis, L.D., 1974: Light scattering in planetary atmospheres, Space Sci. Rev., 16, 527-610, doi:10.1007/BF00168069.

Hatzianastassiou, N., Katsoulis, B., and Vardavas, I., 2004: Global distribution of aerosol direct radiative forcing in the ultraviolet and visible arising under clear skies, *Tellus, 56B*, 4679-4690.

Hess, M., Koepke, P., Schult, I., 1998: Optical properties of aerosols and clouds: The software package OPAC. Bulletin of the American Meteorological Society 79, 831 - 844.

Hignett, P., J. P. Taylor, P.N. Francis, and M.D. Glew, 1999: Comparison of observed and modeled direct aerosol forcing during TARFOX, J. Geophys. Res., 104, 2279-2287.

Holben, B. N., Eck, T. F., Slutsker, I., Tanre, D., Buis, J. P., Setzer, A., Vermote, E., Reagan, J. A., Kaufman, Y. J., Nakajima, T., Lavenu, F., Jankowiak, I., Smirnov, A., 1998: AERONET – A federal instrument network and data archive for aerosol characterization, Remote Sens. Environ. 66*,* 1-16.

Holtslang, A.A:M., de Bruijn, E.I.F., and Pan, H.L., 1990: A high resolution air mass transformation model for short-range weather forecasting, Mon.Wea. rev., 188, 1561-1575.

Husar, R. B., Prospero, J.M., Stowe, L.L., 1997: Characterization of tropospheric aerosols over the oceans with the NOOA advanced very high resolution radiometer optical thickness operational product, J. Geophys. Res*.,* 102, 16889-16909.

Ichoku, C., Chu, D. A., Mattoo, S., Kaufmann, Y.J., Remer, L.A., Slutsker, D. I. and Holben, B.N., 2002: A spatio-temporal approach for global validation and

analysis of MODIS aerosol products, Geophys. Res. Lett., 29**,** doi:10.1029/2001GL013206.

Ichoku, C., Kaufman, Y. J., Remer, L.A., and Levy, R., 2004: Global aerosol remote sensing from MODIS, Adv. Sp. Res*.,* 34, 820-827.

Ichoku, C., Remer, L.A. and Eck, T.F., 2005: Quantitative evaluation and intercomparison of morning and afternoon MODIS aerosol measurements from the Terra and Aqua satellites, J. Geophys. Res., in press.

IPCC, *Climate Change 2001,*IPCC Third Assessmsnt Report, New york, 2000.

Jaenicke, R., and Schutz, L., 1978: A comprehensive study of physical and chemical properties of the surface aerosols in the Cape Verde Islands region, J. Geophys. Res*.,* 83, 3583 – 3599.

Joussame, S., 1990: Three-dimensional simulation of the atmospheric cycle of desert dust particles using a genera circulation model, J. Geophys. Res., 95, 1909-1941.

Kalkstein, L. S., Tan, G., and Skindlov, J. A., 1987 : An evaluation of three clustering procedures for use in synoptic climatological classification, J. Climate Appl. Meteor., 26, 717-730.

Kaufman, Y.J., and Remer, L.A., 1994: Detection of forests using mid-IR reflectance-An application for aerosol studies, IEE Trans. Geosci. Remote Sens*., 32*, 672-683.

Kaufman, Y. J., Wald, A. E., Remer, L. A., Gao, B.-C., Li, R.-R. and Flynn, L., 1997a: The MODIS 2.1 μm Channel – Correlation with visible reflectance for use in remote sensing of aerosol, IEEE Transactions On Geoscience and Remote Sensing., 35**,** 1286 – 1298.

Kaufman, Y.J., , Wald, A. E., Remer, L.A., Gao, B.C., Li, R. R., and Flynn, L., 1997b: The MODIS 2.1μm channel-Correlation with visible reflectance for use in remote sensing of aerosol, IEEE Trans. Geosci. Remote Sens., 25, 1286-1298.

Kaufman, Y.J., Smirnov, A., Holben, B.N., and Dubovik, O., 2001: Baseline maritime aerosol: methodology to derive the optical thickness and scattering properties, J.Geoph. res. Lett., 28, No. 17, 3251-3254.

Kaufman, Y.J., D. Tanre', and O. Boucher, 2002: A satellite view of aerosols in the climate system. Nature*, 419***,** 215-223.

Kaufman, Y.J., Koren, I., Remer, L. A., Tanré, D., Ginoux, P. and Fan, S.,2005a: Dust transport and deposition observed from the Terra-Moderate Resolution Imaging Spectroradiometer (MODIS) Spacecraft over the Atlantic Ocean, J. Geoph. Res., 110, D10S12, doi: 10.1029/2003JD004436.

Kaufman, Y.J.,. Remer, A. L, Tanré, D., Li, R-R., Kleidman, R., Matoo. S., Levy, R. C., Eck, T. F., Holben, B. N., Ichoku, C., Vanderlei Martins, J., and Koren, I., 2005b: A critical examination of the residual cloud contamination and diurnal sampling effects on MODIS estimates of aerosol over ocean, IEEE Trans. Geosci. Remote Sens., 43, 2886 – 2897.

Kazadzis, S., Bais, A., Amidiris, V., Balis, D., Meleti, C., Kouremeti, N., Zerefos, C. S., Rapsomanikis, S., Petrakakis, M., Kelesis, A., Tzoumaka, P., and Kelektsoglou, K., 2007: Nine years of UV aerosol optical depth measurements at Thessaloniki, Greece, Atmos. Chem.Phys., 7, 2091-2101.

Kiehl, J.T., Hack, J.J., Bonan, G.B., Boville, B.A :, Briegleb, B.P., Williamson, D.L., and Rash, P.J., 1996 : description of the NCAR Community Climate Model (CCM3) NCAR Techni. Note, NCAR/TN-420+STR, 152pp.

King, M. D., Kaufman, Y.J., Tanre', D., and Nakajima, T.,1999: Remote sensing of tropospheric aerosols from space: Past, present, and future, Bull. Amer. Meteor. Soc., *80*, 2229-2259.

Kinne S., Lohmann, U., Feichter, J., Schulz, M., Immreck, C., Ghan, S., Easter, R., Chin, M., Ginoux, P., Takemura, T., Tegen, I., Koch, D., Herzog, M., Penner, J., Pitari, G., Holben, B., Eck, T., Smirnov, A., Dubovik, O., Slutsker, I., Tanré, D., Torres, O., Mishchenko, M., Geogdzhayev, I., Chu, D. A., and Kaufman, Y.,2003: Monthly averages of aerosol properties: A global comparison among models, satellite data, and AERONET ground data, J. Geophys. Res., *108,* 4634, doi:10.1029/2001JD001253.

Kleidman R.G., O'Neill, N.T., Remer, L.A., Kaufman, Y.J., Eck, T.F., Tanré, D., Dubovik, O. and Holben, B., 2005: Comparison of Moderate Resolution Imaging Spectroradiometer (MODIS) and Aerosol Robotic Network (AERONET) remote-sensing retrievals of aerosol fine mode fraction over ocean, J. Geoph. Res.,110, doi:10.1029/2005JD005760.

Koepke, P., M. hess, I. Schult, and E.P. Shettle, 1997 : Global aerosol data set, MPI Meteorologie Hamburg Rep., 243, 44 pp.

Kottmeier, C., Fay, B., 1998: Trajectories in the Antartic lower troposphere, J. Geophys. Res. 105, 10,947 – 10,959.

Lelieveld, J., Berresheim, H., Borrmann, S., et al., 2002: Global air pollution crossroads over the Mediterranean, Science, 298, 794-799.

Leung, R., Mearns, L., Giorgi, F., and Wilby R.,1989: Regional Climate Reasearch, BAMS, 89-95.

Levoni, C., Cervino, M., Guzzi, R., Torricella, F., 1997: Atmospheric aerosol optical properties: a database of radiative characteristics for different components and classes, Appl. Optics 36, 8031-8041.

Levy, R.C., and Coauthors, 2003: Evaluation of the MODIS retrievals of dust aerosol over the ocean during PRIDE, J. Geophys. Res., *108*, 8594, doi:10.1029/2002JD002460.

Levy, R. C., Remer, L. A., Martins, J. V., and Kaufman, Y. J., 2005: Evaluation of the MODIS Aerosol Retrievals over Ocean and Land during CLAMS, J. Atmos. Sci*., 62*, 974 – 992.

Li, R. –R., Kaufman, Y.J., Gao, B.C., and Davis, C.O., 2003: Remote sensing of suspended sediments and shallow coastal waters, IEEE Trans. Geosci. Remote Sens., 41, 559-566.

Liou. K.,1980: An introduction to Atmospheric Radiation, Academic Press, 19-25.

Luo, C., Mahowald, N., and del Corral., J., 2003: Sensitivity study of meteorological parameters aon mineral aerosol mobilization, transport and distribution, J. Geophys. Res., 108(D15), 4447, doi:10.1029/2003JD0003483.

Lyamani, H., Olmo F.J., and Alados-Arboledas, L., 2004: Long-term change in aerosol radiative properties at Armilla, Atmospheric Environment, 38, pp. 5935–5943.

Marticorena, B., and Bergametti, G., 1995: Modeling the atmospheric dust cycle, I, Design of soil-derived dust emissiom scheme, J. Geophys. Res., 100, 16416-16430.

Marticorena, B., Bergametti, G., Amount, B., Callot, Y., N'Doume, C., and Legrand, M., 1997a°: Modeling the atmospheric dust cycle,2, Simulation of Sahara sources, J. Geophys. Res., 102, 4387-4404.

Marticorena, B., Bergametti, G., Gilette, D.A., and Belnap, J., 1997b: Factors controllino threshold friction velocity in semiarid areas of the United States, J. Geophys. Res., 102, 23277-23287.

Martins, J.V., Tanrè, D., Remer, L.A., Kaufman, Y.J., Matoo, S., and Kevy, R., 2002: MODIS cloud screening for remote sensing of aerosol over oceans using spatial variability, Geophys. Res Lett., 29, 80009, doi: 10.1029/20001GL01352.

Matthias et al., 2002 : Aerosol climatology for the planetary boundary layer derived from regular lidar measurements, Atm. Res, 63, 221-245.

Meloni, D. A. di Sarra, T. Di Iorio, G. Fiocco, 2005 : Influence of vertical profile of Saharan dust on the visible direct radiative forcing, J. of Quant. Spectr. & Rad. Transf. 9, 397-413.

Mihalopoulos, N., Stephanou E., Kanakidou, M., Pilitsidis, S., and Bousquet, P., 1997 : Tropospheric aerosol ionic composition in the eastern Mediterranean region, Tellus B*,* 49, 314-326.

Moody, J. L., 1986 : The influence of meteorology on precipitation chemistry at selected sites in the Eastern United States. Ph.D. dissertation, University of Michigan, Ann Arbor, 176 pp.

Moody, J. L., and Galloway, J.N., 1998 : Quantifying the relationship between atmospheric transport at two sites in the midwestern United States, Atmos. Environ., 23, 2117-2132.

Muller, D., Mattis, I., Wandinger, U., Ansmann, A., Althausen, D., Dubovik, O., Eckhardt, S., and Stohl, A., 2003 : Saharan dust over a central European EARLINET-AERONET site : Combined observations with Raman lidar and Sun photometer, J.Geophys.Res., 108(D12), 4345, doi :10.1029/2002JD002918.

Nickovic, S., Kallos, S., Papadopoulos, A., and Kakaliagou, O. , 2001 : A model for prediction of desert 25 dust cycle in the atmosphere, J. Geophys. Res., 106, 18113-18129.

O'Neill, N.T., and Miller, J.R., 1984 : Combined solar aureole and solar beam extinction measuremewnts. 1 : Calibration considerations., APpl. OPt., 23 :3691-3696.

O'Neill, N. T., Ignatov, A., Holben, B., Eck, T. F., 2000: The lognormal distribution as a reference for reporting aerosol optical depth statistics; Empirical tests using multi–year, multi-site AERONET sunphotometer data, Geophys. Res. Lett. 27, 3333-3336.

O' Neill, N. T., Dubovik, O. and Eck, T. F., 2001 : A modified angstrom coefficient for the characterization of sub-micron aesosols, Appl. Opt., 40(15), 2368-2374.

O'Neill, N. T., Eck, T. F., Smirnov, A., Holben, B. N. and Thulasiraman, S., 2003 : Spectral discrimination of coarse and fine mode optical depth, J. Geoph. Res., 108(D17), 4559, doi : 10.1029/2002JD002975.

Pace, G., di Sarra, A., Meloni, D., Piacentino, S., and Chamard, P., 2006: Aerosol optical properties at Lampedusa (central Mediterranean) 1. Influence of transport and identification of different aerosol types, Atmos. Chem. Phys., 6, 697-713.

Pal, J.S., Small, E.E., and Elthair, E.A:B., 2000: Simulation of regional-scale water and energy budgets:Representation of subgrid cloud and precipitation processes within RegCM, J. Geophys. Res. Atmospheres, 105(D24), 29,579-29,594.

Papayannis, A. Balis, D., Bais, A., van der Bergh, H., Calpini, B., Durieux, E., Fiorani, L., Jaquet, L., Ziomas, I., and Zerefos, C.S., 1998 : The role of urban and suburban aerosols on solar UV radiation over Athens, Greece, Atmos. Environ., 21, 2193-2201.

Papayannis, A., Balis, D. Amidiris, V., Chourdakis, G., Tsaknakis, G., Zerefos, C., Castanho, A. D. A., Nickovic, S., Kadzadzis, S., and Grabowsky, J., 2005 : Measurements of Saharan dust aerosols over the Eastern Mediterranean using elastic backscatter-Raman lidar, spectrophotometric and satellite observations in the frame of the EARLINET project, Atmos. Chem. Phys., 5, 2065-2079.

Patterson, K. G., Hatzidimitriou, D., Matsoukasl, C., Drakakis, E., Hatzianastsssiou, N., Vardavas, I., 2004 : Ten-year global distribution of downwelling longwave radiation, Atm. Chem. Phys., 4, 127-142.

Perrone, M.R., Santese, M., Tafuro, A.M., Holben, B., and Smirnov, A., 2005: Aerosol load characterization over South-East Italy for one year of AERONET sun-photometer measurements, Atmos. Res., 75, 111-133.

Platnick., S., King, M.D., Ackerman, S.A., Menzel, W.P., Baum, B.A., Riedi, J.C., and Frey, R.A., 2003: The MODIS cloud products: Algorithm and examples from Terra, IEEE Trans. Geosci. Remote Sens., 41, 459-473.

Prospero, J. M., and Carlson, T. N., 1972 : Vertical and areal distribution of Saharan dust over the western equatorial North Atlantic, J. Geophys. Res., 77, 5255-5265, 1972.

Prospero, J.M., Ginoux, P., Torres, O., Nicholson, S. E., and Gill, T. E., 2002: Environmental characterization of global sources of atmospheric soil dust identified with the nimbus 7 total ozone mapping spectrometer (TOMS) absorbing aerosol product, Rew. Geoph., 40, 2(1)- 2(31).

Ramanathan and coauthors, 2001: Indian ocean experiment: an integrated analysis of the climate forcing and effects of the great Indo-Asian haze, J. Geophys. Res., 106, 28731-28398.

Remer, L.A., and Kaufman, Y.J., 1998: Dynamic aerosol model: Urban/Industrial aerosol., J. Geophys. Res., 103, 13859-13871.

Remer, L.A., A. E. Wald, and Y. J. Kaufman, 2001: Angular and seasonal variation of spectral surface reflectance ratios: Implications for the remote sensing of aerosol over land, IEE Trans. Geosc. Remote Sens., 39, 275-283.

Remer, L.A., Tanré, D., Kaufman, Y. J., Ichoku, C., Matoo, S., Levy, R., Chu, D. A., Holben, B., Dubovik, O., Smirnov, A., Martins, J.V., Li, R.-R. and Ahmad, Z., 2002: Validation of MODIS aerosol retrieval over ocean, Geoph. Res Lett., 29, doi:10.1029/2001GL013204.

Remer, L.A.,. Kaufman, Y.J., Tanré, D., Mattoo, S., Chu, . D. A., Martins, J.V., Li, R.-R., Ichoku, C., Levy, R. C., Kleidman, R. G., Eck, T. F., Vermote, E., & Holben, B. N., 2005 : The MODIS aerosol algorithm, products and validation. J. Atmos. Sci., 62, 947-973.

Robles Gonzalez, C., Schaap, M., de Leeuw, G., Builtjes, P. J. H., van Loon, M. , 2003. Spatial variation of aerosol properties over Europe derived from satellite observations and comparison with model calculations. Atmos. Chem. Phys. 3, 521-533.

Russell., P.B., and Coauthors, 1999: Aerosol-induced radiative flux changes off the United-States mid-Atlantic coast:Comparison of values calculated from sunphotometer and in situ data with those measured by airborne pyranometer, J. Geophys. Res., 104, 2289-2307.

Santese, M., De Tomasi, F., and Perrone, M.R., 2007: AERONET versus MODIS aerosol parameters at different spatial resolutions over southeast Italy, J. Geophys. Res., 112, doi:10.1029/2006JD007742.

Satheesh, S.K., 2002: Aerosol radiative forcings over tropical Indian Ocean: Modultion by sea-surface winds, Current Science, 82, 310-316.

Schimel, D. et al., 1996: Radiative forcing of climate change, in Climate change 1995: The Science of Climate Change, Contribution of Working Group I to the Second Assessment Report of the Intergovernmental Panel for Climate Change (IPCC), edited by J.T. Houghton et al., chapter 2 , pp. 65-130, Chambridge University Press, New York.

Shettle, E. P., and R. Fenn, 1979: Models of aerosols of lower troposphere and the effect of humidity variations on their optical properties, AFCRL, Tech. Rep. 79 0214, air Force Chambridge Research Laboratory, Hanscom Air Force Base, MA, 100pp.

Smirnov A., Holben, B. N., Eck, T. F., Dubovik, O., Slutsker, I., 2000:Cloud-Scrining and Quality Control Algorithms for AERONET Database. Rem. Sensing of Environm. 73, 337-349.

Smirnov, A., Holben, B.N., Kaufman, Y.J., Dubovik, O., Eck, T.F., Slutsker, I., Pietras, C., Halthore, R.N., 2002: Optical properties of atmospheric aerosol in maritime environments, J. Atmos. Sci., 59, 501-523.

Smirnov A., Holben, B. N., Dubovik, Eck, T. F., Slutsker, I., 2003. Maritime component in aerosol optical models derived from Aerosol Robotic Network data. J. Geophys. Res. 108, doi:10.102972002JD002701.

Smith, W.L., Charlock, T.P., Kahn, R., Martins, J.V. and Remer, L.,2005: EOS-TERRA aerosol and radiative flux validation, 2004: An overwiev of the Chesapeake Lighthouse and Aircraft Measurements for Satellites (CLAMS) experiment, J. Atmos. Sci., *62*, 903-918.

Smolik J., V. Zdimal, J. Schwartz, M. Lazaridis, V. Harnvanek, K. Eleftheridis, N., Mihalopoulos, C. Bryant, and I. Colbeck, 2003: Size resolved mass concentrations and chemical composition of atmospheric aerosols over the eastern Mediterranean area, Measurements of 15 Particulate Matter, Atmos. Chem. Phys., 3, 2207-2216.

Sokolik, I. N., Toon, O. B., 1999: Incorporation of mineralogical composition into models of the radiative properties of mineral aerosol from UV to IR wavelength, J. Geophys. Res. 104, 9423-9444.

Sokolik,I. N., Winker, D. M., Bergametti, G., Gilette, D.A., Carmichael, G., Kaufman, Y., Gomes, L., Schuetz, L. and Penner, J.E., 2001: Introduction to special section: Outstanding problems in quantifying the radiative impacts of mineral dust, Geophys. Res*., 106,* 18,015-18,028.

Solmon, F., Giorgi, F., and Liousse, C., 2006: Aerosol modeling for regional climate studies: Application to anthropogenic particles and evaluation over a European/African domain, Tellus B, 58(1), 57-72.

Song, C.H., and Carmichael, G.R., 2001: A three-dimensional modeling investigation of the evolution processes of dust and sea-salt particles in Asia, J. Geophys. Res., 106, 18131-18154.

Stohl, A., Eckhardt, S., Forster, C., James, P., and Spichtinger, N., 2002 : On the pathways and timescales of intercontinental air pollution transport, J. Geophys. Res., 107(D23), 4684, doi :10.1029/2001JD001396.

Tafuro, A. M., Barnaba, F., De Tomasi, F., Perrone, M.R. and Gobbi, G.P., 2006: Saharan dust particle properties over the central Mediterranean, Atmos. Res*.,* 81, 67-93.

Tanre', D., Herman, M., and Mattoo, S., 1997: Remote sensing of aerosol properties over oceans using the MODIS /EOS spectral radiances, J. Geophys. Res., 102**,** 16971-16988.

Tanré, D., Remer, L.A., Kaufman, Y.J., Mattoo, S., Hobbs, P.V., Livingston, J.M., Russel, P.B., and Smirnov, A., 1999 :Retrieval of aerosol optical thickness and size distribution over ocean from the MODIS Airborne Simulator during TARFOX, J.Geophys. Res., 104, 2261-2278.

Tripathi, S. N., Sagnik, Dey , Chandel, A., Srivastava, S., Ramesh, Singh, P. and Holben, B., 2005: Comparison of MODIS and AERONET derived aerosol optical depth over the Ganga Basin, India, Annales Geophysicae*,* 23, 1093-1101

Volger P., Bosenberg, J., Schult, I., 1996. Scattering properties of selected model aerosols calculated at UV-wavelengrhs: implications for DIAL measurements of tropospheric ozone. Beitr. Phys. Atmosph. 69*,* 177 – 187.

Wurzler, S., Reisin, T.G., and Levin, Z., 2000: Modification of mineral dust particles by cloud processing and subsequent effects on drop size distributions, J. Geophys. Res*.,* 105, 4501-4512.

Zakey, A.S., Solmon, F. and Giorgi, F., 2006: Implementation and testing of a desert dust module in a regional climate model, Atmos. Chem. Phys., 6, 4687-4704.

Zender, C.S., Miller, R.L., and Tegen, I., 2004: Quantifying mineral dust mass budgets: terminology, constraints and current estimates, Eos. Trans. Am., Geophys. Union, 85, 48, 509-512.

Zhao, T.X.-P., Stowe, L.L., Smirnov, A., Corsby, D., Sapper, J., and McClain, C. R., 2002: Development of a global validation package for satellite oceanic aerosol optical thickness retrieval based on AERONET observations and its application to NOAA/NESDIS operational aerosol retrievals, J. Atmos. Sci., *59*, 294-312.

Zobler, L.A., 1986: World Soil File for Global Climate Modelling, NASA Technical Memorandum 87892, NASA Goddard Institute for Space Studies (GISS), 2880 Broadway, New York, N.Y. 10025, USA.